IMPERIAL

High-Harmonic Generation in Solids: Exploring Bulk Crystals in the Ultrafast Strong-Field Excitation Regime

Hortense Ermelinde Elisabeth ALLEGRE

July 2025

Department of Physics

Imperial College London

Submitted in part fulfilment of the requirements for the degree of

Doctor of Philosophy of Imperial College London

Abstract

High Harmonic Generation (HHG) is a nonlinear process where intense laser fields produce coherent Extreme Ultraviolet (XUV) or soft X-ray radiation. Recently, HHG in solids has gained interest as a spectroscopic tool for resolving attosecond dynamics and as a compact XUV source for industries like semiconductors. Solids, with their higher density of emitters compared to gases, offer the potential for more efficient XUV light emission, making it crucial to understand electron motion within their bands.

This thesis presents an experimental study of HHG in semiconductor ZnO and dielectric MgO. We report the highest recorded photon energy for a harmonic in a solid sample, reaching 50 eV (31^{st} harmonic) in 100 µm thick MgO, using a 780 nm, 30 fs driving pulse. The optical setup, including the focusing regime and flat-field spectrometer, was optimized. Additionally, we study the impact of laser pulse duration on solid high harmonics in MgO, finding no simple correlation between pulse duration and cutoff.

In ZnO, we explore the interplay between electron trajectories and the Carrier-Envelope Phase (CEP) of the laser pulse, demonstrating that CEP dependence provides information on long and short electron trajectories in high-order harmonics. Furthermore, a systematic HHG efficiency study is performed, comparing the cutoff and the harmonic yield of multiple samples in two different regimes: (i) wide bandgap dielectrics illuminated with a Near-Infrared (NIR) wavelength and (ii) semiconductors irradiated with a Mid-Infrared (MIR) field. We find that sample parameters like exciton binding energy and nearest neighbour distance can predict harmonic yield efficiency.

This work suggests that our current understanding of HHG may need expansion and highlights the potential of solid-state HHG, paving the way for further efficiency studies.

Acknowledgements

I would like to thank all the people who have helped me throughout this journey. Firstly, I would like to express my gratitude to both my supervisors, Dr. Mary Matthews and Prof. John Tisch for their guidance and insights throughout this work. More particularly, I sincerely thank Mary, for giving me the amazing opportunity to undertake this project, for broadening my field of expertise by asking challenging questions on my results, inspiring me to push the boundaries of my research and for fun delicious groups dinner, and John, for welcoming me in his lab and giving me support and feedback all along the way. I would also like to thank Jon Marangos for welcoming me in the Extreme Light Consortium and for the advice on my work.

This work would not have been possible without the support of my fellow students from the Extreme Light Consortium. I would like to thank Rose for being an amazing member of the CLITS group, for the conferences trips together, for the constant emotional support. Joey, for the reliable support he has been for me since he joined our group, his patient encouragements, his guidance and challenging ideas helped me become the scientist I am today. Tim, for all the chats we had that helped me widen my understanding of specific subjects. Fruit Club was a great support while writing up. To Jacob, Oli and Sam for the many pub trips and chats about dealing with my PhD and dare I say, for playing board games. Thank you also to Kasia, for the help and advice and to Clément for fruitful chats and experimental recommendations. Thank you also to Yan for sharing the lab. I would like to thank other students who shared with me the PhD adventures in other groups: to Emma, our coffees and lunches on level 8 were always an appeasing moment I was looking forward to. To Steven, demonstrating with him was a highlight in my week.

The technical team at Imperial has been of tremendous help and I would like to thank Susan for her help on repairing equipment and Andy for his amazing work in the workshop, making our ideas come alive.

To Clotilde, my flatmate, thank you for coping with my endless chat about my work, for all our catchups, sharing our PhD's ups and downs together. I would not have made it through without the support of my friends. Thank you to Cerise and Garance for well deserved breaks across the English countryside. Thank you to all my friends who made the trip from France to visit and bring some support: Anna, Marine, Célia, Maï-Trâm, Coline and Hélène, Maxime, Maguelone, Raphaëlle and Antoine, Claire and Camille, Gaspard, Tristan, Elie and Clément. Special thanks to Serena, we started the journey together and kept going together even with a sea between us.

I want to express my gratitude to Christine, my honorary godmother, who have accompanied me through the journey, our monthly walks in the park and catchups were so appreciated, thank you for your warm welcome in London.

Jonathan, you have been my unwavering supporter, you have coped with me every moment, forced me to go outside when needed, have helped me going when it was tough, thank you. I am so grateful to my family, my parents Florence and Frédéric and siblings Constance and Theddy, who have accompanied me with patience and encouragement. And also my grandparents Lucie, Paul, Catherine and Maurice who have seen me grow in the person I am today.

Declaration

I hereby declare that the work presented in this thesis is entirely my own unless cited, acknowledged or declared otherwise.

Hortense Ermelinde Elisabeth ALLEGRE

Copyright Statement

The copyright of this thesis rests with the author. Unless otherwise indicated, its contents are licensed under a Creative Commons Attribution-NonCommercial 4.0 International Licence (CC BY-NC).

Under this licence, you may copy and redistribute the material in any medium or format. You may also create and distribute modified versions of the work. This is on the condition that: you credit the author and do not use it, or any derivative works, for a commercial purpose.

When reusing or sharing this work, ensure you make the licence terms clear to others by naming the licence and linking to the licence text. Where a work has been adapted, you should indicate that the work has been changed and describe those changes.

Please seek permission from the copyright holder for uses of this work that are not included in this licence or permitted under UK Copyright Law.

Contents

Acronyms **12**

1 Introduction **15**

1.1 Thesis Outline 16

1.2 Author's Contribution 17

1.3 Publications 18

2 Theoretical Background **20**

2.1 Physics of Ultrashort Laser Pulses 20

2.1.1 Description of Ultrashort Pulses 20

2.1.2 Dispersion of Ultrashort Pulses 22

2.1.3 Pulse Propagation Through a Medium 24

2.2 Spatial Properties of Laser Beams 26

2.3 Nonlinear Optics 27

2.3.1 Second-Order Processes 27

2.3.2 Third-Order Processes 30

2.4 Characterisation of Ultrashort Pulses 32

2.4.1 Frequency Resolved Optical Gating (FROG) 32

2.4.2 Dispersion Scan (D-Scan) 34

2.5 Theory of Condensed Matter Properties Related to This Thesis 35

2.5.1 Band Structure 35

2.5.2 Crystal Bonding 37

2.5.3 Joint Density of States (JDOS) 37

2.6 Theoretical Understanding of High Harmonic Generation (HHG) 38

2.6.1 HHG in Gases 39

2.6.2 From Gases to Solids: Adaptation of the Model 40

2.6.3 Properties of HHG from Solids 45

2.6.4 Theoretical Modelling 47

3 Experimental Setups and Methods **50**

3.1 Overview of the Apparatus for the Near-Infrared (NIR) Beamline 50

3.1.1 Laser System and Pulse Compression 50

3.1.2 NIR HHG Beamline 59

3.1.3 Optimisation of the Flat-Field XUV Spectrometer for Solid HHG Detection 62

3.2 Overview of the Apparatus of the Mid-Infrared (MIR) Beamline 66

3.2.1 Laser System 66

3.2.2 Carrier-Envelope Phase (CEP) Control al ALLS 67

3.2.3 MIR HHG Beamline at ALLS 70

4 NIR Wavelength Driving Field for HHG in Wide Bandgap Oxide MgO **73**

4.1 Background on HHG Experiments in MgO 73

4.1.1 Crystal Properties of MgO 73

4.1.2 Previous HHG Experiments in MgO 74

4.2 Extension of HHG Cutoff in Solids to 50 eV Using MgO 75

4.2.1 Experimental Parameters 76

4.2.2 Harmonic Spectra of MgO and Krypton 76

4.2.3 Interpretation of the High Cutoff 80

4.3 Impact of the Driving Pulse Duration on the Harmonic Spectrum 82

4.3.1 Driving Pulse Dependent Harmonic Spectra 82

4.3.2 Harmonic Emission with a 2 Cycle Pulse 89

4.4 Conclusion 92

5 MIR Wavelength Driving Field for HHG in the semiconductor ZnO **93**

5.1 Background on HHG Experiments in Semiconductors 93

5.1.1 Motivations for HHG in Semiconductors 93

5.1.2 Crystal Properties of ZnO 94

5.1.3 Previous HHG Experiments in ZnO 94

5.2 The Role of CEP in HHG from ZnO 96

5.2.1 Harmonic Spectra from ZnO Using the Short Pulse (66 fs) 96

5.2.2 Electron Trajectories in ZnO 103

5.3 Anisotropic Behaviour of HHG from ZnO 106

5.3.1 Anisotropic Response of ZnO to a Strong Field 106

5.3.2 Fourier Analysis of the Harmonic Spectrum 107

5.3.3 Anisotropic Response Depending on the CEP 110

5.4 Comparison of HHG Features Between a 6.5 Cycle and a 10 Cycle Pulse 111

5.5 Conclusion . . . 113

6 Study of the Efficiency of HHG in Different Samples 114

6.1 Motivations for Sample Efficiency Comparison . . . 114

6.2 Background on the Samples Under Study . . . 115

6.2.1 Dielectrics Studied . . . 115

6.2.2 Semiconductors Studied . . . 116

6.3 Harmonic Spectra Comparison From a NIR and a MIR Driving Pulse . . . 118

6.3.1 Comparison of Harmonic Emission From a NIR Long 30 fs and a Short 5 fs Driving Pulse in Transmission . . . 118

6.3.2 Comparison of Harmonic Emission From Bulk and Thin Film Samples in Reflection . . . 120

6.3.3 Comparison of Harmonic Emission Using a MIR Driving Field in Transmission 122

6.3.4 Comparison of Harmonic Emission Using a MIR Driving Field in Reflection 126

6.4 Propagation of the MIR Fundamental Through the Sample . . . 127

6.5 Understanding the Properties Needed for an "Efficient" Sample for HHG . . . 129

6.5.1 Photon-to-Bandgap Ratio . . . 129

6.5.2 Band Structure . . . 129

6.5.3 Bandgap Size . . . 130

6.5.4 Nearest Neighbour Distance . . . 130

6.5.5 Keldysh Parameter . . . 131

6.5.6 Direct or Indirect Bandgap . . . 131

6.5.7 Excitonic Processes and Properties . . . 132

6.5.8 Pulse Duration of the Driving Field . . . 132

6.6 Anisotropic Comparative Study of Semiconductors (ZnO, ZnSe, GaN, and $SrTiO_3$) 133

6.7 Conclusion . . . 136

7 Conclusion and Outlook 138

Bibliography 164

A Copyright Permissions 165

B Micro-Channel Plate (MCP) Images of the Harmonics from MgO as a Function of Pulse Duration 166

List of Figures

2.1 Effect of the CEP for a 4 fs TL pulse centred at 800 nm 22

2.2 Effect of the GDD on a 4 fs pulse centred at 800 nm 23

2.3 Effect of the TOD on a 4 fs pulse centred at 800 nm 24

2.4 Description of a Gaussian beam at focus 27

2.5 Schematic representation of the phase-mismatch Δk between the fundamental field and the SHG field 28

2.6 SHG phase matching 29

2.7 Schematic representation of nonlinear effects 30

2.8 SPM on a Gaussian pulse 31

2.9 Optical schematic of a self-referenced SHG-FROG 33

2.10 Spectrograms produced by a SHG-FROG 33

2.11 Optical schematic of a D-Scan setup 34

2.12 Plot of energy E as a function of wavevector k for the free electron (left side) and the bound electron in a lattice (right side) 36

2.13 Band structure depending on the portion of the k-space selected 36

2.14 Typical emission HHG spectrum in gas with three distinctive regions 38

2.15 Three-step model for HHG in gases 39

2.16 Schematic of the evolution of the Keldysh parameter depending on the type of ionisation 41

2.17 HHG in solids comprising three steps 42

2.18 Short and long trajectories in solid HHG 44

3.1 Spectra at the output of the HCF recorded for the HCF filled with argon, neon and under vacuum 53

3.2 Schematic of the laser system used for HHG experiments in the NIR regime in Imperial College London's lab 54

3.3 Measured pulse duration as a function of Ar pressure in the HCF 54

3.4 Intensity control scheme depicting the energy and pulse duration as a function of half waveplate angle . . . 56
3.5 Fundamental spectra of all driving fields for HHG taken for varying pressure in the HCF . . . 57
3.6 Pulse duration scan. Temporal shape of the driving field for each pulse duration . 58
3.7 Spot size of the focused NIR beam with a 50-cm focal length lens . . . 58
3.8 Schematic of the Imperial College London's laboratory beamline . . . 60
3.9 Raw MCP image showing harmonics from a solid (MgO) . . . 61
3.10 Simulations of the spatial distribution of harmonic orders 3 (4.6 eV) to 33 (51 eV) . 63
3.11 Spectrometer angle optimisation. Measured HHG spectra generated in Kr gas as a function of the grating angle of incidence. . . . 63
3.12 Schematic of the flat-field spectrometer . . . 64
3.13 Energy calibration of the flat-field spectrometer . . . 65
3.14 Optical Parametric Chirped Pulse Amplifier (OPCPA) schematic . . . 66
3.15 ALLS laser setup . . . 67
3.16 Spectrum of the driving field for the short pulse (66 fs) and the long pulse (100 fs) 68
3.17 Mode-locked laser output. . . . 68
3.18 CEP variation over 1.5 hours . . . 70
3.19 HHG beamline. . . . 70
3.20 Pulse duration and spot size measurements of the MIR pulses . . . 71

4.1 MgO crystal and band structures . . . 73
4.2 Comparison of HHG from MgO and Kr . . . 77
4.3 Effective absorption length of MgO depending on the energy . . . 78
4.4 Yield of harmonics generated in MgO as a function of the driving intensity . . . 79
4.5 Scaling of the MgO harmonic cutoff with laser intensity . . . 81
4.6 Harmonic spectrum from MgO as a function of driving field intensity for each pulse duration . . . 83
4.7 Harmonic cutoff as a function of pulse duration . . . 84
4.8 Scaling of the MgO harmonic cutoff with laser intensity for different driving pulse durations . . . 84
4.9 Harmonic spectrum for each pulse duration zoomed on the energy region around 20 eV 85
4.10 Fundamental spectra of the driving fields for each pulse duration used for HHG . . 86
4.11 Harmonic spectrum of H5 to H9 for each pulse duration . . . 87
4.12 Harmonic yield of H5 to H9 as a function of driving laser intensity . . . 88
4.13 D-Scan measurements of the pulse with the sample in or out of the laser beam . . 90

4.14 Pulse duration (a) and power measurement (b) as a function of driving laser intensity with the sample in or out of the laser beam 91
4.15 PL emission near the bandgap of MgO 92

5.1 Crystal wurtzite structure of ZnO 95
5.2 ZnO harmonic yield in transmission as a function of driving laser intensity for the short pulse 97
5.3 Fringes of H5 from ZnO 98
5.4 ZnO integrated harmonic yield in transmission as a function of driving laser intensity 98
5.5 Harmonic spectrum as a function of CEP at 2.9 TW/cm^2 and crystal angle $\theta = 42\,^\circ$ 99
5.6 Harmonic spectrum in transmission as a function of intensity for H9 and H11 . . . 99
5.7 Central wavelength shift of the fundamental and the harmonics for the short pulse 100
5.8 Reflection harmonic spectrum in ZnO for three driving field intensities for the short pulse and CEP value 0 101
5.9 Normalised difference of the signals of H9 (a) and H11 (b) for each intensity for the short pulse 101
5.10 Normalised difference of the signal of H5 from ZnO in reflection 102
5.11 Electric field of the short pulse (a) and long pulse (b) modelled for each CEP value set experimentally 103
5.12 Harmonic spectra from ZnO 104
5.13 Calculated harmonic spectra from Al_2O_2 for varying electric field strengths 105
5.14 Wavelength-resolved harmonic spectrum in polar projection in ZnO 106
5.15 Rotational dependence of the harmonic yield of H11 from ZnO for 2.9 TW/cm^2 (5.15a) and 3.2 TW/cm^2 (5.15b) 107
5.16 Spectrum of H11 from ZnO highlighting the same spectral regions as Figure 5.15 . 107
5.17 Integrated spectral yield of regions IV, V and VI of H11 (from Figure 5.15) as a function of crystal angle θ for each intensity 108
5.18 Fourier analysis of the yield of H11 as a function of crystal orientation and for the different spectral regions 108
5.19 Fourier analysis of the yield of H11 as a function of crystal orientation and for different spectral regions 110
5.20 Normalised difference of the signals of H9 and H11 at 3.2 TW/cm^2 for different crystal angles θ 111
5.21 Comparison of the harmonic spectra from ZnO from a 10 cycle pulse (a) and a 6.5 cycle pulse (b) 112

5.22 Comparison of the harmonic spectra as a function of crystal angle θ from ZnO from a 10 cycle pulse (a) and a 6.5 cycle pulse (b) 113

6.1 Transmission curve of MgO, α-Al_2O_3 and CaF_2 115
6.2 Absorption spectra of bulk ZnO and a thin film sample of ZnO 117
6.3 Harmonic spectra of MgO, α-Al_2O_3 and CaF_2 at 9 TW/cm^2 for a 30 fs pulse at 780 nm 118
6.4 Harmonic spectra of MgO, α-Al_2O_3 and CaF_2 at different intensities for the 5 fs pulse 119
6.5 Harmonic cutoff as a function of bandgap for the 5 fs pulse 120
6.6 Harmonic spectra multiplied with the transmission curve of MgO, α-Al_2O_3 and CaF_2 120
6.7 Harmonic spectra of bulk ZnO and a thin film sample of ZnO at 1.9 TW/cm^2 (a) and 2.6 TW/cm^2 (b) for the short 66 fs pulse 121
6.8 Harmonic spectra in transmission of ZnO, ZnSe, GaN, SiC and $SrTiO_3$ at 1.2 TW/cm^2 for the long pulse 123
6.9 Harmonic spectra in transmission of ZnO, ZnSe, GaN and $SrTiO_3$ at 1.2 TW/cm^2 for the short pulse 124
6.10 Visual PL signal of ZnO, GaN and ZnSe 125
6.11 Harmonic yield as a function of bandgap 125
6.12 Harmonic spectra in transmission of ZnO, ZnSe, GaN and $SrTiO_3$ at 3.2 TW/cm^2 for the short pulse 126
6.13 Harmonic spectra in reflection at 1.2 TW/cm^2 for the long pulse (a) and short pulse (b) for the samples under study 127
6.14 Spectrum of the fundamental going through ZnO, ZnSe, GaN and $SrTiO_3$ and without any sample in the beam path for comparison at different intensities 128
6.15 Absorption spectra of GaN 129
6.16 Spectrum of H5 with the 10 cycle driving pulse for $SrTiO_3$, ZnSe and ZnO 133
6.17 Spectrum of H5 with the 6.5 cycle driving pulse for GaN, $SrTiO_3$, ZnSe and ZnO . 134
6.18 Spectrum of H9 for ZnSe with the 10 cycle driving pulse and the 6.5 cycle driving pulse 136

B.1 MCP harmonic image for the 29 fs pulse 166
B.2 MCP harmonic image for the 27 fs pulse 167
B.3 MCP harmonic image for the 17 fs pulse 167
B.4 MCP harmonic image for the 8 fs pulse 168
B.5 MCP harmonic image for the 7 fs pulse 168
B.6 MCP harmonic image for the 5 fs pulse 169

List of Tables

3.1 Laser parameters of all the the driving laser fields used in the NIR beamline 57

3.2 Laser parameters of the short pulse and long pulse used in the MIR beamline . . . 71

4.1 Highest cutoff photon energies reached in a range of wide bandgap dielectrics as a function of the driving wavelength, pulse duration and sample thickness 74

4.2 Laser parameters used for HHG in MgO 79

6.1 Crystal properties of MgO, α-Al_2O_3 and CaF_2 116

6.2 Crystal properties of ZnO, ZnSe, SiC-4H, GaN and $SrTiO_3$ 116

6.3 Bandgap energy relative to the harmonic orders and cutoff observed for all studied samples 125

Acronyms

ALLS Advanced Laser Light Source.

AOPDF Acousto-Optic Programmable Dispersive Filter.

BBO Beta-Barium Borate.

BZ Brillouin Zone.

CB conduction band.

CEP Carrier-Envelope Phase.

CPA Chirped Pulse Amplification.

CW Continuous Wave.

D-Scan Dispersion Scan.

DFG Difference Frequency Generation.

DOS Density of States.

DP differentially pumped.

FFT Fast Fourier Transform.

FROG Frequency Resolved Optical Gating.

FWHM Full-Width at Half-Maximum.

GD Group Delay.

GDD Group Delay Dispersion.

GPA Generalised Projection Algorithm.

GV Group Velocity.

GVD Group Velocity Dispersion.

HCF hollow core fibre.

HHG High Harmonic Generation.

IDRI Intensity Dependent Refractive Index.

INRS Institut National de la Recherche Scientifique.

JDOS Joint Density of States.

LIBS Laser-Induced Breakdown Spectroscopy.

MCP Micro-Channel Plate.

MIR Mid-Infrared.

MPI Multiphoton Ionisation.

Nd:YAG Neodymium-doped Yttrium Aluminum Garnet.

Nd:YLF Neodymium-doped Yttrium Lithium Fluoride.

NIR Near-Infrared.

OPA Optical Parametric Amplification.

OPCPA Optical Parametric Chirped Pulse Amplifier.

PL Photoluminescence.

SBEs Semiconductor Bloch Equations.

SF static filled.

SFG Sum Frequency Generation.

SHG Second Harmonic Generation.

SNR Signal-to-Noise Ratio.

SPIDER Spectral Phase Interferometry for Direct Electric field Reconstruction.

SPM Self-Phase Modulation.

TBP Time-Bandwidth Product.

TDDFT Time-Dependent Density Functional Theory.

TDSE Time-Dependent Schrödinger Equation.

THG Third Harmonic Generation.

TI Tunnelling Ionisation.

TL Transform-Limited.

TOD Third-Order Dispersion.

UV Ultraviolet.

VB valence band.

XUV Extreme Ultraviolet.

YAG Yttrium Aluminum Garnet.

Chapter 1

Introduction

Understanding the interaction between light and matter is crucial for a wide range of applications, from spectroscopic analysis [1] to medicine and sustainable energies [2]. For instance, techniques like Laser-Induced Breakdown Spectroscopy (LIBS) rely on these interactions to probe the materials' contents [3]. The interaction of strong electromagnetic fields with matter is at the heart of attosecond science and more particularly of High Harmonic Generation (HHG). HHG has emerged as a powerful tool in the field of ultrafast science, enabling the production of coherent Extreme Ultraviolet (XUV) emission.

HHG has been extensively studied in gases [4, 5, 6], where the interaction of a strong field with an atomic or molecular system results in the emission of a characteristic harmonic spectrum. However, recent advancements have shifted the focus towards HHG in condensed matter [7], opening new avenues for both fundamental research and practical applications. While a three-step recombination model similar to that used for gases has been proposed for solids [8], the complete understanding of the process remains a subject of debate. This has led to case-by-case studies, making general conclusions in the field challenging.

The study of HHG in solids not only provides insights into the fundamental physics of light-matter interactions but also holds promise for various applications. The generation of high harmonics in solids can lead to the development of compact, tabletop, controllable XUV and soft X-ray sources, which are crucial for applications in spectroscopy, imaging, and lithography. Furthermore, HHG in solids offers a novel approach to probing ultrafast dynamics in condensed matter systems, enabling the study of electron and phonon interactions on attosecond timescales.

In solids, the mechanisms underlying HHG differ from those in gases since the electrons are bound to the crystal lattice. The interaction of strong laser fields with the periodic potential of a crystal lattice results in unique harmonic features, allowing to reconstruct the complex band structure [9], probe the electronic potential on a picoscopic scale [10] and resolve the collective

electron dynamics within a solid [11]. The strong laser field drives the electrons within the material at petahertz (PHz) rates [12], creating ultrafast currents which could lead to a new generation of PHz optoelectronic devices. Furthermore, HHG is a quantum process, and studying this nonlinear process could be a route to quantum coherence in light states and measurement of single-photon statistics [13, 14].

This thesis explores the intricate processes involved in HHG in solids, with a particular emphasis on the different regimes at play. This will allow for a better understanding of the role of electronic band structure, electron trajectories in the crystal lattice and the influence of material properties.

1.1 Thesis Outline

This thesis describes experimental studies of the HHG process in a variety of solids using a range of laser parameters. The goal is two-fold: (1) To understand the electron dynamics at play in two different regimes: (a) dielectric materials illuminated with a Near-Infrared (NIR) field and (b) semiconductors irradiated with a Mid-Infrared (MIR) driving field. My work here provides spectroscopic insights in the HHG process in MgO and ZnO. (2) To determine the most "efficient" solid system for HHG, i.e. the one that gives the highest harmonic yield as well as the highest harmonic energy for use in industrial applications.

The thesis is organised into seven chapters, each either establishing the necessary background to understand the underlying physics or presenting results that focus on specific features of HHG in solids. Chapter 2 provides an overview of the theoretical framework for HHG, including the semi-classical three-step recombination model originally developed for gases and subsequently adapted for solids. Key properties of harmonic emission in solids are discussed, such as the linear extension of the cutoff (the highest harmonic produced) with the electric field and the debated wavelength scaling. Basic properties of solid-state systems are briefly introduced as they are essential for interpreting the experimental results. Additionally, the fundamentals of ultrafast optics and nonlinear effects are detailed in order to give a foundation for understanding the processes at play.

Chapter 3 discusses the experimental techniques used to generate and detect high harmonics in solid-state materials. Two laser systems were used in this work, therefore the two beamlines are presented along with the methods for pulse compression and the characterisation of the pulses. In the first beamline (NIR beamline), adaptations I made to the existing setup for harmonic detection are described.

Chapter 4 presents the results of experimental investigations on HHG from MgO from NIR pumping. The high cutoff observed (in fact, the highest ever recorded in a solid) is correlated with the band structure and the harmonic features are linked to the transitions in high-lying bands.

Harmonics driven by varying pulse durations are presented and the electron dynamics in each case are explored.

Chapter 5 provides a comprehensive analysis of electron dynamics in ZnO illuminated by a MIR driving field. This chapter elucidates the signatures of interfering electron trajectories, demonstrating that these features originate solely from the electron motion rather than from propagation effects. Additionally, the Carrier-Envelope Phase (CEP) of the driving field is proposed as a novel tool for distinguishing the contributions of different electron trajectories, an approach that has not been previously explored.

Chapter 6 focuses on the potential applications of HHG in solids and presents a systematic comparison of the harmonic yield and cutoff for multiple samples in each of the regimes cited above. While harmonics have been observed in materials with different bandgaps (1-12 eV), there is little experimental determination of the global scaling properties. Wide bandgap semiconductors are strong candidates for HHG studies due to their wide applications in nanotechnology and engineered materials [15, 16]. We study the harmonic emission from various materials with similar bandgaps in order to determine the impact of the bandgap on harmonic yield and cutoff.

Chapter 7 summarizes the key findings of the thesis and discusses future directions for research in this exciting field.

Through this work, I aim to contribute to the understanding of HHG in solids and pave the way for innovative applications in ultrafast science and technology.

1.2 Author's Contribution

All the work presented in this thesis was done under the supervision of Dr. Mary Matthews and Prof. John Tisch. I performed all the experimental data collection as well as the data analysis. Throughout this work, Dr. Joseph Broughton provided advice and technical assistance.

For the results on the NIR beamline, I was the main researcher leading the project. The laser system and beamline were developed previously in the group. The operation of the system were done by myself, Dr. Joseph Broughton, Tim Klee and Yan Li. The improvements made to the system were designed and done by myself, Dr. Joseph Broughton and Prof. John Tisch. The NIR HHG data was collected by myself, Dr. Joseph Broughton, Tim Klee, Nikolas Thatte and Yan Li. I did the sample selection. Technical assistance has been provided by Susan Parker and Andrew Gregory.

For the MIR beamline, I wrote the proposal for ALLS beamtime with Dr. Joseph Broughton under the supervision of Dr. Mary Matthews, Prof. John Tisch and Prof. Jon Marangos. I performed the beamline preparation including sample selection, and experimental timeline. The

HHG data was collected by myself, Dr. Joseph Broughton, Madison Dorrzapf and Tim Klee. The beamtime scientists who maintained and characterised the pulse were Dr. Gaëtan Jargot and Dr. Marie Ouille under the supervision of Prof. François Légaré.

All the figures and simulated plots presented in this thesis were done by myself unless stated otherwise.

1.3 Publications

Papers

- **Hortense Allegre**, Joseph J. Broughton, Tim Klee, Yan Li, Katarzyna M. Kowalczyk, Nikolas Thatte, Daniel Lim, Jon P. Marangos, Mary M. Matthews, and John W. G. Tisch, "Extension of high-harmonic generation cutoff in solids to 50 eV using MgO," Opt. Lett. 50, 1492-1495 (2025)

Conference Proceedings

- **Hortense Allegre**, Joseph Broughton, Tim Klee, Yan Li, Katarzyna Kowalczyk, Nikolas Thatte, Daniel Lim, Jon Marangos, Mary Matthews, and John Tisch "Influence of pulse duration on high harmonics emitted from wide bandgap dielectrics", Proc. SPIE 12992, Advances in Ultrafast Condensed Phase Physics IV, 129920A (10 June 2024); https://doi.org/10.1117/12.3021909

Conference Talks and Posters

- **Allegre, Hortense**, Kowalczyk, Kasia, Wyatt, Adam, Springate, Emma, Tisch, John, Marangos, Jon, and Matthews, Mary, "Anisotropic High Harmonic Generation in Wide Bandgap Dielectrics" in Conference on Lasers and Electro-Optics/Europe (CLEO/Europe 2023) and European Quantum Electronics Conference (EQEC 2023), doi:10.1109/CLEO/Europe-EQEC57999.2023.10232413

- **H. Allegre**, K. Kowalczyk, J.J. Broughton, O. Alexander, T. Avni, J.P. Lee, J. Turner, A. Wyatt, Y. Zhang, R. Chapman, E. Springate, J.P. Marangos, J.W.G. Tisch, and M. Matthews, "Anisotropic High Harmonic Generation in Wide Bandgap Dielectrics", in Lasers for Science Facility, Artemis User Meeting

- **H. Allegre**, J. Turner, K. Kowalczyk, A. Pettipher, M. Matthews, and J.W.G Tisch, "Carrier-Envelope Phase Dependent Harmonics in Solids using a Few-Cycle IR Pulse" in Atto, 8^{th} International Conference on Attosecond science and Technology.

- **H. Allegre**, K. Kowalczyk, O. Alexander, T. Avni, J.P. Lee, J. Turner, A. Wyatt, Y. Zhang, E. Springate, J.P. Marangos, J.W.G. Tisch, and M. Matthews, "Comparison of high harmonics generated by wide bandgap dielectrics with a NIR ultrafast pulse", in Fundamental Electronic and Structural Dynamics, Multiphoton Processes, Gordon Research Conference

Manuscripts in Preparation

- **H. Allegre**, J.J. Broughton, M. Dorrzapf, T. Klee, G. Jargot, M. Ouille, J. P. Marangos, F. Légaré, J. W. G. Tisch, and M. Matthews, "Carrier-Envelope Phase Effects on High Harmonic Generation in ZnO: Exploring Electron Trajectory Dependencies"

Submitted Manuscripts

- **Hortense Allegre**, Joseph J. Broughton, Tim Klee, Yan Li, Daniel Lim, Nikolas Thatte, Mary M. Matthews and John W.G. Tisch, "Intensity Control of Few-Cycle Pulses," Applied Optics.

Chapter 2

Theoretical Background

2.1 Physics of Ultrashort Laser Pulses

Ultrashort lasers have seen great advancements in the last decades, starting with microsecond long pulses at the birth of the laser to reach the femtosecond regime years later [17]. Thanks to these advances, it is now possible to resolve attosecond dynamics of matter through the production of ultrashort pulses. Femtosecond pulses allow for high electric field intensities (10^7–$10^{15}\,\mathrm{W/cm^2}$) to be routinely accessed, and form the basis for the study of extreme nonlinear effects. Modelocking allows to generate those ultrashort pulse while intense femtosecond pulses are created by novel amplification technique. The Chirped Pulse Amplification (CPA) technique needed to amplify less than $\sim 100\,\mathrm{fs}$ pulses was first developed by Donna Strickland and Gerard Mourou [18] and is now used in a variety of fields such as laser machining and spectroscopy.

This section introduces the basic components needed to understand the dynamics of these ultrashort pulses and how they interact with a medium.

2.1.1 Description of Ultrashort Pulses

Mathematically, the electric field of a linearly polarised pulse can be written in the temporal domain as

$$E(z,t) = |E(z,t)|e^{-i(\omega t - kz - \varphi(t))} + \text{c.c.} \tag{2.1}$$

where $|E(z,t)|^2$ is the intensity envelope function and the exponential term, with φ(t) a temporal phase offset, is the carrier wave with wavevector defined by Equation 2.2. ω is the centre frequency ($\omega = \frac{2\pi c}{\lambda}$) and $n(\omega)$ is the frequency-dependent refractive index. We use a scalar approximation which is still valid as we do not describe a hard focusing regime.

$$k(\omega) = \frac{n(\omega)\omega}{c} \tag{2.2}$$

The electric field can be expressed in the frequency domain by performing a Fourier transform of Equation 2.1, yielding Equation 2.3, with $\phi(\omega)$, the spectral phase.

$$E(z,\omega) = FT[E(t)] \propto \int_{-\infty}^{\infty} E(z,t)e^{-i\omega t}\,dt \propto |E(z,\omega)| \cdot e^{i\phi(\omega)} \tag{2.3}$$

Since laser pulses are typically Gaussian in time and consequently in frequency, we will now assume in this thesis that **all** described pulses are Gaussian. This assumption means that the envelope function is a Gaussian function, described by Equation 2.4, where $\Delta\tau$ is the FWHM pulse duration and E_0 is the field's amplitude.

$$|E(0,t)|^2 = E_0 e^{-4\ln(2)(\frac{t}{\Delta\tau})^2} \tag{2.4}$$

We can now express the intensity, which is the energy per unit area as a function of the time-dependent electric field, where ϵ_0 is the vacuum permittivity [19].

$$I(t) = \frac{1}{2} cn\epsilon_0 |E(t)|^2 \tag{2.5}$$

A property inherent to this Fourier relation is that a temporally short pulse is spectrally broad. This principle is encapsulated in the Time-Bandwidth Product (TBP) [20]. For a given pulse duration Δt and a given spectral width $\Delta\nu$, we have:

$$\Delta t \Delta\nu \geq \text{TBP} \tag{2.6}$$

The constant TBP has a specific value depending on the pulse shape (for a Gaussian pulse TBP = 0.441) and the equality is reached only when the temporal phase $\phi(\omega)$ is flat across all frequencies, known as Transform-Limited (TL). As short pulses have a broad spectrum, it is difficult to maintain a flat phase across the entire spectrum. Characterisation methods therefore need to measure spectral intensity and phase to gain an accurate description of the pulse (Section 2.4).

The temporal and spatial frequencies of the pulse ($\Phi(t)$ and $\phi(\omega)$) can both be expressed as a Taylor series around the centre time t_0 and frequency ω_0. We will now focus on the spectral phase described in Equation 2.7. The terms CEP, GD, GDD and TOD are described below.

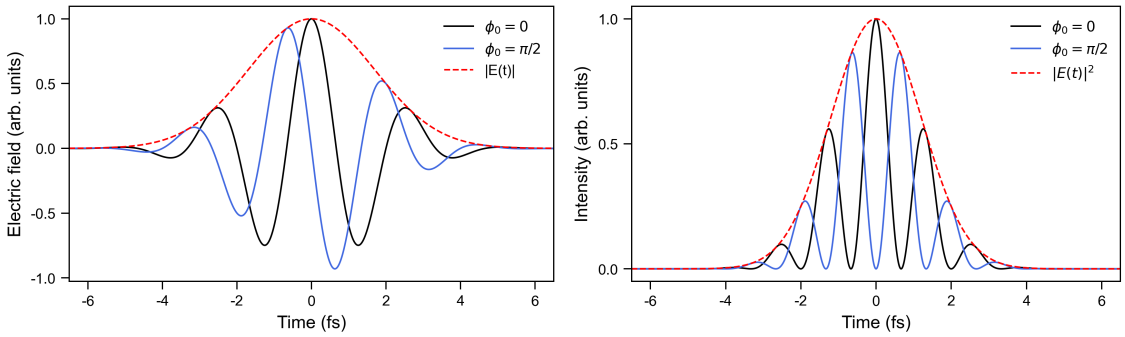
$$\phi(\omega) = \underbrace{\phi(\omega_0)}_{\text{CEP}} + \underbrace{\left.\frac{\partial\phi}{\partial\omega}\right|_{\omega_0}}_{\text{GD}} (\omega-\omega_0) + \frac{1}{2!}\underbrace{\left.\frac{\partial^2\phi}{\partial\omega^2}\right|_{\omega_0}}_{\text{GDD}} (\omega-\omega_0)^2 + \frac{1}{3!}\underbrace{\left.\frac{\partial^3\phi}{\partial\omega^3}\right|_{\omega_0}}_{\text{TOD}} (\omega-\omega_0)^3 + ... \tag{2.7}$$

2.1.2 Dispersion of Ultrashort Pulses

The coefficients $\left.\frac{\partial^n \phi}{\partial \omega^n}\right|_{\omega_0}$ represent the effect of dispersion on a pulse. As a pulse propagates through a medium, the different frequency components travel at different speed, this is dispersion. Dispersion has a major impact on nonlinear interactions and in techniques to generate ultrashort pulses. We will now focus on each of these coefficients $\left.\frac{\partial^n \phi}{\partial \omega^n}\right|_{\omega_0}$ separately.

Carrier-Envelope Phase (CEP)

The first term of the Taylor expansion is know as the Carrier-Envelope Phase (CEP), $\phi_0 = \phi(\omega_0)$. It corresponds to the relative phase between the carrier and the envelope function, i.e. the absolute phase of the pulse. For ultrashort pulses when the duration of the pulse is comparable to an optical period ($T = 2\pi/\omega_0$), also known as few-cycle pulses, the CEP can have a dramatic impact on the waveform, as depicted in Figure 2.1. The peak intensity of the pulse is greatly affected by a change of CEP ($\approx 10\,\%$ intensity variation in the illustrated case of a 4 fs pulse) and so is the temporal symmetry of the pulse. Therefore, if the CEP changes on a shot-to-shot basis, intensity-dependent effects, which are usual in nonlinear optics, have to be accounted for and intensity-dependent measurements will decrease in precision.



(a) (b)

Figure 2.1: Effect of the CEP for a 4 fs TL pulse centred at 800 nm. 2.1a shows the electric field as a function of time for a cos-like pulse ($\phi_0 = 0$) and a sin-like pulse ($\phi_0 = \pi/2$). 2.1b shows the intensity profile of those two pulses.

Group Delay (GD)

The second term of the Taylor expansion is the Group Delay (GD), $\phi_1 = \left.\frac{\partial \phi}{\partial \omega}\right|_{\omega_0}$. It corresponds to the delay in time for the pulse to reach the target, i.e. a linear shift in time. This term does not affect the pulse duration. For single-field experiments, this term is not relevant. However, for multiple field experiments, such as in pump-probe experiments, it is crucial for temporal overlap because this term describes the delay between the pulses.

Group Delay Dispersion (GDD)

The third term in the Taylor expansion of the spectral phase is the Group Delay Dispersion (GDD), $\phi_2 = \frac{\partial^2 \phi}{\partial \omega^2}\Big|_{\omega_0}$. A pulse with GDD is termed "chirped" as the GDD changes the instantaneous frequency in time. The GDD term describes how the different frequency components arrive at different times at the target. Since most materials have positive GDD in the visible region [21], a positive GDD is qualified as "normal": the red frequency components travel faster than the blue ones. Inversely, a negative GDD is said to be "anomalous". For a symmetric pulse in the spectral domain, the GDD imparts a symmetric broadening of the pulse in the temporal domain. The GDD is the term that impacts a pulse the most and therefore, it is crucial to characterise the added GDD to a pulse as it propagates to arrive at the target position. Figure 2.2 shows the impact of a 1 mm fused silica window on the pulse. This material was chosen as it is very common for a pulse to propagate through glass in the lab. With this example, the initial pulse of 4 fs long centred at 800 nm is broadened to $\approx$ 25 fs.

It is worth noting that the sign of the GDD is important for overall pulse lengthening. Indeed, adding a material with positive GDD followed by a material with the same negative GDD will balance the overall GDD (the order of the materials does not matter as this effect is linear).

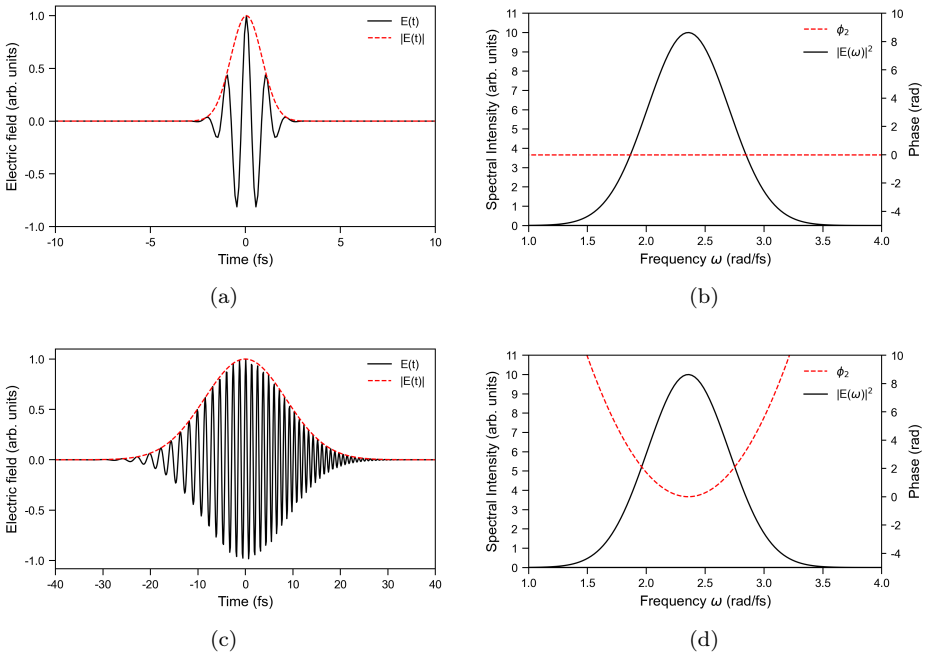
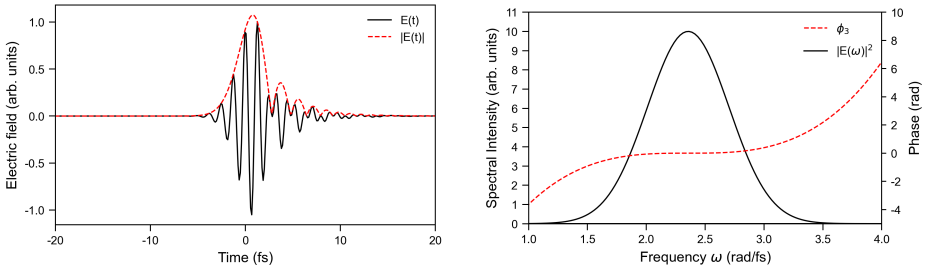


Figure 2.2: Effect of the GDD on a 4 fs pulse centred at 800 nm. 2.2a and 2.2c show the electric field as a function of time for the initial TL pulse and the same pulse with 36 fs^2 GDD (equivalent to adding 1 mm of fused silica in the pulse [21]). 2.2b and 2.2d show the spectrum as a function of frequency for the initial TL pulse and the same pulse with 36 fs^2 GDD (black curves). The red dotted curve corresponds to the spectral phase of these pulses.

Third-Order Dispersion (TOD)

The fourth term in the Taylor expansion of the spectral phase is the Third-Order Dispersion (TOD), $\phi_3 = \frac{\partial^3 \phi}{\partial \omega^3}\Big|_{\omega_0}$. The TOD only weakly affects the pulse duration but distorts the pulse greatly, as seen in Figure 2.3 (same fundamental pulse as above). It is harder to account experimentally for TOD as it is difficult to measure it and most optical components add TOD to the pulse. It is therefore imperative to carefully choose the materials in which the pulse propagates, as this will affect its temporal shape (distortion) and duration.



(a) (b)

Figure 2.3: Effect of the TOD on a 4 fs pulse centred at 800 nm. 2.3a shows the electric field as a function of time for a pulse with 27.5 fs^3 TOD (equivalent to adding 1 mm of fused silica in the pulse [21]). 2.3b shows the spectrum as a function of frequency for the same pulse (black curve). The red dotted curve corresponds to the spectral phase of this pulse.

2.1.3 Pulse Propagation Through a Medium

As the pulse propagates through a medium, it can be distorted by it. Indeed, the electrons in the material start to move and oscillate at the same frequency as the impinging field. These electrons constitute a phase-shifted source of radiation and therefore the total field is modified by this induced field. The pulse induces a polarisation in the medium, which corresponds to a dipole moment per unit volume [22]:

$$P = \epsilon_0 \left(\chi^{(1)} E + \chi^{(2)} E^2 + \chi^{(3)} E^3 + ... \right) \tag{2.8}$$

where $\chi^{(n)}$ is the n^{th} order electric susceptibility and E is the electric field (written as a scalar as we assume a linearly polarised pulse). The linear susceptibility is simply $P = \epsilon_0 \chi^{(1)} E$. As we deal with higher intensities, we need to expand the polarisation P with higher-order terms, responsible for nonlinear effects. Orders above 4 contribute very weakly to the polarisation and will therefore not be discussed [23]. As the dispersion is a linear reponse of the medium, we will focus for now on the linear part of the polarisation P.

The propagation of the pulse through the medium induces a frequency-dependent refractive index defined as:

$$n(\omega) = \sqrt{1 + \chi^{(1)}(\omega)} \tag{2.9}$$

As a result, the original pulse (E_{in}) is modified and yields the pulse emerging (E_{out}) after propagating through a medium of length L:

$$E_{\text{out}} = \exp\left(i\frac{\omega}{c}n(\omega)L\right)E_{\text{in}} \tag{2.10}$$

We now have a frequency dependent wavevector and we can rewrite Equation 2.2 as a function of ω, corresponding to the derivative of the phase as a function of space z:

$$k = \frac{\partial\phi(\omega)}{\partial z} = \frac{\omega}{c}n(\omega) \tag{2.11}$$

This expression can be expressed as Taylor series, in exactly the same way as the spectral phase (Equation 2.7).

$$k(\omega) = k(\omega_0) + \underbrace{\left.\frac{\partial k}{\partial\omega}\right|_{\omega_0}}_{\text{GV}}(\omega-\omega_0) + \frac{1}{2!}\underbrace{\left.\frac{\partial^2 k}{\partial\omega^2}\right|_{\omega_0}}_{\text{GVD}}(\omega-\omega_0)^2 + \frac{1}{3!}\underbrace{\left.\frac{\partial^3 k}{\partial\omega^3}\right|_{\omega_0}}_{\text{TOD}}(\omega-\omega_0)^3 + ... \tag{2.12}$$

Similar to Section 2.1.2, we can analyse each of the terms of the Taylor expansion, where the first term of the expansion $k(\omega_0)$ corresponds to the phase velocity of the pulse ($v_{\text{phase}} = \frac{c}{n(\omega)} = \frac{\omega}{k}$) and the second term corresponds to the Group Velocity (GV) ($v_{\text{group}} = \frac{\partial\omega}{\partial k}$). The third term is the Group Velocity Dispersion (GVD). This definition shows the relation between GDD and GVD given by GDD = GVD $\times$ L, where L is the length of the medium. The GVD can directly be expressed as a function of the wavelength λ:

$$\text{GVD}(\lambda) = \frac{\lambda^3}{2\pi c^2}\frac{\partial^2 n(\lambda)}{\partial\lambda^2} \tag{2.13}$$

The higher-order terms are cumbersome and in order to include them, it is easier to use the Sellmeier equation [24] (Equation 2.14, where B_i and C_i are the Sellmeier coefficients, dependent on the material and found experimentally). However, as described for the spectral phase, these terms contribute weakly to the overall wavevector.

$$n^2(\lambda) = 1 + \sum_i \frac{B_i\lambda^2}{\lambda^2 - C_i} \tag{2.14}$$

When a pulse propagates through a medium, the effects of absorption, scattering and surface reflections should also be considered. The optics and solid targets used in this work are transparent

in the spectral region of the fundamental pulse employed and we can mitigate absorption and scattering effect by using thin materials. However, Fresnel reflections can lead to power losses of the pulse (which can be mitigated by the use of anti-reflection coatings and Brewster angle geometry).

2.2 Spatial Properties of Laser Beams

We have described above the pulse in the temporal domain but it is crucial to understand the spatial properties of laser beams as well. Laser beams are described best with a Gaussian shape [25], where polar coordinates are used ($r^2 = x^2 + y^2$).

$$E(r,z) = E_0 \frac{w_0}{w(z)} \exp\left(- \frac{r^2}{w(z)^2} \right) \exp\left(- i[kz + \frac{kr^2}{2R(z)} + \Phi_{\text{Gouy}}(z)] \right) \tag{2.15}$$

where E_0 is the amplitude of the electric field envelope (to have the full temporal and spatial beam description, E_0 can be replaced by $E(t)$), $R(z)$ is the radius of the wavefront curvature and $w(z)$, the spot size with w_0 the minimum spot size at focus, i.e. the waist of the beam. The parameters introduced here, i.e. the spot size $w(z)$, the radius of the wavefront curvature $R(z)$ and the Gouy phase $\Phi_{\text{Gouy}}(z)$ are defined by Equations 2.17. The spot size is defined at any longitudinal position (along the z-axis) as the transverse distance from the optical axis for which the intensity of the beam has dropped by a factor $1/e^2$. The Gouy phase and the radial phase describe how the beam changes from converging to diverging as it passes through the focus [26]. The definitions of $w(z)$, $R(z)$ and $\Phi_{\text{Gouy}}(z)$ include the Rayleigh range z_R corresponding to the distance along the longitudinal axis where the cross-sectional area of the beam doubles. These parameters are summarised schematically in Figure 2.4 and defined below:

$$z_R = \frac{\pi w_0^2}{\lambda} \tag{2.16}$$

where the wavelength λ corresponds to the vacuum wavelength divided by the refractive index of the medium.

$$w(z) = w_0 \sqrt{1 + \left(\frac{z}{z_R} \right)^2} \tag{2.17a}$$

$$R(z) = z \left[1 + \left(\frac{z}{z_R} \right)^2 \right] \tag{2.17b}$$

$$\Phi_{\text{Gouy}}(z) = -\arctan\left(\frac{z}{z_R} \right) \tag{2.17c}$$

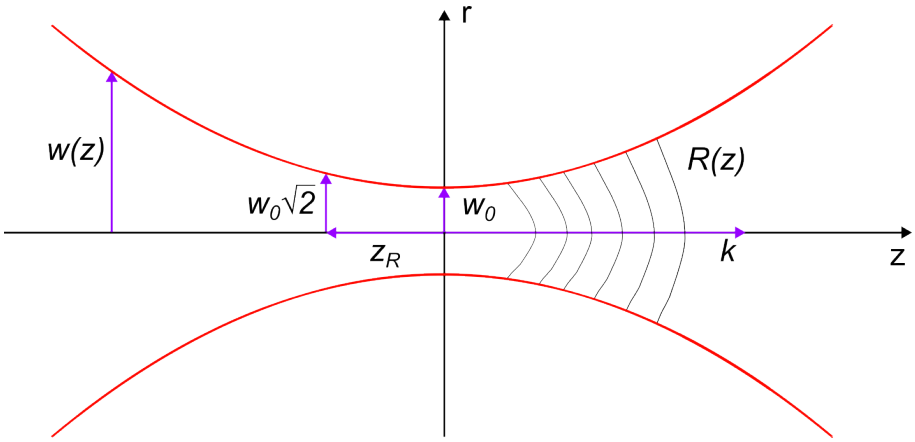


Figure 2.4: Description of a Gaussian beam at focus.

The description above holds for a perfect Gaussian beam, which is rarely the case for a laser beam used in a lab. A quality factor has thus been introduced M^2 [27], defined by the divergence angle of the beam θ. All the above parameters are modified accordingly, following $z'_R = z_R/M^2$. For a perfect Gaussian beam, $M^2 = 1$.

$$M^2 = \frac{\pi w_0}{\lambda}\theta \tag{2.18}$$

When the beam is focused by an optic, typically a lens or focusing mirror of focal length f, the new spot size is defined by:

$$w_f = f\theta = \frac{\lambda f M^2}{\pi w_0} \tag{2.19}$$

2.3 Nonlinear Optics

When the intensity reaches high enough values (typically >10 GW/cm^2), the nonlinear responsivity of the medium needs to be taken into account. The nonlinearity comes from the nonlinear relationship between the input field and the output field of the medium, i.e. new frequencies are created in the medium. Understanding this mathematically means including the nonlinear terms of the polarisation P in our analysis (Equation 2.8).

The order of the process defines how many photons are involved, hence the higher the order, the more photons will be needed and the less efficient will this process be.

2.3.1 Second-Order Processes

Let us first consider the second-order term of the polarisation: $P_{NL} = \epsilon_0 \chi^{(2)} E^2$. In order to have a non-zero $\chi^{(2)}$ (and more generally, even order $\chi^{(n)}$), the material must be non-centrosymmetric. Typically, materials are centrosymmetric, i.e. have a centre of inversion symmetry [28]. However,

a few are non-centrosymmetric and the most common material used is a BBO crystal [29].

Second Harmonic Generation (SHG)

The most common second-order process is Second Harmonic Generation (SHG) where two photons of frequency ω give one photon at frequency 2ω: $\omega + \omega = 2\omega$. Considering a field in the form $E(t) = E_0 \cos(\omega t)$, we obtain:

$$P_{\mathrm{NL}} = \frac{1}{2}\epsilon_0 \chi^{(2)} E_0^2 (1 + \cos(2\omega t)) \tag{2.20}$$

We now have an oscillating field at frequency 2ω and a constant field, the DC field called optical rectification [30]. The fact that we now have two fields propagating in the medium, the fundamental at frequency ω and the second harmonic at frequency 2ω implies that they will not propagate in the same way and there will be a phase-mismatch Δk between these two fields due to dispersion as described by Equation 2.21 and Figure 2.5.

$$\Delta k = 2k(\omega) - k(2\omega) = \frac{2\omega}{c}(n(\omega) - n(2\omega)) \tag{2.21}$$

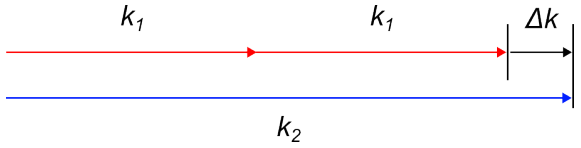


Figure 2.5: Schematic representation of the phase-mismatch Δk between the fundamental field and the SHG field.

It is thus of critical importance to minimise the phase-mismatch as this enables efficient SHG signal. To do so, exploiting the birefringence of crystals is widely used. In a crystal, different polarisations can experience different refractive indexes. The two axes of the crystal are referred to as the ordinary and extraordinary axes, leading to two different common phase matching schemes: Type I (ooe) – in which the two input photons are along the ordinary axis and the output photon is along the extraordinary axis and Type II (eoe) – in which the two input photons are orthogonally polarised [31].

It has been demonstrated using the wave equation that the intensity of the second harmonic depends on the phase matching as expressed by Equation 2.22 [22]. This expression is only valid under the "low-depletion approximation" [32] which consists of considering that the transfer of energy between the fundamental field and its second harmonic is negligible.

$$I_{2\omega} \propto I_\omega L^2 \mathrm{sinc}^2\left(\frac{\Delta k L}{2}\right) \tag{2.22}$$

When $\Delta k = 0$, i.e. when perfect phase matching is reached, the intensity of the second harmonic grows quadratically with the coherence length. However, when $\Delta k \neq 0$, $I_{2\omega}$ exhibits an oscillatory behaviour as a function of L (Figure 2.6).

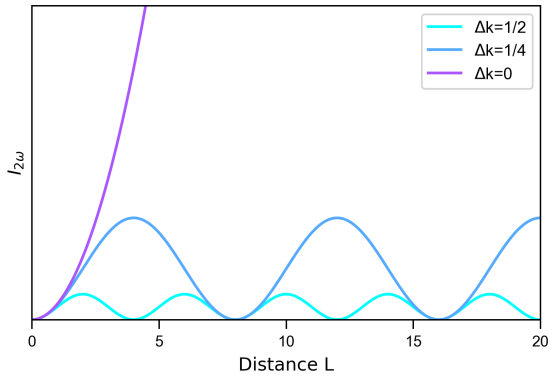


Figure 2.6: SHG phase matching. Intensity of the second harmonic as a function of the distance L travelled through a crystal (solution to Equation 2.22).

We can note that the phase matching bandwidth is inversely proportional to the crystal thickness, signifying that the range of frequencies to phase match an ultrashort pulse is limited by the thickness of the crystal. Thin crystals are preferred in ultrafast optics, however a balance needs to be established between SHG efficiency and phase matching bandwidth.

Other Second-Order Processes

SHG is only a specific case of frequency mixing. Instead of having two photons at the same frequency, we can have two photons at different frequencies giving a third photon: $\omega_1 + \omega_2 = \omega_3$ for Sum Frequency Generation (SFG) and $\omega_1 - \omega_2 = \omega_3$ for Difference Frequency Generation (DFG).

A particular case of DFG is Optical Parametric Amplification (OPA) [33] which relies on the interaction of an intense high-frequency field and a weak low-frequency field resulting in a transfer of energy from the intense field to the weak field as well as the creation of new field at a frequency corresponding to the difference between the two input frequencies. The intense input field is referred to as the pump, the amplified field, the signal and the generated field, the idler.

Figure 2.7 demonstrates those nonlinear effects where arrows pointing upwards are photons absorbed and arrows pointing downwards are photons emitted. The more photons are required for a process, the higher will the order of the process be and the more unlikely it will be.

We can mention the Pockels effect [19] for which a DC field is applied to the material, leading to a change of refractive index and hence birefringence of the material. It can be used as an optical switch.

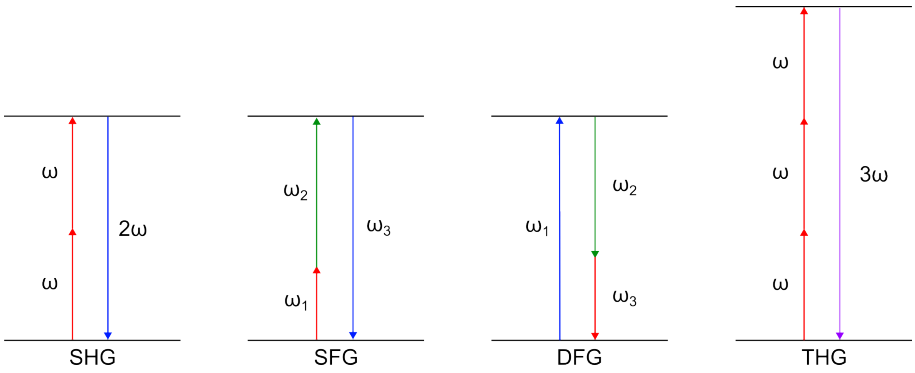


Figure 2.7: Schematic representation of nonlinear effects. SHG, SFG and DFG are second-order effects while THG is a third-order effect detailed in the next section.

2.3.2 Third-Order Processes

Third-order processes depend on the $\chi^{(3)}$ of materials, leading us to consider the part of the nonlinear polarisation depending on this $\chi^{(3)}$: $P_{\text{NL}} = \epsilon_0 \chi^{(3)} E^3$, giving Equation 2.23. Third-order processes can occur in all optical media as there are no requirements on the symmetry of the material.

$$P_{NL} = (\epsilon_0 \chi^{(3)} E_0^3) \left(\underbrace{\frac{1}{4} cos(3\omega t)}_{\text{THG}} + \underbrace{\frac{3}{4} cos(\omega t)}_{\text{IDRI}} \right) \tag{2.23}$$

Third Harmonic Generation (THG)

In the case of Third Harmonic Generation (THG), three input photons of the same frequency are absorbed by the material to create a fourth photon at three times the input frequency (presented on Figure 2.7). This process is however less efficient than SHG.

Intensity Dependent Refractive Index (IDRI)

Another effect visible from the expansion of P_{NL} is the Intensity Dependent Refractive Index (IDRI). It is also known as the optical Kerr effect [19] and corresponds to the case when we consider the linear response and neglect the THG in a centrosymmetric medium. With this nonlinear response, we now have $n = \sqrt{1 + \chi^{(1)} + \chi^{(NL)}}$, which leads to a nonlinear refractive index n_2 (n_0 is the linear refractive index):

$$n \approx n_0 + \frac{3\chi^{(3)} E^2}{8 n_0} = n_0 + n_2 I \tag{2.24a}$$

$$n_2 = \frac{3\chi^{(3)}}{4 n_0^2 c \epsilon_0} \tag{2.24b}$$

The optical Kerr effect leads to a modulation of the refractive index as a function of the

intensity. This effect can lead to self-focusing. The intensity of a Gaussian beam is spatially non-uniform, the centre of the beam is more intense than its wings. Therefore, a lensing effect happens and the refractive index is the strongest on the optical axis, leading to the focusing of the beam, itself leading to an increase in intensity that may cause damage to the medium. Self-focusing in condensed matter can also be useful, e.g. for white light generation [34].

Self-Phase Modulation (SPM)

Self-Phase Modulation (SPM) is a time-domain consequence of the IDRI. If accurately controlled, it can be used for many applications. SPM occurs when the temporal phase of the pulse is self-modified by its own intensity.

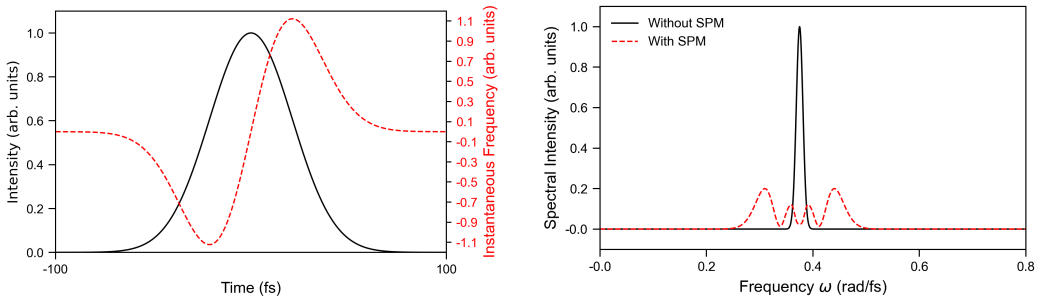
The spectral phase accumulated in space as the pulse propagates along the z-axis is given by:

$$\phi(t) = \omega_0 t - kz = \omega_0 t - \frac{2\pi n(t)}{\lambda_0} z = \omega_0 t - \frac{2\pi(n_0 + n_2 I(t))}{\lambda_0} z \tag{2.25}$$

When we differentiate this spectral phase, we can obtain the instantaneous frequency $\omega(t)$.

$$\omega(t) = \frac{d\phi(t)}{dt} = \omega_0 - \frac{2\pi}{\lambda_0} n_2 z \frac{dI(t)}{dt} \tag{2.26}$$

When considering a time-dependent Gaussian distribution of intensity, $I(t) = I_0 e^{-(t/\tau)^2}$, SPM yields an intensity-dependent change of the instantaneous frequency as shown on Figure 2.8a. When the intensity rises as a function of time, the pulse is red-shifted while the trailing edge is blue-shifted. The spectrum is broadened due to this intensity dependent phase (Figure 2.8b).



(a) (b)

Figure 2.8: SPM on a Gaussian pulse. 2.8a: The black curve corresponds to the intensity of the pulse while the red curve corresponds to the instantaneous frequency. 2.8b compares the spectrum of a 30 fs pulse with and without SPM.

2.4 Characterisation of Ultrashort Pulses

As has been described in the previous section (Section 2.1), ultrashort pulses can be affected by "minor" fluctuations along the beam that will add both linear and nonlinear phase to the pulse. It is therefore necessary to have an understanding of the pulse arriving at the experiment. It is challenging to measure the spectral amplitude and phase in time as these pulses are in the ultrafast domain. Electronic detectors (i.e. photodiodes) have a slow response time compared to the dynamics of the pulse (nanosecond range *versus* femtosecond range). There are no faster events than the pulses themselves to sample the waveform of an ultrashort pulse. The solution to this is to use an optical technique and use the pulse to measure itself, i.e. an auto-correlation. Multiple techniques have been developed to reconstruct the pulse (e.g. Frequency Resolved Optical Gating (FROG) [35], Dispersion Scan (D-Scan) [36], Spectral Phase Interferometry for Direct Electric field Reconstruction (SPIDER) [37] or variants of SPIDER [38]), we will focus on two of them, used in the experiments to diagnose the pulses.

2.4.1 Frequency Resolved Optical Gating (FROG)

FROG [35, 39] draws from the principles of autocorrelation which relies on the pulse interfering with itself. To sample the pulse, nonlinear effects are exploited, mostly second-order processes which allow the characterisation of weak and strong fields. The pulse is separated into two replicas of itself which first interfere in a nonlinear medium, and the spectra of the resulting pulse is recorded on the detector. The nonlinear signal (e.g. second harmonic) produced is measured as a function of the delay between the two replicas. The simplest form of a FROG is the SHG-FROG [40]. Instead of measuring the intensity of the field as the autocorrelation does (with a photodiode), the full spectrum of the generated second harmonic is measured, i.e. a spectrum for each delay is measured which gives a 2D trace (Figure 2.9). The spectrogram measured for the SHG-FROG is given by:

$$I_{\mathrm{FROG}}(\omega,\tau) = \left| \int_{-\infty}^{\infty} E(t)E(t-\tau)e^{i\omega t}\,dt \right|^2 \tag{2.27}$$

where τ is the time delay between the two replicas of the pulse, i.e. the test pulse (pulse to be measured) and the probe pulse (sampling pulse).

In the work reported in this thesis, SHG-FROG is typically used but we can note that other FROG geometries can be put in place, such as polarisation-gate or a transient grating FROG [35] (any instantaneous nonlinearity can be used).

With the FROG, both the phase and the intensity can be measured. Indeed, while the auto-correlation is simple to use, it loses all phase information. The chirp of a pulse can be measured

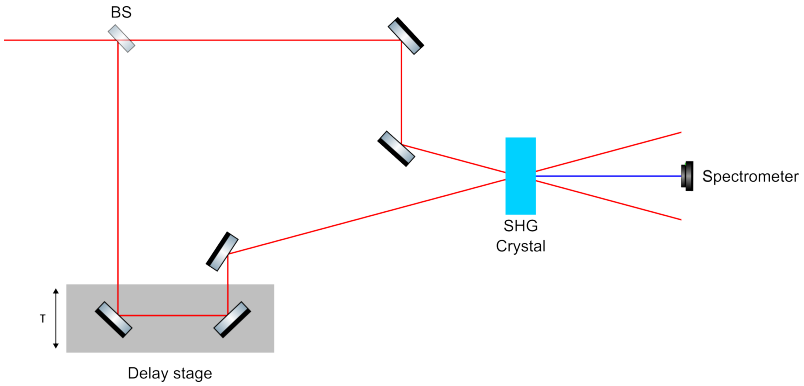


Figure 2.9: Optical schematic of a self-referenced SHG-FROG. The input pulse is split in two replicas with a beam splitter (BS) that are both focused on a nonlinear crystal, generating the second harmonic. Only the SHG signal is collected and measured on the spectrometer as a function of delay τ.

with the SHG-FROG, however, the sign of the chirp cannot be immediately determined because the trace in this case is symmetric (Figure 2.10). It is possible to do multiple measurements with added dispersive media in order to determine the sign of the dispersion. SHG-FROG has a good Signal-to-Noise Ratio (SNR) as the signal beam has a different colour than the fundamental which means the scattered light is easily filtered [41]. It is important to note that the SHG crystal needs to have a sufficient bandwidth to frequency double the entire bandwidth of the measured pulse. Indeed, the nonlinear interactions need to be phase-matched [42] and if the phase matching bandwidth is insufficient, the FROG trace will be reshaped with artefacts. To accommodate for this, thin crystals are used.

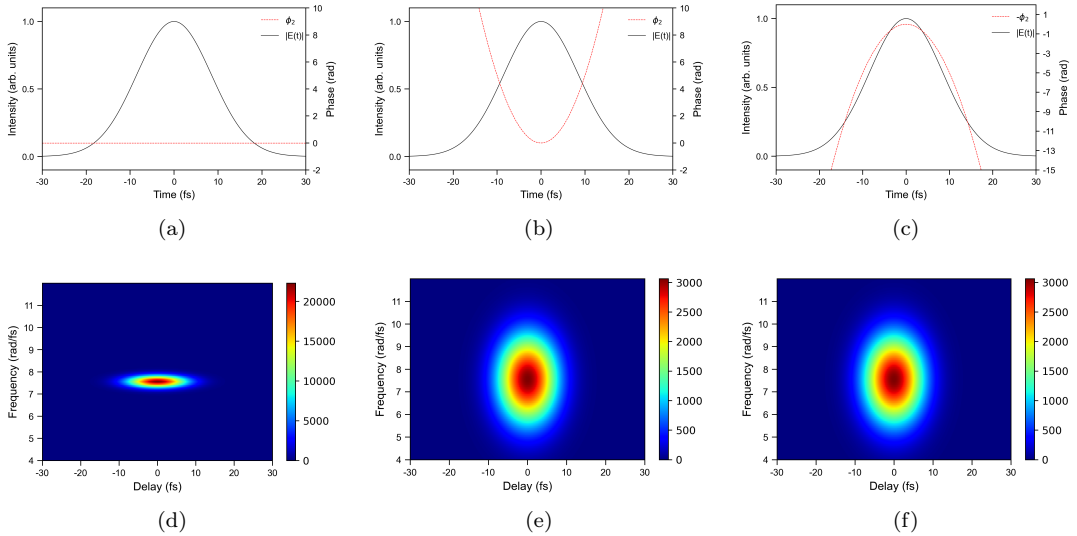


Figure 2.10: Spectrograms produced by a SHG-FROG. Top row (2.10a-2.10c): The intensity of a 20-fs pulse centred at 800 nm where (a) no added chirp, (b) positive chirp, and (c) negative chirp. Bottom row (2.10d-2.10f): Retrieved spectrogram of pulses a-c using a home-built model.

From the recorded spectrogram, the pulse can then be reconstructed with an iterative algo-

rithm using a Generalised Projection Algorithm (GPA) [43]. This algorithm uses iterative Fourier transforms for phase-retrieval, following two constraints: the data constraint (the measured spectrogram) and the mathematical-form constraint (the interaction between signal and gate). When the error between the measured spectrogram and the retrieved one is small enough ($\sim 1\%$), the iterations stop. However, the measurements and the applied algorithm can be slow to acquire, limiting the efficacy of the FROG technique when applied to real-time pulse characterisation.

2.4.2 Dispersion Scan (D-Scan)

For very short pulses, the FROG can have limitations as it is difficult to have SHG crystals that can sustain such large bandwidths. Moreover, all optics used in such devices should be reflective to avoid adding extra dispersion, thus rendering the alignment on a d-cut mirror more complicated than on a beam splitter. Another technique has therefore been developed to be able to measure more easily few-cycle pulses. The Dispersion Scan (D-Scan) was first demonstrated in 2012 [36] and does not require a second pulse (replicate of the pulse or any other signal). The D-Scan technique works by imparting a known dispersion onto the pulse: firstly a fixed amount of dispersion is added to the pulse, usually negative with a set of chirped mirrors and secondly a variable amount of dispersion is then added through the insertion of glass wedges, allowing to reach the optimum compression (Figure 2.11).

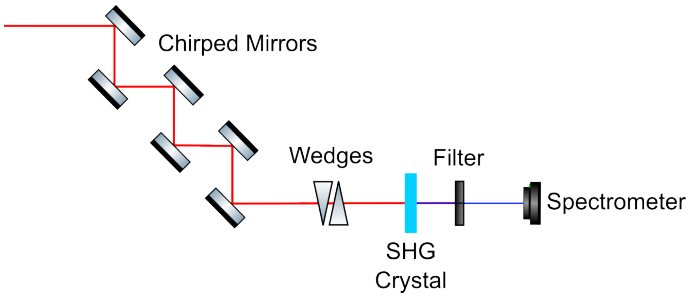


Figure 2.11: Optical schematic of a D-Scan setup. The input pulse goes through chirped mirrors (fixed dispersion) and glass wedges (variable dispersion) and then to a nonlinear crystal, generating the second harmonic. The SHG signal is collected and measured on the spectrometer.

It is important to note that the dispersion can be tuned differently depending on the scheme used, i.e. it is not always needed to first impart a fixed amount of dispersion, this is just to ensure an optimal compression point [44]. A nonlinear crystal is then used to generate the second harmonic of the fundamental which is measured by a spectrometer. Similar to the FROG technique, other nonlinearities can be used, such as the THG [45]. The versatility of this technique that uses only one pulse allows for *in situ* measurements of the pulse at the experiment [46]. As only a single pulse is required, the alignment of the D-Scan is straightforward, does not rely on the temporal overlap between two arms such as in the FROG and one can use hard focusing in the nonlinear

crystal to generate the desired signal efficiently.

The trace collected by the spectrometer corresponds to a 2D spectrogram: for each wedge insertion position, a spectrum is displayed. This trace can be written as [47]:

$$I_{\text{D-SCAN}}(\omega, z) = \left| \int_{-\infty}^{\infty} \left(\int_{-\infty}^{\infty} E(\omega) e^{ikz} e^{i\omega t} \, d\omega \right)^2 e^{-i\omega t} \, dt \right|^2 \tag{2.28}$$

where z is the thickness of the dispersive material in the beam path.

A retrieval algorithm is then applied to the data to reconstruct the amplitude and phase of the pulse [47]. It minimises the root-mean-square error between the measured and simulated spectral intensity function by varying the unknown spectral phase. Depending on the implementation of the D-Scan and the retrieval algorithm, the fundamental spectrum can also be collected by a spectrometer. In this thesis, a SHG-D-Scan was employed adapted from a commercial system (*d-cycle R, Sphere*).

2.5 Theory of Condensed Matter Properties Related to This Thesis

An overview of the theory of the light-matter interactions for HHG will be given in the next section. However, a few key features of solid-state physics are crucial for the understanding of electron dynamics in solids and are briefly presented in this section as a foundation for understanding HHG.

2.5.1 Band Structure

In a solid, the periodic layout of the atoms arranges electrons in energy bands separated by forbidden regions of energy (Figure 2.12). The band structure is explained by the nearly free electron model. The wavefunction of an electron in a periodic potential is described by Bloch waves. Bloch functions are solutions of the wave equation (Schrödinger equation) for a periodic potential and represent the product of a plane wave with a function that has the periodicity of the crystal lattice [48]. The potential splits in bands of allowed energies and forbidden energies because the wavefunctions of the electron needs to satisfy the boundary condition imposed by the periodic potential [49]. The energy gaps arise from Bragg reflection of electron waves in the crystal lattice as the electron waves scatter on the crystal planes.

In the context of HHG in solids, many theoretical approaches use Bloch functions [50, 51] to model the processes [52].

The bands thus created have a non-parabolic shape (non-parabolic functions of momentum)

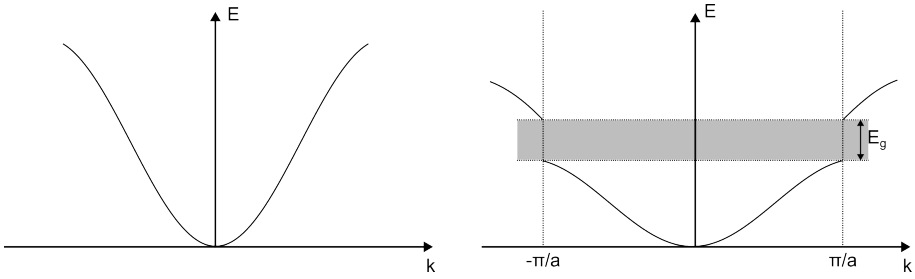


Figure 2.12: Plot of energy E as a function of wavevector k for the free electron (left side) and the bound electron in a lattice (right side). The grey area is the forbidden band. The lattice constant is a.

[49, 53]. The mass of the electrons and holes, called the effective mass, varies with the curvature of the bands, meaning that the direction of the crystal impacts greatly the dynamics of electron motion in a solid [54, 55].

The first Bragg reflection and the first energy gap occur at $k = \pm\pi/a$ (a is the lattice constant). This separation of the k-space gives rise to the first Brillouin Zone (BZ) located between $-\pi/a$ and π/a. Since the behaviour of the energy as a function of the wavevector is periodic, it is sufficient to focus on the first BZ. Figure 2.12 shows the appearance of electronic bands in the k-space, giving rise to a whole band structure, specific for each solid. We can map this band structure only in the first BZ by "folding" the k-space on itself, as imaged on Figure 2.13.

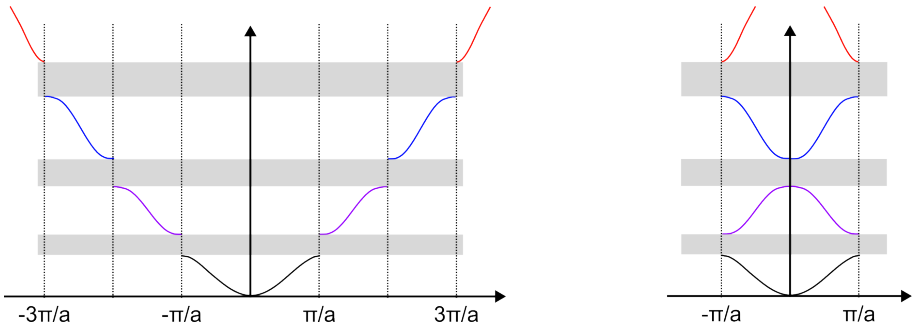


Figure 2.13: Band structure depending on the portion of the k-space selected. Left panel: band structure for all values of k. Right panel: Band structure "folded" on the first BZ.

In the band structure, two bands emerge as key elements for the understanding of the electron motion in the bands, the valence band (VB) and the conduction band (CB). The VB is the highest occupied band and the CB is the lowest unoccupied band. The energy gap between these two bands is called the bandgap E_g. In k-space, the centre of the BZ is called the Γ point. For direct bandgap solids (minimum of CB and maximum of VB at the same momentum), the bandgap is minimal at the Γ point.

2.5.2 Crystal Bonding

Crystals can generally be classified in different categories, depending on the bonding between the different atoms [56]. We focus here on three of them.

The covalent bond is due to quantum-mechanical forces. The covalent bond occurs when atoms share electrons to achieve a stable electron configuration. The bond is formed from two electrons, one from each atom participating in the bond. The covalent bond is directional and is strong (a few eV [57]). SiO_2 is an example of covalent solid.

The ionic bond is due to the electrostatic interaction of oppositely charged ions. The ionic bond occurs when one atom donates electrons to another atom. The bond is thus formed between an anion (negative ion) and a cation (positive ion) that attract each other. The ionic bond is also strong (bonding energies up to 10 eV [57]). MgO is an example of ionic solid.

The Van der Waals bond is a dipole bond due to intramolacular forces. Van der Waals bonds occur because of the fluctuation distribution of electrons in solids. They are much weaker than the covalent and ionic bonds. The Van der Waals bond is mostly responsible for the cohesiveness of noble gas solids.

2.5.3 Joint Density of States (JDOS)

The features of HHG in solids can be explained *via* the Joint Density of States (JDOS) [58, 59]. The Density of States (DOS) corresponds to the number of available electronic states per unit energy per unit volume (i.e. per k-space), i.e. the number of states between E and $E + \delta E$ [49]. At the extrema of the band structure, where the dispersion curve is flat, many states are at the same energy, meaning that the DOS is high.

In order to characterise the strength of allowed transitions between valence and conduction bands, one can use the JDOS, characterising the probability density of the electronic transitions in the crystal [56]. Tancogne-Dejean *et al.* [58] have shown that the JDOS, along with the laser parameters, are key for interband transitions.

In regions where both bands are parallel, the gradient of energy vanishes and van Hove singularities or critical points are visible as peaks in the JDOS. These features can be traced back to an enhancement of the HHG signal [60].

2.6 Theoretical Understanding of High Harmonic Generation (HHG)

When an intense ultrashort pulse is focused into a medium, a characteristic spectrum of odd harmonics of the driving laser field can be observed. The nonlinear interaction of the electric field with matter can be understood in a non-perturbative framework [61]. Indeed, the perturbation theory, detailed in Section 2.3, describing weak light-matter interactions as small corrections to a known system, fails in this regime. The interactions cannot be treated as small perturbations and the electronic structure of the material is modified by the electric field. High Harmonic Generation (HHG) was first discovered in gases in the 80s [4, 6] and later in solids. The first attempts of HHG in solids reached the 7^{th} order in a perturbative regime [62]. The first non-perturbative demonstration of HHG in the condensed phase was achieved by Ghimire *et al.* in 2011 [7] and represented a major breakthrough in the field. Since its discovery, HHG has been widely developed with the intent to create higher fluence Extreme Ultraviolet (XUV) sources. The harmonics generated in the HHG process are on the attosecond time scale [63] and hence allow to resolve sub-cycle dynamics such as electron wavepacket dynamics [64], sub-cycle electron trajectories [65] and sub-cycle ionisation dynamics [66].

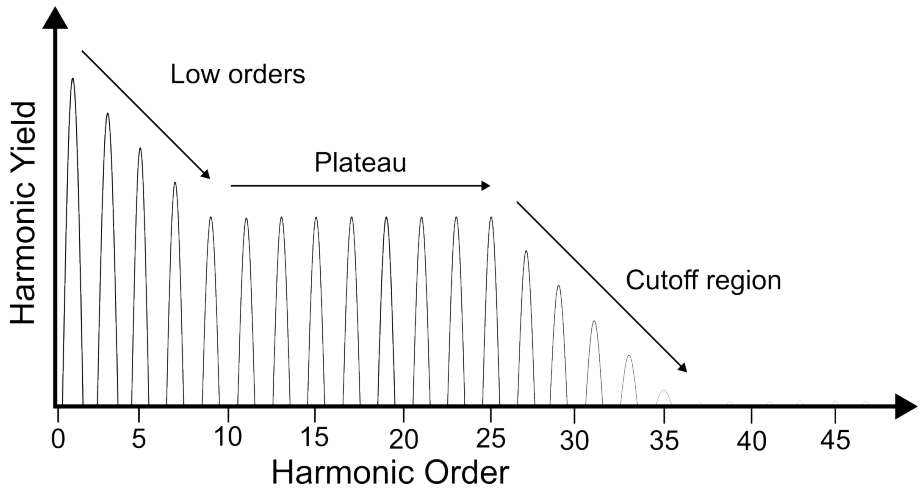


Figure 2.14: Typical emission HHG spectrum in gas with three distinctive regions.

Figure 2.14 depicts a typical HHG spectrum exhibiting three distinct regions: the first region comprises low-order harmonics, typically described by the perturbative description of nonlinear interactions (Section 2.3). In a perturbative process, the strength of the laser field represents only a weak perturbation to the medium, without modifying the properties of the medium. The medium absorbs n photons of the fundamental frequency ω to emit a single photon at frequency $n\omega$. The probability to simultaneously absorb a high number of photons is low hence the perturbative harmonics represent only the lowest orders. The perturbative yield I_{n} scales with the number of

photons n absorbed and the intensity of the fundamental pulse I_{fund}: $I_{\text{n}} \propto I_{\text{fund}}^{n}$ [23]. Low-order harmonics can still be produced in the non-perturbative regime. The second region is the plateau region consisting of harmonics with similar intensities. The third region is the cutoff region in which the harmonic yield decreases by orders of magnitude until harmonics cannot be seen anymore.

2.6.1 HHG in Gases

The HHG process can be understood semi-classically through the three-step model [67] (Figure 2.15). This model describes three steps within one single optical cycle:

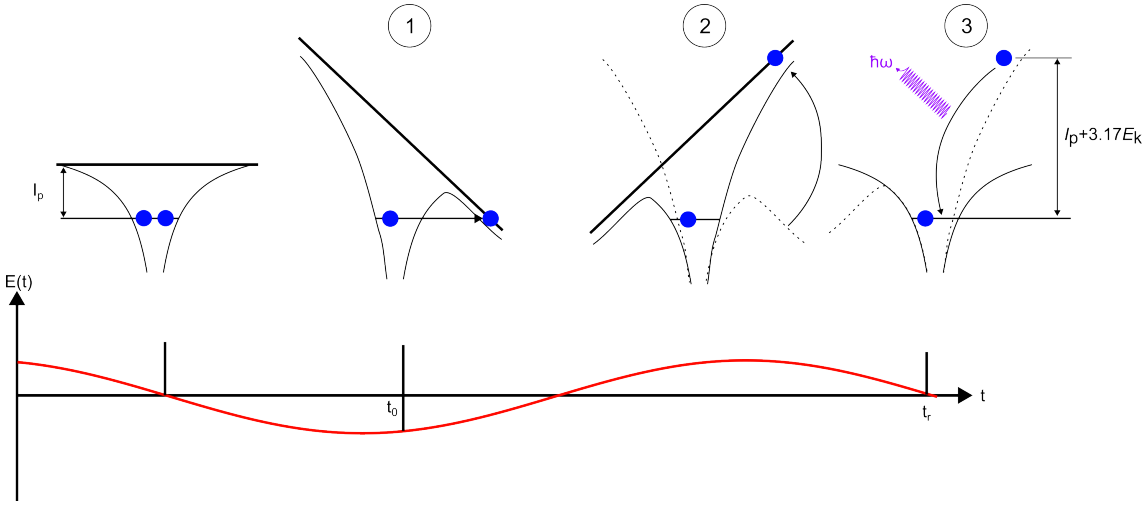


Figure 2.15: Three-step model for HHG in gases. 1. Tunnel ionisation of the electron, 2. Propagation of the electron in the electric field, 3. Recombination of the electron with its parent atom. The equation $I_{\text{p}} + 3.17E_{\text{k}}$, with I_{p} ionisation potential and E_{k} kinetic energy, corresponds to the maximum photon energy that can be emitted from an electron when recombining with its parent ion. The first term is the minimum energy needed to liberate the electron and the second term is the maximum kinetic energy the electron can gain from the laser field. The factor 3.17 comes from solving the classical equations of motion in the oscillating field. Figure adapted from [68].

Tunnel Ionisation: The bound electron that was in the potential well of the atom is ionised by tunnelling through the barrier formed by the laser field distorting the potential. This step is a quantum process. The ionisation happens at a time close to the peak of the field and after treated as "instantaneous".

Propagation: The electron is pulled away from the parent ion and propagates in the field as a free particle. The Coulomb binding potential is neglected as it becomes a small perturbation compared to the laser field. The electron motion $x(t)$ is treated classically and we can define its trajectory in the continuum.

Recombination: Every half-cycle, the field changes sign which allows the electron to recombine with its parent ion and a coherent XUV emission is generated at this step. The energy of the emitted photon corresponds to the excess kinetic energy that the electron acquired in the field plus the ionisation potential I_{p} of the gas. This step is also a quantum process, hence the semi-classical

model described here.

2.6.2 From Gases to Solids: Adaptation of the Model

Solid-state HHG is an attractive alternative for gas HHG for higher harmonic yield as it has a higher density of emitters. The main differences with the atomic case are that solids have a periodic arrangement of atoms and these atoms are closer in space. The electron dispersion is not that of free space but follows the band structure. When an electron is excited, it is lifted from the highest occupied valence band (VB) to the lowest conduction band (CB). The energy difference between these two bands corresponds to the bandgap E_{g}. The bandgap is the equivalent to the ionisation potential I_p of a gas. It is important to note the electrons can directly be ionised to higher-lying conduction bands. The energies of these electrons are much bigger than the bandgap. We will now describe the process generating harmonics in the condensed phase drawing from the theory of HHG in the atomic phase.

Ionisation

Depending on the laser intensity, two different photoionisation regimes can occur [69]:

Multiphoton Ionisation (MPI): for low intensities, the solid absorbs multiple photons at once, promoting directly electrons from the VB to the CB [54, 70]. It is usually the most probable for low-order harmonic generation.

Tunnelling Ionisation (TI): for higher intensities, the electrons penetrate the potential barrier, corresponding to the tilted Coulomb potential under the action of the strong field, adiabatically [71]. This process explains the generation of high-order harmonics.

From the Keldysh theory [72], it is possible to define the unitless adiabatic or Keldysh parameter γ, similar to the atomic case, for solids [70] which describes what type of ionisation is taking place:

$$\gamma = \frac{\omega_0 \sqrt{m^* E_{\mathrm{g}}}}{eE_0} \tag{2.29}$$

where m^* is the effective mass of the electron, E_{g} is the minimum bandgap of the solid, E_0 is the field's amplitude and ω_0 is the field's frequency. For TI, $\gamma << 1$ while for MPI, $\gamma >> 1$. Phenomenologically, we can consider this parameter as the ratio of two forces. The denominator is the laser electric field strength (Lorentz force). The numerator follows the formula of a force, i.e. a mass multiplied by an acceleration. Therefore, ω_0 corresponds to a timescale (inverse of a time) and $m^* \times E_{\mathrm{g}}$ describes the velocity of the electron in the band.

In this framework, it is assumed that the electron and hole start at the same position with no velocity. Figure 2.16 schematically shows those two ionisation processes. In order to generate

harmonics from solids, we need high intensities ($> 0.1\,\mathrm{TW/cm^2}$ [73]) but are limited by the damage threshold of the sample [74]. Therefore, for solids, $\gamma \sim 1$ and this corresponds to an in-between regime in which the electron tunnels through the barrier non-adiabatically [75]. In this case, the electron and hole can be separated at the time of ionisation and have a non-zero velocity, meaning that non-adiabatic tunnelling can occur away from the minimum bandgap, i.e. away from the Γ point [76].

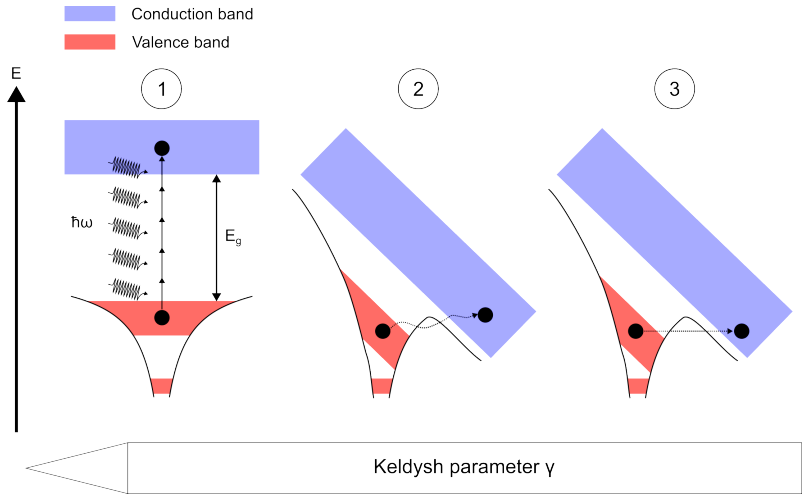


Figure 2.16: Schematic of the evolution of the Keldysh parameter depending on the type of ionisation. 1. MPI: the solid absorbs multiple photons, 2. Regime between MPI and TI: the tunnelling is non-adiabatic, i.e. not straight, 3. TI: the electron from the valence band tunnels adiabatically through the barrier to the conduction band.

Acceleration in the Field

In the atomic case, the driven electron can be considered as a quasi-free particle. However, in a solid, the electron will remain confined by the band structure and may be delocalised. High electron densities result in electron-electron scattering [77]. Moreover, the energy levels are not discrete anymore: the complex electronic structure is described in bands. We can depict the electron motion in real space or in momentum space.

After the ionisation, when the electron is in the conduction band, it is accelerated by the laser field and gains momentum $k(t)$, depending on both the shape of the conduction band dispersion relation and the laser field strength [53].

$$k(t) = \hbar\omega(A(t) - A(t')) \tag{2.30}$$

where $A(t)$ is the vector potential defined as $E(t) = -\frac{\partial A}{\partial t}$ [50].

The velocity of the electron depends on the crystal momentum due to the band structure. The hole left in the valence band also accelerates along the band. In momentum space, the hole and the electron propagate in the same direction but in real space, they travel in opposite directions

[53]. Indeed, we know that $\hbar\frac{dk}{dt} \propto -eE(t) \propto \frac{e}{\hbar}A(t)$ and a hole is the absence of an electron in the valance band. If an electron is missing from the valence band at k_0, it behaves like a positive charge at the same momentum k_0. Under the field, the same equation governs the evolution of $k(t)$ for all Bloch states, i.e. electrons in the conduction band and in the valence band. However, the electron and holes have different group velocities due to the curvature of the different bands but also to the opposite charge. Due to the periodic lattice of a solid, an electron can recombine with a different hole than its parent hole. The excursion distance of the electron has been computed for different types of solids [78].

In real space, the step of acceleration of the electron and the hole in the laser field can be explained as a movement to another lattice site. The most widely accepted understanding is that the XUV photons can be generated *via* different channels [50, 79].

As the electron moves within a band, it generates a nonlinear intraband current j_{intra} due to the anharmonic part of the band structure. Figure 2.17 depicts the schematic of the process.

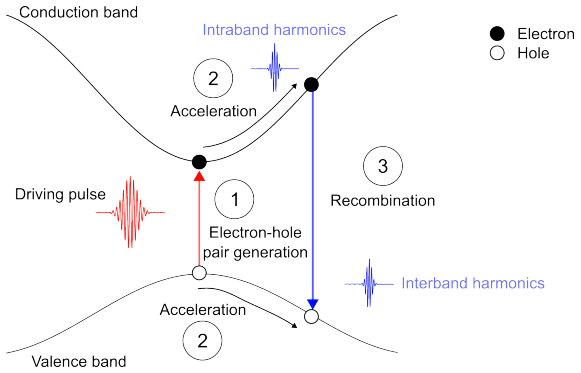


Figure 2.17: HHG in solids comprising three steps. 1. Field excitation and generation of an electron-hole pair, 2. Acceleration of the hole and the electron along the bands, 3. Recombination of the electron with the hole.

The electron can reach different crystal momenta. At the peak of the field, the maximum momentum the electron reaches is [79]:

$$k_{\text{max}} \propto \frac{eE_0}{\omega_0} \tag{2.31}$$

For high crystal momenta, the excursion distance of the electron is limited due to the curvature of the bands. Indeed, for high enough crystal momenta, the curvature of the band changes sign and the velocity is maximum at this inflection point, meaning that the excursion of the electron in the laser field is limited [53].

Depending on the laser parameters, this maximum crystal momentum can reach the edge of the first Brillouin Zone (BZ). In this case, the electrons can scatter on the edge and Bloch oscillations occur [80]: the electrons reflected at the edge of the BZ oscillate at the Bloch frequency defined as $\omega_B = \frac{eE_0a}{\hbar}$ where a is the lattice constant of the solid [48]. For long wavelengths, the intraband

process tends to dominate the HHG process [81].

If the harmonic energy is higher than the maximum bandgap difference between the VB and the first CB, it is important to take more than one conduction band into account. The electron can move to higher-lying conduction bands and the effect of those multiple bands has been reported to be the cause of a second plateau in the harmonic spectrum [82]. The inclusion of multiple conduction bands in a theoretical model can lead to a different signature in a harmonic spectrum than the one known for a single-band model [81].

Recombination of the Electron-Hole Pair and Trajectory Picture

After gaining momentum in the band, the electron and the hole recombine in the VB. The recombination forms an interband polarisation field j_{inter}. Since the hole has also been accelerated in the band, the recombination can happen away from the origin, i.e, the position at which the electron was ionised [83, 84]. We can note that this recombination or recollision can occur in an "imperfect" way [85] as the electron and hole wavepackets can spatially overlap even when their centres do not. At the time of the recombination, an XUV photon is emitted with an energy equal to the bandgap at the crystal momentum of the electron–hole pair at recollision: $\hbar\omega = E_c(k) - E_v(k)$.

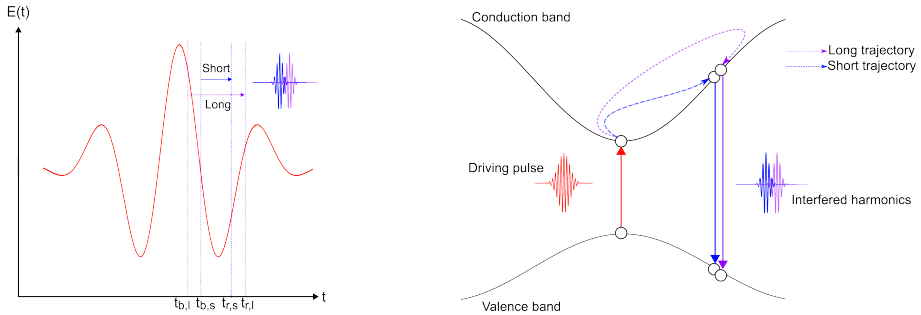
The whole process (ionisation, acceleration and recombination) occurs every half-cycle of the driving field. Therefore, in one cycle, two harmonics are emitted with opposite phase. Each electron can propagate for a different duration in the bands. Indeed, depending on its ionisation time, it will recombine at different times, taking different trajectories. When an electron recombines on a lattice site, it can come from multiple trajectories. We can categorise those different trajectories into two sets that recollide within one optical cycle and that contribute to the same harmonic order: the long and the short trajectories, first demonstrated for gases [86]. In the gas phase, these trajectories have been defined relative to the optimum trajectory generating the highest harmonic in the spectrum, the cutoff harmonic. The trajectories of the electrons excited before the cutoff but after the peak of the laser field are the long ones as the electrons will propagate longer in the field while the trajectories of the electrons excited after the cutoff are the short trajectories. Following this, the XUV photons emitted cover a continuous spectrum. However, they interfere with each other and this leads to a structured harmonic spectrum at odd frequencies of the fundamental [67]. The type of trajectories is directly imprinted on the harmonic spectrum. The photons created from each short and long trajectory can interfere leading to quantum path interference of trajectories [87]. Figure 2.18 shows this interference of short and long trajectories. The harmonics generated for the different trajectories accumulate phase (harmonic q accumulates the phase ϕ_q). The phase is larger for long trajectories. The same harmonic component for the two sets of trajectories interfere, leading to spectral modulations in the harmonic spectrum. We define the accumulated

phase ϕ_q and the centre frequency Ω_q for harmonic order q as a function of the time-dependent laser intensity $I(t)$ [87]:

$$\phi_q(t) = -\alpha_q I(t) \tag{2.32a}$$

$$\Omega_q(t) = q\omega_0 + \alpha_q \frac{\partial I(t)}{\partial t} \tag{2.32b}$$

where α_q is a constant coefficient depending on harmonic order and type of trajectory [88].



(a) (b)

Figure 2.18: Short and long trajectories in solid HHG. 2.18a shows the electric field as a function of time and the short and long trajectories are emitted at $t_{b,s}$ and $t_{b,l}$, respectively. They recombine at $t_{r,s}$ and $t_{r,l}$. 2.18b is the schematic of the long and short trajectories of electrons in the bands. They recombine to generate harmonics at the same energy.

This picture is valid for intensities low enough that the electrons stay in the BZ. Indeed, as soon as they cross the edge of the BZ, trajectories will become more complicated and open more channels for harmonic emission [89]. For high enough fields, this model has flaws as short trajectories can recombine multiple times before a long trajectory recombines [53].

Summary of the Solid HHG Process

The total harmonic spectrum can now be calculated as the sum of the interband and intraband contributions [50]:

$$HHG(\omega) = |FT(j_{\text{intra}} + j_{\text{inter}})|^2 \tag{2.33}$$

The research area of HHG in solids is constantly growing [90] and building from what has been already demonstrated theoretically, new computational methods are developed to match experiments. However, the basic understanding of the process is still under debate, particularly the role of intraband and interband mechanisms [91, 92, 93]. The dominance of one or the other mechanism depends on the solid itself and on the laser parameters most importantly (field strength and wavelength). Experimentally, evidence has suggested that one of the two mechanisms may

dominate: intraband [94, 95, 96, 97, 98] or interband [99, 100, 81]. The differentiation can be made by investigating the chirp of the harmonics [101, 100]. Interband transitions originate from different times in the electric field, hence present an atto-chirp as opposed to harmonics originating from intraband currents, which are emitted at the same time. Moreover, the two processes do not show the same CEP dependences.

2.6.3 Properties of HHG from Solids

The harmonics have specific features depending on key parameters. The most important ones relevant to future results (Chapters 5 and 4) are explained in this section.

Cutoff Law with Field Strength

The spectral cutoff position is one of the major features of HHG. It is now a key goal to generate XUV photons with the highest energies, hence the motivation to extend the cutoff. Moreover, if the cutoff is high enough, the bandwidth of the HHG radiation can be broad enough for the production of attosecond pulses [12].

The derivation of the cutoff law in solids has been debated in the literature and a small summary is presented in this section. Vampa *et al.* derived a cutoff law [79] and first defined the cutoff energy as the "maximum photon energy in the plateau region of the spectrum, before the exponential roll-off of the high harmonic intensity" (Figure 2.14). The cutoff energy is determined by the electron-hole pair that recombines with the highest momentum k_c.

$$E_{\text{cutoff}} = E_{\text{g}}(k_c) \tag{2.34}$$

Equation 2.34 [79] shows that the momentum-dependent bandgap is reflected by the dependence of the cutoff with the field strength. In the atomic case, the electron energy varies quadratically with momentum which means the cutoff varies quadratically with the field and linearly with intensity. In solids, the dispersion of the bands renders the analysis more complicated. Close to the centre of the BZ, the band energy varies linearly with momentum, where the curvature changes sign. With a nearest neighbour band computational model, Vampa *et al.* [79] derived a cutoff law linear with the field that gives more accurate results than a pure classical description. However, their approach becomes inaccurate for high intensities when the electron travels in the entire BZ and band dispersion is not linear anymore.

Ghimire *et al.* [7] verified the model experimentally and derived a linear scaling of the cutoff energy with field strength in ZnO. Additional experimental work revealed similar behaviour in GaSe [94] and SiO_2 [95], although over a narrow intensity range and with few data points. Theoretically, Wu *et al.* [93] have shown that when the spectrum exhibits multiple plateaus, the cutoff of each

plateau was linear with field strength. However, a linear scaling of the cutoff with field strength is not always experimentally observed. Experimentally, in solid argon and krypton (Van der Waals solids) [102], a non-standard cutoff was reported. Finally, Tamaya *et al.* [103] have formulated a clear equation for the cutoff energy depending on which regime of ionisation is taking place. They focused on the diabatic processes of the Bloch electrons and differentiated the Zener tunneling for which the plateau is broader as the bandgap increases (the cutoff shifts to higher energies with the bandgap) and the semimetal regime for which the cutoff energy is independent of the bandgap. Overall, the validity of the linearity of the cutoff energy with field strength is only moderate as it depends tremendously on the laser parameters and the nature of the solid.

Wavelength Scaling

The laser wavelength plays a major role in atomic HHG. Indeed, the cutoff scales with the square of the wavelength $E_{\text{cutoff}} \propto I\lambda^2$ [6]. In solids, the wavelength scaling of the cutoff has been experimentally [104] and theoretically [105, 58] studied. However, no clear law has been formulated, the main difference coming from the fact that electrons are bound to the lattice.

The dependence of the solid HHG cutoff on the wavelength has been proposed to be linear [93]. This is explained by the proportionality of k_{max} (Equation 2.31) with wavelength. In the region where the conduction band is linear, the cutoff can vary linearly with wavelength. However, some groups have also found no significant wavelength dependence in silicon, MgO and ZnO [58, 106, 107]. Ghimire *et al.* [107] explained this by calculating the conductivity of the sample as a function of harmonic energy. The total HHG current depends on the complex conductivity and they showed that the cutoff energy was independent of wavelength because the conductivity scales inversely to the harmonic energy. Liu *et al.* [105] have gone further and demonstrated that the scaling was different for intraband and interband contributions: the cutoff energy of the intraband contribution is wavelength independent while for the interband contribution, it is linear with wavelength. This theory reconciles both views by proposing that the spectrum cutoff scaling with wavelength depends on which mechanism is dominant.

The impact of the wavelength on the harmonic yield has also been investigated, firstly for gases theoretically [108] and experimentally [109]: at constant laser intensity, the yield of the harmonics from krypton scales as $\lambda^{-6.5}$ [109]. In solids, similar investigations have been undertaken and have found a λ^{-4} scaling of the harmonic yield [110] (for specific theoretical parameters). This scaling arises from the wavepacket spreading as well as the overall yield and energy distribution effect. The spectral intensity of the interband and intraband contributions have been simulated [53] and showed that for $\lambda < 5\,\mu\text{m}$, the interband recombination dominated the HHG spectrum but slowly dropped in intensity. This is explained by the fact that the excursion time of the electrons

increases with wavelength and hence the electron presents a lower probability to recombine with a hole. Beyond 5 µm, the intraband mechanism takes over as the electron travels further in the bands, it crosses more than once the BZ in one laser cycle and therefore oscillates more in the field.

Polarisation Ellipticity Scaling

A key difference between solid and gas HHG is the effect of the ellipticity of the driving laser field on the harmonic yield. Atomic HHG is a more localised process which limits the harmonic yield but also implies that as the ellipticity of the laser increases, the yield will drop because the electron will be driven too far from its parent ion and will not recombine [111].

In condensed matter however, the process is delocalised [83] and the electron can recombine with its parent hole with an elliptic field. Many groups have investigated this dependence, for example [7, 102, 112, 16, 113, 114, 115] and it is summarised by Park *et al.* [116]. The ellipticity of the driving field can modify the harmonic yield but can also modify the ellipticity of the harmonics and opens thus a way to understanding selection rules of different harmonics and their polarisation states [117]. Using an elliptical field can generate circularly polarised harmonics, thus allowing a control of the harmonics [118].

2.6.4 Theoretical Modelling

This thesis studies experimentally HHG in solids, therefore the development of a detailed model of solid HHG was beyond the scope of my project. However, as my experimental results will be compared to the literature, I present here a brief summary (based on Yu *et al.* [119]) of the main models existing to simulate harmonics generated from the condensed matter. The goal of this section is not to review the mathematical descriptions in these models but to comment on why there are so many different models.

Time-Dependent Schrödinger Equation (TDSE)

The Time-Dependent Schrödinger Equation (TDSE) can be solved in two different basis: the Bloch state basis and the Houston state basis [82]. In the former, the single-electron case in a stationary field is considered, whereas the latter includes a time-dependent basis. In both cases, the harmonic spectrum is found by performing a Fourier transform on the calculated current, separated in intraband and interband currents only in the Houston state basis. Solving the TDSE for solid HHG was first demonstrated in [120] and then widely applied in this field [81, 102, 121, 122, 123].

Wu *et al.* [93] made a direct comparison between the two basis and showed that for higher intensities, the number of bands was a determining element differentiating them. TDSE has been successful to explain the appearance of multiple plateaus seen experimentally [102]. It is numeri-

cally complex but has the advantage that many bands (more than 50 [93]) can be included. It has thus demonstrated that the features of the harmonic spectrum depend on the energy separation and the coupling strength between the bands. However, this method does not account for the lattice structure. Some groups have therefore transferred the Bloch basis to a Wannier basis followed by a saddle-point integration rendering a quasi-classical approach [84].

In order to improve this model, it has been used in a 2D basis mainly to investigate orientation-dependent harmonic emission [124].

Semiconductor Bloch Equations (SBEs)

Semiconductor Bloch Equations (SBEs) is another model that works well for HHG in solids, especially in semiconductors ($E_g < 5\,\text{eV}$) with MIR excitation [12, 50, 125, 7, 126]. The SBEs model includes transition dipole moments describing the strength of the interaction between the electric field and the electronic states in the semiconductor, i.e. the probability of the transition between the VB and CB. SBEs allow for simple calculations that give a good interpretation of the results as a first approximation. However, it has been demonstrated that it tends to break down for high intensities [94, 91]. Most of these simulations are made with a two-band model but it is possible to include multiple bands, leading to quantum interference between the different excitation paths.

The SBEs represent a system of coupled equations calculating the change of population in the CB (corresponding to the opposite of the one in the VB) as well as the time-varying microscopic polarisation. They directly depend on the bandgap between the valence and conduction bands, the interband excitation and the interband acceleration [50].

Another parameter appears when deriving the SBEs, the phenomenological dephasing parameter T_2 corresponding to the dephasing of the interband harmonics [127]. Dephasing in solids can arise from electron-electron collisions, phonon interactions [128] and disorder [129]. This dephasing term selects the returning trajectories. A short dephasing time suppresses the high-order returns whereas for longer dephasing times, the long trajectories are stronger [53]. As a phenomenological parameter, it can be easily tuned in order to match theoretical spectra to experimental ones. This parameter is however still under debate, as some works have proven it is not needed for convergence [130]. Short dephasing times are usually preferred as they seem to agree well with experimental spectra but it could just be because the BZ is undersampled. Some models have explained the dephasing from electron-hole coherence [131].

Time-Dependent Density Functional Theory (TDDFT)

Time-Dependent Density Functional Theory (TDDFT) has been developed to sudy the microscopic aspects of HHG [132]. Tancogne-Dejean *et al.* [58] has used this model to justify that the use of a

single-particle approximation is valid. This model calculates the currents over a unit cell. TDDFT is therefore a computational heavy model that allows to account for the band structure as well as the real crystal structure [115, 133]. For HHG with propagation effects, TDDFT has been used successfully [134].

Chapter 3

Experimental Setups and Methods

In this section, the two different laser systems used for this thesis are presented. They have different pulse generation techniques and characteristics. The first laser system is located at Imperial College London and it is a Near-Infrared (NIR) system producing pulses with a duration tunable from 4 to 30 fs. The second laser system was used at Advanced Laser Light Source (ALLS) in Canada. It produces Mid-Infrared (MIR) ultrashort pulses.

3.1 Overview of the Apparatus for the Near-Infrared (NIR) Beamline

3.1.1 Laser System and Pulse Compression

Laser System

The use of Ti:S lasers is commonplace for HHG experiments since the ultrashort pulse durations available from Ti:S lasers allow access to high intensities with a relative low energy [135]. The laser system used in this chapter comprises a Ti:S oscillator that seeds a Ti:S multi-pass amplifier. The oscillator (*Femtosource, Femtolasers GmbH*) is pumped by a commercial Continuous Wave (CW) frequency-doubled Nd:YAG laser (*Verdi V5, Coherent Inc.*). It generates 10 fs pulses of a few nJ at 80 MHz via Kerr lens mode-locking [136]. The mode-locked spectrum is centred at 800 nm with a FWHM of 80 nm. This output needs to be amplified by $\sim 10^6$ times (mJ-level) to reach high intensities required for HHG.

The oscillator therefore seeds the amplifier (*Femtopower HE CEP, Femtolasers GmbH*) pumped by a frequency-doubled Nd:YLF laser at 527 nm (*DM30, Photonics Industries*). The amplifier is based on Chirped Pulse Amplification (CPA) [18] and produces 30 fs pulses centred at 780 nm with up to 2.5 mJ energy at 1 kHz repetition rate. The pulses from the oscillator go through a

Faraday isolator to avoid any back reflections and are stretched in 10 cm of SF57 glass to ~ 20 ps to allow amplification of the pulses without any damage to the optics. The output beam of the oscillator overlaps with the amplifier pump beam in the Ti:S crystal which is cryogenically cooled (190 K) in order to prevent thermal lensing in the crystal. The crystal is maintained at vacuum to prevent surface damage from water or aerosol condensation build-up. It is important to note that the lifetime of the gain of Ti:S (few µs) is longer than the pump pulse duration (~ 180 ns), which means that the amplification of the pulse train from the oscillator is efficient when temporally overlapped with the pump.

The oscillator pulse train passes four times through the Ti:S crystal before it reaches saturation for further amplification. In order to continue the amplification process, the repetition rate needs to be lowered from 80 MHz to 1 kHz. This is achieved by a Pockels cell (*BME Bergmann KG*) which rotates the polarisation of one pulse every ms (rate of 1 kHz). The beam also goes through an Acousto-Optic Programmable Dispersive Filter (AOPDF) (*Dazzler, Fastlite*) for pulse shaping. The Dazzler couples an acoustic and an optical wave in a birefringent medium, TeO_2 [137]. The acoustic wave creates an index grating. The different spectral components are thus diffracted on different spatial positions on the other birefringent axis of the crystal. This is equivalent to controlling the group delay of these components, allowing pulse shaping. Indeed, the Dazzler shapes the spectral phase to flatten the phase over the whole spectrum (for perfectly compressed pulses after the compressor) and the spectral amplitude to avoid gain narrowing and get a smooth spectral shape.

The laser beam then goes through another six passes in the crystal for amplification. It is then sent to the grating compressor system, consisting of a pair of transmission gratings in order to shorten the pulse duration of the amplified pulse.

Hollow Fibre Pulse Compression

In order to explore physics in the few-cycle regime, an external compression system (to distinguish from the grating compression inside the laser) is used. Indeed, CPA systems are limited to $\gtrsim 20$ fs pulses due to gain narrowing [18]. Following the Time-Bandwidth Product (TBP) described in Section 2.1, the spectral bandwidth of the laser pulses first needs to be broadened to obtain shorter pulse durations. Increasing the spectral bandwidth is most commonly achieved through exploiting SPM, using a suitable nonlinear waveguide. The most notable techniques using SPM in a nonlinear medium are filamentation [138], a hollow core fibre (HCF) filled with a rare gas [139] and the use of a nonlinear crystal [140]. These techniques each present advantages and disadvantages and in this section, we will focus on HCF as this is the method used in this laser. It is the most widespread technique to generate high-power few-cycle pulses as it is not limited by the damage threshold of a

crystal and has a cleaner spatial and spectral output than filamentation although HCF experiences higher losses [141]. The HCF is filled with a rare gas that serves as the nonlinear medium for SPM and its length (typically $\approx 1\,\mathrm{m}$) and narrow core (few hundreds of µm) allow for large nonlinear interactions. The main application of the HCF is the compression of Ti:S pulses [142].

The guiding of the light relies on grazing incidence reflections of the light at the core cladding interface with the condition that the fibre radius a follows $a >> \lambda$. The fibre is made of a dielectric, in this case, glass. There is therefore little energy loss due to refraction [143]. The fibre supports multiple modes but the most efficient transmission occurs when only the fundamental EH_{11} hybrid mode couples in the fibre and is transmitted. For optimal coupling of a Gaussian laser mode to EH_{11}, the beam spot $1/\mathrm{e}^2$ radius w_0 and the radius a obey Equation 3.1 [144]. The EH_{11} mode has a single peak and suffers the lowest absorption loss in the fibre.

$$w_0 = 0.64a \tag{3.1}$$

The maximum possible energy throughput is mainly limited by plasma formation (ionisation of the gas) at the fibre entrance as well as self-focusing in the waveguide. The former can lead to a deformation of the laser beam at the entrance of the fibre thus degrading the coupling [145]. It is therefore crucial to limit the input power going into the fibre below a specific threshold, called the critical power, P_{crit} (typically lower than $50\,\mathrm{GW}$), in order to balance the trade-off between spectral broadening and energy transmission. Moreover, reproducible alignment with a motorised beam pointing system (discussed in more details later) mitigates any damage to the entrance of the fibre.

To fill the fibre with gas, two different schemes can be implemented: static filled (SF) or differentially pumped (DP) fibre [146]. Employing a DP scheme enables a pressure gradient to form through the fibre (lowest pressure at the entrance), which means that the focusing into the fibre is independent of gas pressure and pulse intensity. Indeed, at the fibre entrance, the pressure is close to vacuum which limits the gas density and nonlinear effects. This means for high input energy, there is no saturation of the output energy [147].

As the pulse propagates through the gas in the guided medium, it experiences a large amount of SPM and the spectral broadening depends on the nature and the pressure of the gas following Equation 3.2. At the output of the fibre, we thus can have a smooth intensity profile (the fibre acts as a spatial filter) that has a spectral bandwidth $\Delta\omega$ defined as [148]:

$$\Delta\omega = \frac{0.86 n_2 \omega_0}{T_0 c A_{\mathrm{eff}}} \int_0^L p(z) P_0 \xi e^{-\alpha z}\, dz \tag{3.2}$$

where n_2 is the nonlinear refractive index of the gas, ω_0 and T_0 are the centre frequency and the

duration of the incoming pulse, respectively. A_{eff} is the effective area of the entrance of the fibre ($A_{\text{eff}} \approx 0.48\pi a^2$), L is the length of the fibre, $p(z)$ is the pressure of the gas along the fibre, ξ is the coupling efficiency, P_0, the input peak power and α the attenuation losses. Three typical spectra from our lab with a fibre at vacuum, filled with argon and neon are shown in Figure 3.1.

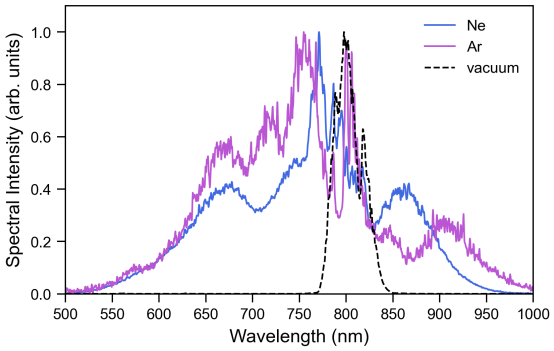


Figure 3.1: Spectra at the output of the HCF recorded for three different cases: 3.5 bar of neon with 1.6 mJ into the fibre, 1 bar of argon, 0.7 mJ into the fibre and under vacuum (no gas).

After the fibre, the pulse is spectrally broadened but is heavily positively chirped and therefore, the pulse must go through a dispersion compensation system. Due to the high intensities, chirped mirrors are preferred to prisms and gratings [149]. Chirped mirrors have negative GDD and reflect the shorter wavelengths first and delay more the longer wavelengths, which penetrate further into the mirror layers. It is usual to impart more negative GDD than necessary in order to then finely tune the dispersion with a pair of thin fused silica wedges later which adds positive dispersion.

The results presented in this thesis made use of a 1-m long HCF with an inner radius of 175 µm. The beam was focused at the entrance with a 1.5-m focal length mirror. Argon was used in the fibre. The type of gas used depends on several experimental parameters such as the input pulse energy, the third-order nonlinearity and the ionisation potential: argon has a higher third-order nonlinearity than neon (n_2=19.4 $\times$ 10^{-19} cm^2/W for argon and n_2=1,8 $\times$ 10^{-19} cm^2/W for neon [150]), which makes it good to use with relatively lower intensities $\sim$ 8 $\times$ 10^{13} W/cm^2 permitting pulses as short as $\sim$ 4 fs [151]. The SF fibre provided a stable output spectrum (Figure 3.1). For solid HHG, lower intensities than required for gas HHG (typically 1$-$10 TW/cm^2) are needed, meaning that we can use either a DP or SF fibre. We chose a SF fibre as it consumes less gas than in the DP case and it is easier to maintain a low pressure of gas, which is necessary for argon due to its relatively high n_2.

Figure 3.2 depicts the schematic of the pulse compression with a HCF. A leakthrough of the beam through the last mirror before the fibre is used for automatic alignment with a two-point beam stabilisation system: on two different cameras (C1 and C2), the near-field and the far-field images of the beam are recorded and the images are sent to a feedback system, tweaking the motorised alignment mirrors for reproducible alignment.

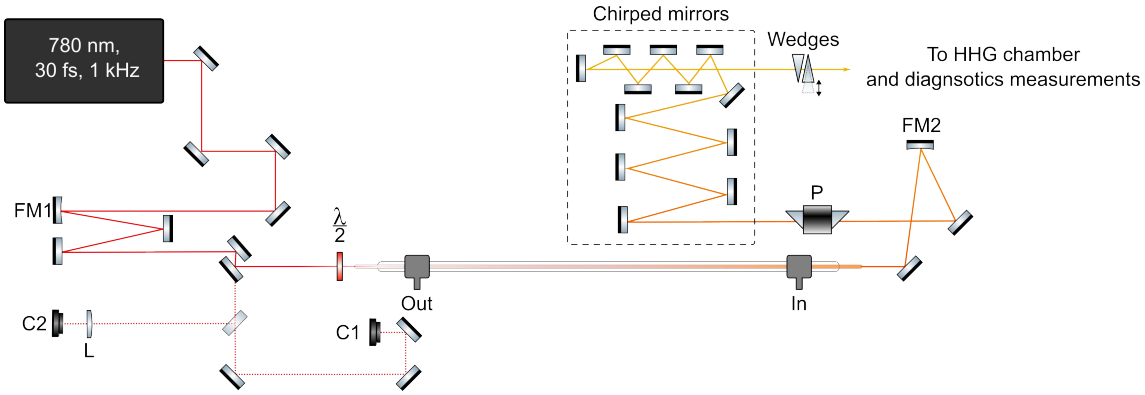
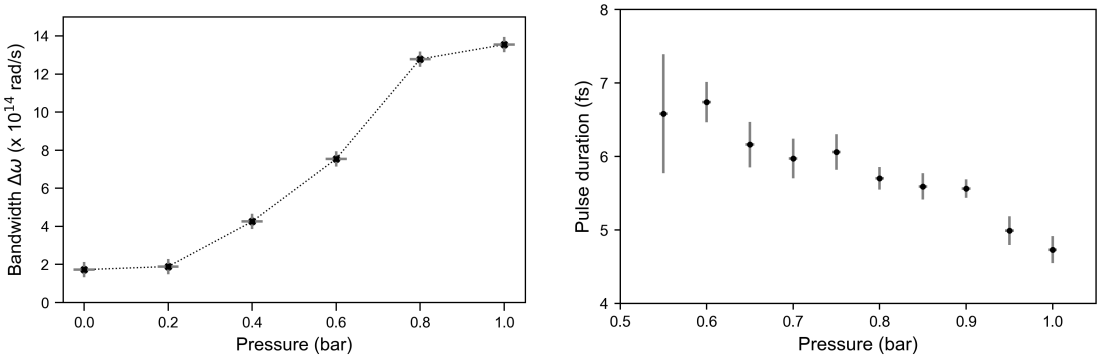


Figure 3.2: Schematic of the laser system used for HHG experiments in the NIR regime in Imperial College London's lab: the pulse is spectrally broadened in a HCF maintained at vacuum that can be filled with a noble gas. The fibre broadens the spectrum of the laser pulse and the chirped mirrors compress the pulse in time. FM1 and FM2 are focusing mirrors. L is a focusing lens and $\frac{\lambda}{2}$ is a half waveplate. P is the polariser. The fibre can be differentially pumped using a turbomolecular pump backed by a scroll or statically filled. 'In' and 'Out' show where the gas is charged into and evacuated from the HCF. The pressure is varied between 0 and 3 bar of noble gas (Ar or Ne).

The argon-filled fibre was placed in a vacuum system with base pressure sub 5 $\times 10^{-2}$ mbar. The entrance and exit windows of the system are placed far before the entrance and exit of the fibre to avoid any nonlinear effects. The beam at the output of the fibre diverges, it is thus recollimated with a 1.25-m focusing mirror (FM2). The transmission of the fibre was measured to be $\sim$ 60 % with argon in the SF fibre configuration.



(a) (b)

Figure 3.3: Measured pulse duration as a function of Ar pressure in the HCF. 3.3a depicts the spectral bandwidth of the broadened pulse as a function of argon pressure with a SF fibre (0.6 mJ). 3.3b shows the relationship between pulse duration and fibre pressure. For low pressures (below 0.6 bar), the D-Scan struggles to take reliable measurements and the errors are $\sim$ 10 %.

Figure 3.3a shows the spectral bandwidth of the broadened pulse as a function of argon pressure with a SF fibre. We know that we reach the limits of the SF fibre regime as the curve for $\Delta\omega$ is close to saturation for high pressures (above 1 bar) [146]. However, for our experiments, we find that only 1 bar of argon is required to create a few-cycle pulse. Therefore, the saturation point is not quite reached and it is acceptable to work in the SF regime. Figure 3.3b shows that varying

the pressure changes the pulse duration in a continuous way whilst maintaining pulses of constant energy [146].

A set of ten double-angle chirped mirrors (*PC70, Ultrafast Innovations*) imparting a total GDD of $-360\,\mathrm{fs}^2$ in the range 500−1050 nm are used. The beam is then directed through a pair of fused silica wedges (*OA124, Femtolasers*) for dispersion tuning. One of the wedges is on a motorised mount, so its insertion in the beam can be varied to impart more or less dispersion to the pulse. Pulses as short as 3.5 fs have been generated with this system [38], corresponding to ~ 2 cycles.

The chirped mirrors require a p-polarised beam in order for them to impart the desired GDD. Therefore, to ensure pure p-polarisation for the chirped mirrors, we use a linear thin-film polariser (*OA513, Femtooptics*) after the output of the HCF. Placing a half waveplate before this polariser enables a spectrally-neutral control of the pulse final pulse intensity.

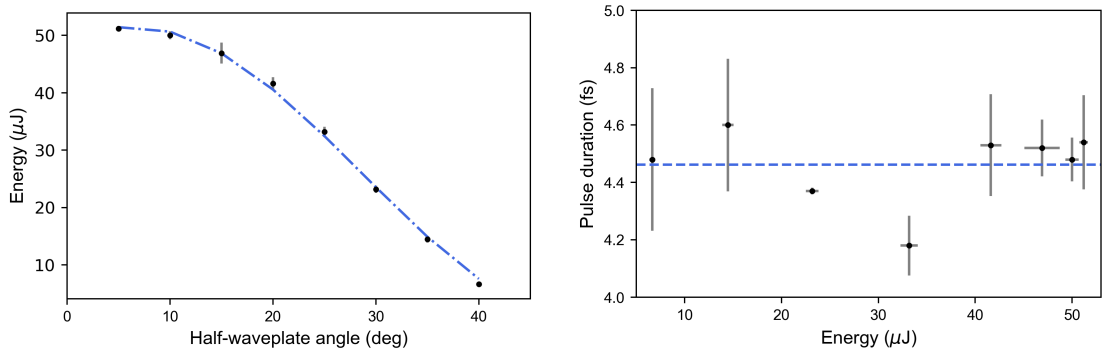
The half waveplate has to cover the whole bandwidth of the few-cycle pulse ($\sim 500-1000\,\mathrm{nm}$) if placed right before the polariser. This scheme is typically implemented in many experiments requiring power control. Indeed, an achromatic half waveplate has a variation of retardance (difference in temporal phase delay between the two polarization states at a given wavelength) with wavelength of less than a few percent over the spectral range of the laser pulse. However, as seen in Section 2.1.2, when the pulse goes through a transmissive optic, it accumulates a spectral phase that needs to be compensated for.

The linear propagation dynamics of pulses in hollow capillary fibres and SPM in a monoatomic gas are independent of the linear polarisation state of the driving pulse and preserve the linear polarisation state. Employing a similar technique to Schmidt *et al.* [152], we thus placed the waveplate (500−900 nm Achromatic, *B.Halle*) before the fibre as the pulse was long and narrow-band in this position, and therefore we avoided introducing a spectral phase on the few-cycle pulse. We also changed the fibre's Brewster windows to normal incidence ones.

The waveplate therefore rotated the polarisation state of the pulse before it went into the fibre. With this configuration, the constraints on the ultra-broadband achromaticity of the waveplate are less stringent as the pulse is spectrally narrow before the HCF. The spectral phase added to the multi-cycle 30-fs pulse is small enough that it can be compensated with the chirped mirrors already present in the setup. This experimental implementation provides smooth control of the intensity of the few-cycle pulse simply by rotating the polarisation state of the incoming pulse on the linear polariser which then selects only the remaining component in the p state. Figure 3.2 describes this intensity control implementation while Figure 3.4 shows results which demonstrate the success of this system.

Figure 3.4 demonstrates that our new way of intensity control is valid and robust as the pulse duration does not depend on intensity. The pulse duration was measured using a D-Scan (similar

specifications to the commercially available *d-cycle R, Sphere*) [36]. This system measures pulses in the range 600−1100 nm, from sub-5 fs to 20 fs and only needs an input of ∼ 1 µJ.



(a) (b)

Figure 3.4: Intensity control scheme. (a) is the variation of the pulse energy with half waveplate angle. The blue line is a fit with a function following $I_0\cos^2(2\theta + \theta_0)$ where θ is the half waveplate angle. (b) is the variation of the measured pulse duration with pulse energy. These measurements were done with 1 bar of argon in the fibre and 0.6 mJ coupling in the fibre. The dotted blue line is the average pulse duration for all pulse energies.

Characterisation of the NIR Pulses

After all the optics presented in Figure 3.2, a movable pick-off mirror sent the pulse to a spectrometer to measure the laser spectrum and to a SHG-FROG or D-Scan to measure the pulse duration. The pulse energy was also measured with a power meter (*PM10-19C, Coherent*). For the results presented in Chapter 4, the pulse duration, spot size and spectrum were characterised. The pressure in the fibre was tuned to produce pulses with varying pulse duration from 4 to 30 fs. The fundamental spectrum of each pulse is presented in Figure 3.5.

The position of the wedges after the chirped mirrors was optimised, ensuring the minimum pulse duration incident on the sample and a flat temporal phase. The pick-off mirror for pulse characterisation was placed after all transmission optics of the setup, ensuring no additional GVD on the measurement. The temporal pulse characterisations are shown in Figure 3.6.

The focal spot size on the HHG sample was found to be 215 µm (e^{-2} diameter), shown on Figure 3.7.

Table 3.1 summarises the parameters of all the driving pulses used in this work.

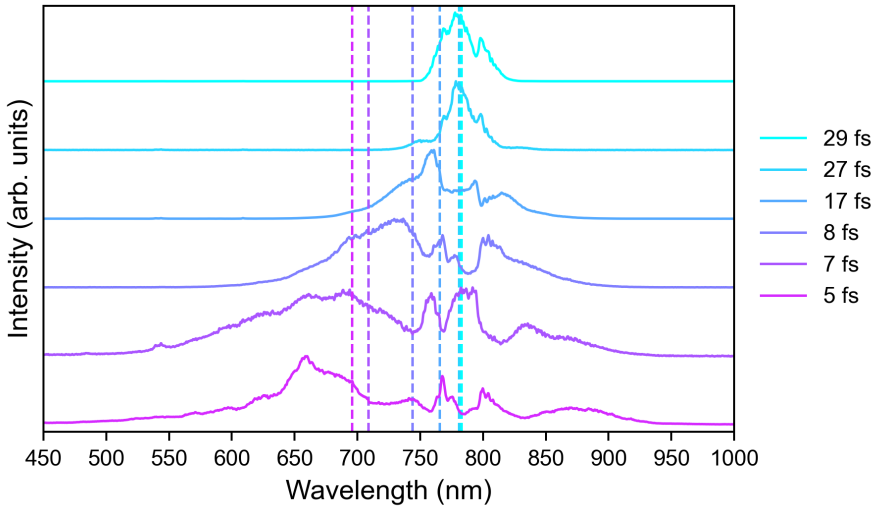


Figure 3.5: Fundamental spectra of all driving fields for HHG taken for varying pressure in the HCF. The dotted line is the centre wavelength calculated as the weighted average of the spectral intensities for each pulse duration.

Parameter	Pulse 1	Pulse 2	Pulse 3	Pulse 4	Pulse 5	Pulse 6
Hollow fibre argon pressure (bar)	0.0	0.2	0.4	0.6	0.8	1.0
Pulse duration τ (fs)	29	27	17	8	7	5
Beam radius w (µm)	108	150	143	110	108	100
Average power range (mW)	4–56	4–52	3–45	2–31	2–43	2–58
Pulse energy (µJ)	4–56	4–52	3–45	2–31	2–43	2–58
Intensity range (TW/cm^2)	0.8–10	0.4–5.2	0.5–7.7	1.2–19	1.4–31	2.7–74
Center wavelength (nm)	782	780	766	744	709	696

Table 3.1: Laser parameters of all the the driving laser fields used in the NIR beamline.

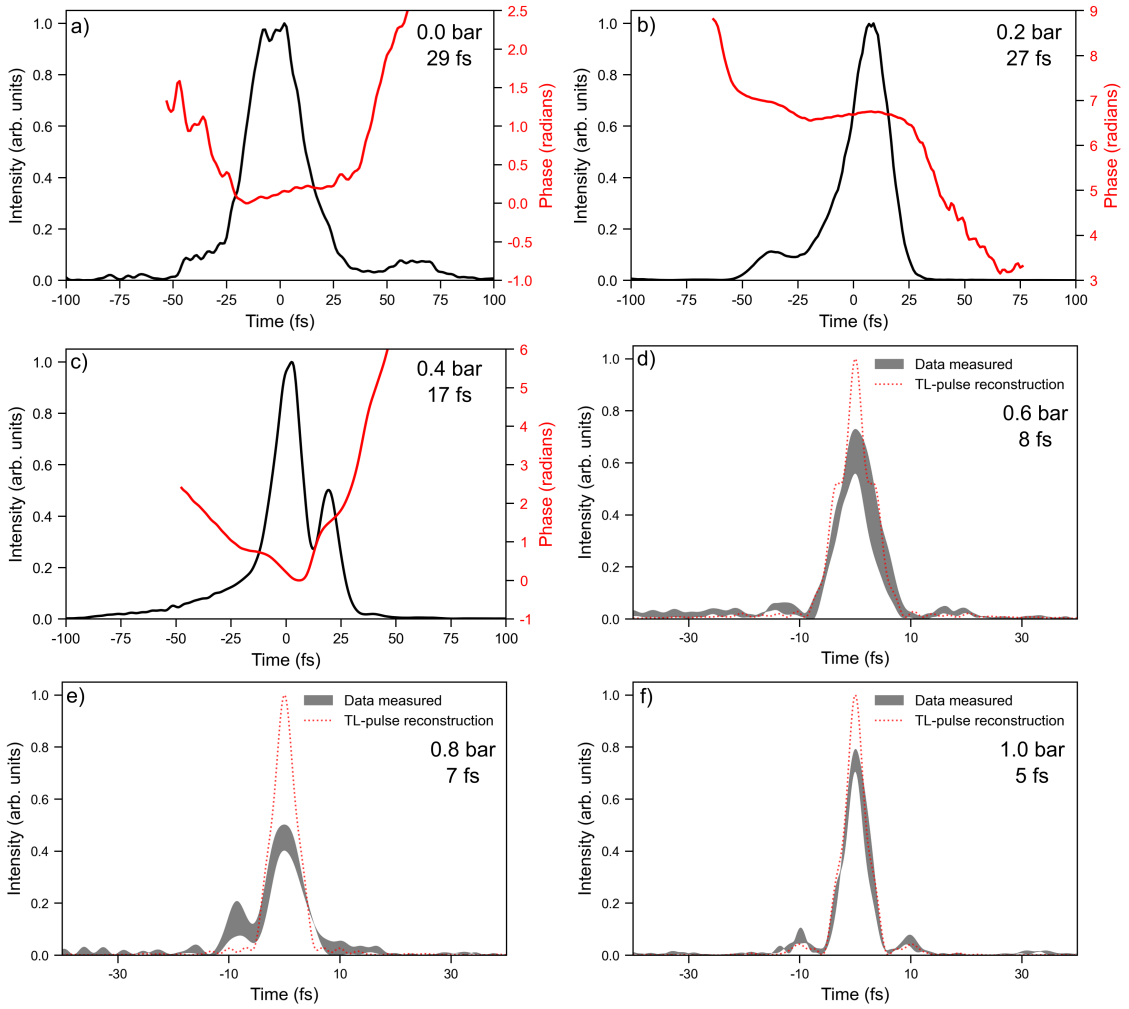


Figure 3.6: Pulse duration scan. Temporal shape of the driving field for each pulse duration. The first three images were measured for low gas pressures of argon in the HCF resulting in multi-cycle pulses. The pulse intensity envelope and temporal phase reconstructions were done with the SHG-FROG. The last three images were measured for higher gas pressures, resulting in shorter pulses hence measurements done with the D-Scan. The measurements were done from 0 bar of argon in the HCF (a) to 1 bar (f) in steps of 0.2 bar. The flat temporal phase indicates the pulses are close to transform limited.

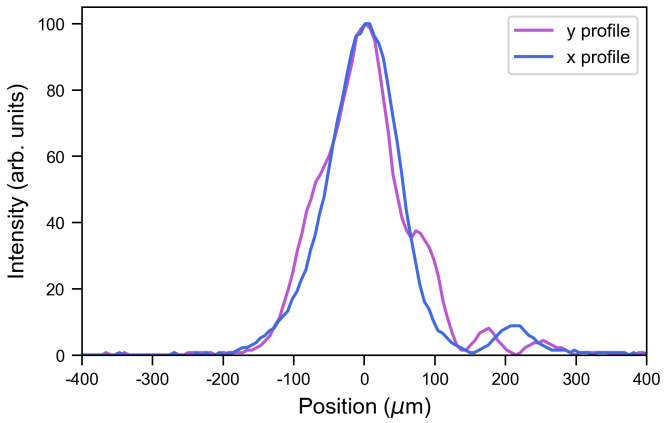


Figure 3.7: Spot size of the focused NIR beam with a 50-cm focal length lens. The diameter was 215 µm (e^{-2} diameter).

3.1.2 NIR HHG Beamline

As shown on Figure 3.2, after the system presented in the previous section, the beam goes to the HHG beamline, composed of three chambers under vacuum (Figure 3.8), the HHG chamber, the filter chamber and the flat-field chamber. The vacuum guarantees no added dispersion due to air propagation and no unwanted nonlinear effects occurring in air at the focus. Moreover, air absorbs radiation below 200 nm [153]. It is thus crucial to detect XUV (2−60 nm [154]) photons in a vacuum system in order to remove any absorbing element.

HHG Chamber

The HHG chamber, sealed with a 0.5-mm-thick fused silica Brewster window, contains the nonlinear medium that produces harmonics under a strong laser field. We can produce harmonics from either a gas or a solid target that we can switch between *in situ*. The solid target was a 10 × 10 mm sample mounted next to a gas jet. Both the solid sample and the gas jet were placed on a motorised stage (*Zaber Technologies*), allowing movement in the direction along the optical axis (z direction) and transverse to the optical axis (x axis). This allowed us to optimise the position of the sample at the focus as well as to change the laser-irradiated spot on the sample for the solid case, e.g. to move off a damaged spot. The gas jet was a laser-drilled tube target [46] of 4 mm diameter backed with a pressure of 60 mbar. This backing pressure can be varied with a needle valve (*Metering Valve SS-6MG-MM, Swagelock*). The gas inlet hole was covered with sellotape drilled when the laser went through, which allowed to have a controlled interaction area and reduced gas leakage in the chamber.

The beam was focused by a 50-cm focal length concave mirror on the sample. At the focus position, the intensity of the driving pulse was high enough to generate nonlinear effects in the solid sample ($\sim 1-\ 80\,\mathrm{TW/cm^2}$). The HHG chamber was maintained under high vacuum ($\sim 10^{-7}$ mbar) with two turbo pumps backed by a roots pump.

A motorised mirror could be inserted into the beam to divert it from its original path towards the sample and instead to send it through a large window on the side of the chamber to the focal spot size measurement. Not shown on Figure 3.8, a mirror was also placed after the sample (blocking the beam so this measurement was not made simultaneously with HHG), sending the beam through the same window in order to measure the pulse duration of the fundamental beam after propagation through the sample with a D-Scan. The focal spot size measurement re-imaged the beam on a beam profiler camera (*BC106N-VIS/M, Thorlabs*) with a 2f-2f imaging system.

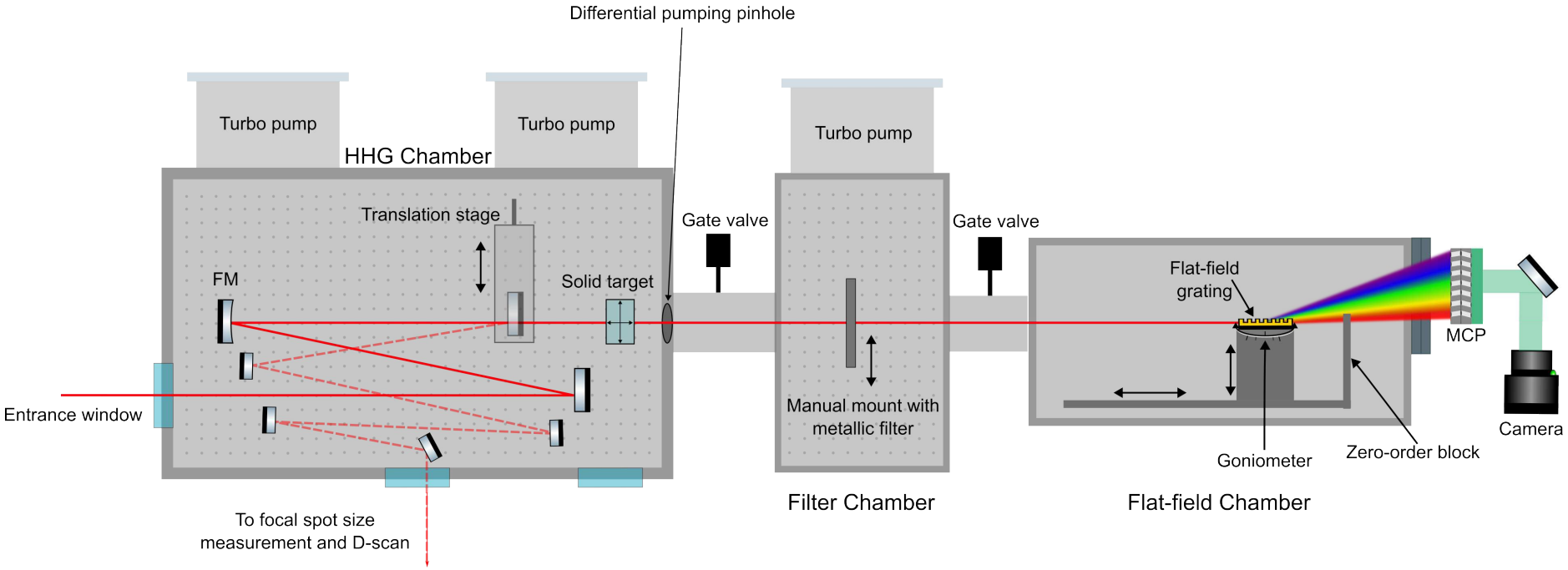


Figure 3.8: Schematic of the Imperial College London's laboratory beamline. The beamline is composed of three chambers: the HHG chamber in which the beam is focused on the solid target, the filter chamber where a filter can be inserted in the beam and the flat-field chamber in which the harmonics are diffracted by a flat-field grating (*251MX, McPherson*) and sent onto the imaging MCP. The chambers are isolated from each other by windowed gate-valves which allow an alignment laser to go through. In the HHG chamber, a mirror is on a translation stage and can be inserted in the beam path to direct the beam to the 2f-to-2f imaging system of the focus or to the D-Scan. FM denotes a focusing mirror ($f = 50\,\text{cm}$). The grating is on translation stages along the beam and also perpendicular to the beam so it can be removed from the beam path for alignment purposes. It sits on a goniometer. The zero-order block allows to block the fundamental order diffracted from the grating to avoid it hitting the MCP. The phosphor screen of the imaging MCP device is imaged by a CCD camera.

Filter Chamber

After the HHG sample, the beam goes through a pinhole to the next vacuum chamber, the filter chamber. The pinhole is used for differential pumping in order to keep the pressure as low as possible in the detection chamber. The chambers can each be isolated with a gate valve with windows in closed position. The window allows the alignment beam (HeNe) to go through a camera located at the end of the beamline. The filter chamber contains a metallic filter on a manual linear motion vacuum feedthrough and contributes to the gradient in pressure for differential pumping.

Flat-Field Spectrometer Chamber

The harmonics were reflected by a flat-field grating placed on a goniometer (more details are provided in the next section). Harmonics were then detected with a 40-mm diameter chevron-stacked imaging Micro-Channel Plate (MCP) (*Photonis*) with MgF_2 sensitisation coating and a phosphor screen. A MCP is an array of µm-scale electron multipliers oriented parallel to one another. A bias voltage is applied across the plates leading to a cascaded production of electrons when a high-energy photon hits the front of the MCP [155]. The MCP used was a double-stack MCP, giving a maximum gain of 10^5 to 10^7 (depending on the applied voltage). The electrons are accelerated onto a phosphor screen (phosphor P 47) which allows visual observation of the incident photons. The spatial distribution of the incident harmonic photons is retained on the phosphor screen.

The phosphor screen is imaged with a CCD camera (*Manta, Allied Vision*) which records spatially-resolved HHG spectra, where one axis corresponds to the harmonic photon energy and the orthogonal axis corresponds to the spatial divergence of the harmonics. A typical spectrum recorded by the MCP is shown in Figure 3.9.

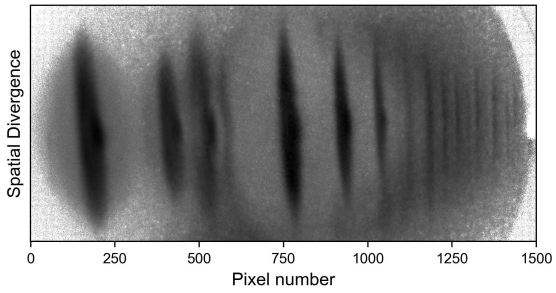


Figure 3.9: Raw MCP image showing harmonics from a solid (MgO). The x-axis is in pixels and corresponds to wavelength (where the wavelength is linearly proportional to the pixel number). The y-axis corresponds to the divergence of the harmonics.

3.1.3 Optimisation of the Flat-Field XUV Spectrometer for Solid HHG Detection

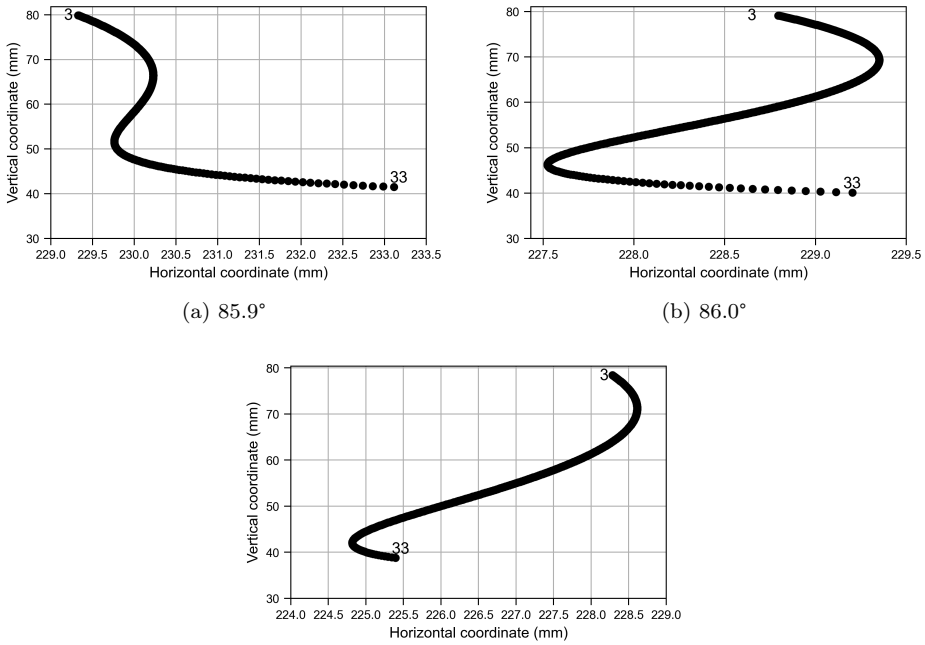
Improvements to the Flat-Field Spectrometer

We used a purpose-built spectrometer, which was operated at a pressure of 7×10^{-8} mbar pumped with oil-free pumps to minimise contamination of XUV optics. The existing XUV spectrometer chamber [156] first developed to detect HHG in gases was optimised for detecting lower-order harmonics from solids. In the old configuration, a spectrometer entrance slit was used. For use with solid HHG, the slit was left open and the laser spot on the sample was imaged onto the detector in order to capture all the light.

The harmonics were dispersed with an aberration-corrected concave diffraction grating. It is a variable line spacing grating which produces a near-flat focal plane [157]. Kita *et al.* in their seminal work on this exact type of grating reported a nominal angle of incidence of 87.0° and a grating-to-detector distance of 235 mm [158] in order to focus high-order harmonics on a flat plane (typically above 50 eV) generated from gases. Originally the spectrometer chamber comprised a grating with 1200 lines/mm. However, the expected cutoff energy of harmonics generated from solids is much lower than for gases and we therefore required an adapted geometry compared to the standard geometry of the flat-field spectrometer [159] in order to optimise the detection efficiency and resolution within our spectral region of interest (5 eV to $\sim$ 60 eV). We chose a grating with 120 lines/mm, Au coated (*251MX, McPherson*). Additionally, we altered the parameters of our flat-field spectrometer in order to maximise the collection of the generated harmonics (grating angle, distances sample to grating and grating to MCP, distance of the MCP relative to the optical axis). To do so, the grating was placed on a motorised goniometer and motorised translation stages to allow for the optimisation of the harmonic spectra.

The harmonics are dispersed spatially by the grating: each order is focused at a specific point in space. The focusing curve needs to be as flat as possible to match the flat MCP surface. The simulations in Figure 3.10 show the behaviour of the harmonic orders 3 to 33 for different angles of incidence according to the equations in [159]. We note the simulations deal with the resolution of the harmonics rather than their flux as the goal is to capture a full harmonic spectrum. As the angle increases from 85.9° to 86.1°, it is clear that the focusing curve of the harmonics changes curvature. For low angles, the low-order (high-order) harmonics are focused below 229.0 mm (above 232.0 mm) while for high angles, these are focused beyond 227.5 mm (below 226.0) and the trend continues for other angle values. The best setting, i.e. the setting for which the most harmonics are focused on the same plane is theoretically found at 86.0°.

We verified these theoretical findings of Figure 3.10 by incrementally adjusting the grating angle



(a) 85.9°

(b) 86.0°

(c) 86.1°

Figure 3.10: Simulations of the spatial distribution of harmonic orders 3 (4.6 eV) to 33 (51 eV) according to the equations given in [159] for theoretical angles.

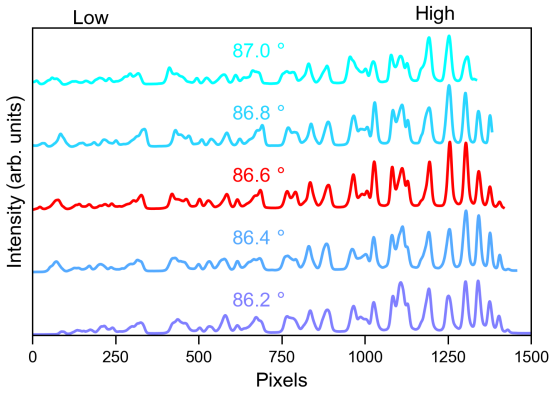


Figure 3.11: Spectrometer angle optimisation. Measured HHG spectra generated in Kr gas as a function of the grating angle of incidence. The x-axis (in pixels) represents the full detection range for each grating angle and is linearly related to wavelength. "Low" and "High" refer to the harmonic orders.

in real time. We varied in small steps the angle of the grating while recording harmonics in krypton as illustrated on Figure 3.11. The x-axis is in pixels and corresponds to wavelength (where the wavelength is linearly proportional to the pixel number, see Figure 3.9). We find experimentally that 86.6° was the best compromise as it was the angle that captures best both ends of the spectrum. With the fixed detection range available, it is important to detect the lowest-order harmonics (they have the highest yield) while still being able to resolve as many higher-order peaks as possible. This angle did not correspond exactly to the one found theoretically most probably due to errors readings the goniometer graduations. Moreover, the maximum distance grating-detector we could

reach *in situ* was 232 mm. We thus kept this optimum *in situ* setting and proceeded to do a calibration of the wavelength axis.

Calibration of the Spectrometer

The raw images collected by our spectrometer have an x-axis in pixels corresponding to wavelength or photon energy, but the relationship between the two is not linear. There are two common ways to calibrate the energy axis. One can use different spectral filters which have transmission in various parts of the XUV spectrum (for example, an aluminium filter transmits between $\sim 18{-}70$ eV). Another way in which a calibration can be performed is *via* the grating equation. These methods can be used in conjunction with one another.

The calibration was made *in situ* using harmonics from solids, meaning that only low-order harmonics are produced, as opposed to the gas phase. As most metallic filters absorb the low energies, the second option (grating equation) was put in place. Figure 3.12 shows the schematic geometry of the grating.

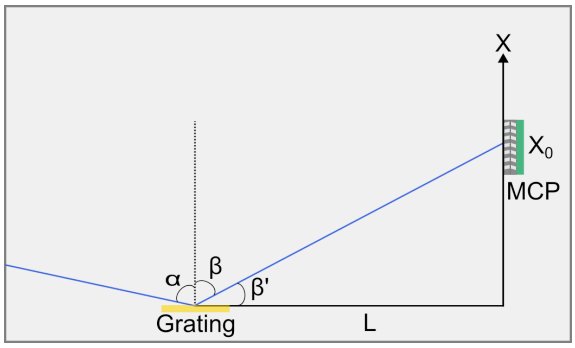


Figure 3.12: Schematic of the flat-field spectrometer. α is the angle of incidence. L is the distance grating-MCP. X is the axis of the detector and X_0 is the position of the bottom of the MCP above the optical axis. The distance was measured as $X_0 = 70.5$ mm.

The grating equation is given by Equation 3.3.

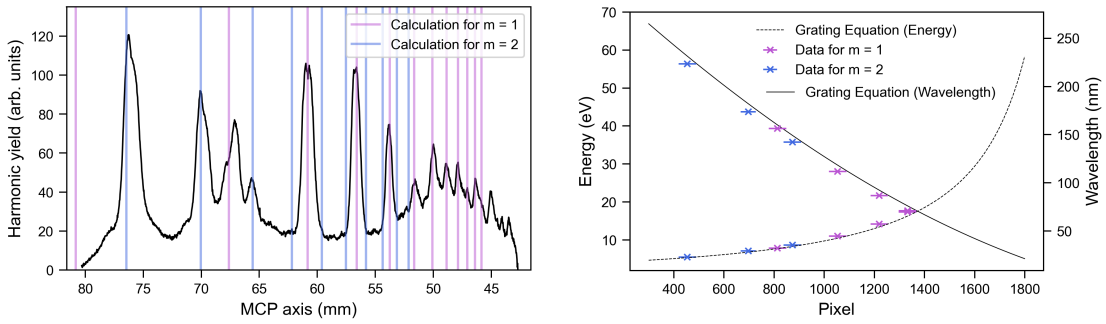
$$mg\lambda = \sin(\alpha) - \sin(\beta) \tag{3.3}$$

where m is the diffraction order, g is the lines per mm of the grating, λ is the wavelength, α is the angle of incidence and β is the diffraction angle. The flat-field grating has $g = 120$ g/mm (average line spacing across the grating). This allows a range of detection from 50 to 200 nm. In order to calculate the wavelengths corresponding to all diffraction angles β, we thus need to calculate β according to simple geometry:

$$\beta = \frac{\pi}{2} - \arctan\left(\frac{X}{L}\right) \tag{3.4}$$

where $X = X_0 - \Gamma P$, P is the pixel number on the camera image and Γ is the conversion factor

between pixels and real space in mm. We found Γ by imaging a scale reference object of known size in the plane we were imaging (on the phosphor screen), $\Gamma = 0.0256\,\mathrm{mm/pix}$. The wavelengths were calculated using only $m = 1$. However, weaker second-order peaks were visible on the spectrum as well, corresponding to the wavelengths calculated with $m = 2$. The second-order peaks appear to have half the energy of their first-order equivalent. They rendered the spectrum more complicated but their position can be used as a benchmark for the accuracy of the calibration.



(a) (b)

Figure 3.13: Energy calibration of the x-axis of the spectra recorded from a solid sample, MgO. 3.13a Lineout of the spectrum generated from MgO (001) along with calculation of the harmonic orders' position. 3.13b From the experimental data, we attribute harmonic orders to the peaks of the spectrum and add those points on the grating equation calculated.

Figure 3.13a shows the lineout of an experimental HHG spectrum taken in a solid sample, MgO. The harmonic orders have been calculated using the grating equation. It enabled the determination of the nominal value of α (read on the goniometer) for which the peaks of the spectrum matched the different diffraction order lines calculated. With this same angle, we could thus use the grating equation and check that the peaks of the harmonic orders lie on this equation within the error bars as defined by the standard deviation of the data (Figure 3.13b).

3.2 Overview of the Apparatus of the Mid-Infrared (MIR) Beamline

The experiments in Chapter 5 have been performed at the Advanced Laser Light Source (ALLS) user facility at Institut National de la Recherche Scientifique (INRS) in Canada and we describe in this section the laser system employed as well as the beamline developed for the MIR regime.

3.2.1 Laser System

The laser source for HHG at ALLS is an Optical Parametric Chirped Pulse Amplifier (OPCPA), which relies on the nonlinear interaction between a pump and a signal. As seen previously, Optical Parametric Amplification (OPA) is a particular case of DFG for which we have

$$\omega_{\text{pump}} = \omega_{\text{signal}} + \omega_{\text{idler}} \tag{3.5}$$

The schematic of an OPCPA is presented in Figure 3.14.

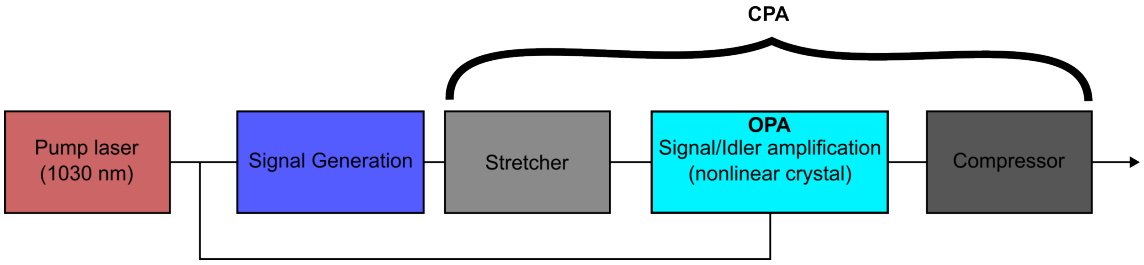


Figure 3.14: Optical Parametric Chirped Pulse Amplifier (OPCPA) schematic. The Ytterbium pump beam is split in two. In one arm, white light generation is produced, which then seeds the signal. For the CPA scheme to happen, the signal is first stretched. The two arms (pump and signal) are then combined to amplify the signal and generate the idler, itself amplified. The idler and signal are then compressed to generate ultrashort MIR pulses.

A more detailed schematic of the laser used for this set of experiments is presented on Figure 3.15. The HHG beamline was designed, built and used by the Imperial College team while the laser was operated by the ALLS team in a separate clean room. For more details, a very similar laser system was used in [140].

The laser comprises an industrial Ytterbium-based laser (*Amphos*) pumping multiple stages of OPA. The pump laser delivers pulses up to 2 mJ at 100 kHz. A supercontinuum is generated in a YAG plate spanning almost an octave. A narrower spectral band centred at 1.5 µm is selected, stretched in 20 mm of silicon and goes through an Acousto-Optic Programmable Dispersive Filter (AOPDF) (*Dazzler, Fastlite*). This device shapes the signal in order to stretch the pulse (to match the pump duration), to select the spectrum, to pre-compensate higher orders of spectral phase induced in the overall system and to stabilise and control the CEP of the system (detailed in a

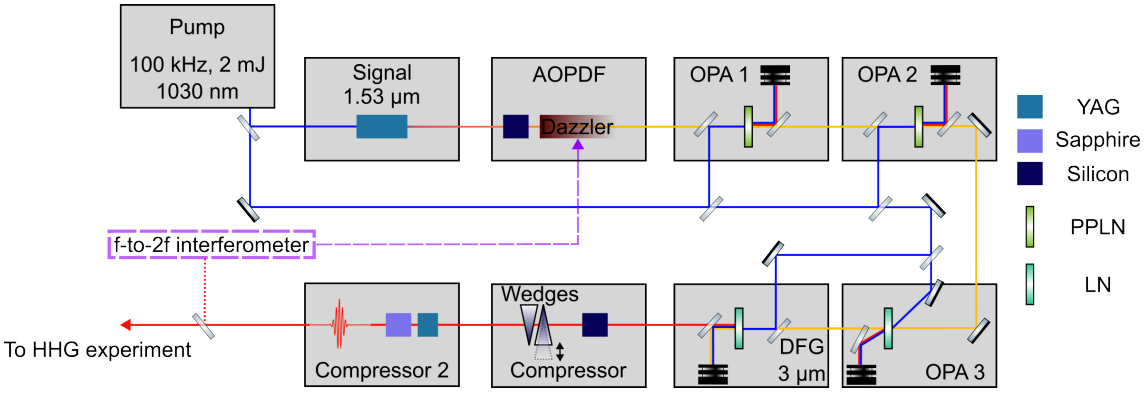


Figure 3.15: ALLS laser setup. The materials used for compression and the nonlinear crystals used for parametric processes are shown on the side. The AOPDF is composed of a $LiNb_3$ crystal. PPLN: periodically poled MgO:$LiNbO_3$ crystal. LN: bulk $LiNbO_3$ crystal.

next section).

The signal is then amplified through a parametric process in three different stages. In the last stage, the idler (see Equation 3.5) is generated in a nonlinar crystal and sent to a compressor (silicon plate and tunable silicon wedges). The pulse measures 100 fs at this stage. By tuning the angle of all the nonlinear crystals, the idler can be tuned from 2.7 µm to 3.5 µm. However, as air absorbs around 2.8 µm [160], we concentrate only on one driving wavelength, 3 µm.

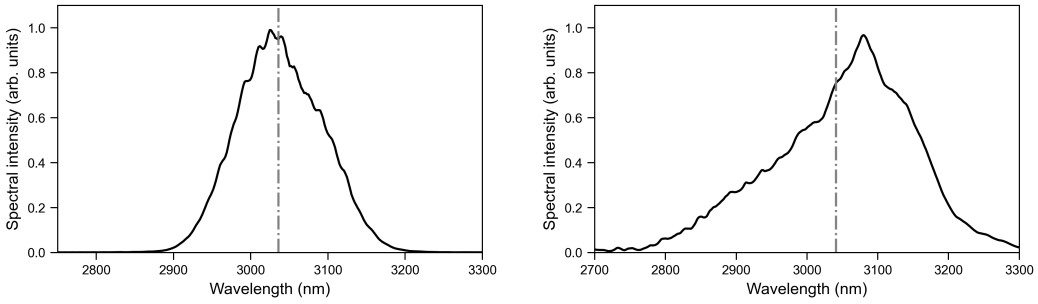
The laser was used for two different beamtimes for the data sets presented here (22/04/2024 to 03/05/2024 and 8/07/2024 to 23/07/2024). The first dataset was acquired with the laser beam directly from the OPCPA, while the second one was recorded using compressed pulses ("Compressor 2" on Figure 3.15). The pulse compression was achieved by adding a YAG plate to broaden the spectrum followed by a 3 mm sapphire plate to compress the pulse. Sapphire has negative dispersion at this wavelength ($-570\,fs^2/mm$ [21]), allowing to compress the pulse to 66 fs at the output of this second compressor.

The goal of these experiments was to understand the effect of pulse duration on the HHG spectra, discussed in further details in Chapter 5. The two different laser configurations at ALLS employed are referred in this thesis as "short pulse" and "long pulse". The fundamental spectra of those two configurations are shown on Figure 3.16.

3.2.2 Carrier-Envelope Phase (CEP) Control al ALLS

CEP and Dispersion

In Chapter 2, we saw that the pulse envelope travels at the group velocity v_g whereas the carrier travels with a different velocity, the phase velocity v_p. The Carrier-Envelope Phase (CEP) shift is therefore modified in the medium depending on the position z of the pulse according to:



(a) (b)

Figure 3.16: Spectrum of the driving field for the short pulse (66 fs) and the long pulse (100 fs). The dotted gray line corresponds to the centre wavelength calculated as the weighted average of the spectral intensities. For the long pulse (a), $\lambda_0 = 3036$ nm and for the short pulse (b), $\lambda_0 = 3041$ nm.

$$\Delta\phi(z) = \omega_0 z\left(\frac{1}{v_g} - \frac{1}{v_p}\right) = -2\pi\frac{dn}{d\lambda}\bigg|_{\lambda_0} z \tag{3.6}$$

Any dispersive medium will modify the CEP of the pulse. If we consider ZnO (relevant for Chapter 5) with a chromatic dispersion of -0.012861 µm^{-1} at 3 µm, we would need a thickness of 40 µm to introduce a CEP phase shift of π. This shows how the CEP is sensitive to dispersion. We therefore study in this thesis relative variations of the CEP rather than absolute values.

CEP Offset Frequency

In order to understand how we can lock the CEP of each pulse in a laser system, we need to consider a modelocked laser with a train of pulses separated by the frequency f_{rep}. Each pulse in time has a different CEP value ϕ_{CEP}.

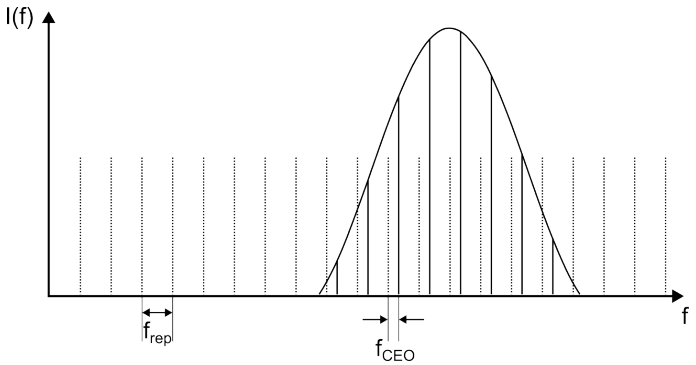


Figure 3.17: Mode-locked laser output. The dashed lines represent the modes of the laser (when the phase and group velocities of the pulse are equal). The solid lines represent the shifted modes of the laser. The frequency offset of the comb, f_{CEO} is related to the CEP shift. The envelope corresponds to the gain spectrum.

Figure 3.17 introduces the frequency offset of the frequency comb of the modelocked laser, f_{CEO}. This frequency offset is related to the CEP shift $\Delta\phi_{\text{CEP}}$ and when $\Delta\phi_{\text{CEP}}$ is kept constant,

the frequency of each tooth of the mode-locked frequency comb f_n can be expressed as:

$$\Delta\phi_{\mathrm{CEP}} = \frac{2\pi f_{\mathrm{CEO}}}{f_{\mathrm{rep}}} \tag{3.7a}$$

$$f_n = nf_{rep} + f_{CEO} \tag{3.7b}$$

Stabilisation of the CEP

The stabilisation of the offset frequency has been demonstrated to be efficient by using a feedback control loop based on a self-referencing technique [161], the f-to-2f interferometer.

The lower frequencies of the octave-spanning spectrum ($f_n = nf_{\mathrm{rep}} + f_{\mathrm{CEO}}$) are frequency-doubled ($2f_n = 2(nf_{\mathrm{rep}} + f_{\mathrm{CEO}})$) with an appropriate nonlinear crystal, which then interfere with the high frequencies of the spectrum ($f_{2n} = 2nf_{\mathrm{rep}} + f_{\mathrm{CEO}}$). In order to have an octave spanning spectrum, coherent white light generation processes are used to keep the coherence of the comb. In order to create the interference, the fundamental and its second harmonic are projected on the same polarisation axis. The beat frequency obtained is

$$2f_n - f_{2n} = 2(nf_{\mathrm{rep}} + f_{\mathrm{CEO}}) - 2nf_{\mathrm{rep}} + f_{\mathrm{CEO}} = f_{\mathrm{CEO}} \tag{3.8}$$

Experimentally, this hererodyne beat frequency can be measured with radio frequency spectrum analysers. It can be used as an error signal to lock the offset frequency.

In this thesis, passive-CEP locking is used at ALLS as introduced in [162]. It allows to lock the CEP of the idler by ensuring that the signal and the pump have the same phase. In this configuration, the pump is spectrally broadened to generate the signal. To ensure temporal overlap, a delay line is included in the pump arm. However, phase fluctuations can occur because of the white light generation and the interferometry between two different arms.

The CEP stability is measured with a fringe detector (*Fringeezz, Fastlite*) reading the spectra from an f-to-2f interferometer. The error signal from this measurement is fed back to the AOPDF which corrects in real-time the CEP drifts by introducing a very small delay between the signal and the idler. A measurement of the CEP stability is presented on Figure 3.18.

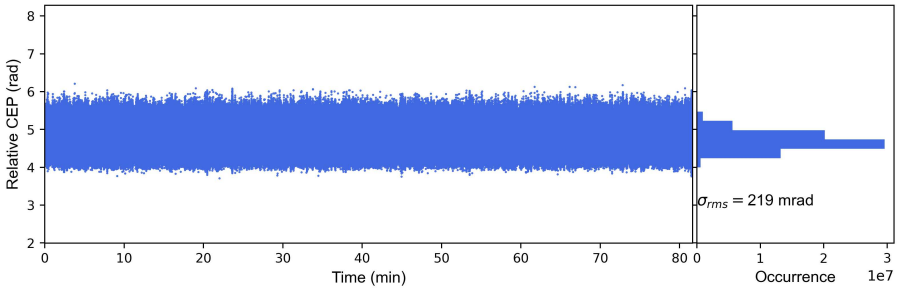


Figure 3.18: CEP variation over 1.5 hours. This duration corresponds on average to the duration of a typical data scan in this thesis.

3.2.3 MIR HHG Beamline at ALLS

Experimental Setup

The setup is shown in Figure 3.19. The laser went through two irises, used for alignment but also as a shutter (I1) and to clean the beam (I2). The wire-grid polariser (*WP25H-B BaF_2 Holographic wire grid polariser, Thorlabs*) controlled the power of the beam.

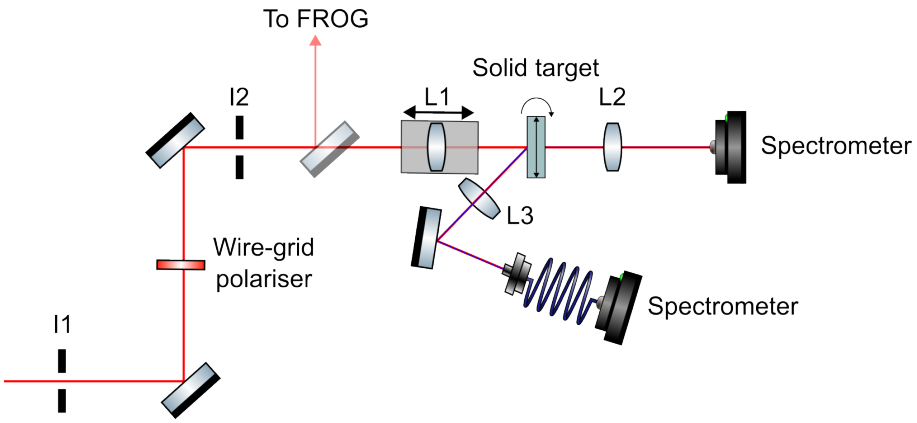


Figure 3.19: HHG beamline. I1 and I2 denote irises (used for alignment but also to clean the mode of the beam). L1, L2 and L3 are focusing lenses. L1 is on a motorised translation stage. The solid target is on a motorised rotation stage and manual translation stage.

A flip mirror can be inserted in the beam to send the pulse to a SHG-FROG for temporal characterisation.

A 100-mm lens (L1) focused the beam on the sample. The lens was placed on a motorised stage along the beam to control where to place the focus. The sample was mounted on a motorised rotation stage, allowing for polarisation scans. This stage itself was mounted on a manual transverse stage in order to change spot in case of damage. The harmonics were then re-imaged with a 40-mm focusing lens (L2) directly on the spectrometer in the transmission geometry. In order to have simultaneously a harmonic polarisation scan in both transmission and reflection, the correct beam alignment must be maintained. This is very hard to achieve as the polarisation scans are achieved by rotating the sample. If the sample is not perfectly straight in the mount, it affects the alignment

of the reflected beam. Due to this experimental difficulty, reflection and transmission scans were acquired separately. In the transmission geometry, the sample is perpendicular to the beam and a HHG spectrum is acquired for every intensity and every rotational position of the sample (0 °to 193 °, steps of 3 °). For reflection harmonics, the sample was rotated perpendicularly to the beam by 10 ° and the beam was re-imaged on a fibre used to couple light to the spectrometer with a 50-mm lens (L3). The sample was not rotated in its mount for those reflection scans, only the power was varied. The detector was a UV-VIS spectrometer (*Ocean Optics*).

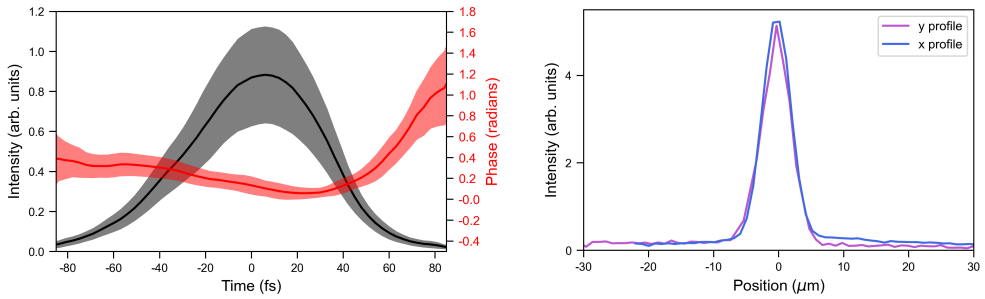
The laser spot size was measured by placing a CCD camera (*Zelux CS165MU, Thorlabs*) where the sample was positioned and the power was measured by placing a power meter (*UP19K-15S-W5-D0, Gentec*) just after I2. The spectrum of the fundamental beam was measured after the sample (sample out) with a scanning spectrometer (*Mozza, Fastlite*).

Characterisation of the MIR Pulses

As discussed previously in Section 3.2.1, two different compression settings were used in order to generate two pulses with different pulse durations, referred to as the "short" pulse and the "long" pulse. Table 3.2 summarises the parameters of those two pulses used in the experiments and Figure 3.20a displays the temporal measurement of the short pulse with a SHG-FROG.

Parameter	Short Pulse	Long Pulse
Pulse duration τ (fs)	66	100
Beam radius w (µm)	30	27
Average power range (mW)	25−300	40−700
Pulse energy (µJ)	0.3−3.0	0.4−7.0
Intensity range (TW/cm^2)	0.2−3.0	0.3−5.7
Center wavelength (nm)	3041	3036

Table 3.2: Laser parameters of the short pulse and long pulse used in the MIR beamline.



(a) (b)

Figure 3.20: 3.20a Pulse duration measurement of the short pulse with a SHG-FROG. The retrieved pulse duration is 66 fs with an error of 6 %. 3.20b Spot size measurement of the long pulse.

The two sets of measurements with the short pulse and the long pulse (Figure 3.20b) were

made at two different times, with a full realignment of the laser in-between, meaning that the beam radius for the pulses was slightly different (Figure 3.20b). The beam radius was calculated as the $1/e^2$ radius of the beam profile, taking into account the three photon absorption of the camera (centre wavelength is at 0.41 eV and the bandgap of silicon is 1.1 eV). We note that the configuration was different to the NIR case, the beam is more tightly focused.

Chapter 4

NIR Wavelength Driving Field for HHG in Wide Bandgap Oxide MgO

Thorpe *et al.* [163] described the existence of two regimes for solid HHG: Near-Infrared (NIR) HHG dominated by intraband processes *versus* Mid-Infrared (MIR) HHG dominated by interband processes (for above-bandgap harmonics). In this chapter, we will focus on the first regime in which HHG stems from dielectrics illuminated by NIR driving fields. We report the highest cutoff harmonic detected in solid HHG.

4.1 Background on HHG Experiments in MgO

4.1.1 Crystal Properties of MgO

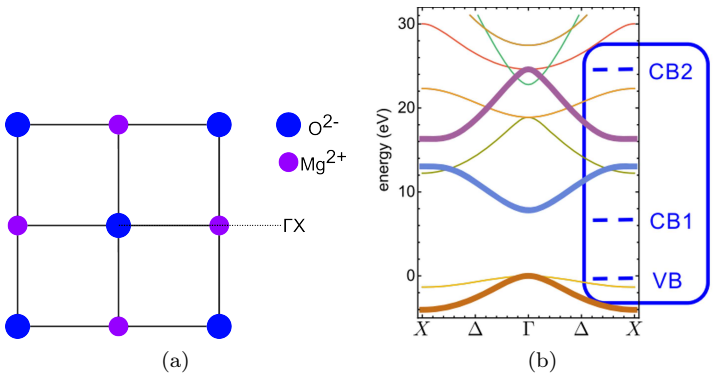


Figure 4.1: MgO crystal structure 4.1a and band 4.1b structure. The solid lines in 4.1b correspond to three major bands responsible for HHG. Figure reproduced from [100] under the terms of the Optica Open Access Publishing Agreement.

One of the most common wide bandgap dielectric materials [164] used for HHG is MgO, a compound between a metal and an oxygen, forming a metal oxide. It has a cubic structure that

is cohesive with ionic bonding [165]. The crystal and band structures of MgO are represented in Figure 4.1. MgO has an electron effective mass $m^* = 0.35m_e$.

4.1.2 Previous HHG Experiments in MgO

MgO has been shown to be a good candidate for HHG, both experimentally [100, 166, 167, 112, 168] and theoretically [133, 169]. Bulk dielectrics, such as MgO, are readily available optical media that do not require complicated fabrication processes. Wide bandgap dielectrics represent an ideal target for solid high energy harmonics, e.g., for applications in industry. MgO's widespread use in solid HHG is due to its high damage threshold ($> 50\,\mathrm{TW/cm^2}$ [170]) which is a result of its large direct bandgap (7.8 eV, 159 nm [171]) with respect to available driving lasers wavelengths. This limits multiphoton absorption at longer driving wavelengths and means the optical transparency of MgO extends into the UV. MgO has an inhomogeneous electron-nuclear potential due to its ionic bonding, similar to the atomic case, making it an ideal candidate for HHG (for efficient harmonic generation, the gradient of the electron-nuclei potential needs to be greater than zero) [133].

MgO has been used in multiple HHG experiments, such as for atto-chirp control [100], attosecond pulse measurement [172] and ionisation measurements [173]. Using a second driving field, usually the second harmonic of the fundamental driving field, is a common way to explore the electron dynamics within a solid during HHG and has been reported in MgO experimentally [174, 175] and theoretically with the third harmonic as the secondary beam [169]. Understanding the electron motion is also possible through anisotropic studies in which the harmonic yield varies with the crystal orientation [112, 176, 59, 177, 124]. Investigations have been conducted in MgO to determine whether the interband polarisation or intraband current is responsible for the HHG process [100, 178].

We focus in this section on the extension of the cutoff in MgO and we report in Table 4.1 the highest cutoffs reported in the literature for a range of solids in order to put the work achieved in this thesis into perspective.

Sample	Thickness (µm)	Driving Wavelength (µm)	Pulse Duration (fs)	Cutoff Energy (eV)	Ref.
Solid Ar and Kr	5	1.33	50	40	[102]
α-Al_2O_3	430	0.80	12	31	[179]
MgO	200	1.70	11	25	[100]
MgO	100	1.30	50	30	[59]
SiO_2	0.120	0.80	~ 2	33	[95]
SiO_2	0.120	0.83	~ 2	34	[12]

Table 4.1: Highest cutoff photon energies reached in a range of wide bandgap dielectrics as a function of the driving wavelength, pulse duration and sample thickness. Table reproduced from [180] under the terms of the Optica Open Access Publishing Agreement.

Different schemes have been developed to incrementally extend the harmonic cutoff using a single-colour driver. You *et al.* [100] varied the Carrier-Envelope Phase (CEP) to reach higher

photon energies in MgO, showing a linear slope of the cutoff as a function of CEP (up to 25 eV). Korobenko *et al.* [167] and Vampa *et al.* [168] exploited different optical geometries to enhance phase matching and reduce absorption, using detection in transmission with a counter-propagating pulse in one setup, and a reflection detection setup in another. In both cases, the observed cutoff was ~ 25 eV. You *et al.* [112], Uzan-Narovlansky *et al.* [59] and Li *et al.* [181] studied the variation in the high harmonic yield with laser polarisation along different bonds of the sample, observing a higher efficiency along the Mg-O bond. Nefedova *et al.* [166] doped MgO with Cr to enhance the harmonic yield, reaching 25 eV. All these investigations used different driving laser wavelengths, peak intensities and pulse durations but only achieved modest increases of the harmonic cutoff of about ~ 2 eV. These experimental studies employ similar harmonic detection schemes, well established for detecting gas phase HHG, consisting of a spectrometer with flat-field grating followed by an MCP imaging detector (except [166], where a back-illuminated CCD camera was used).

We note that detection systems for HHG in MgO in the literature can limit the detected cutoff. Indeed, the highest cutoffs reported in Table 4.1 can be limited by the spectrometer itself. You *et al.* [100] have a grating range of 13 to 25 eV, limited by the collection angle of the spectrometer. Nefedova *et al.* [166] have a detection limit of 24.4 eV. Noise can also contribute to the detection limit with low integration times and high pressures. Korobenko *et al.* [167] used very short integration times, limiting the number of laser shots collected (50-200 shots) while Vampa *et al.* [168] showed harmonics generated in 5×10^{-6} mbar, a very low pressure where the SNR is low. Many references provide sparse detail on their detection setup, rendering a comparison difficult.

Recent modelling using *ab inito* TDDFT predicts both isolated attosecond pulses from MgO, but also emission energies beyond 43 eV, using a 1800 nm driver with its second harmonic [133]. While that study describes a scheme for two-colour experiments, it suggests that considerably higher-orders of harmonics than those previously reported in MgO are feasible.

Knowing that our detection system is tailored for high energy detection and that is it theoretically possible to produce harmonics above 40 eV in MgO, we describe in this chapter the highest harmonics detected in MgO to our knowledge, extending to 50 eV, corresponding to the 31^{st} harmonic order of a 800 nm driving wavelength.

4.2 Extension of HHG Cutoff in Solids to 50 eV Using MgO

In this section, a study of HHG in MgO with a multicycle ~ 30 fs pulse is presented using a 800 nm driving field. The characteristic features of the harmonic spectrum are described and this section provides a basis for understanding HHG in solids with a NIR driving wavelength. The results presented in this section are published in Allegre *et al.* [180].

4.2.1 Experimental Parameters

The beamline used for this experiment has been described in Chapter 3. Experimental parameters that were varied include power control through the half waveplate and polariser (described in Figure 3.2) and beam size control with an adjustable iris placed in the beam just before it goes to the HHG chamber. Pulse characterisation was achieved with the SHG-FROG and the 2f-2f equivalent plane imaging system was used to measure the spot size. A power meter (*PM10-19C, Coherent*) was used to record the laser pulse energy.

The sample was a 100 µm thick MgO (001 cut) sample, double-side polished (*Pi-Kem*). We note that the Rayleigh range of the laser ($z_R \approx 45\,\text{mm}$) was much larger than the thickness of the sample, making our setup insensitive to the target position along the optical z-axis (i.e. loose focusing regime). The sample was placed at $z = 0$ (focus).

The peak intensity at the sample was varied in the range $0.5-10\,\text{TW/cm}^2$. The intensities used remain below the damage threshold and this was verified through inspection of the sample surfaces for damage and monitoring of the HHG spectra as a function of time. It is important to discuss the errors on the intensities here. The intensity of a gaussian pulse is defined as $I = \frac{2\times 0.94\times P_\text{a}}{f_\text{rep}\tau A}$ where P_a is the average power, f_rep is the repetition rate of the laser, τ is the pulse duration of the pulse and A is the focal area defined as $A = \pi w^2$ (w is the beam radius). There are a few caveats when considering the on-target intensity of a solid sample. From Fresnel reflections at the front surface of the sample (refractive index n), the beam suffers from a slight energy loss corresponding to the factor $\frac{4n}{(n+1)^2}$ (0.93 for $n = 1.73$ for MgO at 800 nm). Unless expressed otherwise, the intensities stated do not take into account this factor to facilitate comparison of intensities throughout the whole thesis.

Harmonics were generated in transmission geometry and the laser polarization was along the cubic bond (Mg-O) where the highest efficiency is achieved [112]. To optimise the detection of harmonics, the gain of the MCP could be adjusted, as well as the integration time on the camera. Optimal settings yielding high SNR were integrations of 25,000 laser shots representing the average of five different spectra (5,000 shots each), each taken on a fresh spot of the sample to avoid damage.

4.2.2 Harmonic Spectra of MgO and Krypton

Figure 4.2 presents the harmonic spectrum collected for the MgO sample along with a spectrum generated from 60 mbar of krypton. All other experimental parameters are identical. In order to obtain this spectrum from the CCD camera images, we integrate over the spatial divergence of the harmonics.

For the same laser intensity of $\sim 10\,\text{TW/cm}^2$, MgO and Kr exhibit a comparable harmonic yield for low energies between 7.5 eV and 19 eV. Beyond 20 eV, harmonics are no longer generated

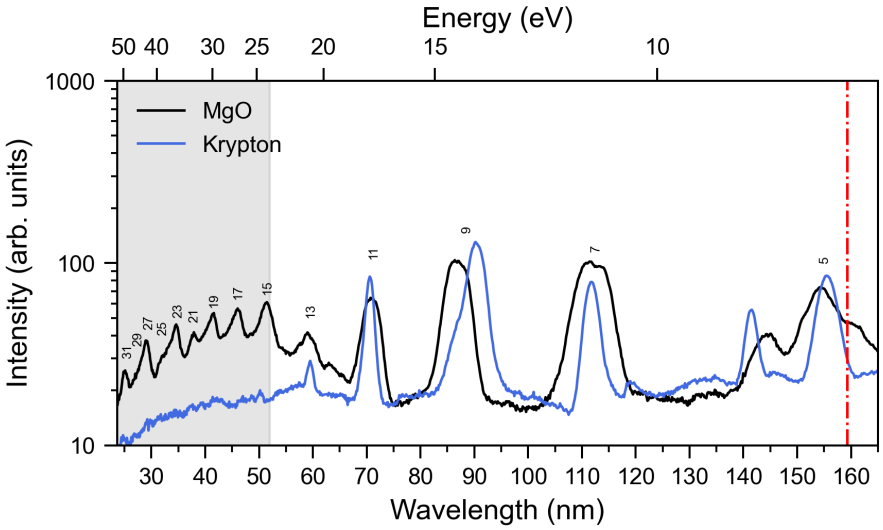


Figure 4.2: Comparison of HHG from MgO and Kr. HHG spectrum measured from 001 MgO (black curve) and 60 mbar of Kr gas (blue curve) under identical laser and detection parameters. The spectrum shows odd harmonic orders from 5 to 31 for MgO. The y-axis is on a logarithmic scale. The peak laser intensity was 10 TW/cm^2. The gray shaded area represents what appears to be a secondary plateau region. The dotted red line indicates the bandgap of MgO at 7.8 eV. Figure reproduced from [180] under the terms of the Optica Open Access Publishing Agreement.

in Kr whereas the HHG spectrum of MgO extends to the 31$^{\text{st}}$ harmonic, centered at 50 eV (25 nm), approximately 20 eV higher than the previous maximum photon energy observed in MgO [59]. This is the limit of where we could reliably resolve the energy of the harmonic peaks above the noise level.

We can confirm the intensity calculation by analysing the krypton cutoff. From the cutoff law in gas, $E_{\text{cutoff}} = I_p + 3.17U_p$ with I_p the ionisation potential ($I_p = 14.0$ eV for krypton) and $U_p = \frac{e^2E^2}{4m_e\omega_0^2}$, the ponderomotive energy (E field amplitude, e electron charge, m_e electron mass and ω_0 central angular frequency) [6], we can calculate the theoretical intensity needed to generate the cutoff harmonic, which is here the 11$^{\text{th}}$ harmonic at ~ 17 eV. We find $I \approx 16$ TW/cm^2. This yields a factor ~ 1.6 difference with the measured intensity. Such a difference in intensity can arise from a shift in position of z_R on the optical axis, which constitutes a source of error on the intensity. Other sources of error need to be analysed. If we consider that the beam radius measured was in fact at $z = z_R$, then a change of 5 mm can correspond to a 1.1 times increase of intensity. Experimentally, the exact position of the focus relative to the target can be hard to find. When measuring the intensity experimentally, errors on the average power (P), the beam radius (w) and the pulse duration (τ) were also measured, allowing a calculation on the intensity error following:

$$\frac{\Delta I}{I} \propto \sqrt{\left(\frac{\Delta w}{w}\right)^2 + \left(\frac{\Delta P}{P}\right)^2 + \left(\frac{\Delta \tau}{\tau}\right)^2} \tag{4.1}$$

Moreover, the fact that the beam is not perfectly Gaussian needs to be considered. Calculating

all these sources of error on the intensity gave a value of 20 %, i.e. $I \approx 10 \pm 2\,\mathrm{TW/cm^2}$. We note that the combination of loose focusing and the long target length ($\approx 4\,\mathrm{mm}$) for Kr harmonics would further enhance the harmonic flux.

We note that Kr is among the most efficient nonlinear media at this intensity. A comparison between solid and gas HHG has already been undertaken by Luu *et al.* [95]. They showed similar results, where for the same intensity ($\sim 10\ \mathrm{TW/cm^2}$ is considered as a low intensity for gas HHG), the harmonic yield from their sample, thin film SiO_2 was five times higher than the yield from 200 mbar from krypton. However, it is important to compare the number of emitters in order to make a true comparison between the efficiency of gas and solid for the same intensity. This number gives an indication of the possible sources of HHG. We calculate this number of emitters for our case.

The density of MgO is $\rho = 3.58\,\mathrm{g/cm^3}$ and the molar mass is $M = 40.30\,\mathrm{g/mol}$, yielding a density $n_{\mathrm{MgO}} = N_A\rho/M = 5.3 \times 10^{28}$ molecules/m^3 (N_A is the Avogadro number). The spot size radius is $\sim 107\,\mu\mathrm{m}$. The effective length in which the harmonics are emitted depends on the harmonic order. Figure 4.3 presents the effective length for each harmonic energy, corresponding to harmonic orders 7 to 31 (data from [182]). The effective length is for which the transmission falls to $1/e$. If we take a mean absorption length of $\sim 20\,\mathrm{nm}$, then this value yields 3.8×10^{13} emitters.

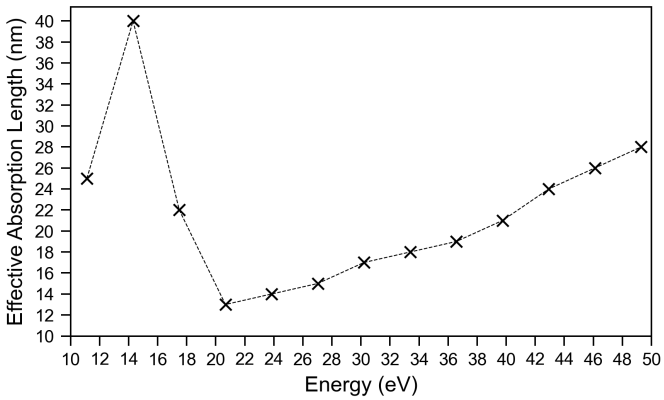


Figure 4.3: Effective absorption length of MgO depending on energy. The data is from [182].

In 60 mbar of krypton, the density of emitters is $n_{kr} = P/k_BT = 1.5 \times 10^{24}\,\mathrm{atoms/m^3}$. If we consider an interaction length of 4 mm and the same spot size radius of $\sim 107\,\mu\mathrm{m}$, we obtain 2.2×10^{14} emitters.

The number of emitters in both cases differ by less than one order of magnitude, allowing a meaningful comparison between the two cases. We can thus conclude that for the same intensity, and accounting for the emitters' number, MgO is more efficient than krypton.

We note our use of a longer than typical focal length for HHG in solids, ensuring a large interaction volume. This increases the signal collected as we have a larger number of possible

emitters. Other reported experiments used a shorter focal length yielding a tight focused spot size (see Table 4.2). The combination of pulse energy, spot size and pulse duration makes it possible to reach intensities sufficient to drive non-perturbative harmonic generation in every case.

Sample	Energy (µJ)	Wavelength (µm)	Diameter spot size (µm)	Pulse Duration (fs)	Intensity (TW/cm^2)	Ref.
MgO	70	1.3	90	100	6	[181]
MgO, MgO:Cr	20	0.8	100	40	10	[113]
MgO, MgO:Cr	4	1.55	$\sim$ 45	22	18	[166]
MgO	50	0.8	140	7	12	[167]

Table 4.2: Laser parameters used for HHG in MgO.

The careful optimization of our detection system described in Chapter 3, i.e., the non-standard geometry of the flat-field grating, the lack of contamination in the vacuum system, the high SNR and the loose focusing regime, together with the use of a NIR multicycle driving pulses to improve the emission efficiency, has enabled the detection of these higher-order harmonics. We have carefully tailored our setup to capture the full spectral range of interest, ensuring that our measurements are not constrained by system losses, or low SNR.

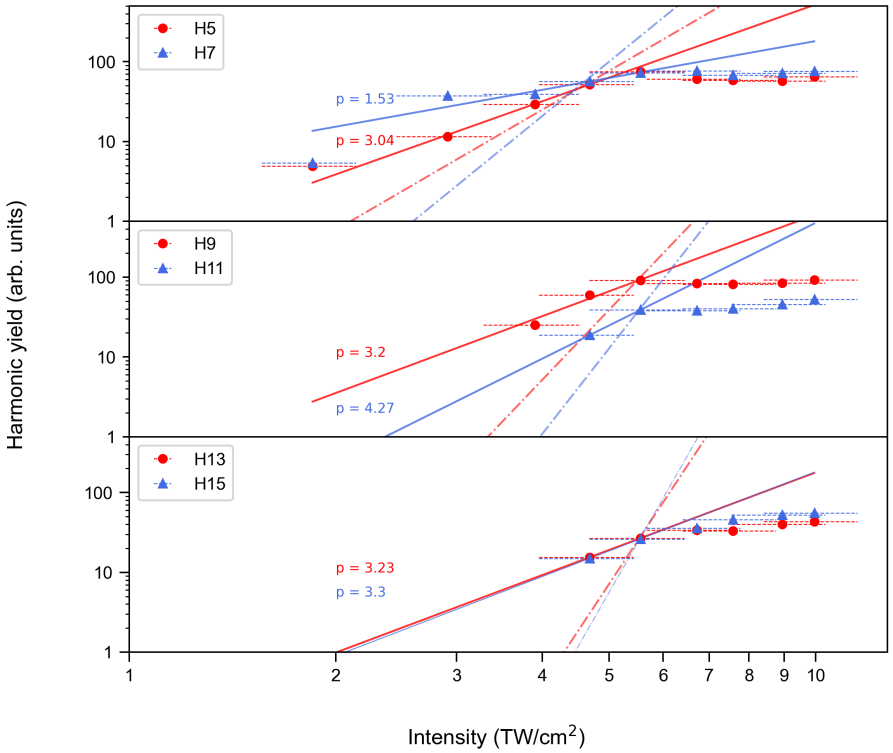


Figure 4.4: Yield of harmonics generated in MgO as a function of the driving intensity for harmonic orders H5 to H15. Both axes are in log scale. The dashed lines represent the perturbative power law for each harmonic. The solid lines represent a linear fit on log-log scale of the data. The gradient of the fit corresponding to the harmonic effective power is noted as p on each panel.

An intensity scaling of the harmonics from MgO is shown on Figure 4.4. It shows the laser intensity dependence of the harmonic yield for orders 5−15 on a log-log scale. The harmonic yield is found by integrating the MCP signal for each harmonic over its full spectral width and

spatial extent. We observe a marked deviation from perturabtive scaling, i.e., q^{th} harmonic yield proportional to q^{th} power of laser intensity, as shown in previous studies for low-order harmonics [113]. For the 5^{th} and 7^{th} harmonics, there is the suggestion of a change of slope at $\sim 1.8\,\text{TW/cm}^2$. This behaviour has been seen in earlier work, e.g. for HHG in ZnO [183] where for low intensities, harmonics follow the power law of perturbative harmonics and for high intensities, these same harmonics deviate form the perturbative regime to enter the non-perturbative one, following a different power law.

4.2.3 Interpretation of the High Cutoff

The most striking feature in these results is the highest cutoff, located at 50 eV, recorded in MgO or in any solid. We propose here a possible explanation for the appearance of such a high cutoff.

In Figure 4.2, we identify two spectral regions of interest which we refer to as Region I (white area) and Region II (gray area). Region I extends up to 22 eV and represents the low-order harmonics (H5 to H13), showing a decreasing harmonic yield. Above this energy, Region II spans from $\sim$ 24 eV to 50 eV (H15 to H31).

Region I covers the first and second conduction bands in MgO [100, 59, 181]. The first conduction band spans from $\sim$ 8 eV to $\sim$ 18 eV while the second conduction band covers the range $\sim$ 18-25 eV at the Γ point (Figure 4.1b). The use of a NIR driving wavelength results in a relatively large harmonic spacing ($\sim$ 3 eV) which prevents clear resolution of the CB1 to CB2 band edge. However, we do observe a drop in yield for the single harmonic in the CB2 energy range, H13, which is expected to have a lower yield than harmonics generated within the CB1 energy range. These spectral features are broadly consistent with previous NIR studies, such as that of Korobenko *et al.* [167], where H13 and H15 were observed with decreasing yield compared to H11.

The secondary plateau region (Region II) presents a linearly decreasing series of harmonics from H15 to H31. The presence of multiple plateaus had already been observed in solid Ar and Kr [102], MgO [100], amorphous quartz [101] and theoretically predicted in MgO by [124] and was related to the involvement of multiple conduction bands, largely through interband couplings identified in both experimental and theoretical studies [100, 133, 82]. Although we cannot entirely rule out a contributory intraband current component, it is likely that higher-order conduction bands are involved in the emission above 25 eV.

However, modelling of these higher bands is limited, as the literature generally only covers the second conduction band (up to 25 eV). Furthermore, while the harmonic yield in this region is decreasing, the overall change spans only a single order of magnitude – contrary to expectations for transitions involving population in higher-order bands, such as those from VB$-$CB2. This yield can be initially explained by the use of a driving photon energy of 1.59 eV for a bandgap of

7.8 eV, enabling more efficient ionisation compared to a 0.73 eV driving wavelength (1.7µm, used in [100], which limited the cutoff to 25 eV). Indeed, electrons are more efficiently driven into the CB, requiring only at least 5 photons *versus* 10 photons in the other case.

In a strong field, dynamical Stark shifting of the higher-lying bands could open new channels for HHG. The dynamical Stark shift has already been observed in different experiments [184, 185]. This shift can enable higher photon energies to be reached [163]. Indeed, at these energies, field-free band structure calculations may no longer be accurate as the energy levels shift due to strong fields. Furthermore, with a two-colour experiment, Uzan-Narovlansky *et al.* [174] have demonstrated a light-induced closing of the bandgap under a strong field in MgO. A laser-induced modification of the band structure could therefore contribute to explaining the high cutoff observed in this work.

We also cannot exclude wave-mixing between the fundamental and its third harmonic generated in the sample, which could also extend the cutoff [169].

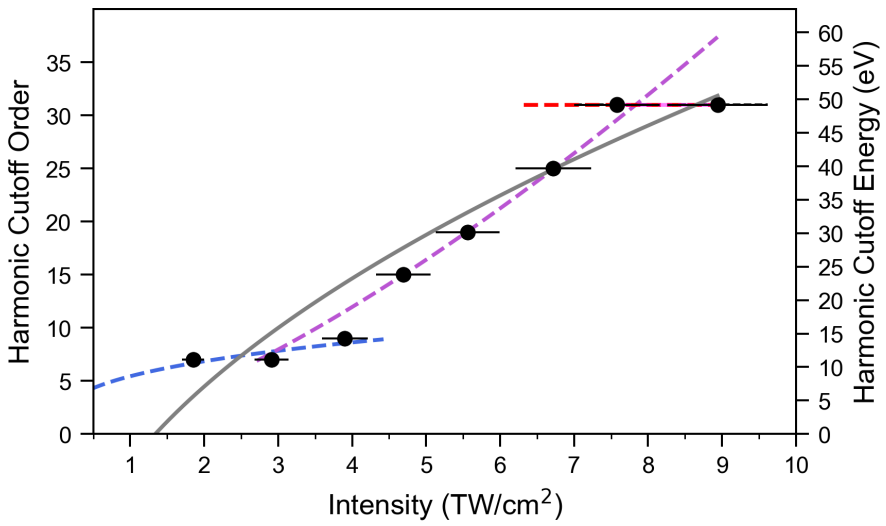


Figure 4.5: Scaling of the MgO harmonic cutoff with laser intensity, illustrating a clear departure from the expected square root dependence (gray solid line). The dashed lines represent three piecewise linear fits to the data, highlighting the non-trivial scaling behaviour. Figure reproduced from [180] under the terms of the Optica Open Access Publishing Agreement.

Figure 4.5 shows the harmonic cutoff as a function of the driving laser intensity. We define the cutoff as the point where the harmonic yield drops to twice the noise floor. Previous experimental [95, 94, 7] and theoretical [79] studies have demonstrated that the cutoff scales with the square root of the intensity (i.e. linearly with the field) because of the curvature of the bands for covalent solids (see Section 2.6.3). However, the data in Figure 4.5 does not show this square root dependence. Instead, it shows a more complex behaviour, similar to the findings of Ndabashimiye *et al.* [102] for HHG in the van der Waals solids of Ar and Kr. They attributed this complex behaviour as arising from the localisation of the electrons on the individual atomic sites rather than their delocalisation along the bond. Those findings hint that MgO, as a ionic solid, presents a modified

HHG mechanism.

4.3 Impact of the Driving Pulse Duration on the Harmonic Spectrum

In this section, we investigate the impact of the driving pulse duration on the harmonic spectra features, such as the cutoff and the spectral modulations of the harmonics. The sample under study is still MgO to allow a comparison with the previous section. The polarisation of the laser is aligned with the ΓX direction of the sample. The impact of the pulse duration on the harmonic spectrum is an open question and few studies have investigated this area.

4.3.1 Driving Pulse Dependent Harmonic Spectra

We present in Figure 4.6 the harmonic spectrum as a function of intensity for each driving pulse characterised in Chapter 3. We notice that the intensities for each pulse duration covers a different range. This is mainly due to the difference in spot size. Indeed, experimentally, we found that the HHG emission was strongly dependent on the spot size. We confirmed this in the last section by underlining the importance of the loose focusing regime we worked in. We adjusted the size of the iris for each case and the laser parameters of each pulse are summarised in Table 3.1.

Overall, we see that the structure of the HHG spectra does not change with intensity. Moreover we perform pulse duration measurements in Section 4.3.2. We can therefore suggest that the features described in this section are not due to dispersion or nonlinear effects. We note the harmonic yields are similar for all pulse durations, indicating we maintained a similar harmonic flux.

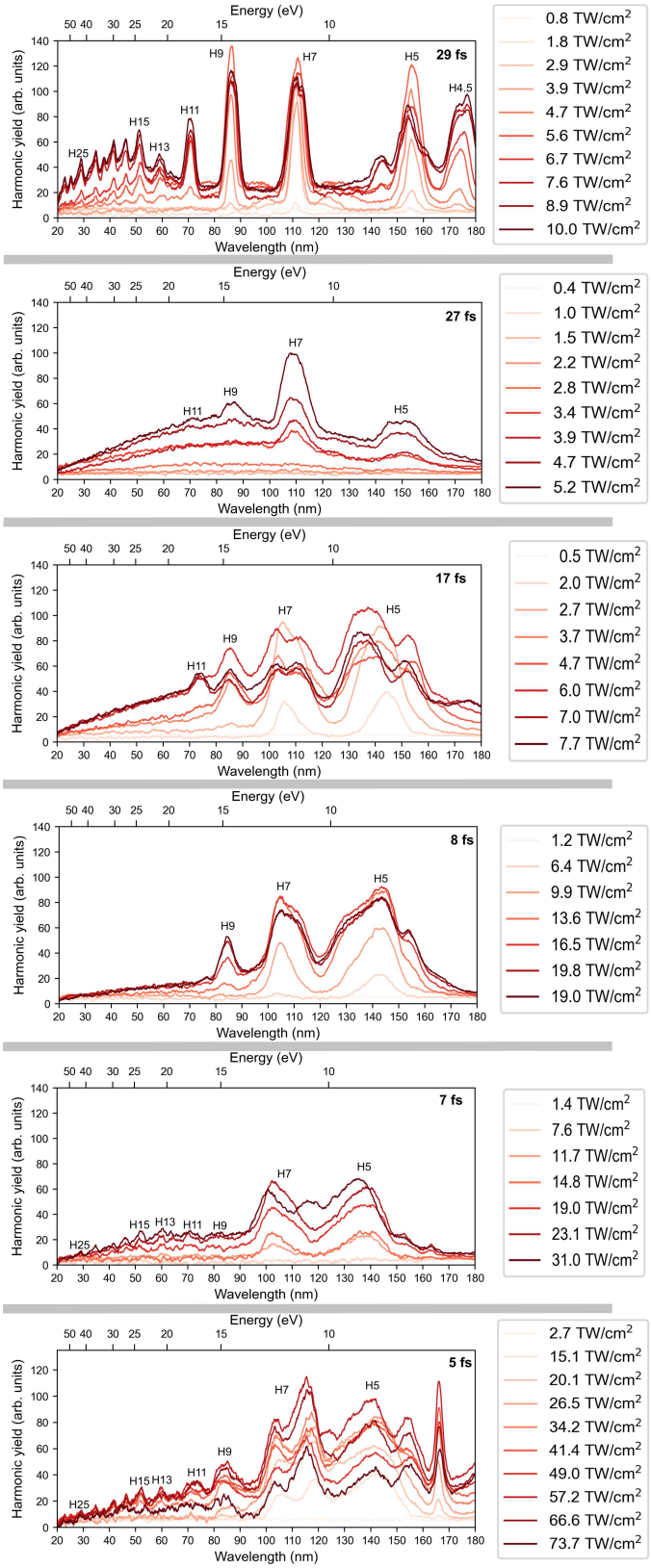


Figure 4.6: Harmonic spectrum from MgO as a function of driving field intensity for each pulse duration.

Harmonic Cutoff

For each pulse duration, it is clear that more harmonics are generated as the intensity increases. The structure shifts dramatically with as little as a 1−2 fs change in the pulse duration, which corresponds to a half-cycle to a full-cycle change. We define the cutoff as the last harmonic visible in the spectrum above the noise, or as XUV emission above the noise level when the harmonic is not well-defined. The harmonics are defined to be statistically significant when they are above a noise level of 2×10^0 on the figures from Appendix B. The cutoff depends on the pulse duration.

Figure 4.6 shows that the cutoff varies between $\sim$ 15 eV (for 8 fs) to 50 eV (29 and 5 fs). Figure 4.7 displays the harmonic cutoff for different driving field pulse durations.

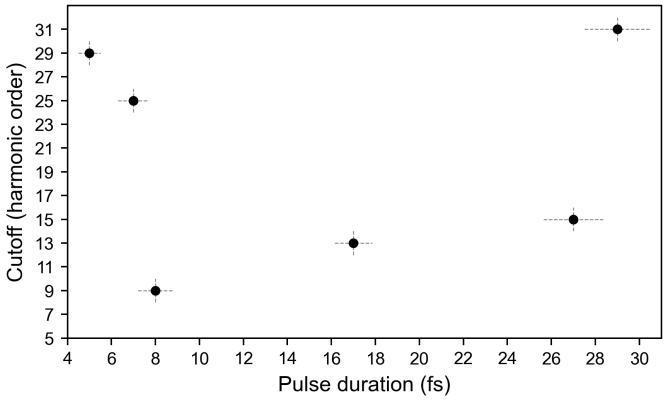


Figure 4.7: Harmonic cutoff as a function of pulse duration. The cutoff data is gathered from Figure 4.6 and the MCP images in the Appendix.

No direct trend is visible on Figure 4.7. For a short pulse (5 and 7 fs), the cutoff is high, above the 25$^{\text{th}}$ order ($>$ 45 eV). Then as the pulse duration increases, the cutoff drops to energies between the 9$^{\text{th}}$ and 15$^{\text{th}}$ order (15−30 eV). Suddenly, for a long pulse (29 fs), the cutoff rises back to high orders ($\sim$ 50 eV).

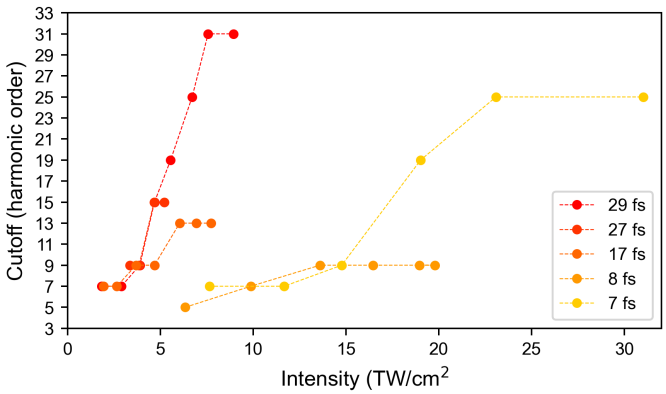


Figure 4.8: Scaling of the MgO harmonic cutoff with laser intensity for different driving pulse durations.

We can however look at the trend of the cutoff with intensity or field strength. The same

nonlinear behaviour as for the long 29 fs pulse is seen for all driving pulse durations. Figure 4.8 displays the non-trivial cutoff law of MgO in all studied cases. The 11^{th} harmonic is at the edge of the first CB, which means that the harmonics driven by the 8 fs pulse stem only from intraband currents as they remain below the bandgap.

The impact of the pulse duration on HHG in solids remains largely an unexplored parameter. Freeman *et al.* [186] have attempted to investigate the peak visibility of the spectrum for different pulse durations in the NIR regime with diamond. They showed that a multicycle pulse generates more efficient harmonics due to more cycles near the peak of the field participating to the process. Moreover, a short driving pulse does not allow detection of the higher-order returns. They only compare a 200 fs pulse at 800 nm with a 30 fs pulse at 800 nm. We vary the pulse duration from 29 fs to 5 fs and therefore study a large range, including the few-cycle regime. The spectrum of both the longest and shortest pulses present the highest cutoff, signature of higher-order returns (electrons returning to the associated hole after propagating in the field for a longer time than the direct returning electrons), in contradiction with the analysis of Freeman *et al.* [186]. However, we can nuance this statement by comparing the cutoff for the same intensities, and the longest pulse of 29 fs is clearly displaying systematically the highest cutoff.

Structure in the harmonic spectrum can be expected from MgO. A trough at 20 eV has been predicted with a NIR field [187]. Using a transition dipole matrix calculation, similar to other works done in MgO [188, 189, 190], the destructive interference between harmonics generated through different paths (transition CB1-VB or CB2-VB) has been shown to be responsible for a dip in the spectrum at 20 eV [187]. Figure 4.9 displays the harmonic spectrum for each pulse duration zoomed on the region around 20 eV. We notice that a dip is present in the spectrum for 29, 27 and 5 fs, although its resolution is low. It is possible that in our case, interference effects are present, but a further theoretical analysis is required to make a more conclusive statement.

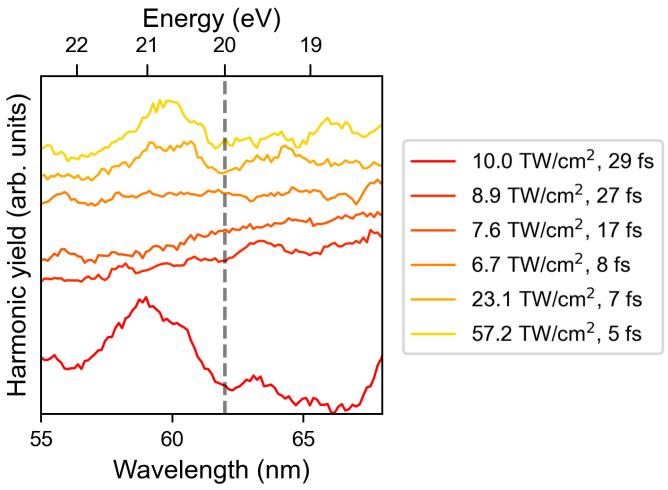


Figure 4.9: Harmonic spectrum for each pulse duration zoomed on the energy region around 20 eV.

We know that HHG is a half-cycle process and each event has a phase that sums constructively or destructively to give the final harmonic spectrum. Carrier-Envelope Phase (CEP) dependence studies in the solid phase have shown shifts of the harmonics with CEP [95], confirming that the HHG process is sensitive to the timing of the electric field. The structure of the harmonic spectra for each pulse duration is similar below 18 eV (below the second CB), but above this energy, the XUV emission changes shape and the interference effects between successive cycles might be responsible for this change. The HHG structural shape is potentially a consequence of the structure of the electric field. The harmonic yield is affected by the number of cycles and the peak intensity.

Figure 4.10 displays the fundamental spectrum of each driving field. As the pulse duration decreases, the bandwidth broadens and the central wavelength shifts in wavelength towards the blue end of the spectrum. The bandgap of MgO is 7.8 eV. To cover the bandgap with four photons, the excitation wavelength is 636 nm, whereas to cover it with five photons, it is at 795 nm. The pulse duration scan performed here covers this range of wavelength. The dip in the cutoff as the pulse duration decreases could potentially arise from the transitional regime of excitation. We only discussed the bandgap between the VB and CB, yet higher bandgaps between the higher-lying CB could also condition the highest XUV emitted. Additionally, the shape of the spectrum changes and a strong modulation appears around 800 nm. The shape of the spectrum itself could explain the dependence of the cutoff with pulse duration.

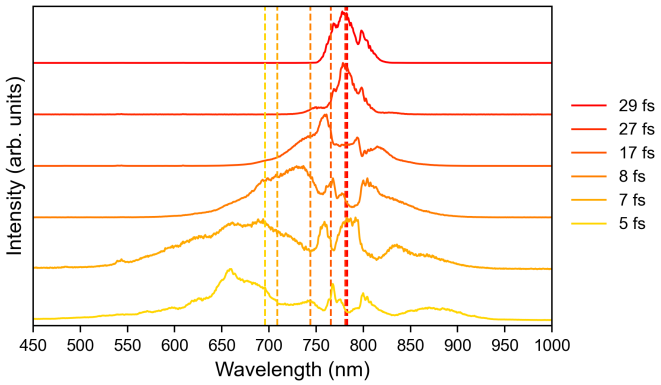


Figure 4.10: Fundamental spectra of the driving fields for each pulse duration used for HHG. The dotted line is the centre wavelength calculated as the weighted average of the spectral intensities for each pulse duration.

The trend of the cutoff with pulse duration remains unclear. This work shows that solid HHG emission in higher-lying bands could be (1) cycle or electric field dependent, meaning that if the timing of the recollision or acceleration along the bands is off, there is no harmonic emission, or (2) spectrum dependent.

A numerical simulation seems necessary to understand the electron motions. Private discussions with Simon Jensen and Nicolas Tancogne-Dejean (Max Planck for the Structure and Dynamics

of Matter, Hamburg) are ongoing, attempting at unravelling the dynamics at play responsible for such a change in harmonic behaviour as a function of input pulse duration. Currently, it is not possible to conclude on the dependence of the harmonic cutoff and yield with pulse duration.

Harmonic Yield Dependence on Laser Intensity

We now consider the yield of the harmonics. We focus on H5 to H9 as they are produced by all driving pulses. Figure 4.11 displays the harmonic spectrum for all driving pulses, zoomed in on the region from H5 to H9. The shape of the spectra varies: as the driving pulse duration decreases, the harmonics broaden and tend to be less "clear" [186].

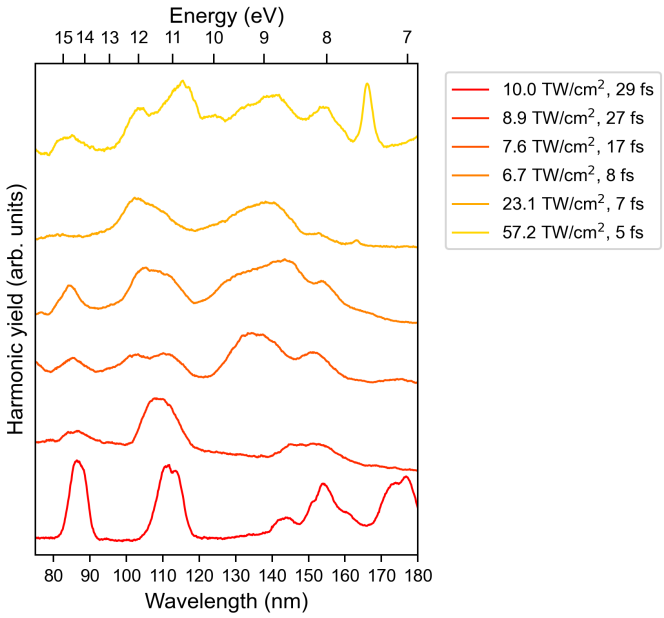


Figure 4.11: Harmonic spectrum of H5 to H9 for each pulse duration.

Figure 4.12 shows the spatially integrated yield over the bandwidth of H5 to H9 as a function of driving laser intensity. Each harmonic for each pulse duration behaves similarly: the yield of the harmonic increases with a high slope and then either saturates or decreases slightly. In some cases, the yield increases again for higher intensities. The eventual decrease in yield can be linked to damage. However, when looking at the spectra, we see that low order harmonics (H5 to H9) decrease in yield as the intensity increases while higher-order harmonics increase in yield. These two regimes (yield of high- and low-order harmonics behaving differently with intensity) can be seen for all driving pulses except the 27 fs driving pulse. Additionally, there was damage for the 5 fs driving pulse for the highest intensity, 73.7 $\mathrm{TW/cm^2}$. Indeed, there is a drop in harmonic yield across the whole spectrum. The damage was confirmed by visual inspection. It is the only case of sample damage in this study.

The dip in harmonic yield as the intensity increases has also been reported by Shao *et al.*

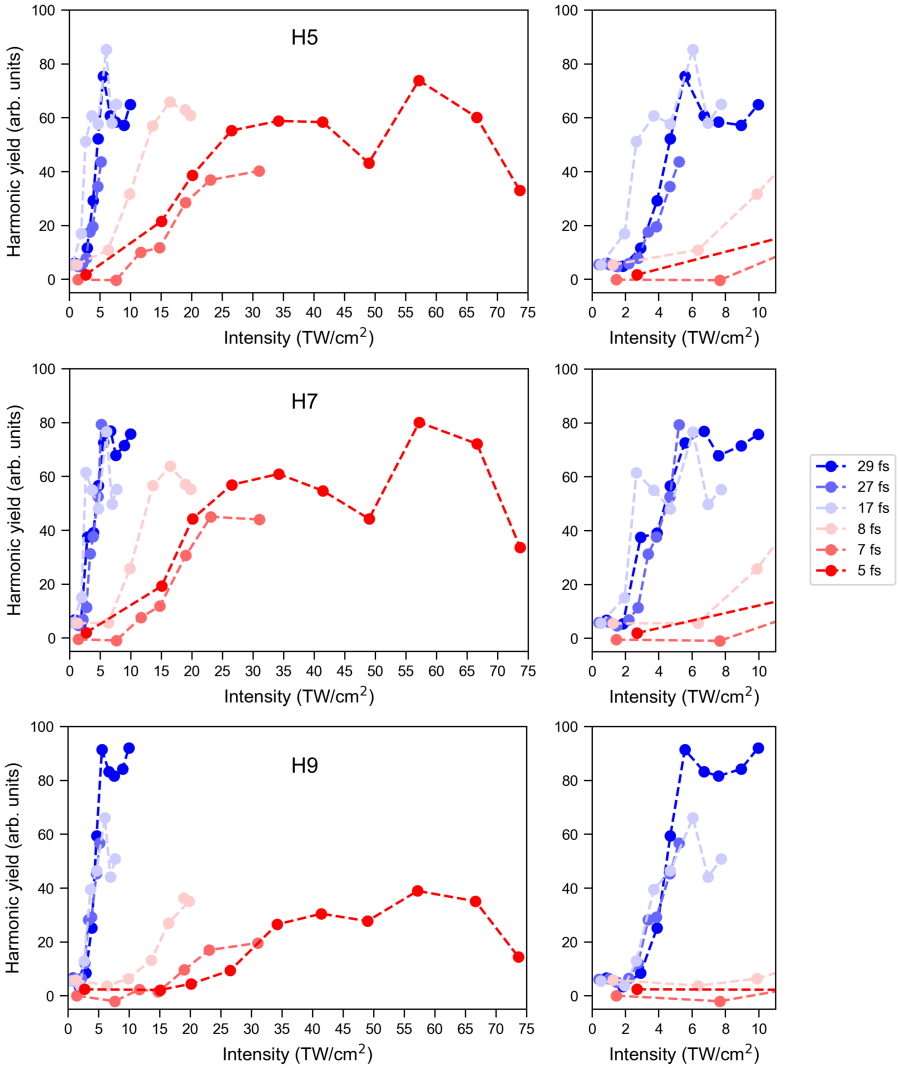


Figure 4.12: Harmonic yield of H5 to H9 as a function of driving laser intensity. The yield is integrated on the central divergence of the harmonic and over its full bandwidth.

[169] in MgO. With a 1600 nm driving wavelength, it was seen that H19 split into two peaks and dropped in yield compared to the surrounding harmonic orders. It was demonstrated that this was the signature of quantum path interference, i.e. the coherent interference of the long and short trajectories. We see similar behaviour (dip in the spectrum), although not only for one harmonic but for multiple, all above-bandgap. Multiple studies have shown that in MgO, interband harmonics are dominant above the bandgap [79, 100, 169], although intraband harmonics can also dominate in specific cases [58]. Indeed, in a cubic crystal, Tancogne-Dejean *et al.* [58] linked the Joint Density of States (JDOS) to the clarity of the harmonics. We have looked at the JDOS of MgO [191] but the limited number of peaks prevented us from drawing any clear correlation with the HHG spectrum. The harmonic spectra of Figure 4.6 show a splitting: H5 and H7 split in all cases except for 27 fs. All of the remaining cases present a dip in the yield, except for the 7 fs case, which could be because the intensities are too low to see the dip. The split in the spectrum of H9

is not visible. However, the dip is still visible in the harmonic yield for increasing intensity. It is therefore difficult to conclude on the interference of the trajectories for H9 but H5 and H7 do seem to present an interference pattern that has not been reported, as far as we know.

4.3.2 Harmonic Emission with a 2 Cycle Pulse

We focus in this section on the 5 fs driving field, which corresponds to 2 cycles centred at 700 nm. The CEP of the pulse was unlocked. As ultrashort pulses are more sensitive to dispersion elements in the beampath (Section 2.1), we first analyse the transmission of the pulse through the MgO sample.

Pulse Characterisation With a D-Scan

We record for four laser intensity values the transmitted laser spectrum along with the reconstructed phase obtained with a D-Scan. For reference, the spectrum without the sample inserted in the beam is also recorded. Multiple measurements were acquired, enabling to calculate errors on the data. These measurements are presented on Figure 4.13.

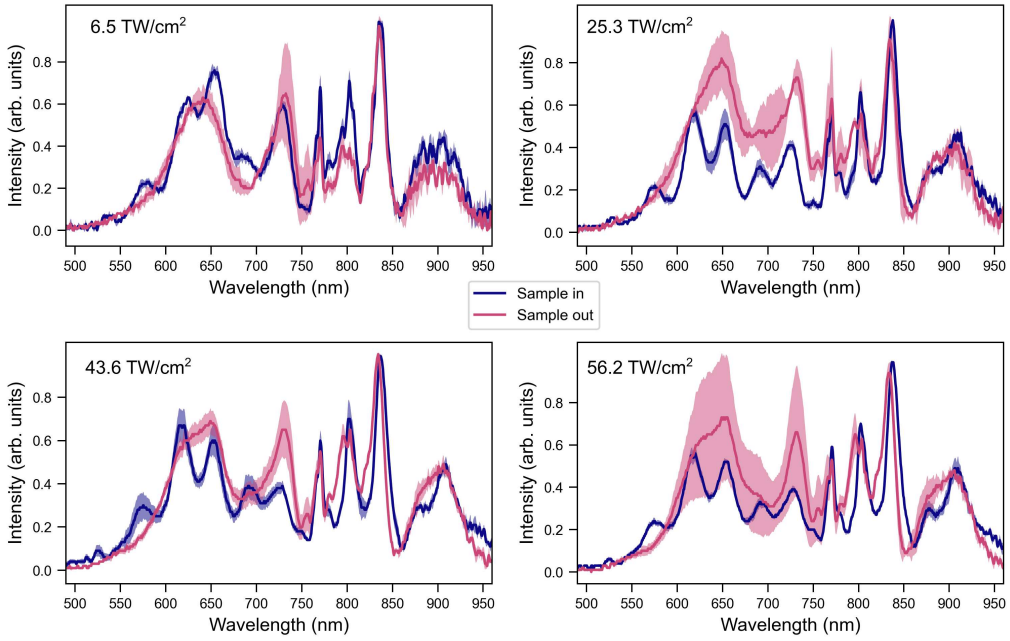
In the region 500−700 nm, the beam is more attenuated by the sample than in the region 750−950 nm. The sample also adds spectral modulations in the first region. MgO is transparent to the whole 500−950 nm range of wavelengths [192]. However the spectral phases display nearly identical patterns with or without the sample inserted in the beam.

Figure 4.14 shows the measured pulse duration as a function of laser intensity. Three sets of data are presented, one where the measurements were done with the sample, one without and the last one corresponds to the calculation of the pulse elongation due to GDD.

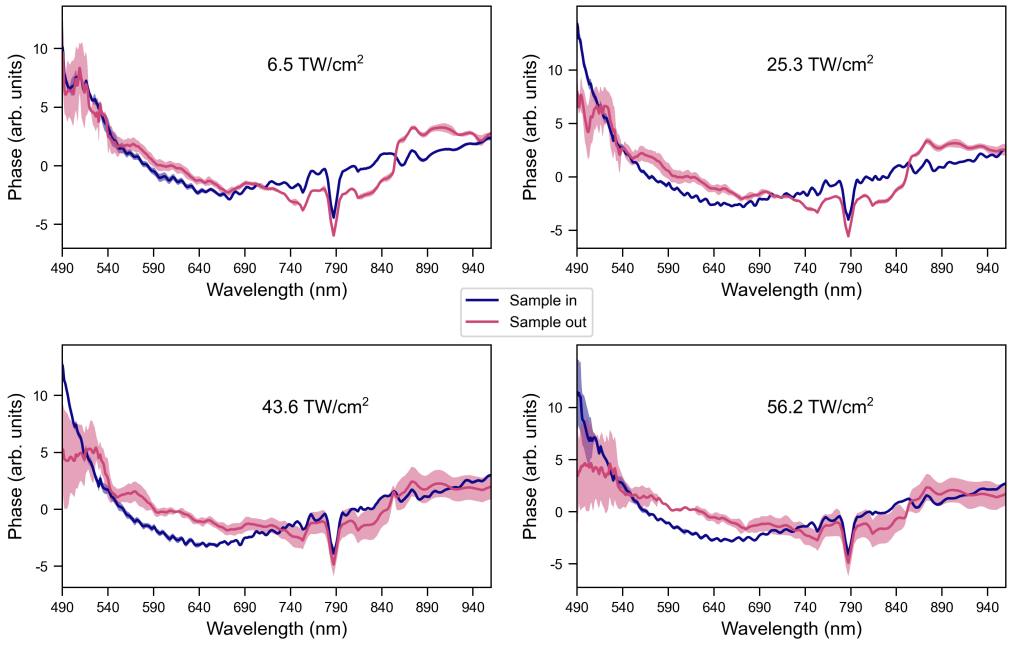
The measurement of power transmission ($\frac{P_{\text{out}}}{P_{\text{in}}}$) is indicative that there is low or negligible absorption by the sample. The error bars overlap and all the measurements are consistently above 0.8. The transmitted pulse has an increased pulse duration at all intensities although this is only outside the margin of error at the highest intensity, making it difficult to quantify the pulse broadening in the sample. Moreover, the measurements of the pulse broadening are consistently below the calculations of a linear broadening (GDD). It is possible that nonlinear effects compress the pulse in the sample [193] or that the errors of the measurements were underestimated. Nevertheless, we can postulate that linear propagation effects in the 100 µm MgO sample are not responsible for the harmonic features observed.

Potential Signature of Photoluminescence (PL)

A particular spectral structure arises in the harmonic spectrum for the shortest pulse durations. Indeed, a sharp peak appears in the harmonic spectrum just below the bandgap and it does not



(a)



(b)

Figure 4.13: D-Scan measurements of the pulse with the sample in or out of the laser beam. 4.13a: Spectrum for different intensities. 4.13b: Phase for different intensities. The measurement was always done at the same position outside the HHG chamber. As the sample is on a motorised stage, it can be inserted in the beam.

correspond to a harmonic due to its energy of emission and to its sharp peak compared to the other harmonics. Figure 4.15 displays the harmonic spectrum over the range of this spectral feature centred at $\sim 7.5\,\text{eV}$. Exciton emission has been studied in MgO and its energy of emission varies between 7.5 and 7.7 eV, depending on the experimental parameters, including the sample temperature [194, 195, 196]. Exciton emissions are located just below the bandgap [197]. The

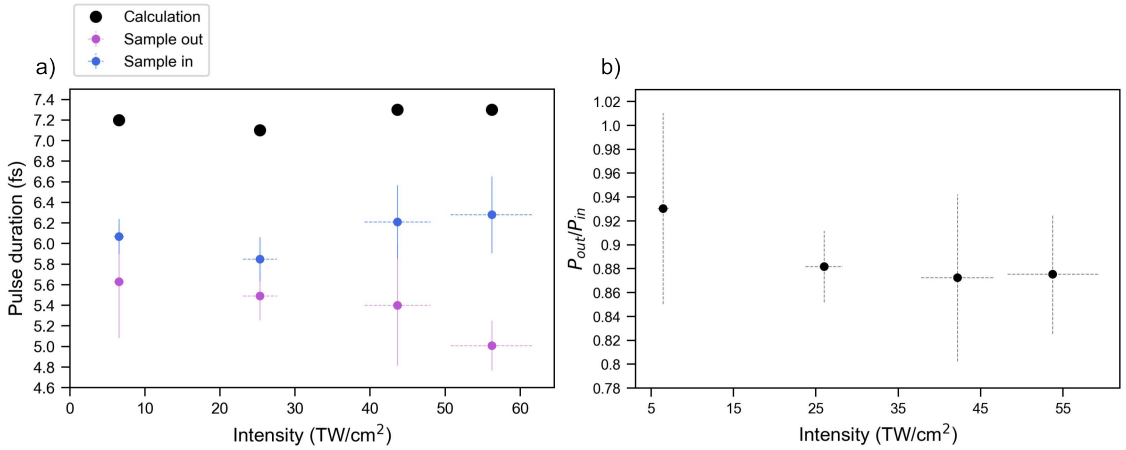


Figure 4.14: Pulse duration (a) and power measurement (b) as a function of driving laser intensity with the sample in or out of the laser beam. (a): The pulse duration is measured with a D-Scan. As the sample is on a motorised stage, it can be inserted in the beam. The black dots correspond to the calculation of the linear broadening of the pulse going through 100 µm of MgO. The errors are calculated as the standard deviation of the data. (b): P_{in} corresponds to the power incident on the sample, P_{out} corresponds to the power after the sample.

spectral feature mentioned is thus attributed to an exciton emission. Moreover, we measure the spectral bandwidth of the emission from the 5 fs pulse to be 3.1 nm (FWHM) which corresponds to a Transform-Limited (TL) pulse duration of $\sim$ 30 fs FWHM, which is shorter than the typical timescales expected from exciton emission [198], but not inconsistent as the emission may have poor temporal coherence; furthermore, the bandwidth may be overestimated due to the resolution of the spectrometer.

The fact that we see the excitonic emission only for the shortest laser pulse durations might be linked to the higher intensity required to create the exciton [199], explaining why we do not see this emission for intensities below 20 TW/cm^2. However, this emission could also be due to a sequential excitation, i.e. excitation into the conduction band and then further excitation, or it could also be a timing effect linked to the shape of the electric field. The origin of this emission requires more work.

Figure 4.15 shows the MCP images of the potential excitonic emission for the two shortest pulse durations. Excitonic emission is a PL emission and we expect this emission to be more spatially divergent than the harmonics. Figures 4.15b) and c) show the spatial divergence of the collected spectrum on the y-axis for the 5 fs pulse (b) and the 7 fs pulse (c). The PL emission has similar divergence to the neighbouring harmonic, H5. The geometric calculation gives similar full-angle divergences of 16 mrad for H5 and 12 mrad for the PL emission by a Gaussian fitting. Chapter 6 explains the insight we can gain from PL emission. Further studies, similar to Jensen *et al.* [200], are required to build on the preliminary results presented on exciton emission.

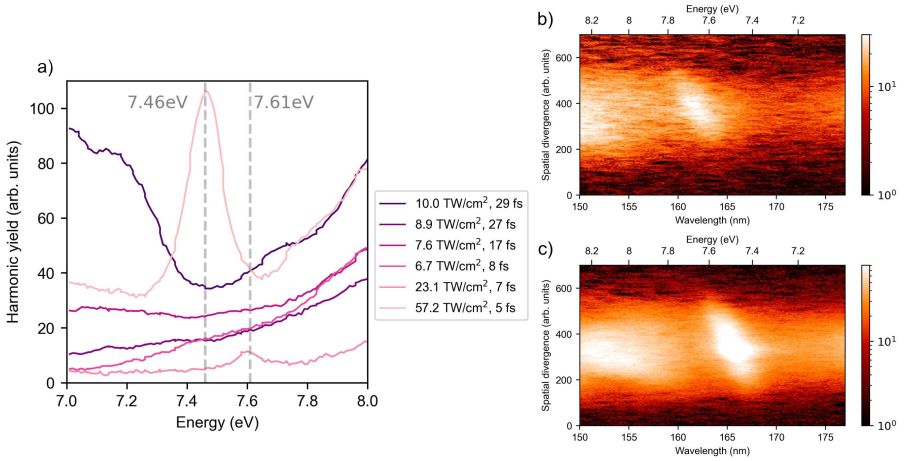


Figure 4.15: PL emission near the bandgap of MgO. (a) Spectrum of the PL emission centred around 7.5 eV for all pulse durations. (b) and (c): MCP images of the harmonic spectrum for the 5 fs pulse (b) and the 7 fs pulse (c).

4.4 Conclusion

We have studied harmonic emission from a wide bandgap dielectric, MgO with a NIR driving wavelength (800 nm) matching its bandgap, and reported on the highest energy HHG emission from MgO or any solid. The band structure is responsible for the multiple plateaus in the harmonic spectrum and the particular interaction geometry and configuration of our spectrometer enabled the observation of such a high cutoff. The cutoff scaling with intensity does not resemble any scaling reported previously and this holds for all the driving pulse durations we used (5−29 fs). To better understand the underlying mechanisms for such high energy emission we investigated the dependence of the emission on pulse parameters, in particular the intensity and pulse duration. We found that a high cutoff is observed for a short 5 fs pulse as well as a long 29 fs pulse but in-between these pulse durations, the cutoff drops to harmonics with energies located in the first and second conduction bands. We also investigated the effect of the interaction on the transmitted pulse by looking at the transmitted spectrum, pulse duration and absorption. Linear propagation effects in the sample were shown not to play a significant role in the harmonic emission detected. Finally, we observe another type of emission, Photoluminescence (PL), which is only present for short pulses (5 and 7 fs) but a deeper understanding is required to make a valid conclusion on the exact origin of this emission.

Chapter 5

MIR Wavelength Driving Field for HHG in the semiconductor ZnO

Solid HHG has been separated in two regimes by Thorpe *et al.* [163]: Near-Infrared (NIR) HHG dominated by intraband processes *versus* Mid-Infrared (MIR) HHG dominated by interband processes (for above-bandgap harmonics). In this chapter, we will focus on the second regime in which the driving wavelength is in the MIR range and the samples are semiconductors.

5.1 Background on HHG Experiments in Semiconductors

5.1.1 Motivations for HHG in Semiconductors

Theoretically, if the field is strong enough, harmonics can be generated in any solid. However, the damage threshold of a material ultimately sets the upper bound for the intensity at which HHG can be driven. It is therefore imperative that the intensity of the driving field is chosen to be sufficiently high such that harmonics can be generated without leading to the degradation of the sample. Achieving the balance of harmonic flux is difficult to attain as the damage threshold of the material is strongly dependent on the driving wavelength. It is also crucial to consider the laser photon energy relative to the bandgap of the solid under study. The Keldysh parameter γ, introduced in Chapter 2, is proportional to the ratio of the bandgap to the driving photon energy. Earlier in Chapter 4, we studied large bandgap materials ($\sim 8\,\mathrm{eV}$) with a driving photon energy of $1.55\,\mathrm{eV}$. This gives $\gamma \sim 1.5$ (with $I = 5\,\mathrm{TW/cm^2}$, $m^* = 0.35m_\mathrm{e}$), which means both Tunnelling Ionisation (TI) and Multiphoton Ionisation (MPI) mechanisms are occurring. If we want to study the HHG process in semiconductors, we need to use a lower driving photon energy (longer wavelength) in order to avoid damage to the sample and to maintain similar bandgap to

driving wavelength ratios.

Semiconductors are widely studied and ubiquitous materials in modern life due to their key role in advanced technologies [201]. They are used for varied applications such as renewable energy (e.g. solar cells [202]), healthcare diagnostics tools, electronics, etc [203]. Devices based on semiconductors include transistors, switches, diodes, photovoltaic cells, detectors, etc [49]. They are extensively used in the nanotechnology and engineered materials sectors. Understanding the physics underlying semiconductors is therefore major for industrial applications. Understanding their band structure for example or the electron motion within the bands can be achieved with spectroscopy. We therefore use HHG as a spectroscopic tool to understand better these materials.

Thorpe *et al.* [163] had already emphasised the difference in the two regimes: NIR HHG tend to be dominated by intraband processes whereas MIR HHG tends to be dominated by interband processes (for above-bandgap harmonics). These findings are still under debate though and no strict rule has been demonstrated. We will focus in this chapter on the second regime and investigate what processes can be distinguished in HHG from ZnO as it has been demonstrated to yield efficient HHG [7].

Indeed, we study here HHG in a wide bandgap semiconductor ZnO ($E_g \sim 3\,\text{eV}$) using a driving wavelength centred at 3 µm. The driving wavelength corresponds to an energy of 0.41 eV which is low enough to avoid immediate damage even for the lowest intensities. This combination yields a Keldysh parameter of $\gamma \sim 0.3$ (with I=5 TW/cm^2, $m^* = 0.29 m_e$).

5.1.2 Crystal Properties of ZnO

ZnO possesses a hexagonal wurtzite structure [56] that lacks inversion symmetry (see Figure 5.1). Its minimum direct bandgap is 3.37 eV [204]. The sample used in our experiment was cut along the 0001 direction. The bonding type is a mixture between covalent and ionic bonding. The nature of the bond can impact the efficiency of the HHG process as the efficiency has been linked to the gradient of the electron-nuclei potential [58] and an ionic bond resembles more the atomic case [133]. ZnO is widely used in industry for applications ranging from medicine to optoelectronics [205]. It is also a readily available material.

5.1.3 Previous HHG Experiments in ZnO

The first demonstration of solid non-perturbative HHG was done by Ghimire *et al.* in 2011 in their seminal work describing high harmonics in ZnO [7]. Since then, ZnO has been widely studied in the context of HHG to measure structural and dynamic information either in the bulk [206, 114, 207, 208], supported thin films [209, 210], engineered nanostructures [211, 16] or monolayer samples [212].

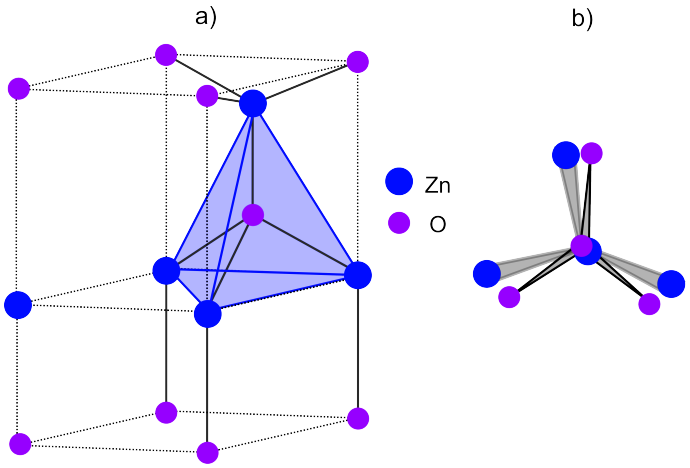


Figure 5.1: Crystal wurtzite structure of ZnO. (a) View normal to 0001. (b) View along 0001. Figure adapted from [204].

Ghimire *et al.* [7] measured a harmonic cutoff at 21 eV with a driving wavelength at 3.25 µm, which still remains one of the highest harmonic energies detected from ZnO. Other studies have focused on the sub-cycle dynamics in ZnO, using pump-probe schemes: Ghimire *et al.* [207] and Wang *et al.* [99] used different schemes. In [207], the sample was illuminated with a pump at 3.25 µm and a broadband probe centred at the bandgap wavelength ($\sim$ 370 nm). These laser conditions placed the interaction in the tunnelling regime (ponderomotive energy exceeding the drive photon energy and the bandgap), allowing a change in absorption of ZnO to be observed. Wang *et al.* [99] used a pump at 400 nm with a probe at 3.25 µm. They presented results which supported the idea of different contributions from interband and intraband channels by controlling the carrier injection through this pump-probe scheme.

Other works have studied the role of specific laser parameters such as the pulse duration [213], demonstrating an enhancement in yield and cutoff with a shorter pulse; the wavelength [183]; and the ellipticity of the driving pulse [114]. Anisotropy studies on an *a*-cut ZnO sample [206, 211] are quite common. They show the appearance of even harmonics for specific angles with a four-fold symmetry. The sample studied in this thesis is a *c*-cut sample. Few studies have looked at the anistropy of HHG in a *c*-cut ZnO sample. However, ZnO can produce a higher harmonic flux than most other medium bandgap samples, and this is one of the reasons it is widely studied. Sivis *et al.* [16] measured the flux of the fifth harmonic to be $\sim 10^6$ photons/s generated from a 2 µm driver. This flux is similar to other solids such as SiO_2 [214] but slightly higher than in gases for comparable laser parameters [95].

Finally, an important parameter that has been investigated in ZnO HHG is the laser CEP. Hollinger *et al.* [215] have measured the relative value of the CEP through spectral interference of adjacent odd harmonics with a 3.1 µm driving wavelength. They did the first CEP measurement in ZnO. CEP studies have also been carried out in other solids such as MgO [100], SiO_2 [95] and

GaSe [94]. In GaSe, Schubert *et al.* [94] presented different CEP dependence of below- and above-bandgap harmonics and observed an interference signature in the spectrum for above-bandgap harmonics attributed to the different excitation paths. In MgO [100], the same behaviour was also witnessed and attributed to the interplay of the interband and intraband regimes: the harmonic peaks shift towards higher photon energies for interband harmonics.

5.2 The Role of CEP in HHG from ZnO

In this section, we describe experiments done at ALLS to investigate the spectral modulations of the harmonic spectrum from ZnO and explore how the value of the CEP affects the harmonic yield, drawing comparisons with the literature. This is an important verification step for understanding HHG but also for testing models at different wavelengths and time regimes. As described in Chapter 3, we used two pulse configurations, a 66 fs pulse (referred to as "short pulse") and a 100 fs pulse (referred to as "long pulse"). Both driving fields were centred ~ 3040 nm. Harmonic spectra were recorded in each case with a UV-VIS spectrometer (*Ocean Optics*).

5.2.1 Harmonic Spectra from ZnO Using the Short Pulse (66 fs)

Transmission Spectrum

Harmonics were collected on the spectrometer in the transmission geometry (see Section 3.1.2). We recorded two sets of spectra with different acquisition times for different parts of the spectrum to increase the SNR, one set with 1 s for the $200-500$ nm region and one set with 10 ms for the $500-1000$ nm region, due to the saturation of this later range with a long integration time. We rotated the crystal relative to the laser polarisation. The relative angle between the crystal orientation and the laser polarisation is referred to as θ. A spectrum was acquired every 3°. It is important to note that in this section, the spectra presented were calculated as the average spectrum over all θ. This increased the SNR, and allowed us to investigate general trends of the solid's response. In Section 5.3, the response of the solid as a function of θ (i.e. the impact of the lattice structure on HHG emission) will be presented.

Figure 5.2 shows the measured harmonic yield as a function of the laser intensity. For this discussion, we can divide the harmonics into above- and below-bandgap harmonics. The bandgap for ZnO has been measured at 3.37 eV (~ 368 nm) [204], therefore, the below-bandgap harmonics are H3-H7. The above-bandgap harmonics are H9 and H11, still within the first conduction band (CB) [216].

The detector's limited range prevented us from studying H3 as it is on the detection edge. However, the detector would allow us to detect H13 harmonic but we didn't measure any signal

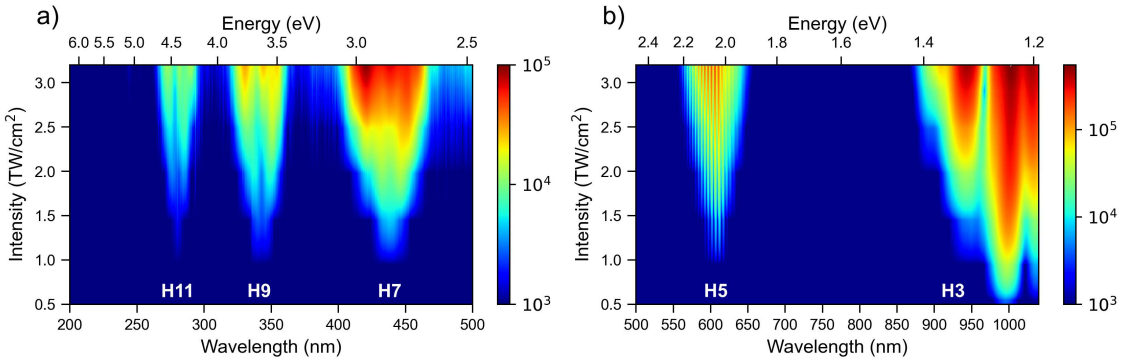


Figure 5.2: ZnO harmonic yield in transmission as a function of driving laser intensity for the short pulse with CEP = 0. (a) shows H7−H11 (200-500 nm), using an integration time of 1 s, and (b) shows H3−H5 (500-1040 nm) with an integration time of 10 ms.

for H13.

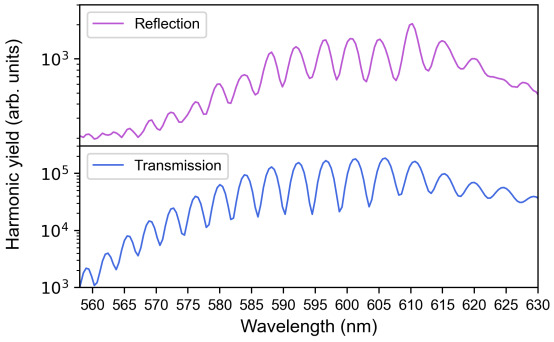
For the above-bandgap harmonics, there is a clear spectral splitting that increases with intensity. Spectral splitting has already been seen in sapphire [87], ZnO [217] and MgO [169] and has been inferred to arise from quantum path interference, a concept first developed for gases [218].

For H5, a below-bandgap harmonic, there are clear spectral fringes, given by the interference between harmonics generated at the front and back surfaces of ZnO. These fringes have been previously reported in ZnO by Hollinger *et al.* [215]. Notably, the modulations do not depend on the CEP and have been further studied by analysis of the fringe spacing. The same type of analysis is presented here in Figure 5.3a for H5, adding the data from the reflection HHG spectrum. The fringe spacing $\delta\lambda$ can be calculated according to Equation 5.1 with $d = 300\,\mu$m the thickness of the crystal.

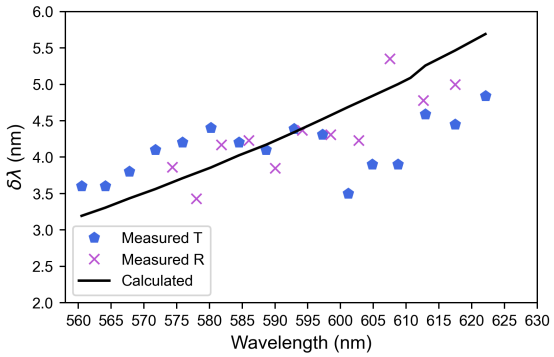
$$\delta\lambda = \frac{\lambda^2}{c\Delta t} = \frac{\lambda^2}{cd}\left(\frac{1}{v_g(\lambda)} - \frac{1}{v_g(\frac{\lambda}{5})}\right)^{-1} \tag{5.1}$$

where $v_g = \frac{c}{n}\left(1 - \frac{\lambda}{n}\frac{dn}{d\lambda}\right)^{-1}$ is the group velocity of the fundamental (wavelength λ) and the 5^{th} harmonic (wavelength $\frac{\lambda}{5}$) taken as the centre of mass of the fringe, n is the refractive index and c the speed of light. In order to calculate the fringe spacing, all the group velocities are taken from [21]. The variation of the fringe spacing $\delta\lambda(\lambda)$ is shown on Figure 5.3b. The modulation frequency changes over the spectrum, however, this is less pronounced than in Hollinger *et al.* [215] where a variation of more than 15 nm was observed. Their findings may be due to the fact that they used a thinner ZnO sample (they used 100 µm and we used 300 µm). The trend of the experimental data follows the calculation for wavelengths below ≈ 600 nm. The wide spectrum of H5 causes the modulation frequency to change over the spectrum. Similarly to Hollinger *et al.*, beyond 600 nm, the calculation does not match the experimental data anymore.

It is clear that as the intensity increases, the yield of the harmonics increases, as shown in more



(a)



(b)

Figure 5.3: Fringes of H5 from ZnO. 5.3a Spectrum in the vicinity of H5 in reflection and transmission. The spectrum exhibits fringes due to the interference of the front and back reflections of H5. 5.3b Measured and calculated spectral fringe spacing in H5.

detail on Figure 5.4. The yield is computed by integrating the signal over the bandwidth of the harmonic. The power law I^n with n the harmonic order is also plotted on the figure. We can see from these fitted power laws that the harmonics are produced from a non-perturbative process, not a perturbative one, as the scaling I^n does not apply.

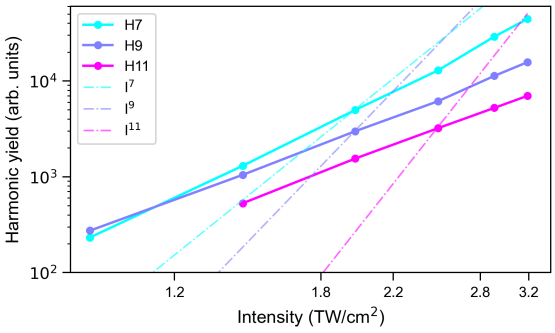


Figure 5.4: ZnO integrated harmonic yield as a function of driving laser intensity. The power laws I^n with n the harmonic order are plotted, but are significantly different to the measured harmonics.

Along with the intensity, the CEP is a key experimental parameter, allowing us to gain access to sub-cycle dynamics. Figure 5.5 displays the harmonic spectrum as a function of CEP. We observe that as the CEP increases, the central wavelength of the harmonics stays constant. We do not see

a shift towards lower wavelengths (higher energies) of each above-bandgap harmonic as had been reported in previous works in various solids (MgO [100], SiO_2 [95] and GaSe [94]).

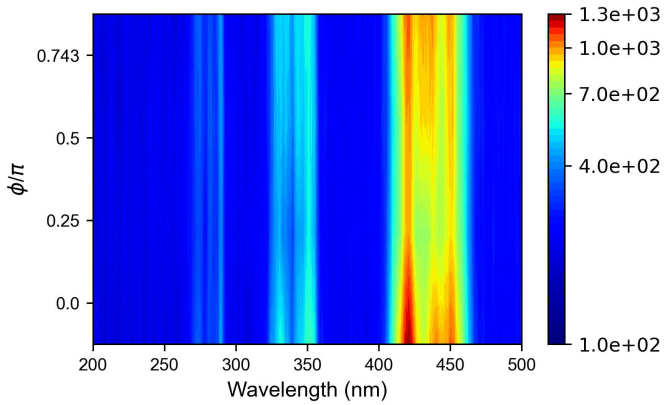


Figure 5.5: Harmonic spectrum as a function of CEP at 2.9 TW/cm^2.

Figure 5.6 displays the spectrum collected for relative CEP = 0 of H9 and H11 in transmission for each intensity. The harmonic spectrum is spectrally modulated and is not uniform on the harmonic spectral range. The harmonic peaks are broader and split as the intensity increases. We next investigate the origin of the splitting of the harmonics.

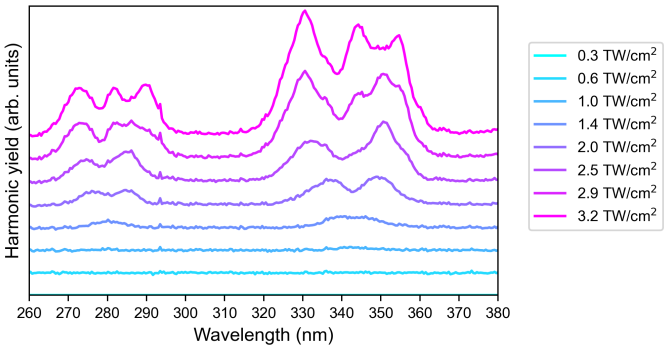
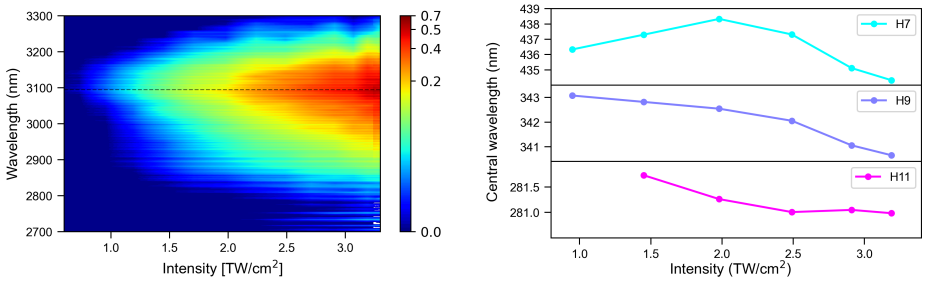


Figure 5.6: Harmonic spectrum in transmission as a function of intensity for H9 and H11.

Propagation Effects

Propagation effects [219, 107] can play a major role in the harmonic features observed. Indeed, propagation effects encapsulate all the optical phenomena that can impact the fundamental field and distort it. The main ones are SPM and phase mismatching. With SPM, different parts of the pulse accumulate different phases due to the IDRI, leading to pulse chirping. A phase mismatch between the driving laser and the generated harmonics can cause interference and distortion in the generated harmonic spectrum. It is thus imperative to consider the possibility that the observed features (splitting and broadening) arise from propagation. Hussain *et al.* [177] studied the signature of nonlinear propagation effects in ZnO with a MIR driving wavelength (2.123 µm, 85 fs). They

demonstrated that propagation effects cause the fundamental spectrum, as well as the harmonics spectra, to shift in centre wavelength towards the blue end, with a shift of at least 15 nm for the fundamental and 2 nm for the harmonics. However, Figure 5.7a displays the constant fundamental central wavelength we observed as the intensity was increased (the fundamental spectrum is taken after the ZnO sample). Figure 5.7b shows the centre of mass of H7 to H11. As the harmonic peaks are splitting, we did not use a Gaussian fit to determine the central wavelength. Instead the centre of mass was calculated as the weighted average of the spectral intensities on each harmonic range. H11 has an almost constant central wavelength while the central wavelength of H7 starts by red shifting as the intensity increases and then blue shifts by less than 1 nm compared to the initial central wavelength at low intensity. Moreover, the fundamental spectrum does not split. It therefore appears that propagation effects are not responsible for the features observed on Figure 5.6.



(a) (b)

Figure 5.7: Central wavelength shift of the fundamental and the harmonics for the short pulse. 5.7a: Fundamental spectrum of the short pulse going through the ZnO sample as a function of intensity. 5.7b: Centre of mass of H7, H9 and H11 as a function of intensity.

Furthermore, investigating the spectra in reflection allows to completely rule out propagation effects. Figure 5.8 presents the harmonic spectrum for different intensities in the reflection geometry. The spectra we recorded in reflection were weaker than in transmission as already observed [168]. This difference in harmonic yield is likely due to phase mismatching [220] and absorption. The harmonics were not intense enough to see the same cutoff as the transmission spectra. The highest harmonic detected is H5 in the reflection geometry which is below the bandgap of ZnO. The material is transparent for this wavelength ($\sim$ 606 nm) [221], inducing interference between the front and the back reflected harmonics. This interference is visible on the spectrum as fringes, similar to the transmission case. After smoothing the fringes with a Savitzky–Golay filter [222] (keeping the precision of the data without distorting the signal tendency), there is an overall trend visible in the reflection spectrum: the harmonic splits as the intensity increases. For low intensities, the red peak (above 600 nm) is stronger than the blue one (below 600 nm) but for higher intensities, the trend inverts and the blue peak of the harmonic dominates the spectrum.

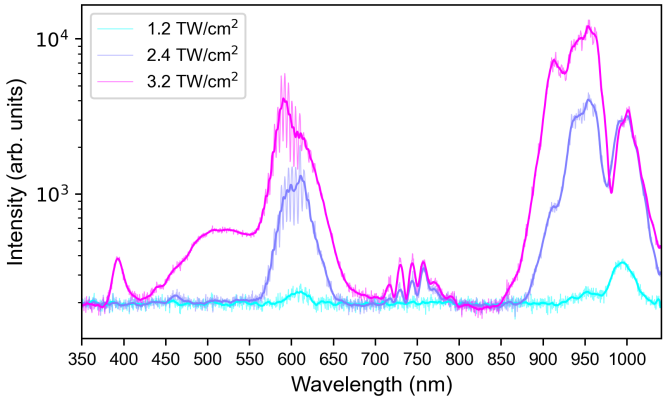


Figure 5.8: Reflection harmonic spectrum in ZnO for three driving field intensities for the short pulse and CEP value 0. The thicker line corresponds to the smoothed spectrum of the thinner line.

We can thus rule out nonlinear propagation as the origin of the variation of the harmonic spectrum as a function of intensity.

CEP Effects in Transmission Geometry

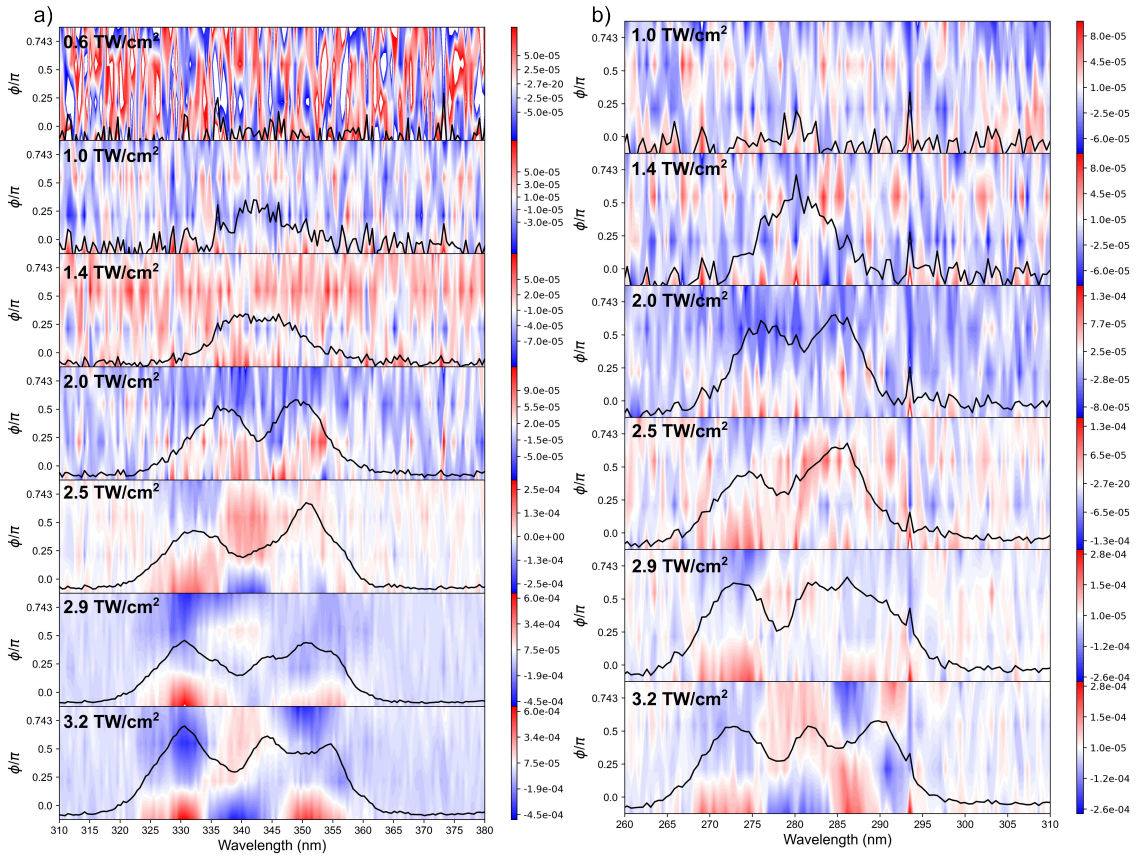


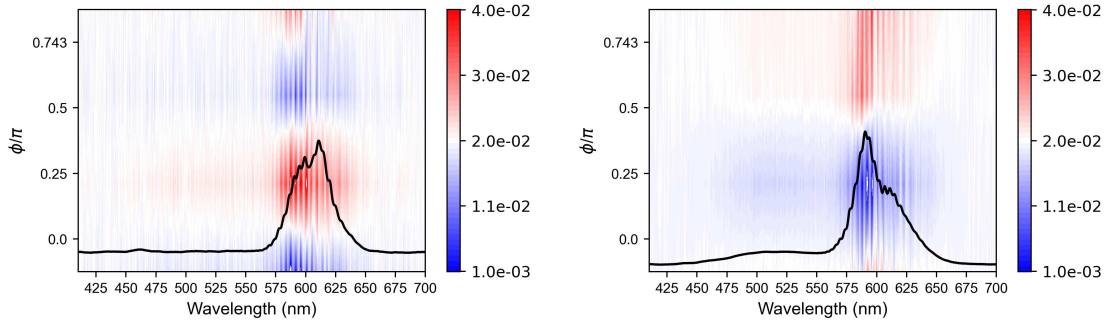
Figure 5.9: Normalised difference of the signals of H9 (a) and H11 (b) for each intensity for the short pulse. The black curve is the spectrum taken for $\phi = 0$.

We now focus on the CEP results collected in transmission geometry. In Figure 5.9, we present the normalised difference $\frac{S(\phi)-R}{S(\phi)+R}$ between the CEP-dependent harmonic spectrum, $S(\phi)$ (where the

CEP ϕ is locked and controlled), and the CEP-averaged spectrum R, employing a similar analysis to Hollinger *et al.* [215]. All the data is background subtracted. We note that within one harmonic, the different spectral regions show different CEP dependence, i.e. the normalised difference changes sign for the peaks and dips of the spectra. The phase variation looks "chequerboard like", which would imply neighbouring variations in and out of phase.

CEP Effects in Reflection Geometry

We confirm the results in transmission by applying a similar analysis to the reflection spectra. Figures 5.10a and 5.10b display the normalised difference between the CEP-dependent harmonic spectrum and the CEP-averaged spectrum for two intensities: 2.4 and 3.2 TW/cm^2. The first one displays a spectrum in which the red peak is stronger than the blue one, and the second one is dominated by the blue peak. Depending on which peak dominates (blue or red), the CEP affects differently the spectrum. Indeed, for $\phi = \pi/4$ (ϕ relative CEP value), the normalised difference is either positive or negative.



(a) (b)

Figure 5.10: Normalised difference of the signal of H5 from ZnO in reflection for 2.4 TW/cm^2 (5.10a) and 3.2 TW/cm^2 (5.10b). The "zero point" in phase is at 0.02 due to the background. The black line corresponds to the spectrum for ϕ=0.

Modelling the Electric Field for Different CEP Values

One possibility is that these observations of harmonic modulation with CEP are due to laser intensity variations. CEP effects are typically only prominent with few-cycle pulses [223]. However, work by Sansone *et al.* [224] has demonstrated that even with multiple cycles, CEP effects can still be observed, although generally less pronounced. The two pulses we had available are 6.5 cycles for the short pulse and 10 cycles for the long pulse. Their fields are shown in Figure 5.11.

The ratio of the CEP-dependent field $S(\phi)$ with the field envelope S gives an indication of the variation of the driving laser intensity with CEP. Figure 5.11 displays this value $S(\phi)/S$. In both the long and the short pulse cases, this ratio is higher than 0.99, meaning that there is less than

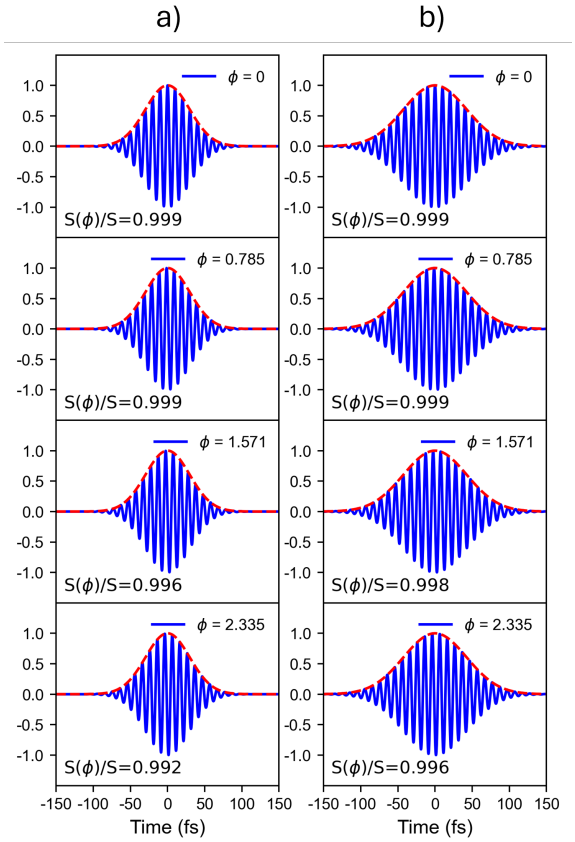


Figure 5.11: Electric field of the short pulse (a) and long pulse (b) modelled for each CEP value set experimentally. The value $S(\phi)/S$ corresponds to the ratio of the CEP-dependent field $S(\phi)$ with the field envelope S.

1 % change in intensity between pulses with different CEP. It thus appears that CEP effects do not arise from intensity variations.

5.2.2 Electron Trajectories in ZnO

This section presents a discussion on the results presented so far. As the harmonics are emitted from recombining electrons, an analysis on the paths these electrons took can explain the features seen. We note that the harmonics detected are all within the first conduction band (CB) of ZnO [216].

The splitting of harmonics in different spectral regions has already been witnessed in Al_2O_3 [87] and ZnO [217]. These works are very relevant to this experiment as they observed similar behaviours with parameters close to the ones used in this work. Wang *et al.* [217] experimentally and theoretically mapped the harmonic emission to the electron trajectories in the same crystal studied here, ZnO. Their driving wavelength was 3600 nm, placing them in the MIR range as well and the pulse duration employed was 150 fs. Their harmonic spectrum reproduced on Figure 5.12 shows the same behaviour as the harmonics collected in our case, i.e. splitting of every harmonic in multiple peaks and broadening of the harmonics. Their results were corroborated by

spectra collected in reflection, ensuring that the splitting was not due to propagation effects. Their analysis consisted of modelling the spectrum with SBEs, which include a dephasing time. As seen in Chapter 2, a short dephasing time (typically 0.2 optical cycle [79]) suppresses the contribution of long trajectories to the overall spectrum. They determined the dephasing time according to the spatial divergence of the harmonics, described as the far-field filtering method, by matching the model to the experimental result. The time they found (0.5 optical cycle) was long enough to allow the long trajectories to contribute to the overall radiation emission and thus this long dephasing time allowed the short and long trajectories to interfere, which caused the spectrum to broaden and split. We note the dephasing time is phenomenological and a construct of HHG simulations, it is not purely physical. Wang *et. al* went further in the trajectory analysis in ZnO, by controlling these trajectories with a two-colour field experiment.

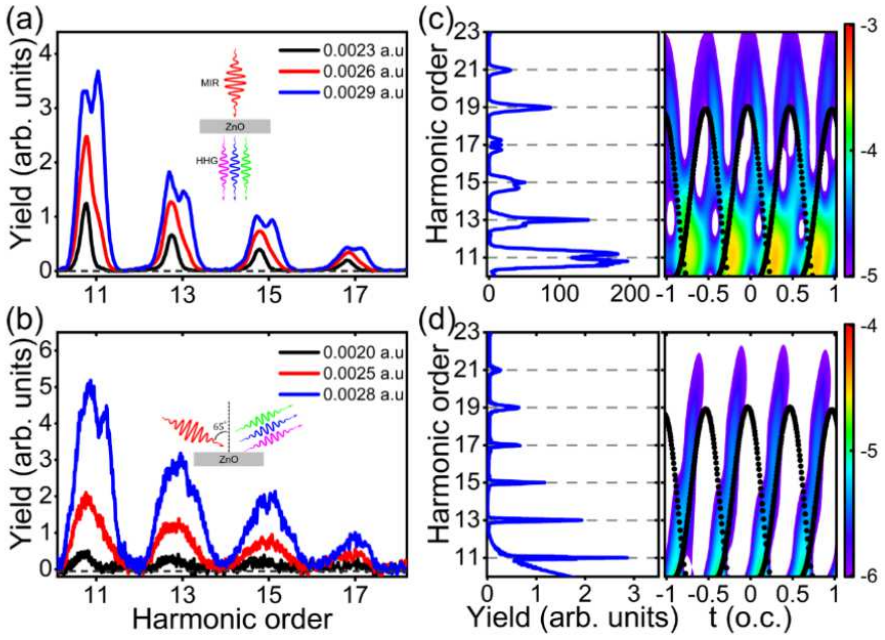


Figure 5.12: Harmonic spectra from ZnO reproduced from [217] under the terms of the Optica Open Access Publishing Agreement. Experimental harmonic spectra for different field strengths in transmission (a) and reflection (b). The inset is a schematic diagram of harmonic emission. Calculated harmonic spectra (left panel) and time-frequency-analysis (right panel) with a "long" dephasing time, allowing both type of trajectories (c) and "short" dephasing time, allowing only short trajectories to contribute (d).

Kim *et al.* mapped the spectral regions to the different trajectories in Al_2O_3, their results are reproduced on Figure 5.13. When both trajectories interfere, the splitting and broadening was clearly visible, the long trajectories dominating in the red region while the short ones dominated in the blue region. They also observed that as they increased the intensity, H7 split in two peaks, the new blue peak growing in yield to dominate the spectrum for the highest field strengths.

As the splitting and broadening of the harmonics collected in our case is very similar to these two experiments, it is plausible that the spectral broadening and splitting comes from trajectory

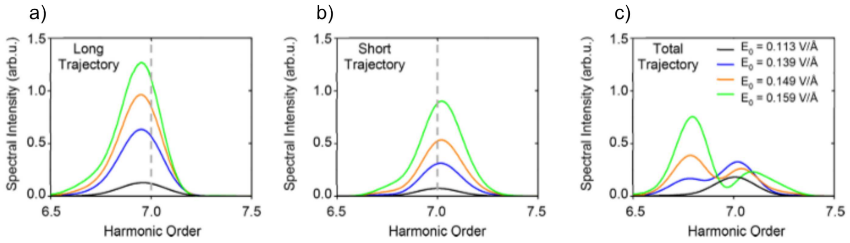


Figure 5.13: Calculated harmonic spectra from Al_2O_2 for varying electric field strengths for short trajectories (a), long trajectories (b) and long and short trajectories combined (c). Figure reproduced from [87] (authorisation in the Appendix).

interference. We know these features are not due to propagation. In the reflection geometry, the change of the dominant part of the spectrum with intensity is very similar to Kim *et al.*.

Building on these results from Wang *et al.* [217] and Kim *et al.* [87], we go further than just observing the interference of the different trajectories. We investigate how to distinguish the dominant trajectories by looking at their CEP dependence.

In Figure 5.9, we can thus attribute the different peaks within one harmonic to the contribution of short trajectories in the blue part of the spectrum and long trajectories in the red part of the spectrum. The harmonic peaks split in three, potentially indicating more complex phenomena than previously seen. We can attribute the centre peak of the spectrum to a joint contribution of short and long trajectories, the peak at the blue end is dominated by the short trajectories and the peak at the red end by the long trajectories (Figure 5.13). The most striking observation of these different peaks within one harmonic is that they do not behave the same way with CEP and we know that CEP effects indicating trajectory interferences have already been observed for such long pulse durations [224]. For H9, the two ends of the spectrum have the same sign of change with CEP, whereas the central part differs, thus allowing a differentiation between the contributions of the trajectories. In H11, the behaviour with CEP is even more complex, showing four regions that have different CEP modulations, reflection of a variation of the trajectory contributions. The peaks and the dips due to the splitting do not show the same harmonic yield for a same CEP value, i.e. the normalised difference changes sign. Depending on the CEP value, it is therefore possible to distinguish which type of trajectories dominates the HHG process.

This work lays only the foundation but it is clear that the CEP presents itself as a strong tool to distinguish the different trajectory contributions, allowing for a deeper understanding of the involvement of the electron paths within the solid bands. Sansone *et al.* [225] have already investigated in gases the role of the CEP on the trajectories and seen that long trajectories were more sensitive to CEP changes, even in the muticycle regime.

5.3 Anisotropic Behaviour of HHG from ZnO

5.3.1 Anisotropic Response of ZnO to a Strong Field

In this section, we now differentiate the HHG emission depending on the bond direction to identify the role of the lattice in the HHG process. In order to understand which bonds contribute the most to the harmonic features visible, we rotated the crystal relative to the laser polarisation. The relative angle θ between the crystal orientation and the laser polarisation is the parameter used from now on to describe the bonds along which the electrons can move along in a real-space picture.

Figure 5.14 displays the total harmonic spectrum over two subplots corresponding to the two different integration times. The lower-order harmonics (H3-H7) do not present any rotational dependence. However, for higher-orders (H9-H11), a rotational dependence appears, especially for H11. The rotational dependence is periodic and within each harmonic (H9 and H11), the periodicity of the signal depends on the spectral region of the harmonic considered.

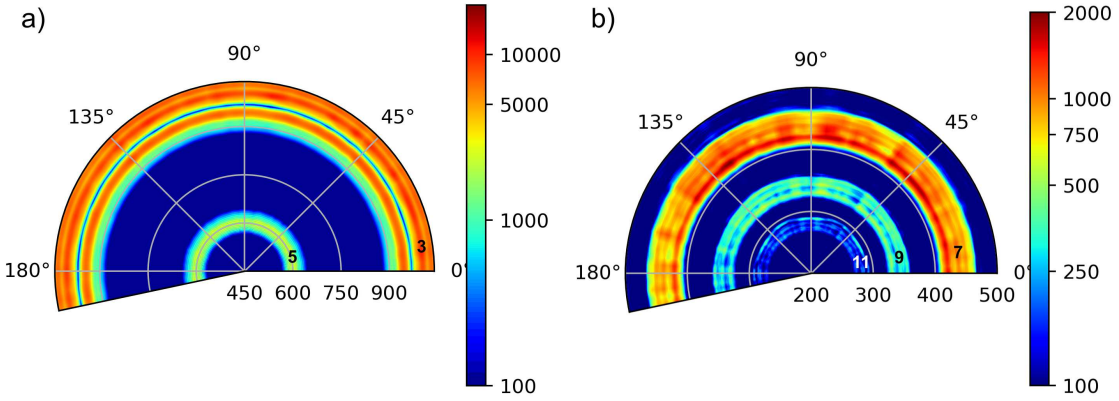
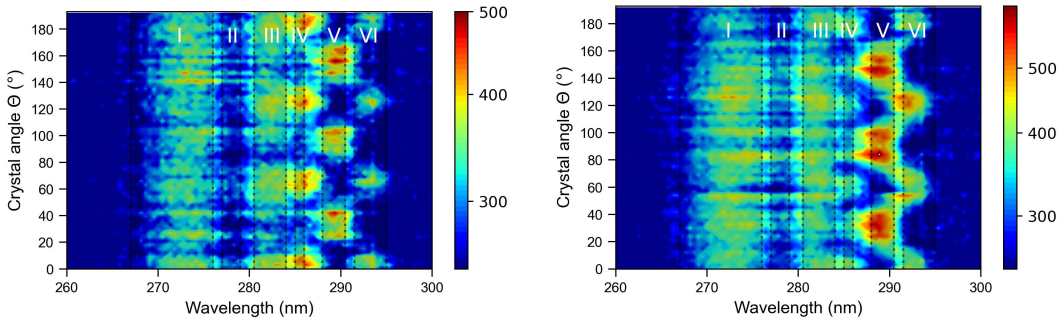


Figure 5.14: Wavelength-resolved harmonic spectrum in polar projection in ZnO. The radial axis is the wavelength axis (nm) and the harmonic orders are labelled. The angle corresponds to the relative angle between the laser polarisation and the crystal orientation. a) H3 and H5, acquired with 1 ms integration time. b) H7, H9 and H11 acquired with 1 s integration time. The intensity of these plots is 3.2 TW/cm^2.

Indeed, we investigate in more details H11. Figure 5.15 displays the same data as Figure 5.14 but zoomed in on the spectral region corresponding to H11 and in planar projection for the two highest intensities, 2.9 TW/cm^2 and 3.2 TW/cm^2. The different spectral regions within this harmonic are labelled I to VI. These regions have different dependences of the harmonic yield as a function of the crystal angle.

In order to understand where these spectral regions arise from, we plot the spectra of the same regions I to VI in Figure 5.16. It is clear that the rotational dependence of the harmonic yield is directly linked to the peaks and dips of the harmonic spectrum. These features of the harmonic spectrum have been linked to the electron trajectories in Section 5.2. Therefore, we can conclude



(a) (b)

Figure 5.15: Rotational dependence of the harmonic yield of H11 from ZnO for 2.9 TW/cm^2 (5.15a) and 3.2 TW/cm^2 (5.15b). The different spectral regions are labelled.

that the electrons travelling more or less far in the lattice (long and short trajectories) are directly affected by the crystal lattice layout in real space (crystal angle).

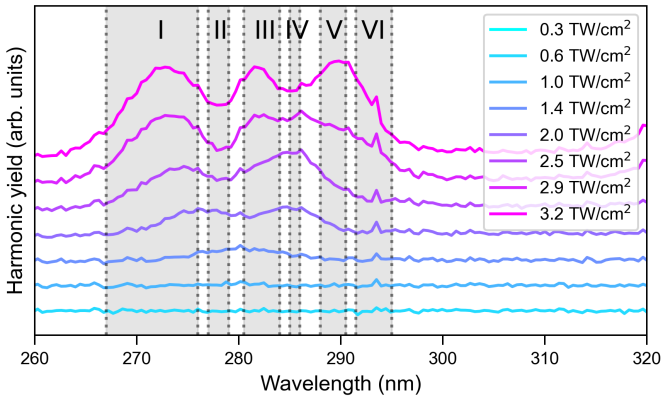


Figure 5.16: Spectrum of H11 from ZnO highlighting the same spectral regions as Figure 5.15 for increasing intensities.

Figure 5.16 shows that the spectral modulation depends on the intensity. We thus plot the integrated spectral yield of the three regions of H11 that present the strongest rotational modulation as a function of crystal angle θ for each intensity on Figure 5.17. Below 2.9 TW/cm^2, even though the spectral modulation appears, there is no rotational dependence. At 2.9 TW/cm^2, the rotational modulation is strong and seems periodic, with a 3 peaks overs 180 °, corresponding to a 6-fold symmetry, matching the hexagonal structure of ZnO. However, at 3.2 TW/cm^2, region IV loses its periodicity. Region III does not seem to have a periodicity for any intensity. We will thus analyse in more detail this spectral dependence for the two highest intensities.

5.3.2 Fourier Analysis of the Harmonic Spectrum

H11 presents the strongest anisotropy and this anisotropy varies across its spectrum. We now investigate how the different spectral regions, which have been linked to trajectory contributions, behave

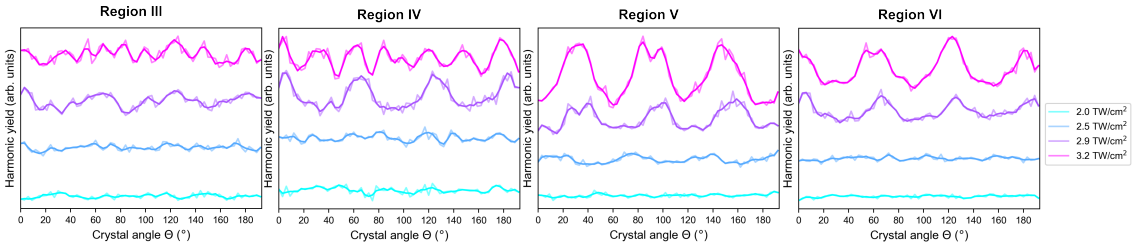


Figure 5.17: Integrated spectral yield of regions III, IV, V and VI of H11 (from Figure 5.15) as a function of crystal angle θ for each intensity. These regions are selected as they present the strongest rotational modulation as a function of θ.

depending on the bonds the electrons propagate along (θ). A technique developed by Gertsvolf *et al.* [54] introduces Fourier analysis to understand the anisotropy of nonlinear absorption.

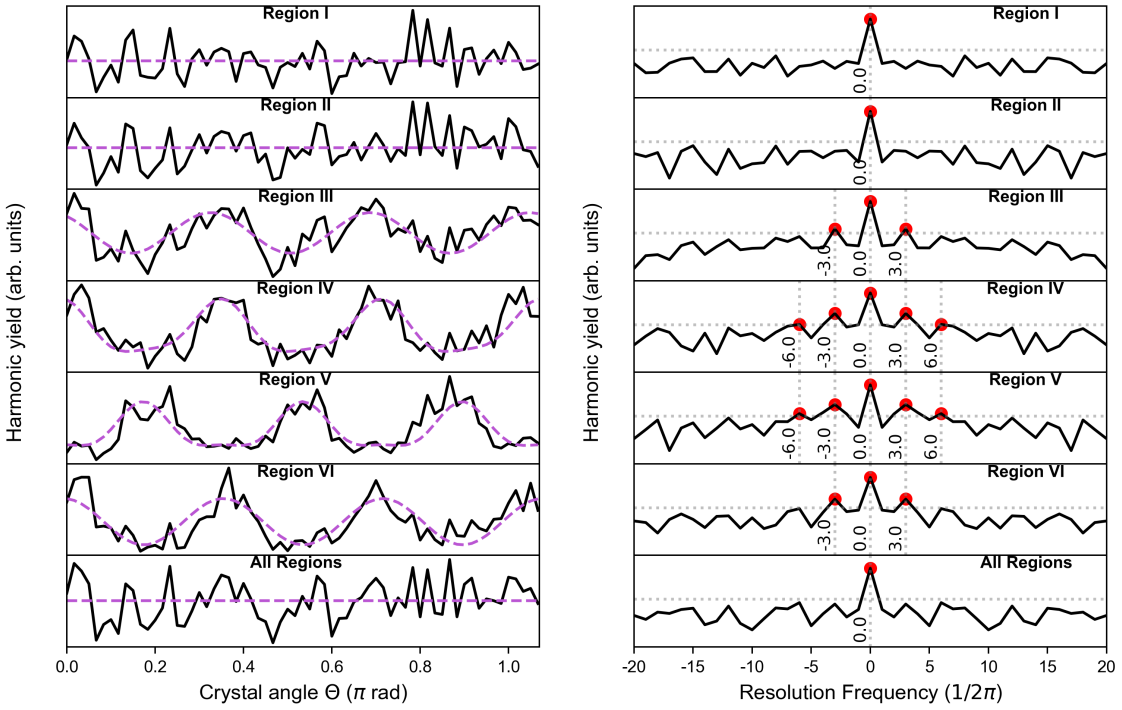


Figure 5.18: Fourier analysis of the yield of H11 as a function of crystal orientation and for the different spectral regions. Left column: the black line represents the experimental harmonic yield as a function of crystal angle and the dashed purple line corresponds to the inverse Fourier transform of the right column only taking into account the frequency peaks above 2 % of the offset frequency peak centred at 0. Right column: Amplitude of the Fourier transform of the experimental data of the left column (real part). The red dots represent the peaks above 2 % of the peak at frequency 0. The y-axis is in log scale. The intensity of the driving pulse for this set of data is 2.9 TW/cm^2.

We employ a similar technique by applying a Fast Fourier Transform (FFT) on the data corresponding to the harmonic yield as a function of crystal orientation. The results are presented in Figure 5.18. The x-axis of the plots in the right column corresponds to the resolution frequency. The curves for the different regions display peaks corresponding to the dominant frequencies in the data. Peaks at frequencies $f = n$, where n is an integer, correspond to a n-fold symmetry of the crystal. The height of the different peaks reflects the strength of the modulation. When directly

applying the Fourier transform to the data, we expect a peak at $f = 0$ corresponding to the offset of the data that has a sinusoidal shape. In order to distinguish the dominant frequencies from the noise level, we set a threshold value in amplitude. This threshold is set as 2 % of the peak at $f = 0$.

Figure 5.18 shows multiple peaks of the Fourier amplitude at $f = 3$ and $f = 6$ (frequencies multiples of 3) for regions III, IV, V and VI for an intensity of 2.9 TW/cm^2. Regions I and II along with the total spectral width of H11 show no frequency peaks, meaning that the harmonic yield is not dependent on the anisotropy of the solid. For the regions where a peak at frequency 3 is present, we can deduce a six-fold symmetry (3 oscillations over π). The red part of the spectrum (280−295 nm region) is sensitive to the crystal orientation while the anisotropy of the full harmonic's bandwidth is washed out by the angle-independent blue part of the spectrum. The red part above 280 nm is dominated by the long trajectories as detailed previously. The variation of the yield of the harmonic with crystal orientation is a direct signature of the trajectories.

The rules on crystal symmetry dictate that a 6-fold symmetry is the highest possible [226]. Hence, the peaks at frequency 6 in regions IV and V could be an evidence of the electrons travelling further than the first BZ and across multiple unit cells in the crystal.

For comparison, Figure 5.19 shows the same analysis as Figure 5.18 for a higher intensity (3.2 TW/cm^2). The two columns correspond to different threshold values (2 % and 4 % of the peak at $f = 0$) to detect the peaks. They both show similar results except for region III and V. Indeed, region III shows a peak at frequency 3 for a low threshold value (2 %) and no peak for a higher threshold (4 %). On Figure 5.17, it is clear there is no periodicity for the highest intensity (3.2 TW/cm^2) but below this intensity, the periodicity is unclear and the Fourier analysis refines these observations by allowing to see the frequency peaks and conclude on a 6-fold symmetry. It is possible that the higher frequency peaks ($f > 6$) are due to laser fluctuations, air currents or vibrations, as it is probably the case for region V. The observation of the presence of different peaks depending on the threshold in regions III and V shows the need to select carefully the threshold value to have consistent results. Only three regions show physically real modulation corresponding to a 6-fold symmetry matching the hexagonal structure of ZnO, regions III, V and VI. As already noted in Figure 5.17, region IV has no obvious periodicity, and therefore does not show any Fourier peaks.

The modulation of the harmonic yield with high intensity (3.2 TW/cm^2) is different to the modulation for lower intensity (2.9 TW/cm^2). Furthermore, we know that the maximum crystal momentum depends on the field strength, i.e. intensity (Equation 2.31). It is therefore plausible that the trajectory is intensity-dependent, causing it to go through different lattice sites and explaining the change of anisotropy with intensity.

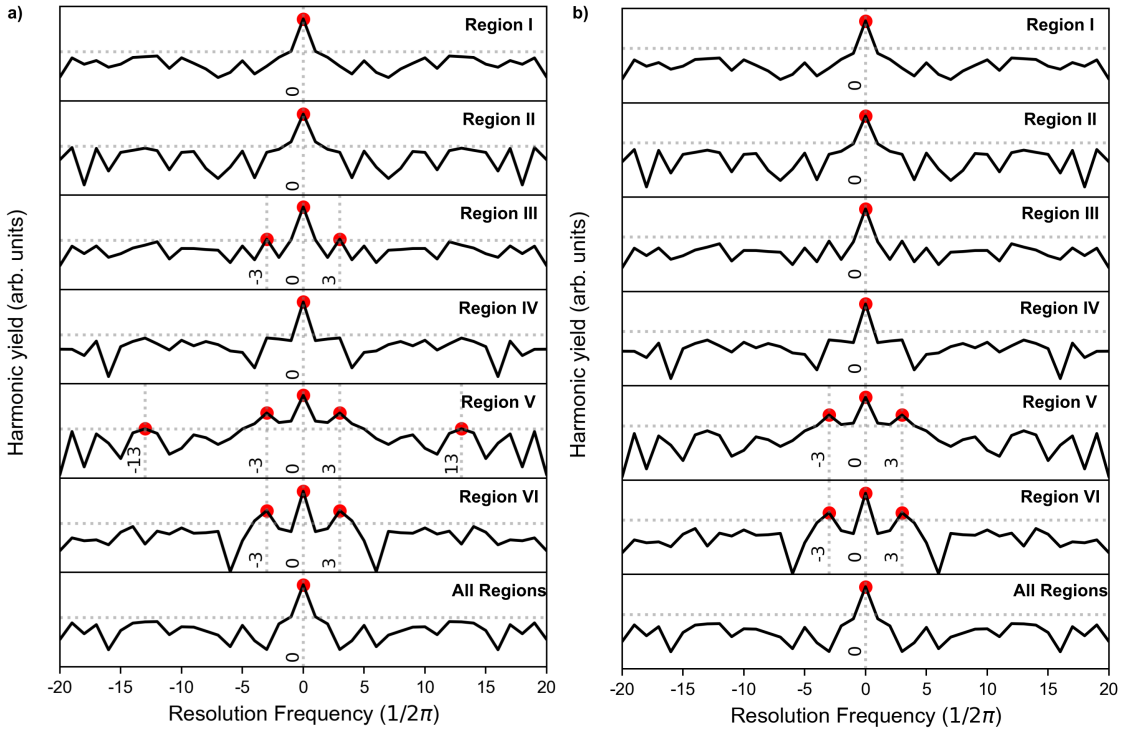


Figure 5.19: Fourier analysis of the yield of H11 as a function of crystal orientation and for different spectral regions. The black curve corresponds to the amplitude of the Fourier transform of the experimental data of Figure 5.15b (real part). The red dots represent the peaks above 2 % (a) and 4 % (b) of the peak at frequency 0 . The intensity of the driving pulse for this set of data is 3.2 TW/cm^2.

5.3.3 Anisotropic Response Depending on the CEP

Similar to Figure 5.9, Figure 5.20 shows the spectrum at CEP $\phi = 0$ plotted on the colormap of the normalised difference between the signal obtained at a given CEP and the CEP-averaged signal for different crystal angles θ. Depending on the crystal orientation, i.e. the crystal bond direction, the signal strength is modulated and the dependence of the normalised difference with the CEP drastically varies. H9 is more sensitive to the CEP variation and both H9 and H11 follow the same pattern for each crystal angle θ.

The harmonic yield of H9 shows a weaker anisotropy than H11. The Fourier analysis is not shown as the results did not yield any conclusion. However, the study of the CEP dependence provides another tool to study the anisotropy of harmonics. The angles chosen are muliples of 60 °. If there would be a 6-fold or 3-fold symmetry, we would see a repetition of the CEP pattern. However, no such repetition is present. Nevertheless, the harmonic yield still exhibits dependence on the CEP, showing the potential of the CEP as a tool to probe a simpler crystal structure. More work (including theoretical modelling) would be required to build on these preliminary results.

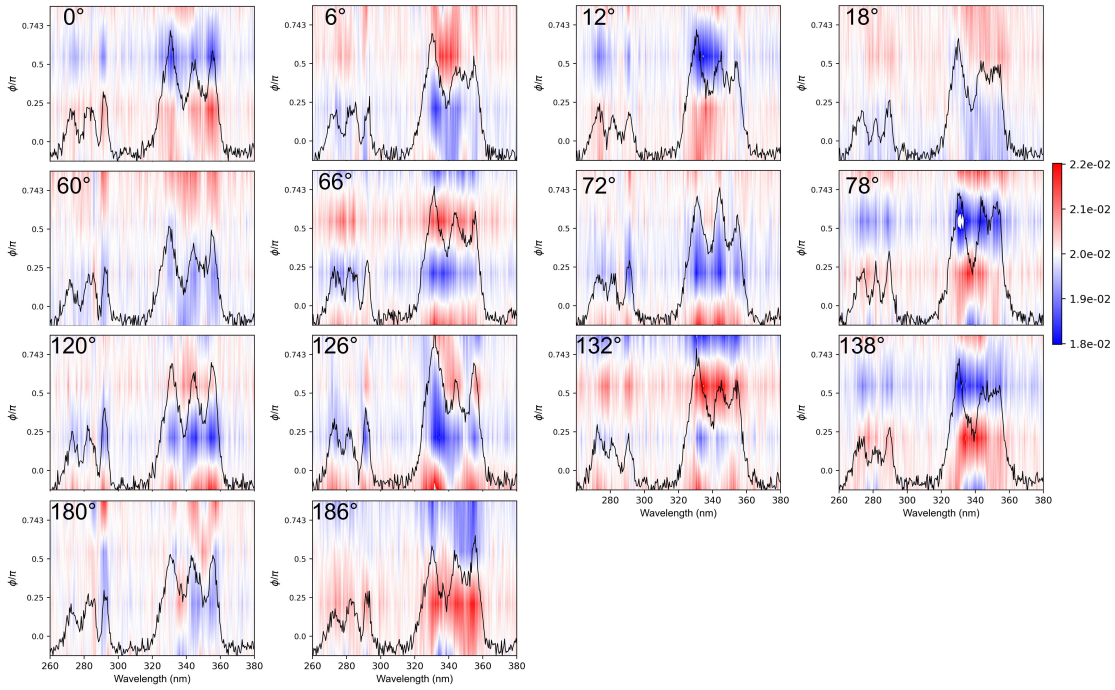


Figure 5.20: Normalised difference of the signals of H9 and H11 at 3.2 TW/cm^2 for different crystal angles θ. The black curve is the spectrum taken for $\phi = 0$.

5.4 Comparison of HHG Features Between a 6.5 Cycle and a 10 Cycle Pulse

In Chapter 3, the two pulses used for the experiments were introduced (Figure 3.16) both centred around $\sim$ 3040 nm. Figure 5.21 shows the spectrum of H5 to H13 for the long pulse (top) and the short pulse (bottom). For H7 produced with the long pulse, the emission around $\sim$ 400 nm starts at very low intensity and is attributed to Photoluminescence (PL) of the sample [227].

With the long pulse, H7 to H11 do not broaden and split (contrary to what has been observed in the previous section) and the measured cutoff is higher; the last harmonic detected is H13 for the long pulse and H11 for the short pulse. We are limited by the range of our spectrometer which prevents the detection of harmonics above H13. The observation of a higher cutoff with a longer pulse contradicts the results of Gholam-Mirzaei *et al.* [213]. In this work, they also studied HHG from a 300 µm ZnO sample with a 3.8 µm driver and compared the HHG spectrum from a 90 fs pulse (7 cycles) and a 35 fs pulse (3 cycles). They attributed the difference in harmonic behaviour to the different intensities of the long and the short pulse, which were 0.6 and 1.9 TW/cm^2, respectively. Yet, we have seen that the HHG process is strongly dependent on intensity. We have similar intensities for our short and long pulses (0.3−3.2 TW/cm^2), allowing to make a valid comparison between these pulses, revealing that the difference in our case is not due to intensity effects. Moreover, in our experiment, the spot size is similar in both cases ($\sim$ 29 µm). The yields of

H5−H7 are within the same order of magnitude for the long and short pulses. However, the yields of H9−H13 are greater for the long pulse despite similar laser intensities, contradicting the explanation of Gholam-Mirzaei *et al.* [213]. This is also a different behaviour to HHG in gases, for which shorter pulses have proved to extend the cutoff [228, 152]. In solids, the higher cutoff of the long pulse could be explained by the dephasing effect that prevents all the trajectories from recombining [79].

However, we see similar trends to Gholam-Mirzaei *et al.* [213] with a stronger broadening of the harmonics with the short pulse. They link the broadening of the harmonics with the short pulse to a "temporal gating of the HHG process".

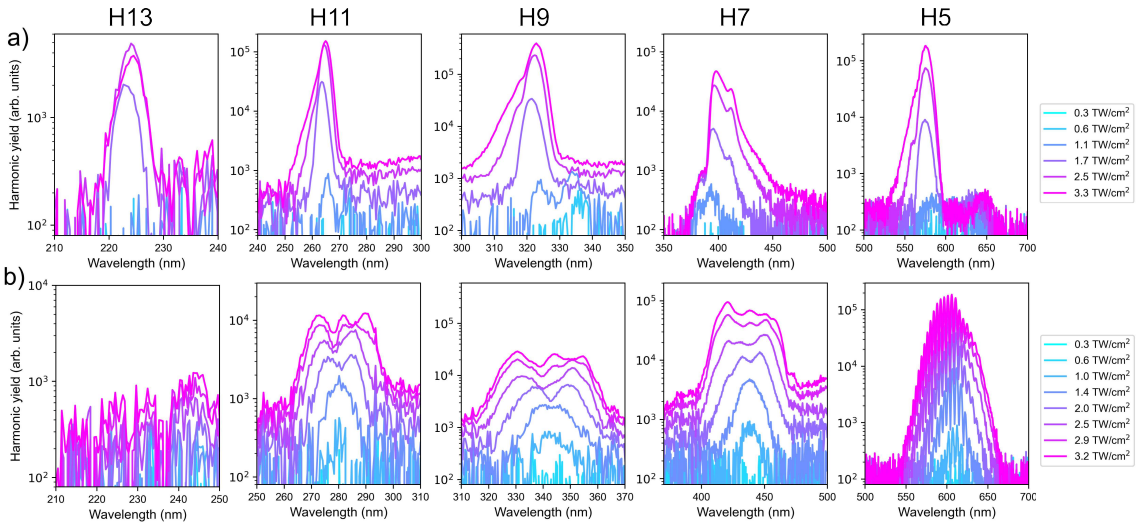


Figure 5.21: Comparison of the harmonic spectra from ZnO from a 10 cycle pulse (a) and a 6.5 cycle pulse (b).

In order to fully compare the HHG emission from ZnO with two pulse durations, the harmonic spectra as a function of the crystal angle θ is plotted in Figure 5.22. For the long pulse, the harmonics are almost independent of sample rotation. This is further demonstrated by the Fourier analysis, where there were no obvious peaks corresponding to a crystal symmetry. Just below $\sim$ 400 nm (near the bandgap), the blue edge of the harmonic is very sharp, confirming that the emission in the blue end of the spectrum of H7 is due to PL [227]. The broadening of all harmonics is clearly visible on this figure ($\sim$ 15 % broadening).

It is thus clear that the harmonics from the short and long laser pulses behave very differently as the intensity increases and with crystal angle θ. The dynamics of the long pulse do not allow for trajectory interference. In the previous section, we focused on H11 and saw that the blue end of the spectrum, corresponding to the short trajectories, do not depend on the crystal orientation. H11 generated from the long pulse is fully orientation-independent. We can thus postulate that the harmonics from the long pulse may only include the short trajectories.

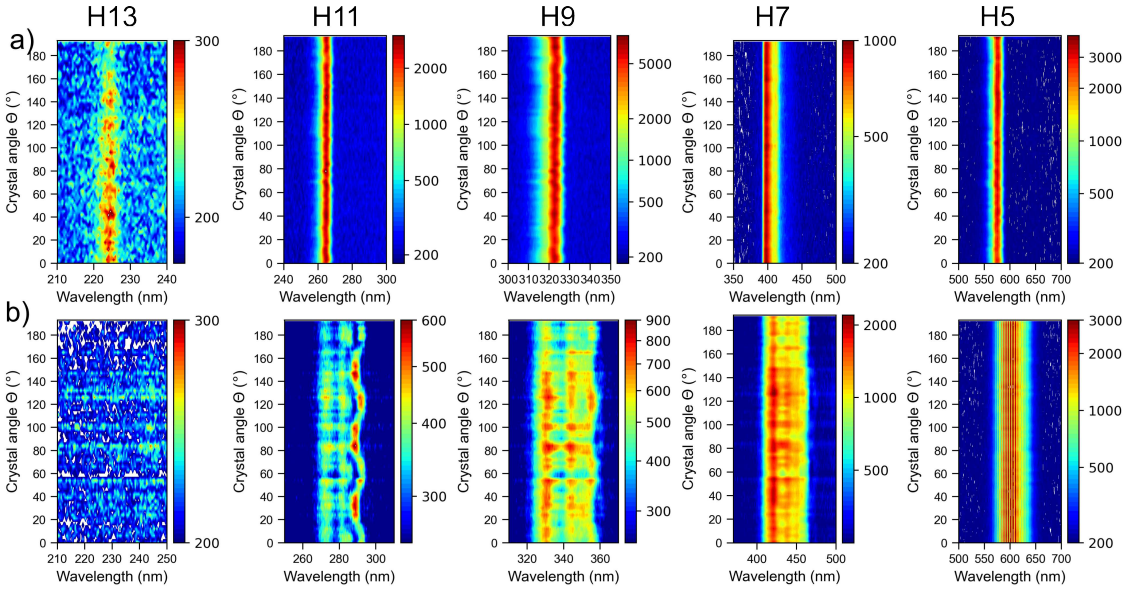


Figure 5.22: Comparison of the harmonic spectra as a function of crystal angle θ from ZnO from a 10 cycle pulse (a) and a 6.5 cycle pulse (b).

5.5 Conclusion

The measurements and analysis presented suggest that the trajectories of the recombining electrons in HHG from ZnO are directly influenced by the laser CEP. We have demonstrated that these trajectories are evident in the harmonic spectrum and that the CEP can serve as a spectroscopic tool to access the trajectories and potentially control them. The CEP dependence could thus provide a new tool in solid HHG research for general conclusions instead of case by case studies. Further theoretical modelling is still required to fully understand these dynamics.

Chapter 6

Study of the Efficiency of HHG in Different Samples

We present in this chapter a comparison of harmonic yield between MgO, Al_2O_3 and CaF_2 samples in the NIR driving field regime as well as between ZnO, ZnSe, GaN, $SrTiO_3$ and SiC samples in the MIR driving field regime.

6.1 Motivations for Sample Efficiency Comparison

The results presented so far in this work have been focused on the spectroscopic nature of HHG in solids. However, HHG is also an interesting potential source of attosecond pulses of XUV radiation [73]. Indeed, using gases as the generating medium, attosecond pulses have been successfully produced for two decades (and this recently won the Nobel prize) [229], allowing time-resolved studies, e.g. transient absorption spectroscopy [230]. The study of time-dependent electron dynamics in matter is improved by the use of an isolated attosecond pulse [231].

HHG in solids has also proved to be a source of isolated attosecond pulses [133, 12, 232], showing the future potential of solids as a medium for HHG to resolve temporal dynamics in a pump-probe experiment [233]. The condensed phase enables to produce ultrashort pulses in a compact setup and more efficiently than in gases, i.e. for lower intensities.

HHG has been undertaken in a wide range of solid samples such as bulk crystals [116], nanostructured samples [211, 234, 16, 235], 2D materials [236, 237, 238] and epsilon near-zero materials [239]. Each of these works has focused on a specific aspect of the harmonics, such as their behaviour with driving field properties, i.e. CEP, ellipticity, polarisation or their temporal dynamics, e.g. pump-probe scheme. These investigations have given valuable insights into the strongly driven electron dynamics in those samples and their potential applications. While previous work has fo-

cused on the understanding of a particular material, there has been little work investigating how to optimise the efficiency and cutoff of an HHG source. A comparison of cutoff in different samples as a function of wavelength is given in [104]. Nonlinear absorption has been studied as a function of intensity and crystal angle in [173]. However, no comparison of harmonic yields form different samples has been undertaken, to our knowledge. From the perspective of future applications, comparing the yield from different samples for the same driving field parameters is important to narrow down the choice of samples from the almost infinite pool of choices, as theory is unable to reliably predict a high cutoff or efficiency.

We compare two sets of samples: (i) wide bandgap dielectrics (7.8−11.8 eV), and semiconductors of different bandgaps ($\sim$ 3 eV), for the same laser intensities and pulse durations, and the same detection parameters, enabling a comparison independent of any external parameter.

6.2 Background on the Samples Under Study

6.2.1 Dielectrics Studied

Chapter 4 detailed HHG in MgO for different pulse durations. Focusing on the two extreme regimes, i.e. long pulse of 30 fs and short pulse of 5 fs, here we compare the harmonic yield of MgO with two other wide bandgap dielectrics, α-Al_2O_3 and CaF_2. These three samples are optically transparent in the range of the generated harmonics (10−50 eV, see Figure 6.1) which makes them ideal candidates for the generation of XUV. Both α-Al_2O_3 and CaF_2 have already been shown to produce HHG [10, 179]. Their relevant properties are shown in Table 6.1. These three samples have ionic bonding, meaning that they have a high gradient of the electron-nuclei potential, predicted to be suited for efficient HHG [58].

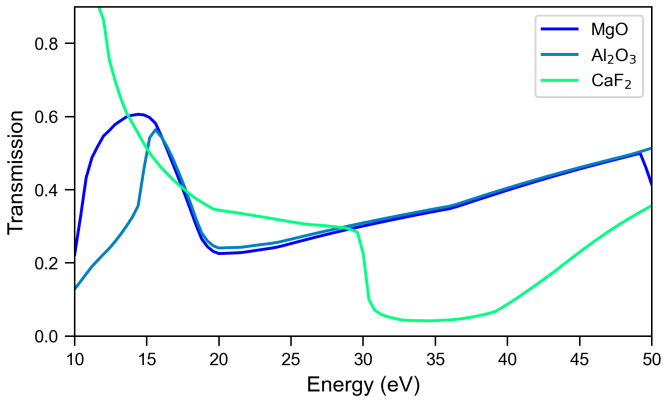


Figure 6.1: Transmission curve of MgO, α-Al_2O_3 and CaF_2 for a sample length of 20, 15 and 20 nm respectively. Those length values correspond to the mean absorption length found to be the value at which the mean transmission over the harmonic range is $1/e$. The data is from [182].

Property	MgO	α-Al_2O_3	CaF_2
Orientation	001	0001	001
Sample Thickness (µm)	100	100	200
Crystal structure	cubic	hexagonal	cubic
Minimum Bandgap (eV)	7.8 [171]	8.9 [240]	11.8 [241]
Lattice Constant (Å)	4.2 [165]	$a = b = 4.73$ $c = 13$ [242]	5.46 [241]
Nearest Neighbour Distance (Å)	2.1 [165]	2, 1.9 [165]	4.73
Effective Electron Mass ($1/m_0$)	0.35 [165]	0.4 [240]	–
Nonlinear Refractive Index n_2 (m^2/W)	3.9×10^{-20} [243]	$3.3–2.8 \times 10^{-20}$ [244]	1.8×10^{-20} [245]

Table 6.1: Crystal properties of MgO, α-Al_2O_3 and CaF_2

6.2.2 Semiconductors Studied

The samples chosen for the MIR comparison are, apart from ZnO previously studied in Chapter 5, ZnSe, SiC-4H, GaN and $SrTiO_3$. Their properties are described in Table 6.2. These samples have small bandgaps that match well the driving photon energy and their bandgaps are all similar (2.7−3.75 eV), allowing us to draw conclusions on the relevance of the driving-wavelength-to-bandgap-ratio as a measure of HHG efficency [246]. They all present an ionic-covalent bond type. Some of these samples have already been used as an HHG source. Indeed, previous measurements in ZnSe have demonstrated the possibility to reconstruct the band structure with below-bandgap harmonics [96] while GaN has been used by Seres et al. [247] to study the variation of harmonic yield with focus position. To our knowledge, no HHG study has been reported in $SrTiO_3$ nor SiC. However, they possess bandgaps (3.75 and 3.23 eV, respectively) in between ZnSe and ZnO, making them suitable to compare the HHG yield between the samples.

Property	ZnO	ZnSe	SiC-4H	GaN	$SrTiO_3$
Orientation	0001	001	0001	0001	001
Sample Thickness (µm)	300	300	100	300	200
Crystal Structure	wurtzite	zincblende (cubic)	wurtzite	wurtzite	cubic perovskite
Minimum Bandgap (eV)	3.37 [204]	2.70 [248]	3.23 (indirect) [249]	3.42 [250]	3.75 (indirect) [251]
Excitonic binding energy E_b (meV)	60 [252]	20 [253]	20 [254]	26 [252]	–
Lattice Constant (Å)	$a = 3.2$ $c = 5.2$ [255] $u = 0.4$	5.7 [256]	$a = 3.1$ $c = 10.1$ [249]	$a = 3.2$ $c = 5.2$ [257] $u = 0.4$	$a = 3.9$
Nearest Neighbour Distance (Å)	1.80 [255]	2.45	1.90 [258]	1.90 [257]	1.95
Effective Electron Mass ($1/m_0$)	0.24 [255]	0.17 [259]	0.29 [249]	0.34 [260]	10 [261]

Table 6.2: Crystal properties of ZnO, ZnSe, SiC-4H, GaN and $SrTiO_3$.

A comparison between a bulk and a thin film ZnO sample was also undertaken. Indeed, an alternative to bulk samples is the use of thin films which mitigate propagation effects. A few works have reported the use of thin films in HHG experiments with ZnO [209], WSe_2 [262], ReS_2 [263] and VO_2 [233]. Hollinger *et al.* [210] have made a comparison between bulk and thin film samples of ZnO. They studied the response of these two samples under the illumination of a strong MIR field and varied the ellipticity of the field in order to understand the electronic process responsible for HHG as well as Photoluminescence (PL). When the solid absorbs a photon, in addition to

harmonic generation, PL emission can occur, which is an incoherent process [264].

The two sample studied in this chapter are on the one hand, the same sample as in Chapter 5, 0001 orientation, 300 µm thick and on the other hand, a thin film ZnO sample (500 nm) on a sapphire substrate (500 µm).

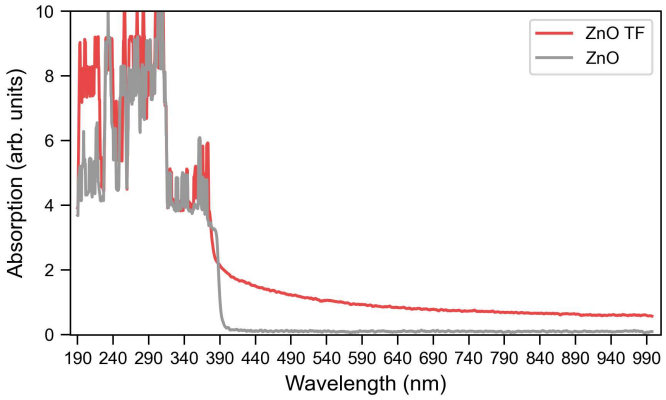


Figure 6.2: Absorption spectra of bulk ZnO and a thin film sample of ZnO measured with a UV-VIS spectrometer.

We have measured the absorption spectrum of both samples using a UV-VIS spectrometer (*Cary 60 UV-Vis, Agilent Technologies*), shown in Figure 6.2. The spectrometer could not detect any signal for wavelengths below ~ 390 nm, explaining the noise-like behaviour of the data. The samples show similar behaviour: they are transparent below the bandgap and the absorption saturates above the bandgap. However, the thin film still absorbs below the bandgap, contrary to what could be expected. This observation could be explained by defects in the structure or an amorphous crystalline structure.

6.3 Harmonic Spectra Comparison From a NIR and a MIR Driving Pulse

6.3.1 Comparison of Harmonic Emission From a NIR Long 30 fs and a Short 5 fs Driving Pulse in Transmission

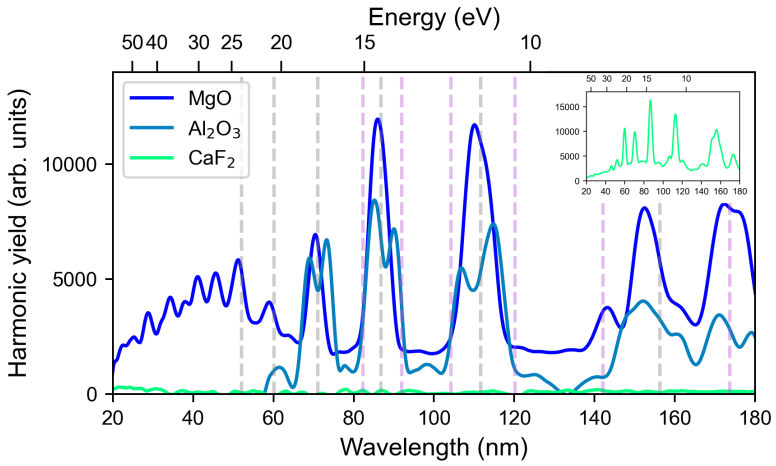


Figure 6.3: Harmonic spectra of MgO, α-Al_2O_3 and CaF_2 at 9 TW/cm^2 for a 30 fs pulse at 780 nm. Inset: CaF_2 spectrum at 23 TW/cm^2. The grey lines correspond to the harmonic peak positions and the purple lines correspond to the second order peaks. Only one second order peak is visible at $\sim$ 182 nm, corresponding to the second order of the ninth harmonic.

Figures 6.3 and 6.4 show the harmonic spectra of MgO, α-Al_2O_3 and CaF_2 with a 780 nm driving field for the long 30 fs pulse and the short 5 fs pulse respectively. The data acquisition process is the same as in Chapter 4, i.e. 5 spectra of 5 s integration time, each averaged together and background subtracted (laser illuminating the MCP, no sample in the beam path). The samples are compared for the same intensities. The two figures show different spectral features and different relative yields.

In the long pulse case, at 9 TW/cm^2, the cutoff of MgO is much higher than for the two other samples, reaching the 31st harmonic. The cutoff of α-Al_2O_3 is at the 13th order while CaF_2 shows no harmonics for this intensity. The inset in Figure 6.3 displays the harmonic spectrum from CaF_2 at 23 TW/cm^2, showing that CaF_2 produces harmonics with this driving pulse, up to the 17th order at $\sim$ 30 eV but the harmonics appear for higher intensities than for MgO and α-Al_2O_3 and the cutoff is extended. The CaF_2 sample was inspected visually and no damage occurred at 23 TW/cm^2. For the long pulse, MgO is the most efficient sample (at 9 TW/cm^2), i.e. the sample that shows the strongest harmonic yield. We can make the following ranking based on these measurements of efficiency and cutoff: MgO > α-Al_2O_3 > CaF_2 for the 30-fs pulse at 780 nm and 9 TW/cm^2. This ranking follows the order of the bandgap: $E_{g-MgO} < E_{g-Al_2O_3} < E_{g-CaF_2}$.

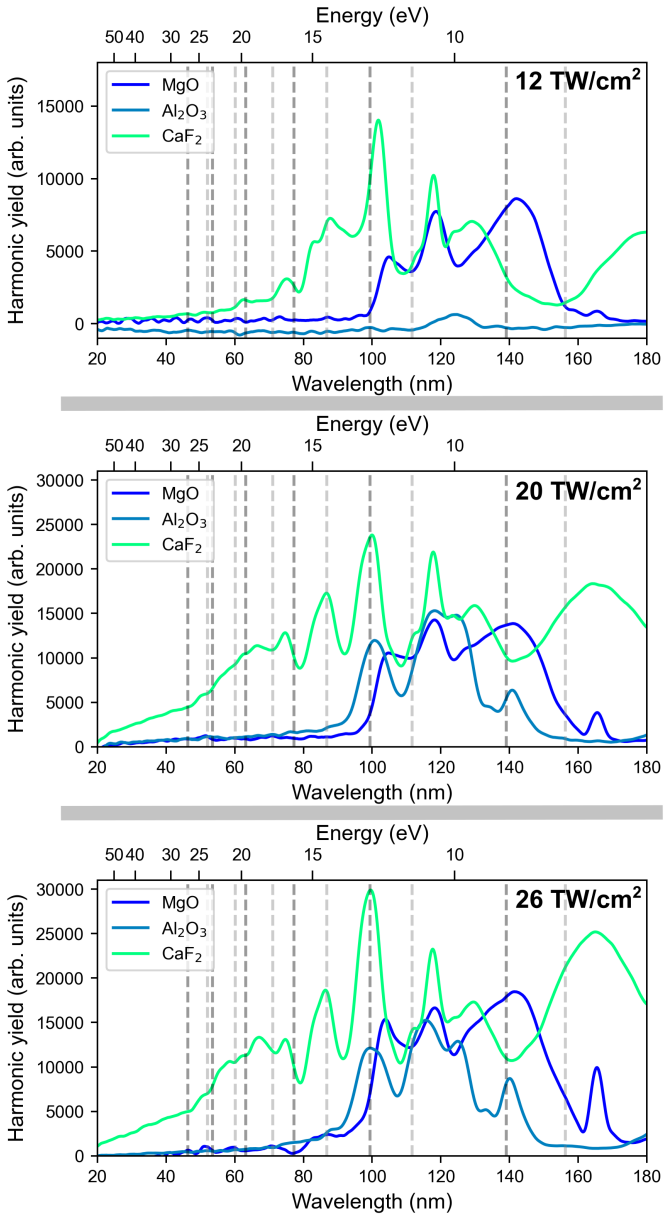


Figure 6.4: Harmonic spectra of MgO, α-Al_2O_3 and CaF_2 at different intensities for the 5 fs pulse. The grey lines correspond to the harmonic peak positions of a 780 nm driving field and the black lines, to the harmonic peaks of a 695 nm driving field (central wavelength of the 5 fs pulse).

In the short pulse case, it is possible to compare the three samples for three overlapping intensities. The first observation is that, as mentioned in Chapter 5, the harmonic peaks are less defined. Indeed, as the driving pulse is shorter, its bandwidth is larger, meaning harmonics are produced from a broad laser spectrum. The harmonics are therefore spectrally broader than in the long pulse case and tend to merge into each other. The cutoff of all the samples increases with intensity, CaF_2 having the highest harmonic observed, as shown on Figure 6.5. CaF_2 is also the sample that has consistently the highest harmonic yield, by more than a factor 1.6 compared to MgO and α-Al_2O_3.

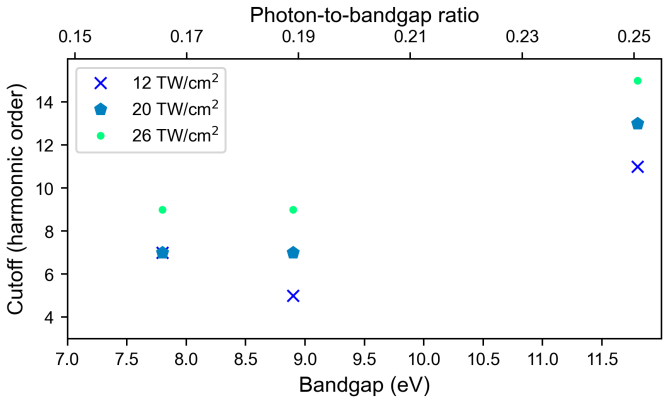


Figure 6.5: Harmonic cutoff as a function of bandgap or the 5 fs pulse.

Differing absorption could be responsible for the different yields observed. We plot on Figure 6.6 the harmonic spectra of the three samples multiplied by the transmission curves of Figure 6.1. Despite the high absorption of CaF_2 in the region above 30 eV, its harmonic signal is still clearly visible and remains higher than MgO and α-Al_2O_3. α-Al_2O_3 is likely affected by its low transmission in the region 10−15 eV. The analysis of absorption helps explain the difference in yield, but does not give the complete picture. Moreover, only the mean absorption length above 10 eV has been computed and a variation of the absorption length across the whole harmonic range could complicate the observations.

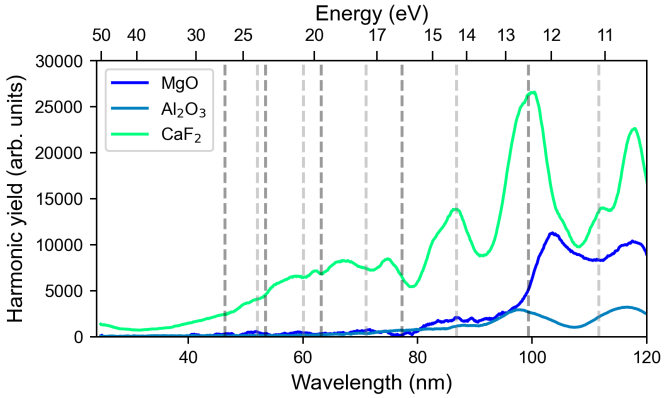


Figure 6.6: Harmonic spectra multiplied with the transmission curve of MgO, α-Al_2O_3 and CaF_2 at 26 TW/cm^2 for the 5 fs pulse. The grey lines correspond to the harmonic peak positions of a 780 nm driving field and the black lines, to the harmonic peaks of a 695 nm driving field (central wavelength of the 5 fs pulse).

6.3.2 Comparison of Harmonic Emission From Bulk and Thin Film Samples in Reflection

Hollinger *et al.* [210] used a transmission geometry to make their comparison between a thin film and a bulk sample. This choice of geometry is challenging as nonlinear effects can still occur in the

substrate before reaching the thin film (the laser passes through the substrate first). In this case, the pulse producing the harmonics is altered by propagation effects. We thus decided to compare the harmonic yield of the two samples in reflection in order to remove any potential propagation effect in the sample.

Figure 6.7 shows the harmonic spectrum of the bulk ZnO sample and the thin film ZnO sample for two different intensities with a 3 µm driving field. We can see H3 and H5, centred at 1000 nm and 610 nm, respectively. The emission of H5 for both samples is equally efficient, following a similar trend for increasing intensity. A peak splitting of H5 is observed for the bulk, not seen in the thin film. Fringes due to front and back surface reflections interfering are visible on this H5 signal from the bulk. H3 presents a higher efficiency for the bulk, showing a yield approximatively 15 times greater than for the thin film.

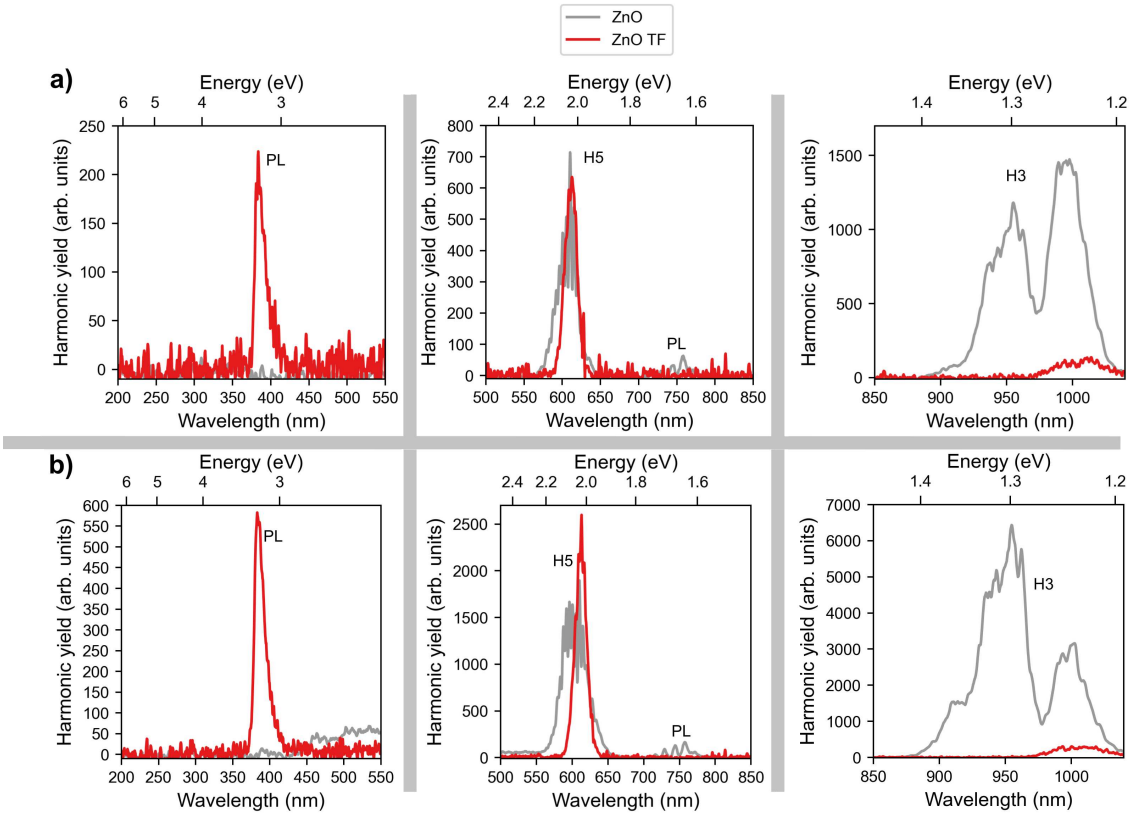


Figure 6.7: Harmonic spectra of bulk ZnO and a thin film sample of ZnO at 1.9 TW/cm^2 (a) and 2.6 TW/cm^2 (b) for the short 66 fs pulse (6.5 cycles) with a 3 µm driving field.

The peaks at 390 nm and $\sim$ 750 nm do not correspond to harmonics. The 390 nm peak is a near-band-edge emission corresponding to PL of ZnO attributed to free excitons close to the bandgap [265]. The PL is much stronger for the thin film than for the bulk. Another PL peak is seen only for the bulk at $\sim$ 750 nm [227]. This peak has been less studied than the near-band-edge PL peak and has been potentially attributed to a point defect emission, explaining its weaker yield [227].

Hollinger *et al.* [210] showed in their experiment that the thin film was more efficient than the bulk for HHG due to the reabsorption of the harmonics in the bulk. It is hard to make the same conclusion in reflection as we see only two below-bandgap harmonics. However, the trend of a stronger H3 in the bulk followed by H5 of comparable yield in both samples suggests that the same conclusion may apply.

To produce HHG, the choice between bulk and thin film is not straightforward and depends strongly on the desired harmonic wavelength. As seen in Chapter 5, the harmonics are weaker in the reflection geometry than in transmission but the HHG efficiency of the thin film might depend on the substrate used. The substrate might contribute to the harmonic signal and attenuate the transmitted fundamental beam [266]. Furthermore, the modified electronic structure of the film and its defects might explain the difference observed [114].

6.3.3 Comparison of Harmonic Emission Using a MIR Driving Field in Transmission

Harmonic spectra for the short and long pulses, already detailed in Chapter 3 are presented here. In the transmission geometry, as the beam goes through the sample, it produces harmonics. The above-bandgap harmonics can be reabsorbed by the sample whereas the sample absorbs less below-bandgap harmonics. These below-bandgap harmonics can present fringes due to reflections at the back and front surfaces, as discussed in Chapter 5. We present here the harmonic spectra of the short and long pulses for the five samples under study in transmission. Table 6.3 summarises where the bandgap is relative to the harmonic orders. The spectra presented are separated in different spectral regions in order to adapt the scale on each region and render each peak visible on the figures. The comparison is done at the same intensity of $1.2\,\mathrm{TW/cm^2}$ for all of the samples in order to have the same parameters concerning the driving field. This intensity corresponds to the maximum intensity before damage of ZnSe and SiC in the long pulse case.

Figure 6.8 presents the whole harmonic spectrum from the long driving pulse. Two integration times are used, 1 s and 10 ms due to the saturation of the spectrometer. As the harmonic yield of all of the samples cover a wide range, two different y-scales are used: a small-range y-axis is displayed on the left side of the figure and when needed, a wide-range y-axis is added on the right side of the plot.

It is evident that ZnSe shows the highest cutoff with the last detected harmonic at 220 nm (H14). Both even and odd harmonics are produced in ZnSe as its crystal structure is optically isotropic but noncentrosymmetric [96]. ZnO and $SrTiO_3$ have very noisy HHG spectra for this intensity, making it difficult to reliably detect any harmonic peak in the region $200-320\,\mathrm{nm}$ (frame (b)). GaN produces harmonics up to H11 ($\sim 276\,\mathrm{nm}$), although the yield of H11 is much lower

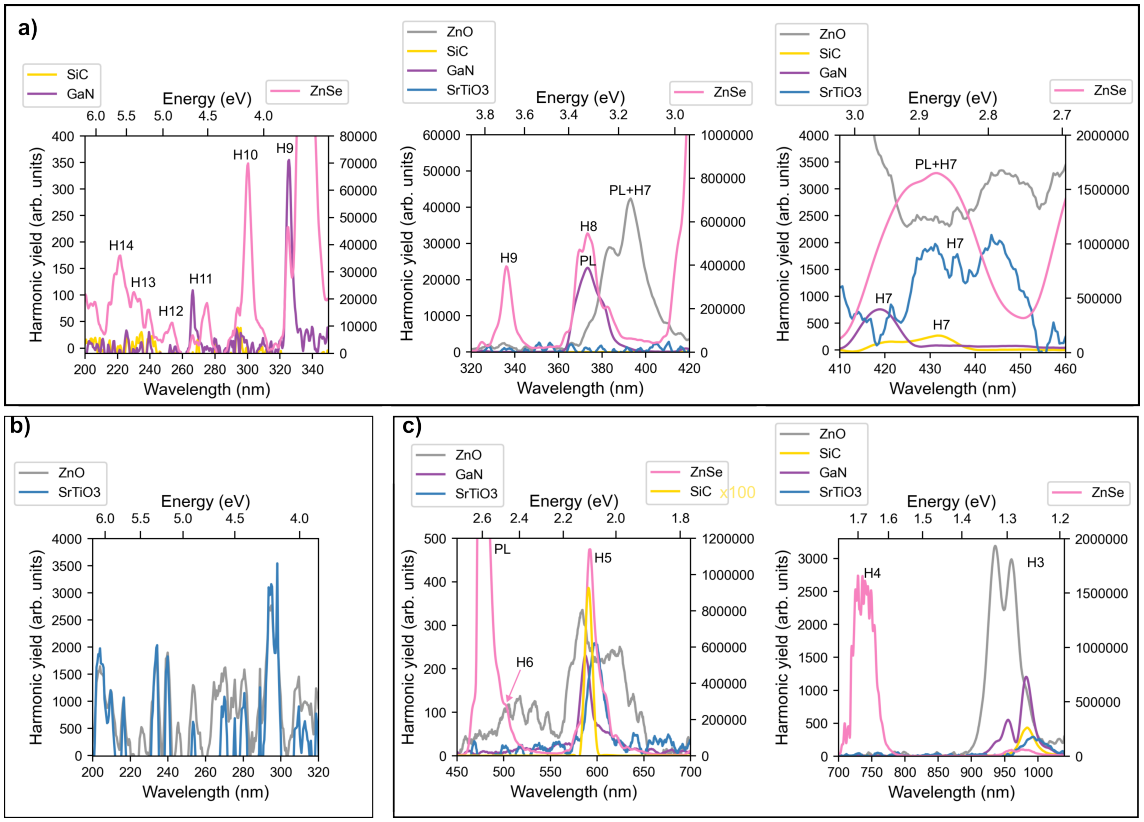


Figure 6.8: Harmonic spectra in transmission of ZnO, ZnSe, GaN, SiC and $SrTiO_3$ at 1.2 TW/cm^2 for the long pulse. Two y-scales are used, the legend on the left (right) side corresponds to the y-scale on the left (right) side. (a) and (b) 1 s integration time, (c) 10 ms integration time. (a) and (c) cover the whole spectrometer range. (b) shows the noisy spectrum collected for ZnO and $SrTiO_3$.

compared to ZnSe (factor ~ 40). H9 of ZnSe is orders of magnitude higher than all other harmonics in the range 200−350 nm, therefore the scale does not allow to see it in this range, but this is evident in the next range displayed, 320-420 nm.

Between 320 and 460 nm, PL peaks are visible, blurring the peak of H7 for most of the samples. These PL peaks include the PL peak of GaN around 370 nm [267], recognisable as it is broader than the harmonic peaks. It could originate from a defect, however, this is not certain [267]. The PL peaks of ZnO [265] and ZnSe [268] are due to free excitons recombining near the band edge.

The yield of ZnSe is orders of magnitude higher than for the other samples. H6 for ZnSe is also obscured by a bandgap PL signal, which reaches the saturation limit of the spectrometer. H3 and H5 are clearly visible for all the samples. The spectral range is limited by the spectrometer, making a study on H3 unreliable as we do not detect its whole bandwidth.

Figure 6.9 presents the spectrum of the short pulse (66 fs) for four studied samples (as SiC was not very efficient and time was limited for the second experiment at ALLS, SiC was not tested again). Starting in the upper left quadrant for the lower wavelengths, H11 and H9 are visible for ZnSe and ZnO. H11 is very low in yield and is almost lost in the noise. We can also distinguish H10 for ZnSe. ZnSe shows a higher yield than the other samples from H7 to H11. The same broad PL peak for GaN as for the long pulse is visible, centred around 530 nm, probably due to a defect [267]. The same PL peak observed previously in the thin film and bulk comparison, which also has a possible origin from a point defect, is visible at $\sim$ 750 nm for ZnO [227]. H7 is produced by ZnO, ZnSe and GaN while all four samples generate H5 and H3. ZnO has the strongest H3 and H5 yields.

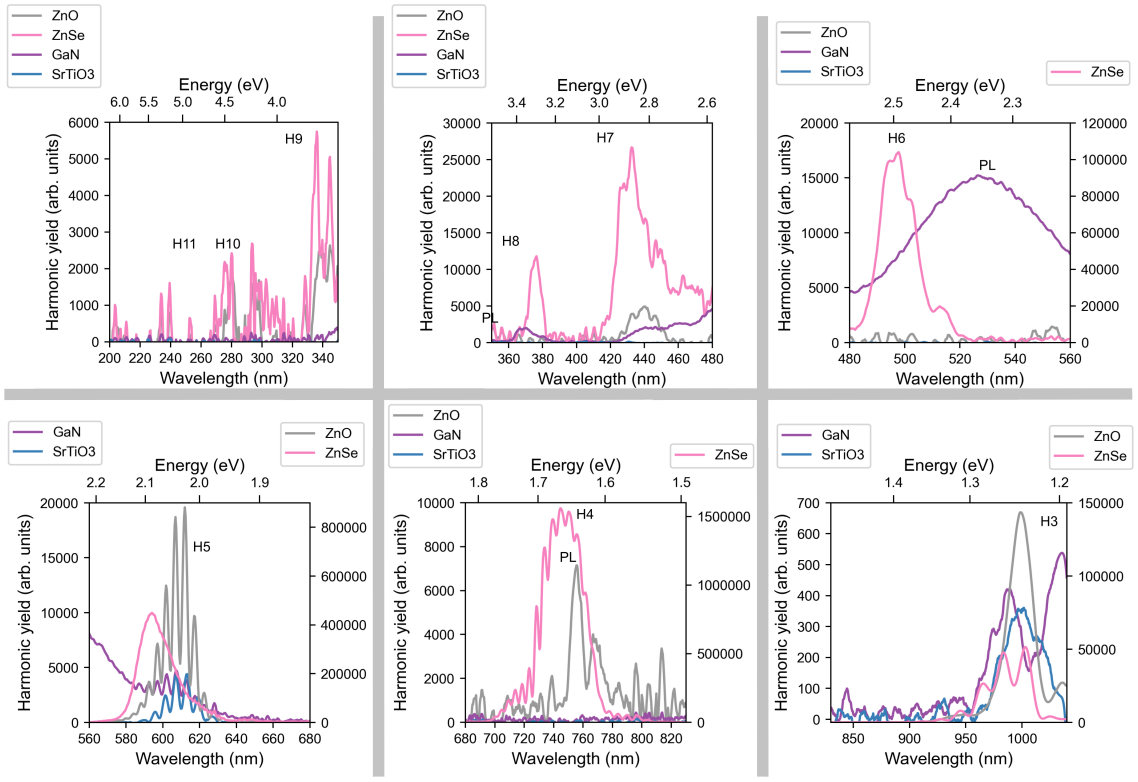


Figure 6.9: Harmonic spectra in transmission of ZnO, ZnSe, GaN and $SrTiO_3$ at 1.2 TW/cm^2 for the short pulse. Two y-scales are used, the legend on the left (right) side corresponds to the y-scale on the left (right) side. All of the spectra are recorded with 1 s integration time except the last one recorded for 10 ms integration time due to saturation of the spectrometer.

We can make the following observations on the PL emissions seen in both cases of the short and long pulses. The PL emission is usually more efficient than the harmonic emission for a given sample. Hollinger *et al.* [210] emphasised that the PL signal directly reflects the number of excited electrons, therefore gives an indirect measure of the efficiency of the photon absorption. When acquiring the harmonics, we observed strong visible PL emission, which usually coincided with efficient HHG signal, as shown on Figure 6.10. Each colour corresponds to a wavelength near the bandgap of each sample.

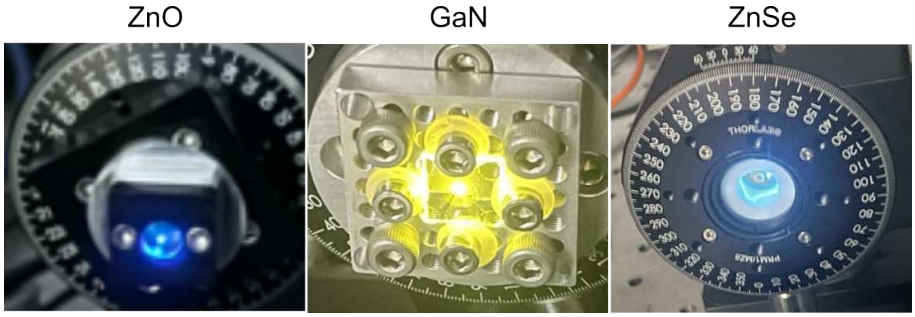


Figure 6.10: Visual PL signal of ZnO, GaN and ZnSe. The PL signal of SiC and $SrTiO_3$ were not observed visually in the lab.

Table 6.3 summarises the observations made on these spectra and Figure 6.11 shows the yield of H5 and H7 for the short driving pulse and only of H5 for the long pulse, as a reliable discrimination between PL and harmonic signal was not possible for H7. ZnSe is the most efficient sample. SiC and $SrTiO_3$ consistently have weak yields. GaN and ZnO are more efficient for the short pulse, H5 of ZnO being even slightly above ZnSe in terms of yield.

Sample	Last below-bandgap harmonic	Bandgap (eV)	First above-bandgap harmonic	"Cutoff" SP	"Cutoff" LP	Visible PL?	Keldysh parameter γ
ZnSe	H6	2.70	H7	H11	H14	Yes	0.3
$SrTiO_3$	H7	3.25	H9	H5	H7	No	2.8
SiC	H7	3.26	H9	–	H7	No	0.8
ZnO	H7	3.37	H9	H11	H7	Yes	0.4
GaN	H7	3.42	H9	H7	H11	Yes	0.5

Table 6.3: Bandgap energy relative to the harmonic orders and cutoff observed for all studied samples. The cutoff corresponds to the last harmonic seen. In the case of ZnSe, the real cutoff could be higher, hence the term "cutoff". LP: long pulse, SP: short pulse. The Keldysh parameter is calculated for 1.2 TW/cm^2

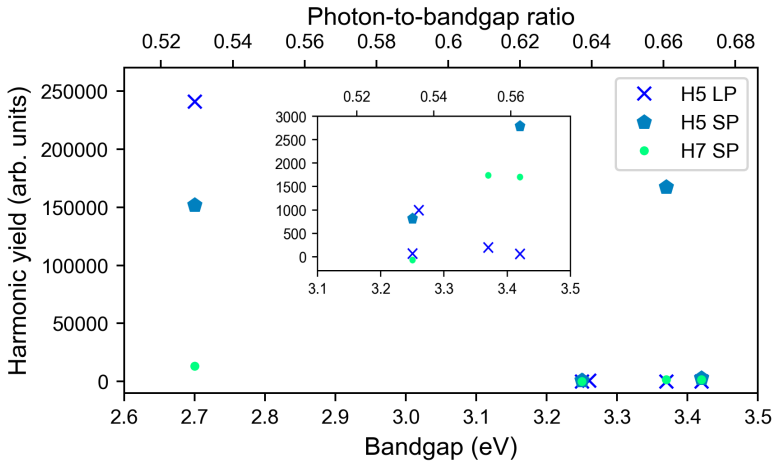


Figure 6.11: Harmonic yield as a function of bandgap. The inset corresponds to a zoom on the region 3.1 to 3.5 eV.

Importantly, we note that this efficiency ranking observed at 1.2 TW/cm^2 for the short pulse stays true for higher intensities. Figure 6.12 displays the harmonic spectrum of the short driving pulse for 3.2 TW/cm^2. The PL peaks are much stronger and have overtaken some harmonic peaks but the ranking of the efficiency of the samples stays the same, although with an extended cutoff for ZnSe. We can therefore express the ranking of yields as follows: ZnSe $>$ GaN $\sim$ ZnO $>$ $SrTiO_3$ $\sim$ SiC.

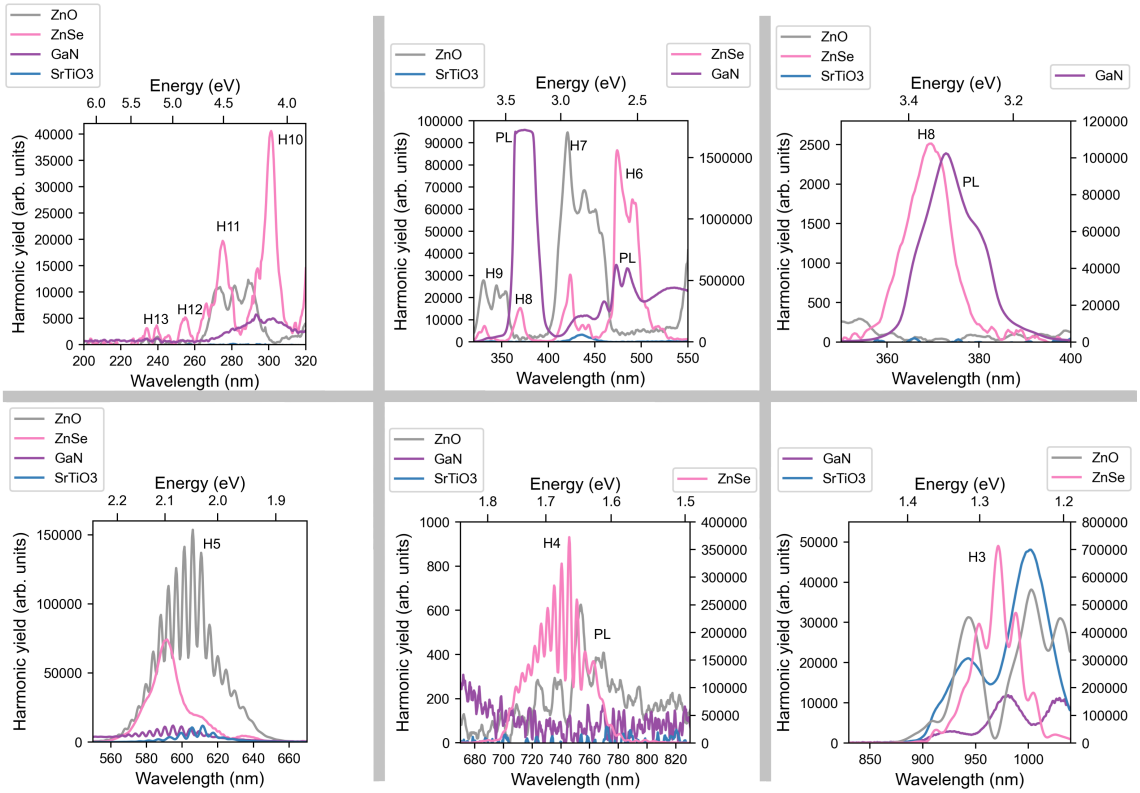


Figure 6.12: Harmonic spectra in transmission of ZnO, ZnSe, GaN and $SrTiO_3$ at 3.2 TW/cm^2 for the short pulse. Two y-scales are used, the legend on the left (right) side corresponds to the y-scale on the left (right) side. The first two spectra of the top row are recorder with 1 s integration time and the rest of the spectra are recorded for 10 ms integration time due to saturation of the spectrometer.

6.3.4 Comparison of Harmonic Emission Using a MIR Driving Field in Reflection

We now consider the harmonic emission of those semiconductor samples in reflection geometry. Figure 6.13 displays the full harmonic spectrum of the five samples for the short and long pulses.

The broad peak centred at 500 nm for GaN, as well as the sharp peak at $\sim$ 370 nm are due to PL [267]. The 500 nm peak is immediately recognisable by its broad shape for both the short pulse and long pulse driving fields and was already seen in transmission. The sharper peak at $\sim$ 370 nm is due to excitons recombining (possibly a mixture between free excitons and excitons bound to

neutral shallow donors [267]). The sharp peak for the long pulse of the ZnSe spectrum at $\sim 470\,\mathrm{nm}$ is also due to near-band-edge PL [268]. The PL of both ZnSe and GaN is much stronger for the long pulse (factor 2 for the broad peak of GaN, absent sharp peaks for the short pulse).

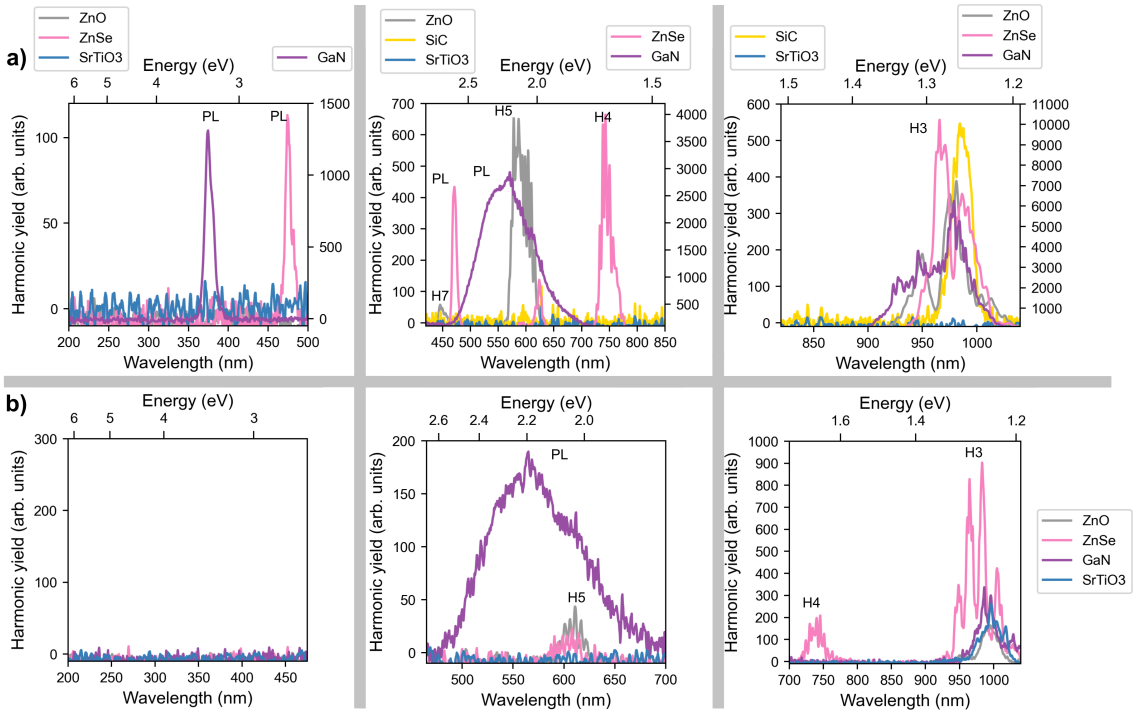


Figure 6.13: Harmonic spectra in reflection at $1.2\,\mathrm{TW/cm^2}$ for the long pulse (a) and short pulse (b) for the samples under study. In (a), two y-scales are used, the legend on the left (right) side correspond to the y-scale on the left (right) side.

H7 appears for ZnO but is very weak. H5 is produced in ZnSe and ZnO in both cases. The PL peak of GaN covers H5 but we can see a sharp peak within the broad PL peak for the long pulse (top row of Figure 6.13) and in SiC, H5 is produced only in the long pulse case. The fourth harmonic H4 is generated in ZnSe as expected due to the symmetry of the crystal. H3 is produced by all samples, although very weakly for $SrTiO_3$ with a short driving pulse.

The reflection spectra confirm the transmission observations that ZnSe is the most efficient sample. GaN is more efficient in reflection compared to the other samples than it was in transmission. ZnO comes next in the yield ordering and then $SrTiO_3$ and SiC, which hardly produce any high harmonics.

6.4 Propagation of the MIR Fundamental Through the Sample

In order to compare the HHG efficiency for these similar bandgap materials, we also have to consider the effects of propagation. In Figure 6.14, we compare the fundamental propagation through the

sample, monitoring changes in its spectrum, and comparing this to the initial spectrum. We note that all of these samples add a minor amount of GDD, stretching the pulse by less than a percent, i.e. linear propagation effects are negligible.

From Figure 6.14, it is clear that GaN has the most pronounced effect on the fundamental spectrum, as the spectral intensity is reduced by more than a factor 2 and GaN blue-shifts the central wavelength. However, the central wavelength is red-shifted as the intensity increases for GaN. As seen in the previous chapter, ZnO weakly affects the fundamental. ZnSe and $SrTiO_3$ both do not shift the central wavelength but absorb $\sim 40\,\%$ of the fundamental beam. Those observations lead us to conclude that GaN affects the most the fundamental and therefore its harmonics will suffer from propagation effects. Moreover, we measured the absorption spectra of GaN with the same spectrometer as previously used for ZnO (Figure 6.15) and saw that GaN is transparent to all below-badgap harmonics.

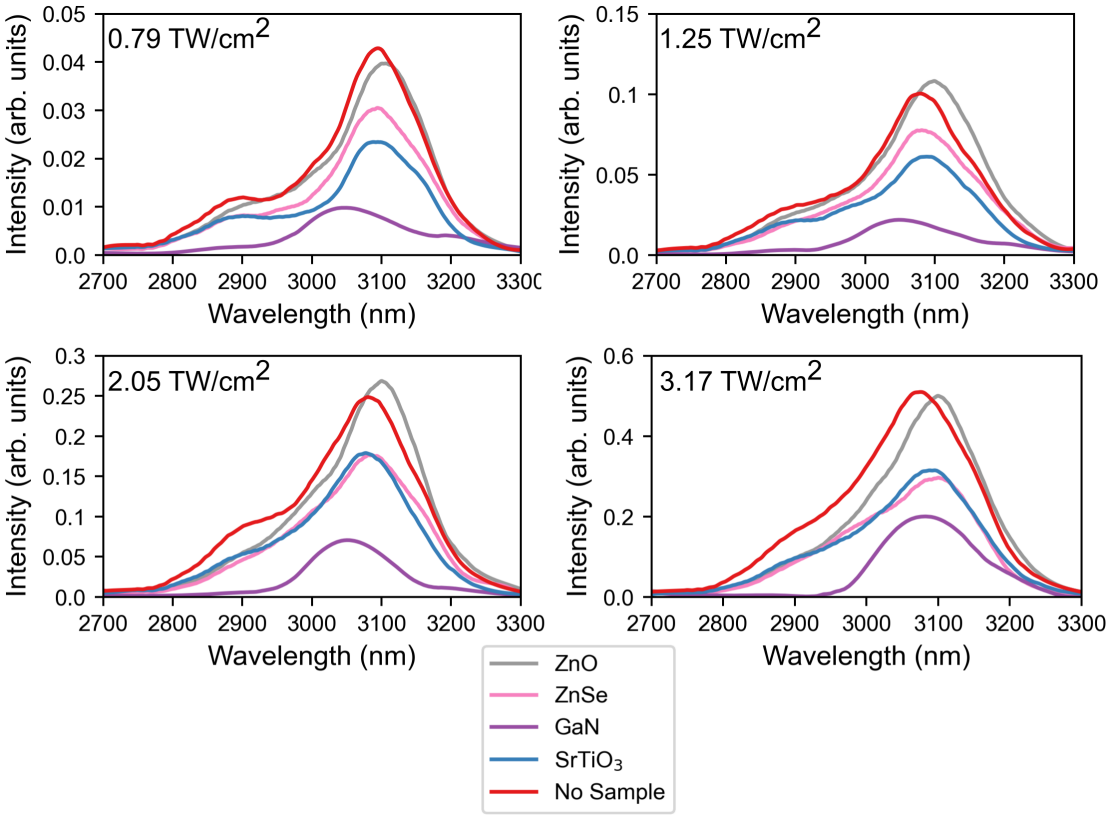


Figure 6.14: Spectrum of the fundamental going through ZnO, ZnSe, GaN and $SrTiO_3$ and without any sample in the beam path for comparison at different intensities.

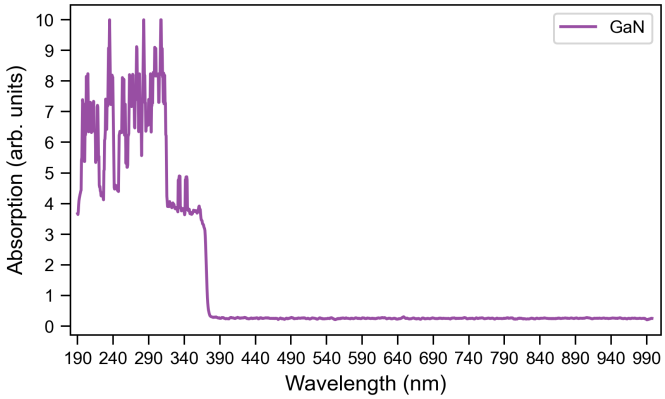


Figure 6.15: Absorption spectra of GaN measured with a UV-VIS spectrometer.

6.5 Understanding the Properties Needed for an "Efficient" Sample for HHG

We present in this section some sample properties that could explain the difference in harmonic emission observed in the previous section and which would allow to draw conclusions onto what characteristics are key for an "efficient" harmonic sample.

6.5.1 Photon-to-Bandgap Ratio

The trend for harmonic efficiency in solid HHG has been attributed to the high photon-to-bandgap ratio as it is easier to ionise the electrons with a low bandgap. However, Figure 6.5 shows that this statement does not seem to hold as the highest bandgap material has the highest cutoff and also the highest yield. Deeper analysis is required (e.g. of the multiphoton excitation rate [269]) in order to better understand the difference in the process.

6.5.2 Band Structure

The electron dynamics in MgO have been studied in Chapter 4 in the long pulse case and the high cutoff is likely a consequence of populating higher-order bands. α-Al_2O_3 (sapphire) counts a high number of high-lying bands (above the second CB) and the band structure is therefore complex to model. To our knowledge, no HHG study has linked high-lying conduction bands of sapphire to its harmonic emission [270].

The difference in yield could arise from the crystallographic structure. Indeed, the laser polarisation as well as the sample position were fixed in the experiment. However, anisotropy work in α-Al_2O_3 has shown an important difference in yield depending on the bond probed [179], although the cutoff detected was also H13. CaF_2 needs higher intensities before being able to produce harmonics which might be linked to its higher bandgap. Similar to MgO in the long pulse regime, the

second conduction band can be reached in CaF_2 [241]. However, those observations of harmonic signals at energies in the second CB do not allow us to conclude why the electrons reach higher conduction bands.

6.5.3 Bandgap Size

ZnSe consistently shows the highest cutoff, producing for both the short and long pulse cases above-bandgap harmonics. The interband mechanism dominates for above-bandgap harmonics [79] and below-bandgap harmonics are mainly produced *via* intraband currents. The particularly low bandgap of ZnSe could provide a simple explanation for the efficient production of above-bandgap harmonics. However, SiC has a similar bandgap and does not show such a high cutoff.

6.5.4 Nearest Neighbour Distance

A recent study by Xie *et al.* [271] has linked the bond length between C and N in the molecule CH_3NO_2 to the harmonic yield and cutoff. They measured an increase in harmonic yield and cutoff as they increased the length of the C-N bond. Their worked opened up new insight for the solid-state case. CaF_2 has the largest nearest neighbour distance among the three samples studied with the NIR field (Table 6.1) and has consistently the highest yield in the short pulse case. The efficiency of CaF_2 might therefore be attributable to its longest nearest neighbour distance.

Xie *et al.* linked the increase in harmonic yield to the number of molecular orbitals participating in the process. A similar idea was proposed by Jimenénez-Gálan *et al.* [263], who took an orbital perspective approach on HHG from solids. They studied the anisotropic behaviour of ReS_2 as a function of intensity and explained this anisotropy by the participation of different orbitals to the process. They expressed the total current responsible for HHG emission as a sum of the currents from all orbitals in the lattice in a real-space depiction of the solid-state HHG process. They then grouped the currents coming from all the orbitals of one atom into a single current. However, a long bond length can result in a higher harmonic yield than a short bond length, meaning that the delocalisation of the orbitals along the bond needs to be taken into account. Our sample comparison raises doubt about the validity of grouping the currents.

These explanations hold only for a short pulse duration, potentially meaning that when the electron propagates for longer in the field (longer pulse durations), scattering can increase and the effects of the bond are weaker.

Similar to the NIR case, we can look at the nearest neighbour distance for the MIR regime. ZnSe has the highest near neighbour distance, which could be traced back to its high yield, as mentioned by Xie *et al.* [271].

6.5.5 Keldysh Parameter

MgO and α-Al_2O_3 have close Keldysh parameters for 9 TW/cm^2, 1.2 and 1.3, respectively. Multi-photon Ionisation (MPI) is likely to happen but there is probably a mixture of MPI and Tunnelling Ionisation (TI) taking place.

The Keldysh parameters for the semiconductor materials are shown in Table 6.3. Except for $SrTiO_3$, we have $\gamma < 1$, placing the HHG process in these samples predominantly in the Tunnelling Ionisation (TI) regime. In this regime, the electrons from the valence band (VB) tunnel adiabatically through the barrier to the conduction band (CB). The excited electrons either recombine with the holes *via* direct bandgap recombination, generating harmonics or *via* deep defect levels leading to PL [210]. ZnSe has the lowest Keldysh parameter γ, indicating a strong tunneling ionisation that could explain the high efficiency of the process. However, the low Keldysh parameter can only be a partial explanation due to all the studies already made, having a wide variety of Keldysh parameters.

In all sample, the difference in efficiency therefore does not arise from a difference of ionisation regime.

6.5.6 Direct or Indirect Bandgap

Among the semiconductors studied under a MIR field illumination, $SrTiO_3$ and SiC, are the least efficient, producing weakly only below-bandgap harmonics while the other three samples producing PL also generate harmonics more efficiently.

PL from excitons occurs when an electron and a hole, bound together by Coulomb attraction, recombine and emit a photon. The PL peaks of GaN ($\sim$ 370 nm) [267], ZnO ($\sim$ 400 nm) [265] and ZnSe ($\sim$ 435 nm) [268] originate from this excitonic near-band-edge recombination. The other PL peaks from these samples have a different origin: in GaN, the broad PL peak observed around 560 nm (in the harmonic spectrum and visibly) has an uncertain origin, possibly from a defect [267] while the PL peak of ZnSe around 470 nm has an unknown origin [268]. $SrTiO_3$ [272, 273] and SiC [274] have both demonstrated the ability to produce PL emission, originating from the recombination of excitons. However, we have not observed any PL from these two samples.

Strong PL emission seems to be linked to "efficient" harmonic generation. The low yield of $SrTiO_3$ and SiC could be traced back to their indirect bandgap. The pathway of the electrons when they are ionised or recombine is not straightforward and the tunnelling rate might be lowered. The difference in band alignment could therefore explain why $SrTiO_3$ and SiC are less efficient than the other samples and implies a criteria for a "good" HHG sample is the need for a direct bandgap.

6.5.7 Excitonic Processes and Properties

We can explore deeper the link between efficient HHG and visible PL emission by investigating the link between PL emission and excitonic process and therefore between HHG yield and excitonic process. This leads us to look at the excitonic binding energy E_b, indicated in Table 6.2. The exciton binding energies are: ZnSe (20 meV), SiC (20 meV), GaN (26 meV), and ZnO (60 meV). A valid excitonic energy could not be found in the literature for $SrTiO_3$ as its value differs greatly depending on many conditions.

The choice of a "good" HHG target has already been related to the excitonic binding energy by Kohrell *et al.* [252]. They state that a good target for HHG is a material which is a strong photon emitter, i.e. which has a high excitonic binding energy. We explore this avenue: ZnSe has the lowest binding energy although it presents the highest yield. However, ZnO is more efficient than GaN in the short pulse case. An exciton can stay stable if $k_\mathrm{B}T < E_\mathrm{b}$ [197]. For a lab temperature of 22 °C, $k_\mathrm{B}T = 25$ meV. The binding energy of ZnSe is below this limit, which means that the excitons are not stable and free electron-hole pairs are created, potentially making the recombination step easier. SiC would behave the same as it has the same binding energy. Its indirect bandgap could also impact the exciton dynamics.

The link with the excitonic binding energy is not straightforward. More experiments on PL emission, analysed using binding energies could shed light on the interplay between HHG and PL. Additionally, the excitonic binding energy has been shown to depend on the intensity of the strong field applied [275]. Indeed, in WS_2, the excitonic binding energy has been measured to be 710 meV [276] but only 310 meV when a strong field was applied [275].

It has also been demonstrated that HHG can be affected by excitonic effects. Jensen *et al.* [200] have shown that the HHG process is enhanced with sidebands in the harmonic spectrum due to excitons, using a pump-probe scheme. Moreover, they claim that "the presence of an exciton level allows for new excitation and recombination pathways". Performing such an experiment in these samples might confirm the excitonic effects responsible for a high yield.

6.5.8 Pulse Duration of the Driving Field

ZnSe, GaN and $SrTiO_3$ all show an extended cutoff in the long pulse case. At 1.2 TW/cm^2, ZnO does not follow the same trend although as the spectrum is very noisy, it is hard to reliably identify the cutoff. Moreover, we saw in Chapter 5 that the cutoff was extended with a long pulse driver at higher intensities. Concerning the yield, the conclusions are more nuanced. Figure 6.11 shows that ZnSe has a 1.6 times higher yield for the long pulse than for the short pulse for H5. For the rest of the samples, as the yield is lower, the difference is less striking. Freeman *et al.* [186] have theoretically studied the effect of the pulse duration on the harmonic spectrum in the MIR regime

with pulse durations of 200 and 70 fs at 3 µm. They saw that a short pulse produces a harmonic spectrum with a lower cutoff than for a long pulse due to the impossibility to capture the higher-order returns as the electrons that have gone further in the field cannot recombine. Additionally, the spectrum is "clearer" [186] for a long pulse, the harmonic orders are more distinct as they do not blur in the noise. The role of the dephasing is determining in the harmonic emission (they look at orders 3 to 27), leading to a need to carefully select the pulse duration for efficient HHG.

6.6 Anisotropic Comparative Study of Semiconductors (ZnO, ZnSe, GaN, and $SrTiO_3$)

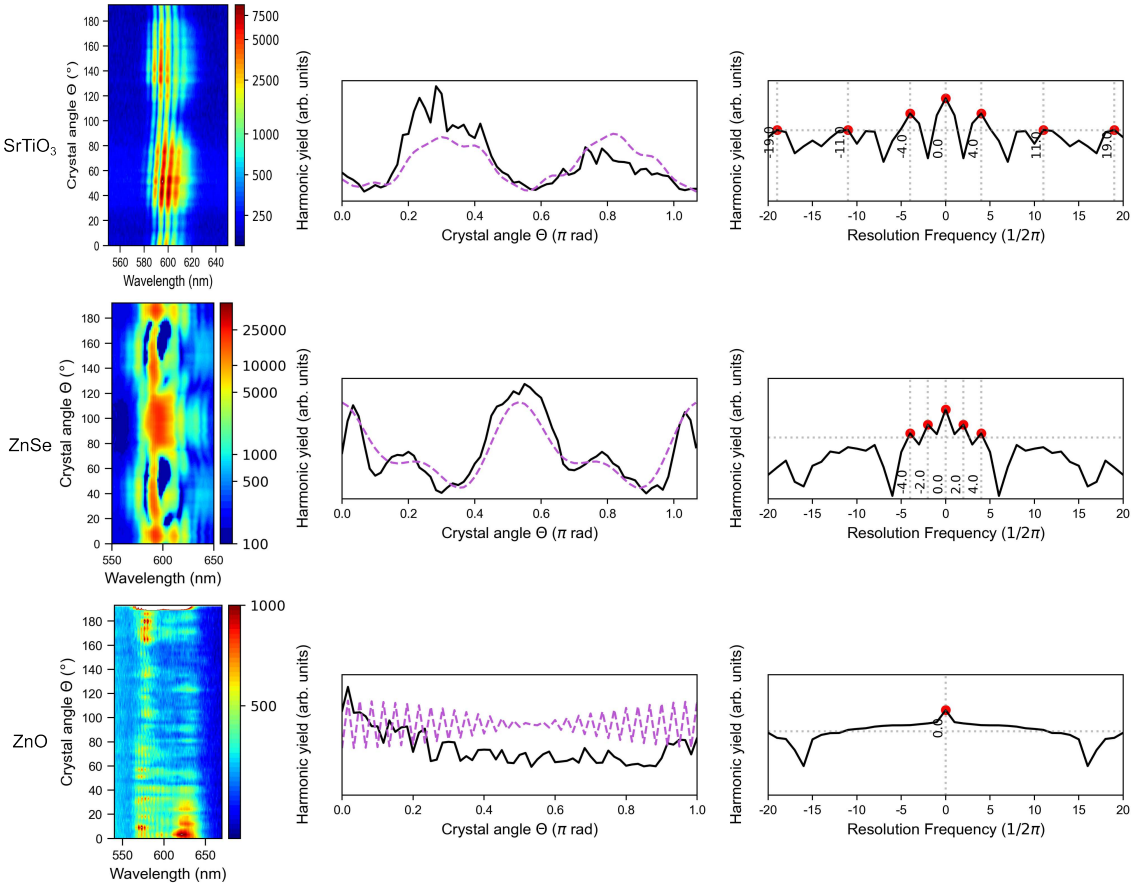


Figure 6.16: Spectrum of H5 with the long pulse for $SrTiO_3$, ZnSe and ZnO. The first column corresponds to the harmonic yield as a function of the crystal angle θ. The second and third columns show the Fourier analysis of the yield of H5 as a function of crystal orientation. Second column: the black line represents the experimental integrated harmonic yield as a function of crystal angle and the dotted purple line corresponds to the inverse Fourier transform of the right column only taking into account the frequency peaks above a fixed threshold (2 % for $SrTiO_3$, 10 % for ZnSe and 4 % for ZnO of the offset frequency peak centred at 0). Third column: Amplitude of the Fourier transform of the experimental data of the second column (real part). The red dots represent the peaks above the threshold. The intensity of the driving pulse for this set of data is 1.2 TW/cm^2.

We have characterised the efficiency of the HHG process in terms of harmonic yield and cutoff.

We can now think about how efficiently the electron probes the lattice of the sample, leading us back to a spectroscopic approach analysing the electron trajectories. We looked at the anisotropy of four of the samples studied in this work for the 6.5-cycle driving pulse as well as the 10-cycle pulse. Figures 6.17 and 6.16 show the spectrum of H5 in both cases. H5 is chosen in order to do a comparison between all the samples for both cases with a good SNR.

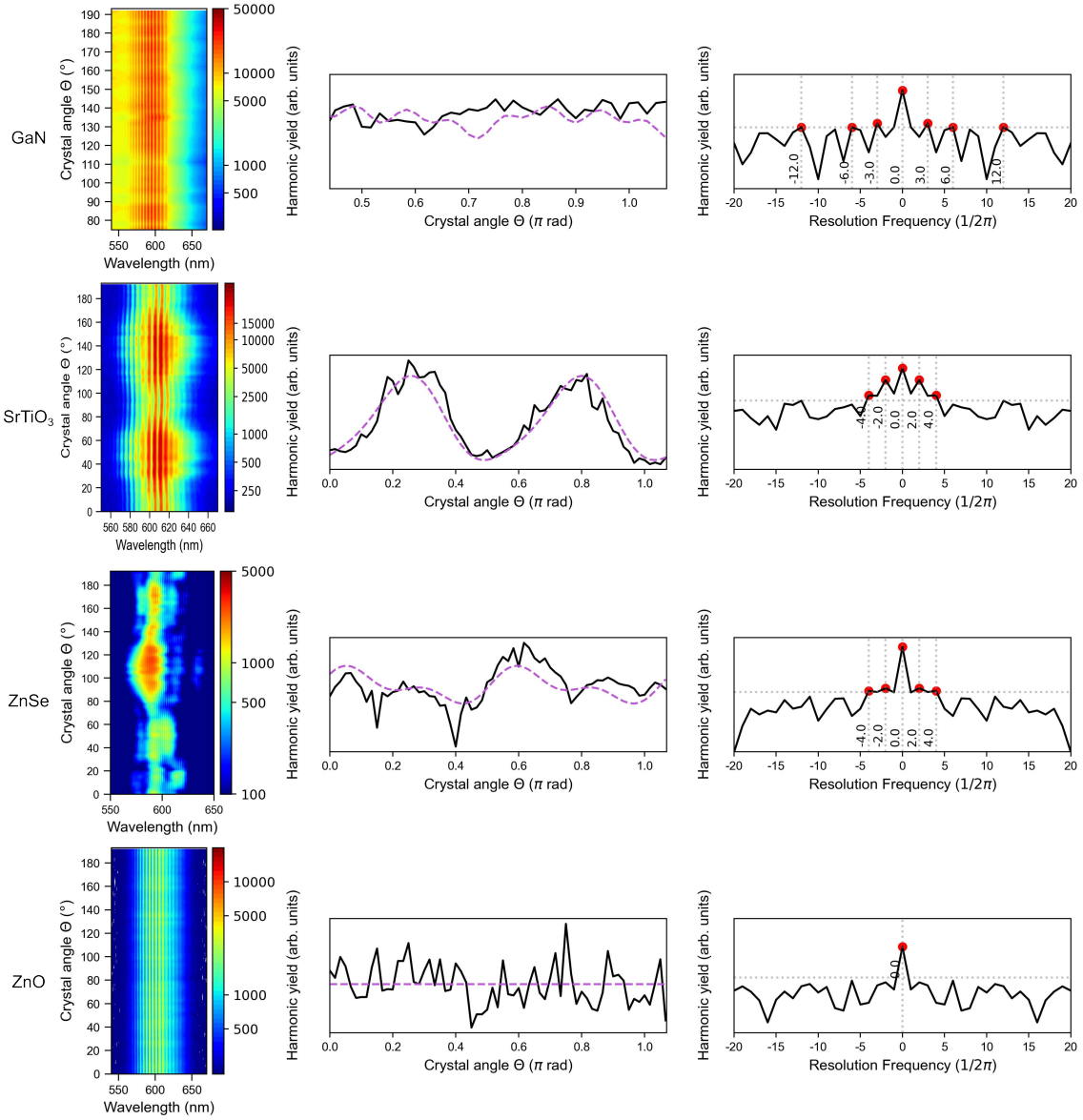


Figure 6.17: Spectrum of H5 with the 6.5 cycle driving pulse for GaN, $SrTiO_3$, ZnSe and ZnO. The first column corresponds to the harmonic yield as a function of the crystal angle θ. The second and third columns show the Fourier analysis of the harmonic yield of H5 as a function of crystal orientation. Second column: the black line represents the experimental integrated harmonic yield as a function of crystal angle and the dotted purple line corresponds to the inverse Fourier transform of the right column only taking into account the frequency peaks above a fixed threshold (2 % for $SrTiO_3$, 4 % for GaN, 2 % for ZnSe and 2 % for ZnO of the offset frequency peak centred at 0). Third column: Amplitude of the Fourier transform of the experimental data of the second column (real part). The red dots represent the peaks above the threshold. The intensity of the driving pulse for this set of data is 3.2 TW/cm^2.

In the previous section, we applied the findings of Freeman *et al.* [186] to our work and concluded that high-order harmonics are weakly produced with a few-cycle pulse probably because of the decoherence effect preventing the return of the electrons. Comparing the anisotropic behaviour of the samples in the short and long pulse cases allows to test this hypothesis further. You *et al.* [176, 112] have shown that the anisotropic response of HHG can be understood in a real-space perspective.

Figure 6.16 shows a strong dependence of the harmonic yield with crystal angle for ZnSe and $SrTiO_3$. The analysis performed is the same Fourier analysis explained in Chapter 5. The Fourier analysis shows a four-fold symmetry for $SrTiO_3$, expected from its cubic structure and also a four-fold symmetry for ZnSe. In both cases, the inverse Fourier transform agrees with the data. For ZnO, the harmonic is too weak at $1.2\,\mathrm{TW/cm^2}$ for reliable analysis. In the short pulse case, Figure 6.17, the behaviour of the samples is different: ZnSe shows peaks at frequencies 2 and 4 but the inverse Fourier transform does not follow all the peaks in the data. GaN does not show any rotational dependence as does ZnO. We expect these two samples to behave similarly as they have the same crystal structure.

It thus seems that the harmonics produced with the short pulse carry a weaker signature of the lattice, meaning that a short pulse does not probe as much the lattice as a long pulse in the MIR regime. We investigate the first above-bandgap harmonic of ZnSe, H9, in Figure 6.18. We calculate the momentum the electron picks up from the driving strong field according to Equation 2.31, $k_{\mathrm{max}} \approx 0.27\,\mathrm{a.u.}$ We compare this value to the size of the BZ of ZnSe along the high symmetry axes: for ΓL, $k \approx 0.25\,\mathrm{a.u.}$, for ΓX, $k \approx 0.28\,\mathrm{a.u.}$ and for ΓK, $k = 0.31\,\mathrm{a.u.}$ [96]. The electron can thus propagate across the entire BZ and reach the edge in the ΓL direction, thus probing the full band structure.

The yield of the harmonic as a function of crystal angle for the long pulse is strongly modulated, a periodicity appearing in some cases. In the Fourier analysis, clear peaks appear at frequencies 2 and 4. A higher peak at frequency 8 also appears. As the rules on crystal symmetry forbid any symmetry higher than 6 [226], the peak at 8 could indicate that the electron probes more than the central BZ. With the short pulse, the Fourier analysis also shows peaks at frequency 4. However, the inverse Fourier transform does not match the signal and no periodicity is seen in the spectral harmonic yield. These observations show the limits of the present Fourier analysis and particularly the need to augment it with a visual analysis.

Accounting for the full distribution of the BZ is important to understand the full anisotropic HHG response [277]. Figure 6.18 allows us to conclude that even if the electron momentum can probe the entire BZ, tailoring of the pulse duration is crucial to access the spatial information of the lattice carried by the electron.

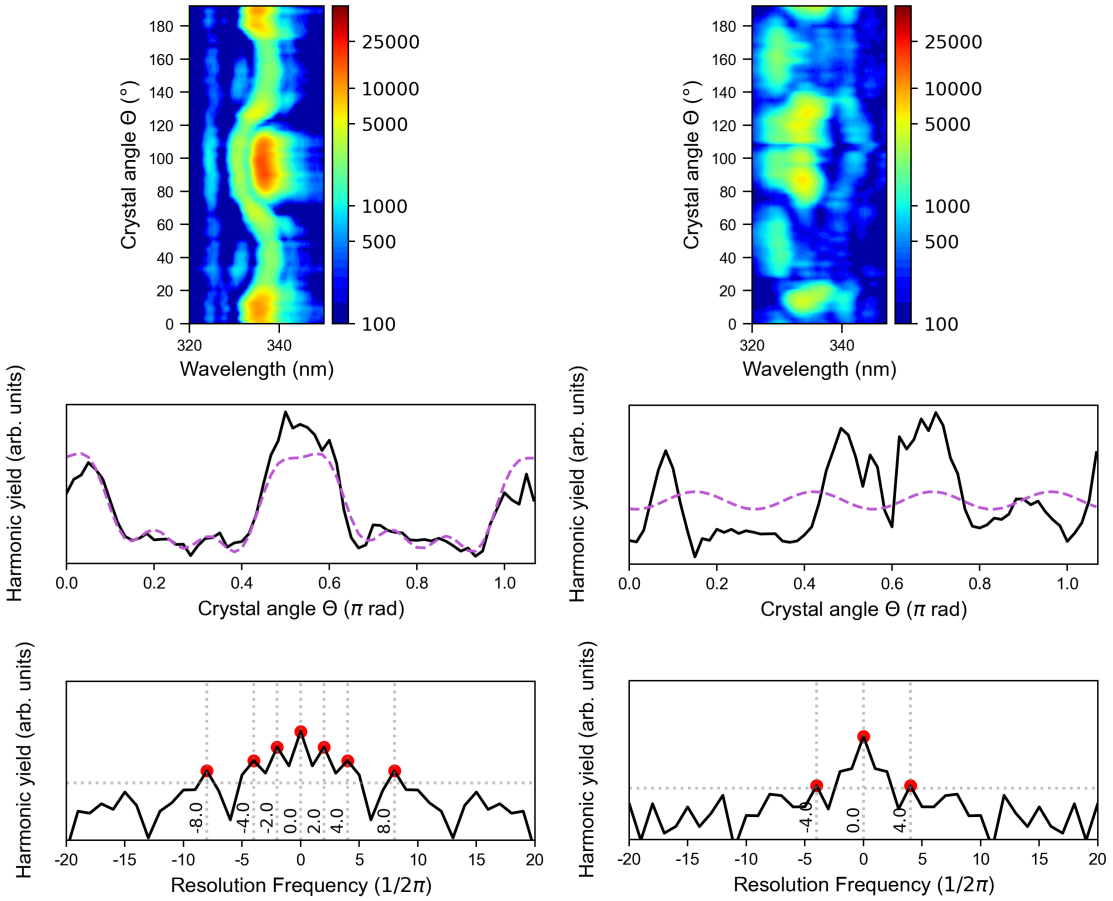


Figure 6.18: Spectrum of H9 for ZnSe with the 10 cycle driving pulse in the first column and the 6.5 cycle driving pulse in the second column. The first row corresponds to the harmonic yield as a function of the crystal angle θ. The second and third rows show the Fourier analysis of the yield of H9 as a function of crystal orientation. Second row: the black line represents the experimental integrated harmonic yield as a function of crystal angle and the dotted purple line corresponds to the inverse Fourier transform of the third row only taking into account the frequency peaks above a fixed threshold (4 % for both cases of the offset frequency peak centred at 0). Third row: Amplitude of the Fourier transform of the experimental data of the second row (real part). The red dots represent the peaks above the threshold.

6.7 Conclusion

We have compared the harmonic yield and cutoff of multiple samples (MgO, Al_2O_3 and CaF_2 on the one hand and ZnO, ZnSe, SiC, GaN and $SrTiO_3$ on the second hand), first with a NIR driving field and secondly with a MIR field. We have seen that the HHG efficiency of the samples depends first of all on the laser pulse duration. We have investigated several sample parameters such as the bond length, the excitonic binding energy and the bandgap, but so far, no strong trend has emerged and it is still difficult to predict a priori which sample would be the best suited target for HHG. We also studied the effect of the pulse duration on these different samples and saw that the anisotropy of the HHG signal was strongly dependent on the pulse duration. Theoretically, we offer several suggestions to try to improve this characterisation, such as a better understanding of the excitonic effects within the HHG process and modelling of the orbitals of an atom to gain a deeper

understanding of the role of the electron delocalisation. These results demonstrate the complexity of HHG in solids and that current theory is unable to encapsulate the myriad of parameters or even identify which ones are important. The results highlight that the band structure retrieval is only really possible with simple samples and known structures. The field of HHG in solids has many unanswered questions, and shedding further light on harmonic efficiency may provide clues to their answers.

Chapter 7

Conclusion and Outlook

This thesis has described the experimental investigation of HHG in wide bandgap dielectrics and semiconductors. It has explored the intricate phenomena involved in HHG in solids, providing a detailed description of the underlying mechanisms and experimental techniques. Through a spectroscopic analysis, we examined the electron motion within the band structure and through an efficiency analysis, we put forward key features required of an efficient target. The work was structured into five chapters, each contributing new insights and advancements in the field.

Chapter 2 laid out the theoretical foundations and necessary background material needed for understanding HHG in solids. This chapter provided a detailed overview of the principles governing HHG, setting the stage for the subsequent experimental investigations. The Keldysh parameter was presented as a way to determine if the dominating ionisation process is Multiphoton Ionisation (MPI) or Tunnelling Ionisation (TI). These two regimes result from the combination of the bandgap and driving energy.

Chapter 3 focused on the experimental methodologies and optical setups employed in this study. The meticulous design and implementation of these setups were crucial for the reliable generation and optimised detection of high harmonics in various solid materials. In the NIR beamline, the modifications done have enabled an improved detection of the harmonics with a good SNR and a wide range of harmonics.

Chapter 4 presented novel results on HHG in MgO using a NIR driving field. We reported the observation of the highest harmonic ever recorded in any material, and a detailed study of the impact of the driving pulse duration on the harmonic spectrum. This readily available material has already been widely studied for solid HHG, and it holds great promise for XUV emission under the right driving field and detection conditions. These findings not only pushed the boundaries of current HHG capabilities but also provided valuable data for future theoretical and experimental studies.

Chapter 5 shifted the focus to HHG in ZnO using a MIR field. The detection of trajectory interference through the splitting and broadening of the harmonic peaks had already been reported, but the demonstration of CEP as a tool for differentiating these interferences is a significant new contribution. The peaks and dips of the harmonic spectrum react differently to a change in the CEP, permitting a clear selection of a specific type of trajectory. This chapter underscored the importance of precise control over laser parameters in achieving and understanding complex HHG phenomena.

Chapter 6 described a comparative study of HHG in various samples in both NIR and MIR regimes. The comparison of efficiency and cutoff across different materials revealed that while no clear selection criterion emerged, key factors such as neighbouring distance and excitonic binding energy play crucial roles. This analysis could provide a roadmap for future research aimed at optimising HHG in solids.

In summary, this thesis has made significant strides in advancing the understanding and application of HHG in solids. The understanding stems from the spectroscopic analysis of Chapters 4 and 5, while the application focus is addressed in Chapter 6. We have studied the difference between the NIR and MIR regimes, highlighting the role of material properties and laser parameters. The experimental observations and theoretical insights presented here not only contribute to the existing knowledge base but also pave the way for future innovations in the field. The potential applications of HHG in solids, ranging from ultrafast spectroscopy to attosecond science, are vast and promising.

Future Work

The groundwork for many future experimental works has been presented in this thesis. Drawing from the results presented in this thesis, a potential avenue to improve the explanation of the process in MgO would be to investigate theoretically the atypical cutoff seen in Chapter 4. Simon Jensen and Nicolas Tancogne-Dejean in Angel Rubio's group at the Max Planck for the Structure and Dynamics of Matter in Hamburg are currently modelling MgO spectra using exactly our experimental parameters, including our reconstructed electric field from the FROG measurement. Too many theoretical studies make conclusions from generic solids by using a specific model, making many unexplained approximations to match experimental findings. Our goal is also to understand the small difference in yield between the two plateaus compared to what has been predicted [100]. Overall, theoretical models should be developed to better predict and understand the complex interplay between material properties and HHG dynamics.

On the experimental side, it is possible to use a field synthesiser in the lab at Imperial College,

in which the MgO works have been done. A field synthesiser produces multiple fields temporally synchronised at the target that enhance the HHG process [278]. Using a two-colour field on MgO and varying the delay between the two would give further insights on the band structure itself [9, 96], allowing potentially to map the higher bands. The same experiment in ZnO could give further understanding on the temporal dynamics of the trajectories and access control on them through the CEP [217].

Furthermore, future work should focus on exploring new materials to further enhance HHG efficiency and cutoff. We have given a few key parameters that seem to determine a "good" target: the excitonic binding energy and the atomic neighbouring distance impacted the most our results. Future studies should focus on those trends, targeted for industrial applications. The Photoluminescence (PL) has proved to be a determining feature for efficient HHG. It therefore seems crucial to be able to discriminate between PL and HHG signal. As the PL peak is isotropic, it is possible to block the central part of the transmitted beam and to only detect the PL signal. Further studies could focus on this emission from the samples. Additionally, the PL emission is dependent on temperature and in most materials, the PL emission increases with decreasing temperature as the thermal energy decreases, preventing non-radiative losses. A possible avenue for research is therefore HHG in cooled samples [279, 252] to gain access to a new HHG regime.

Bibliography

[1] S. Kim, T. I. Jeong, J. Park, M. F. Ciappina, and S. Kim. Recent advances in ultrafast plasmonics: from strong field physics to ultraprecision spectroscopy. *Nanophotonics*, 11(11):2393–2431, 5 2022.

[2] C. Lienau, M. A. Noginov, and M. Lončar. Light–matter interactions at the nanoscale. *Journal of Optics*, 16(11):110201, 11 2014.

[3] X. Bai, H. Allègre, M. Gosselin, P. Dillmann, M. Lopez, F. Téreygeol, and V. Detalle. Impact of laser-induced breakdown spectroscopy implementation for the quantification of carbon content distribution in archaeological ferrous metals. *Spectrochimica Acta Part B: Atomic Spectroscopy*, 172(September):105964, 10 2020.

[4] M. Ferray, A. L'Huillier, X. F. Li, L. A. Lompre, G. Mainfray, and C. Manus. Multiple-harmonic conversion of 1064 nm radiation in rare gases. *Journal of Physics B: Atomic, Molecular and Optical Physics*, 21(3):L31–L35, 2 1988.

[5] X. F. Li, A. L'Huillier, M. Ferray, L. A. Lompré, and G. Mainfray. Multiple-harmonic generation in rare gases at high laser intensity. *Physical Review A*, 39(11):5751–5761, 6 1989.

[6] P. B. Corkum. Plasma perspective on strong field multiphoton ionization. *Physical Review Letters*, 71(13):1994–1997, 1993.

[7] S. Ghimire, A. D. Dichiara, E. Sistrunk, P. Agostini, L. F. DiMauro, and D. A. Reis. Observation of high-order harmonic generation in a bulk crystal. *Nature Physics*, 7(2):138–141, 2011.

[8] E. Goulielmakis and T. Brabec. High harmonic generation in condensed matter. *Nature Photonics*, 5 2022.

[9] G. Vampa, T. J. Hammond, N. Thiré, B. E. Schmidt, F. Légaré, C. R. McDonald, T. Brabec, D. D. Klug, and P. B. Corkum. All-Optical Reconstruction of Crystal Band Structure. *Physical Review Letters*, 115(19), 11 2015.

[10] H. Lakhotia, H. Y. Kim, M. Zhan, S. Hu, S. Meng, and E. Goulielmakis. Laser picoscopy of valence electrons in solids. *Nature*, 583(7814):55–59, 7 2020.

[11] H. Cui, L. Li, Y. Zhang, S. Qiao, D. Wu, P. Lan, and P. Lu. Wavelike dynamics for high harmonic generation in solids. *Physical Review B*, 109(19):195206, 5 2024.

[12] M. Garg, M. Zhan, T. T. Luu, H. Lakhotia, T. Klostermann, A. Guggenmos, and E. Goulielmakis. Multi-petahertz electronic metrology. *Nature*, 538(7625):359–363, 10 2016.

[13] G. Wang and T. Y. Du. Quantum decoherence in high-order harmonic generation from solids. *Physical Review A*, 103(6), 6 2021.

[14] D. Theidel, V. Cotte, R. Sondenheimer, V. Shiriaeva, M. Froidevaux, V. Severin, A. Merdji-Larue, P. Mosel, S. Fröhlich, K.-A. Weber, U. Morgner, M. Kovacev, J. Biegert, and H. Merdji. Evidence of the Quantum Optical Nature of High-Harmonic Generation. *PRX Quantum*, 5(4):040319, 11 2024.

[15] S. Fröhlich, X. Liu, A. Hamdou, A. Meunier, M. Hussain, M. Carole, S. Kaassamani, M. Froidevaux, L. Lavoute, D. Gaponov, N. Ducros, S. Février, P. Zeitoun, M. Kovacev, M. Fajardo, W. Boutu, D. Gauthier, and H. Merdji. Self-probed ptychography from semiconductor high-harmonic generation. *Optics Letters*, 2022(19):4865, 2022.

[16] M. Sivis, M. Taucer, G. Vampa, K. Johnston, A. Staudte, A. Y. Naumov, D. M. Villeneuve, C. Ropers, and P. B. Corkum. Tailored semiconductors for high-harmonic optoelectronics. *Science*, 357(6348):303–306, 7 2017.

[17] S. Fede. Recent developments in compact ultrafast lasers. *Nature*, 424(August):831–838, 2003.

[18] D. Strickland and G. Mourou. Compression of amplified chirped optical pulses. *Optics Communications*, 56(3):219–221, 1985.

[19] E. Hecht. *Optics*. Pearson Education, Incorporated, 1987.

[20] C. Rullière. *Femtosecond Laser Pulses*. Advanced Texts in Physics. Springer New York, New York, NY, 2005.

[21] M. N. Polyanskiy. Refractiveindex.info database of optical constants. *Scientific Data*, 11(1), 12 2024.

[22] G. New. *Introduction to Nonlinear Optics*. Cambridge University Press, Cambridge, 2011.

[23] R. W. Boyd. *Nonlinear Optics*. Elsevier, fourth edition edition, 2020.

[24] B. Edlén. The Refractive Index of Air. *Metrologia*, 2(2):71–80, 4 1966.

[25] B. E. A. Saleh and M. C. Teich. *Fundamentals of photonics*. Wiley, 1991.

[26] S. Feng and H. G. Winful. Physical origin of the Gouy phase shift. *Optics Letters*, 26(8):485, 4 2001.

[27] A. E. Siegman. How to (Maybe) Measure Laser Beam Quality. In *DPSS (Diode Pumped Solid State) Lasers: Applications and Issues*, volume during, page MQ1, Washington, D.C., 1998. OSA.

[28] R. J. D. Tilley. *Crystals and Crystal Structures*. Wiley, 2020.

[29] D. N. Nikogosyan. *Nonlinear Optical Crystals: A Complete Survey*. Springer New York, New York, 2005.

[30] M. Bass, P. A. Franken, J. F. Ward, and G. Weinreich. Optical Rectification. *Physical Review Letters*, 9(11):446–448, 12 1962.

[31] M. V. Hobden. Phase-matched second-harmonic generation in biaxial crystals. *Journal of Applied Physics*, 38(11):4365–4372, 1967.

[32] R. L. Sutherland. *Handbook of Nonlinear Optics*. CRC Press, 4 2003.

[33] G. Cerullo and D. Brida. Ultra-Broadband Optical Parametric Amplifiers. In *Ultrafast Nonlinear Optics*, pages 23–43. Springer International Publishing, Heidelberg, 1 2013.

[34] A. Brodeur and S. L. Chin. Ultrafast white-light continuum generation and self-focusing in transparent condensed media. *Journal of the Optical Society of America B*, 16(4):637, 4 1999.

[35] R. Trebino. *Frequency-Resolved Optical Gating: The Measurement of Ultrashort Laser Pulses*. Springer, Boston, MA, 2000.

[36] M. Miranda, C. L. Arnold, T. Fordell, F. Silva, B. Alonso, R. Weigand, A. L'Huillier, and H. Crespo. Characterization of broadband few-cycle laser pulses with the d-scan technique. *Optics Express*, 20(17):18732, 8 2012.

[37] C. Iaconis and I. A. Walmsley. Spectral phase interferometry for direct electric-field reconstruction of ultrashort optical pulses. *Optics Letters*, 23(10):792, 5 1998.

[38] T. Witting, F. Frank, W. A. Okell, C. A. Arrell, J. P. Marangos, and J. W.G. Tisch. Sub-4-fs laser pulse characterization by spatially resolved spectral shearing interferometry and attosecond streaking. *Journal of Physics B: Atomic, Molecular and Optical Physics*, 45(7), 4 2012.

[39] D. J. Kane and R. Trebino. Characterization of Arbitrary Femtosecond Pulses Using Frequency-Resolved Optical Gating. *IEEE Journal of Quantum Electronics*, 29(2):571–579, 1993.

[40] K. W. DeLong, R. Trebino, J. Hunter, and W. E. White. Frequency-resolved optical gating with the use of second-harmonic generation. *Journal of the Optical Society of America B*, 11(11):2206, 1994.

[41] R. Trebino, K. W. DeLong, D. N. Fittinghoff, J. N. Sweetser, M. A. Krumbügel, B. A. Richman, and D. J. Kane. Measuring ultrashort laser pulses in the time-frequency domain using frequency-resolved optical gating. *Review of Scientific Instruments*, 68(9):3277–3295, 1997.

[42] G. Taft, A. Rundquist, M. M. Murnane, I. P. Christov, H. C. Kapteyn, K. W. DeLong, D. N. Fittinghoff, M. A. Krumbugel, J. N. Sweetser, and R. Trebino. Measurement of 10-fs laser pulses. *IEEE Journal of Selected Topics in Quantum Electronics*, 2(3):575–585, 1996.

[43] D. J. Kane and R. Trebino. Single-shot measurement of the intensity and phase of a femtosecond pulse. *Springer Series in Chemical Physics*, 18(55):138–139, 1993.

[44] N. C. Geib, R. Hollinger, E. Haddad, P. Herrmann, F. Légaré, T. Pertsch, C. Spielmann, M. Zürch, and F. Eilenberger. Discrete dispersion scan setup for measuring few-cycle laser pulses in the mid-infrared. *Optics Letters*, 45(18):5295, 9 2020.

[45] M. Hoffmann, T. Nagy, T. Willemsen, M. Jupé, D. Ristau, and U. Morgner. Pulse characterization by THG d-scan in absorbing nonlinear media. *Optics Express*, 22(5):5234, 2014.

[46] H. M. Crespo, T. Witting, M. Canhota, M. Miranda, and J. W. G. Tisch. In situ temporal measurement of ultrashort laser pulses at full power during high-intensity laser–matter interactions. *Optica*, 7(8):995, 8 2020.

[47] E. Escoto, A. Tajalli, T. Nagy, and G. Steinmeyer. Advanced phase retrieval for dispersion scan: a comparative study. *Journal of the Optical Society of America B*, 35(1):8, 1 2018.

[48] H. Kurz, H. G. Roskos, T. Dekorsy, and K. Kohler. Bloch oscillations. *Philosophical Transactions: Mathematical, Physical and Engineering Sciences*, 354(1717):2295–2310, 1996.

[49] C. Kittel and P. McEuen. *Introduction to Solid State Physics*. John Wiley & Sons., eighth edition edition, 2018.

[50] G. Vampa, C. R. McDonald, G. Orlando, D. D. Klug, P. B. Corkum, and T. Brabec. Theoretical analysis of high-harmonic generation in solids. *Physical Review Letters*, 113(7):1–5, 2014.

[51] L. Liu, J. Zhao, J. M. Yuan, and Z. X. Zhao. Role of Bloch oscillation in high-order harmonic generation from periodic structure. *Chinese Physics B*, 28(11), 2019.

[52] W. Kohn. Analytic Properties of Bloch Waves and Wannier Functions. *Physical Review*, 115(4):809–821, 8 1959.

[53] G. Vampa and T. Brabec. Merge of high harmonic generation from gases and solids and its implications for attosecond science, 3 2017.

[54] M. Gertsvolf, H. Jean-Ruel, P. P. Rajeev, D. D. Klug, D. M. Rayner, and P. B. Corkum. Orientation-dependent multiphoton ionization in wide band gap crystals. *Physical Review Letters*, 101(24), 12 2008.

[55] P. Suthar, F. Trojánek, P. Malý, T. J.Y. Derrien, and M. Kozák. Role of Van Hove singularities and effective mass anisotropy in polarization-resolved high harmonic spectroscopy of silicon. *Communications Physics*, 5(1):1–8, 2022.

[56] M. Grundmann. *The Physics of Semiconductors*. Springer International Publishing, Cham, 2021.

[57] P. Atkins, L. Jones, and L. Leroy. *Chemical Principles: The Quest for Insight*. W. H. Freeman, 7th edition, 2016.

[58] N. Tancogne-Dejean, O. D. Mücke, F. X. Kärtner, and A. Rubio. Impact of the Electronic Band Structure in High-Harmonic Generation Spectra of Solids. *Physical Review Letters*, 118(8), 2 2017.

[59] A. J. Uzan, G. Orenstein, Á. Jiménez-Galán, C. McDonald, R. E.F. Silva, B. D. Bruner, N. D. Klimkin, V. Blanchet, T. Arusi-Parpar, M. Krüger, A. N. Rubtsov, O. Smirnova, M. Ivanov, B. Yan, T. Brabec, and N. Dudovich. Attosecond spectral singularities in solid-state high-harmonic generation. *Nature Photonics*, 14(3):183–187, 3 2020.

[60] T. Kanai, Y. Lee, and D. E. Kim. Role of Van Hove singularities on high harmonic generation in solids by high power mid-IR pulses. In *Conference on Lasers and Electro-Optics*, page SW3H.7, Washington, D.C., 2020. Optica Publishing Group.

[61] F. Krausz and M. Ivanov. Attosecond physics. *Reviews of Modern Physics*, 81(1):163–234, 2009.

[62] A. H. Chin, O. G. Calderón, and J. Kono. Extreme midinfrared nonlinear optics in semiconductors. *Physical Review Letters*, 86(15):3292–3295, 2001.

[63] K. Midorikawa. High-Order Harmonic Generation and Attosecond Science. *Japanese Journal of Applied Physics*, 50(9R):090001, 9 2011.

[64] F. Krausz and M. I. Stockman. Attosecond metrology: from electron capture to future signal processing. *Nature Photonics*, 8(3):205–213, 3 2014.

[65] P. Lan, M. Ruhmann, L. He, C. Zhai, F. Wang, X. Zhu, Q. Zhang, Y. Zhou, M. Li, M. Lein, and P. Lu. Attosecond Probing of Nuclear Dynamics with Trajectory-Resolved High-Harmonic Spectroscopy. *Physical Review Letters*, 119(3), 7 2017.

[66] K. Amini, J. Biegert, F. Calegari, A. Chacón, M. F. Ciappina, A. Dauphin, D. K. Efimov, C. Figueira de Morisson Faria, K. Giergiel, P. Gniewek, A. S. Landsman, M. Lesiuk, M. Mandrysz, A. S. Maxwell, R. Moszyński, L. Ortmann, J. A. Pérez-Hernández, A. Picón, E. Pisanty, J. Prauzner-Bechcicki, K. Sacha, N. Suárez, A. Zaïr, J. Zakrzewski, and M. Lewenstein. Symphony on strong field approximation. *Reports on progress in physics. Physical Society (Great Britain)*, 82(11):116001, 2019.

[67] Z. Chang. *Fundamentals of Attosecond Optics*. CRC Press, 1st edition, 2011.

[68] J. P. Marangos and M. Oppermann. Attosecond Generation and High Field Physics. In *Ultrafast Nonlinear Optics*, pages 45–72. Springer International Publishing, Heidelberg, 1 2013.

[69] R. Zuo, X. Song, S. Ben, T. Meier, and W. Yang. Revealing the nonadiabatic tunneling dynamics in solid-state high harmonic generation. *Physical Review Research*, 5(2), 4 2023.

[70] D. Grojo, S. Leyder, P. Delaporte, W. Marine, M. Sentis, and O. Utéza. Long-wavelength multiphoton ionization inside band-gap solids. *Physical Review B - Condensed Matter and Materials Physics*, 88(19), 11 2013.

[71] V. S. Popov. Tunnel and multiphoton ionization of atoms and ions in a strong laser field (Keldysh theory). *Physics-Uspekhi*, 47(9):855–885, 9 2004.

[72] L. V. Keldysh. Ionization in the field of a strong electromagnetic wave. *Journal of Experimental and Theoretical Physics(USSR)*, 20(5):1945–1957, 11 1965.

[73] J. Li, J. Lu, A. Chew, S. Han, J. Li, Y. Wu, H. Wang, S. Ghimire, and Z. Chang. Attosecond science based on high harmonic generation from gases and solids. *Nature Communications*, 11(1):2748, 6 2020.

[74] C. B. Schaffer, A. Brodeur, and E. Mazur. Laser-induced breakdown and damage in bulk transparent materials induced by tightly focused femtosecond laser pulses. *Meas. Sci. Technol*, 12:1784–1794, 2001.

[75] S. Y. Kruchinin, F. Krausz, and V. S. Yakovlev. Colloquium: Strong-field phenomena in periodic systems. *Reviews of Modern Physics*, 90(2), 4 2018.

[76] S. Yang, X. Liu, H. Zhang, X. Song, R. Zuo, T. Meier, and W. Yang. Sub-cycle strong-field tunneling dynamics in solids. *Optics Express*, 32(9):15862, 4 2024.

[77] H. Haug and S. W. Koch. *Quantum Theory of the Optical and Electronic Properties of Semiconductors*. World Scientific, 1 2009.

[78] G. Vampa, C. McDonald, A. Fraser, and T. Brabec. High-harmonic generation in solids: Bridging the gap between attosecond science and condensed matter physics. *IEEE Journal on Selected Topics in Quantum Electronics*, 21(5), 9 2015.

[79] G. Vampa, C. R. McDonald, G. Orlando, P. B. Corkum, and T. Brabec. Semiclassical analysis of high harmonic generation in bulk crystals. *Physical Review B - Condensed Matter and Materials Physics*, 91(6), 2 2015.

[80] C. R. McDonald, G. Vampa, P. B. Corkum, and T. Brabec. Interband Bloch oscillation mechanism for high-harmonic generation in semiconductor crystals. *Physical Review A - Atomic, Molecular, and Optical Physics*, 92(3), 9 2015.

[81] P. G. Hawkins, M. Y. Ivanov, and V. S. Yakovlev. Effect of multiple conduction bands on high-harmonic emission from dielectrics. *Physical Review A - Atomic, Molecular, and Optical Physics*, 91(1), 1 2015.

[82] M. Wu, D. A. Browne, K. J. Schafer, and M. B. Gaarde. Multilevel perspective on high-order harmonic generation in solids. *Physical Review A*, 94(6), 12 2016.

[83] E. N. Osika, A. Chacón, L. Ortmann, N. Suárez, J. A. Pérez-Hernández, B. Szafran, M. F. Ciappina, F. Sols, A. S. Landsman, and M. Lewenstein. Wannier-bloch approach to localization in high-harmonics generation in solids, 5 2017.

[84] A. M. Parks, G. Ernotte, A. Thorpe, C. R. McDonald, P. B. Corkum, M. Taucer, and T. Brabec. Wannier quasi-classical approach to high harmonic generation in semiconductors. *Optica*, 7(12):1764, 12 2020.

[85] L. Yue and M. B. Gaarde. Imperfect Recollisions in High-Harmonic Generation in Solids. *Physical Review Letters*, 124(15), 4 2020.

[86] M. Lewenstein, P. Balcou, M. Y. Ivanov, A. L'Huillier, and P. B. Corkum. Theory of high-harmonic generation by low-frequency laser fields. *Physical Review A*, 49(3):2117–2132, 3 1994.

[87] Y. W. Kim, T. J. Shao, H. Kim, S. Han, S. Kim, M. Ciappina, X. B. Bian, and S. W. Kim. Spectral Interference in High Harmonic Generation from Solids. *ACS Photonics*, 6(4):851–857, 4 2019.

[88] C. M. Heyl, J. Güdde, U. Höfer, and A. L'Huillier. Spectrally resolved maker fringes in high-order harmonic generation. *Physical Review Letters*, 107(3), 7 2011.

[89] T. Y. Du, D. Tang, X. H. Huang, and X. B. Bian. Multichannel high-order harmonic generation from solids. *Physical Review A*, 97(4), 4 2018.

[90] S. Ghimire and D. A. Reis. High-harmonic generation from solids. *Nature Physics*, 15(1):10–16, 2019.

[91] D. Golde, T. Meier, and S. W. Koch. High harmonics generated in semiconductor nanostructures by the coupled dynamics of optical inter- and intraband excitations. *Physical Review B - Condensed Matter and Materials Physics*, 77(7), 2 2008.

[92] L. Li, P. Lan, X. Zhu, T. Huang, Q. Zhang, M. Lein, and P. Lu. Reciprocal-space-trajectory perspective on high-harmonic generation in solids. *Physical Review Letters*, 122(19), 5 2019.

[93] M. Wu, S. Ghimire, D. A. Reis, K. J. Schafer, and M. B. Gaarde. High-harmonic generation from Bloch electrons in solids. *Physical Review A - Atomic, Molecular, and Optical Physics*, 91(4), 4 2015.

[94] O. Schubert, M. Hohenleutner, F. Langer, B. Urbanek, C. Lange, U. Huttner, D. Golde, T. Meier, M. Kira, S. W. Koch, and R. Huber. Sub-cycle control of terahertz high-harmonic generation by dynamical Bloch oscillations. *Nature Photonics*, 8(2):119–123, 2 2014.

[95] T. T. Luu, M. Garg, S. Y. Kruchinin, A. Moulet, M. T. Hassan, and E. Goulielmakis. Extreme ultraviolet high-harmonic spectroscopy of solids. *Nature*, 521(7553):498–502, 5 2015.

[96] A. A. Lanin, E. A. Stepanov, A. B. Fedotov, and A. M. Zheltikov. Mapping the electron band structure by intraband high-harmonic generation in solids. *Optica*, 4(5):516, 5 2017.

[97] M. Hohenleutner, F. Langer, O. Schubert, M. Knorr, U. Huttner, S. W. Koch, M. Kira, and R. Huber. Real-time observation of interfering crystal electrons in high-harmonic generation. *Nature*, 523(7562):572–575, 7 2015.

[98] M. Garg, H. Y. Kim, and E. Goulielmakis. Ultimate waveform reproducibility of extreme-ultraviolet pulses by high-harmonic generation in quartz. *Nature Photonics*, 12(5):291–296, 2018.

[99] Z. Wang, H. Park, Y. H. Lai, J. Xu, C. I. Blaga, F. Yang, P. Agostini, and L. F. DiMauro. The roles of photo-carrier doping and driving wavelength in high harmonic generation from a semiconductor. *Nature Communications*, 8(1), 12 2017.

[100] Y. S. You, M. Wu, Y. Yin, A. Chew, X. Ren, S. Gholam-Mirzaei, D. A. Browne, M. Chini, Z. Chang, K. J. Schafer, M. B. Gaarde, and S. Ghimire. Laser waveform control of extreme ultraviolet high harmonics from solids. *Optics Letters*, 42(9):1816, 5 2017.

[101] Y. S. You, Y. Yin, Y. Wu, A. Chew, X. Ren, F. Zhuang, S. Gholam-Mirzaei, M. Chini, Z. Chang, and S. Ghimire. High-harmonic generation in amorphous solids. *Nature Communications*, 8(1):1–5, 2017.

[102] G. Ndabashimiye, S. Ghimire, M. Wu, D. A. Browne, K. J. Schafer, M. B. Gaarde, and D. A. Reis. Solid-state harmonics beyond the atomic limit. *Nature*, 534(7608):520–523, 6 2016.

[103] T. Tamaya, A. Ishikawa, T. Ogawa, and K. Tanaka. Diabatic Mechanisms of Higher-Order Harmonic Generation in Solid-State Materials under High-Intensity Electric Fields. *Physical Review Letters*, 116(1), 1 2016.

[104] Z. Wan, Z. Guan, J. Liu, H. Yang, K. Tian, L. He, M. Xiang, B. Hu, W. Wang, X. Yang, Y. Li, H. Wu, C. Jin, X. B. Bian, and H. Liang. Wavelength scaling of high harmonic yields and cutoff energies in solids driven by mid-infrared pulses. *Optics Express*, 31(19):30294, 9 2023.

[105] X. Liu, X. Zhu, X. Zhang, D. Wang, P. Lan, and P. Lu. Wavelength scaling of the cutoff energy in the solid high harmonic generation. *Optics Express*, 25(23), 2017.

[106] O. D. Mücke. Isolated high-order harmonics pulse from two-color-driven Bloch oscillations in bulk semiconductors. *Physical Review B*, 84(8):081202, 8 2011.

[107] S. Ghimire, A. D. Dichiara, E. Sistrunk, G. Ndabashimiye, U. B. Szafruga, A. Mohammad, P. Agostini, L. F. DiMauro, and D. A. Reis. Generation and propagation of high-order harmonics in crystals. *Physical Review A - Atomic, Molecular, and Optical Physics*, 85(4), 4 2012.

[108] J. Tate, T. Auguste, H. G. Muller, P. Salières, P. Agostini, and L. F. DiMauro. Scaling of wave-packet dynamics in an intense midinfrared Field. *Physical Review Letters*, 98(1), 2007.

[109] A. D. Shiner, C. Trallero-Herrero, N. Kajumba, H. C. Bandulet, D. Comtois, F. Légaré, M. Giguère, J. C. Kieffer, P. B. Corkum, and D. M. Villeneuve. Wavelength scaling of high harmonic generation efficiency. *Physical Review Letters*, 103(7), 8 2009.

[110] X. Liu, L. Li, X. Zhu, T. Huang, X. Zhang, D. Wang, P. Lan, and P. Lu. Wavelength dependence of high-order harmonic yields in solids. *Physical Review A*, 98(6), 12 2018.

[111] P. Dietrich, N. H. Burnett, M. Ivanov, and P. B. Corkum. High-harmonic generation and correlated two-electron multiphoton ionization with elliptically polarized light. *Physical Review A*, 50(5):R3585–R3588, 11 1994.

[112] Y. S. You, D. A. Reis, and S. Ghimire. Anisotropic high-harmonic generation in bulk crystals. *Nature Physics*, 13(4):345–349, 2017.

[113] M. Hussain, F. Lima, W. Boutu, H. Merdji, M. Fajardo, and G. O. Williams. Demonstration of nonperturbative and perturbative third-harmonic generation in MgO by altering the electronic structure. *Physical Review A*, 105(5):053103, 5 2022.

[114] C. Liu, Y. Zheng, Z. Zeng, and R. Li. Effect of elliptical polarization of driving field on high-order-harmonic generation in semiconductor ZnO. *Physical Review A*, 93(4), 4 2016.

[115] N. Tancogne-Dejean, O. D. Mücke, F. X. Kärtner, and A. Rubio. Ellipticity dependence of high-harmonic generation in solids originating from coupled intraband and interband dynamics. *Nature Communications*, 8(1), 12 2017.

[116] J. Park, A. Subramani, S. Kim, and M. F. Ciappina. Recent trends in high-order harmonic generation in solids. *Advances in Physics: X*, 7(1), 2022.

[117] N. Klemke, N. Tancogne-Dejean, G. M. Rossi, Y. Yang, F. Scheiba, R. E. Mainz, G. Di Sciacca, A. Rubio, F. X. Kärtner, and O. D. Mücke. Polarization-state-resolved high-harmonic spectroscopy of solids. *Nature Communications*, 10(1), 12 2019.

[118] N. Saito, P. Xia, F. Lu, T. Kanai, J. Itatani, and N. Ishii. Observation of selection rules for circularly polarized fields in high-harmonic generation from a crystalline solid. *Optica*, 4(11):1333, 11 2017.

[119] C. Yu, S. Jiang, and R. Lu. High order harmonic generation in solids: A review on recent numerical methods, 1 2019.

[120] L. Plaja and L. Roso-Franco. High-order harmonic generation in a crystalline solid. *Physical Review B*, 45(15):8334–8341, 4 1992.

[121] Z. Guan, X. X. Zhou, and X. B. Bian. High-order-harmonic generation from periodic potentials driven by few-cycle laser pulses. *Physical Review A*, 93(3), 3 2016.

[122] T. Ikemachi, Y. Shinohara, T. Sato, J. Yumoto, M. Kuwata-Gonokami, and K. L. Ishikawa. Trajectory analysis of high-order-harmonic generation from periodic crystals. *Physical Review A*, 95(4), 4 2017.

[123] J. Z. Jin, X. R. Xiao, H. Liang, M. X. Wang, S. G. Chen, Q. Gong, and L. Y. Peng. High-order harmonic generation from a two-dimensional band structure. *Physical Review A*, 97(4), 4 2018.

[124] M. Wu, Y. S. You, S. Ghimire, D. A. Reis, D. A. Browne, K. J. Schafer, and M. B. Gaarde. Orientation dependence of temporal and spectral properties of high-order harmonics in solids. *Physical Review A*, 96(6), 12 2017.

[125] D. Golde, M. Kira, T. Meier, and S. W. Koch. Microscopic theory of the extremely nonlinear terahertz response of semiconductors. *Physica Status Solidi (B) Basic Research*, 248(4):863–866, 4 2011.

[126] T. T. Luu and H. J. Wörner. High-order harmonic generation in solids: A unifying approach. *Physical Review B*, 94(11), 9 2016.

[127] L. Yue and M. B. Gaarde. Introduction to theory of high-harmonic generation in solids: tutorial. *Journal of the Optical Society of America B*, 39(2):535, 2022.

[128] F. C. Waldermann, B. J. Sussman, J. Nunn, V. O. Lorenz, K. C. Lee, K. Surmacz, K. H. Lee, D. Jaksch, I. A. Walmsley, P. Spizziri, P. Olivero, and S. Prawer. Measuring phonon dephasing with ultrafast pulses using Raman spectral interference. *Physical Review B - Condensed Matter and Materials Physics*, 78(15), 10 2008.

[129] G. Orlando, T. S. Ho, and S. I. Chu. Simple model of dephasing for high-order harmonic generation in solids. *Journal of the Optical Society of America B*, 37(5):1540, 5 2020.

[130] M. Kolesik and J. V. Moloney. Numerical discreteness and dephasing in high-harmonic calculations in solids. *Physical Review B*, 108(11), 9 2023.

[131] G. G. Brown, Á. Jiménez-Galàn, R. E. F. Silva, and M. Ivanov. Real-space perspective on dephasing in solid-state high harmonic generation. *Physical Review Research*, 6(4):043005, 10 2024.

[132] K. Yabana, T. Sugiyama, Y. Shinohara, T. Otobe, and G. F. Bertsch. Time-dependent density functional theory for strong electromagnetic fields in crystalline solids. *Physical Review B - Condensed Matter and Materials Physics*, 85(4), 1 2012.

[133] Z. Nourbakhsh, N. Tancogne-Dejean, H. Merdji, and A. Rubio. High Harmonics and Isolated Attosecond Pulses from MgO. *Physical Review Applied*, 15(1), 1 2021.

[134] I. Floss, C. Lemell, G. Wachter, V. Smejkal, S. A. Sato, X. M. Tong, K. Yabana, and J. Burgdörfer. Ab initio multiscale simulation of high-order harmonic generation in solids. *Physical Review A*, 97(1), 1 2018.

[135] P. Lacovara, L. Esterowitz, and M. Kokta. Growth, spectroscopy, and lasing of titanium-doped sapphire. *IEEE Journal of Quantum Electronics*, 21(10):1614–1618, 10 1985.

[136] H. Kitano and S. Kinoshita. Stable multipulse generation from a self-mode-locked Ti:sapphire laser. *Optics Communications*, 157:128–134, 1998.

[137] P. Tournois. Acousto-optic programmable dispersive filter for adaptive compensation of group delay time dispersion in laser systems. *Optics Communications*, 140:245–249, 1997.

[138] C. P. Hauri, A. Guandalini, P. Eckle, W. Kornelis, J. Biegert, and U. Keller. Generation of intense few-cycle laser pulses through filamentation - parameter dependence. *Optics Express*, 13(19):7541, 2005.

[139] M. Nisoli, S. De Silvestri, and O. Svelto. Generation of high energy 10 fs pulses by a new pulse compression technique. *Applied Physics Letters*, 68(20):2793–2795, 1996.

[140] N. Thiré, R. Maksimenka, B. Kiss, C. Ferchaud, G. Gitzinger, T. Pinoteau, H. Jousselin, S. Jarosch, P. Bizouard, V. Di Pietro, E. Cormier, K. Osvay, and N. Forget. Highly stable, 15 W, few-cycle, 65 mrad CEP-noise mid-IR OPCPA for statistical physics. *Optics Express*, 26(21):26907, 10 2018.

[141] M. Nisoli. Hollow Fiber Compression Technique: A Historical Perspective. *IEEE Journal of Selected Topics in Quantum Electronics*, 30(6):1–14, 11 2024.

[142] A. Suda, M. Hatayama, K. Nagasaka, and K. Midorikawa. Generation of sub-10-fs, 5-mJ-optical pulses using a hollow fiber with a pressure gradient. *Applied Physics Letters*, 86(11):1–3, 3 2005.

[143] E. A. J. Marcatili and R. A. Schmeltzer. Hollow Metallic and Dielectric Waveguides for Long Distance Optical Transmission and Lasers. *Bell System Technical Journal*, 43(4):1783–1809, 7 1964.

[144] R. Abrams. Coupling losses in hollow waveguide laser resonators. *IEEE Journal of Quantum Electronics*, 8(11):838–843, 11 1972.

[145] G. Fibich and A. L. Gaeta. Critical power for self-focusing in bulk media and in hollow waveguides. *Optics Letters*, 25(5):335, 3 2000.

[146] J. S. Robinson, C. A. Haworth, H. Teng, R. A. Smith, J. P. Marangos, and J. W.G. Tisch. The generation of intense, transform-limited laser pulses with tunable duration from 6 to 30 fs in a differentially pumped hollow fibre. *Applied Physics B: Lasers and Optics*, 85(4):525–529, 12 2006.

[147] W. A. Okell, T. Witting, D. Fabris, D. Austin, M. Bocoum, F. Frank, A. Ricci, A. Jullien, D. Walke, J. P. Marangos, R. Lopez-Martens, and J. W. G. Tisch. Carrier-envelope phase stability of hollow fibers used for high-energy few-cycle pulse generation. *Optics Letters*, 38(19):3918, 10 2013.

[148] G. P. Agrawal. *Fiber-optic communication systems*. Wiley, 2010.

[149] N. Matuschek, F. X. Kartner, and U. Keller. Theory of double-chirped mirrors. *IEEE Journal of Selected Topics in Quantum Electronics*, 4(2):197–208, 1998.

[150] Á. Börzsönyi, Z. Heiner, A.P. Kovács, M. P. Kalashnikov, and K. Osvay. Measurement of pressure dependent nonlinear refractive index of inert gases. *Optics Express*, 18(25):25847, 12 2010.

[151] F. Silva, B. Alonso, W. Holgado, R. Romero, J. S. Román, E. C. Jarque, H. Koop, V. Pervak, H. Crespo, and Í. J. Sola. Strategies for achieving intense single-cycle pulses with in-line post-compression setups. *Optics Letters*, 43(2):337, 1 2018.

[152] B. E. Schmidt, A. D. Shiner, M. Giguère, P. Lassonde, C. A. Trallero-Herrero, J. C. Kieffer, P. B. Corkum, D. M. Villeneuve, and F. Légaré. High harmonic generation with long-wavelength few-cycle laser pulses. *Journal of Physics B: Atomic, Molecular and Optical Physics*, 45(7), 4 2012.

[153] H. Horvath. *Light absorption in the atmosphere*. Springer Berlin Heidelberg, Berlin, Heidelberg, 2016.

[154] P. Jaeglé. *Coherent Sources of XUV Radiation: Soft X-Ray Lasers and High-Order Harmonic Generation*. Springer New York, 2006.

[155] J. Ladislas Wiza. Microchannel plate detectors. *Nuclear Instruments and Methods*, 162(1-3):587–601, 6 1979.

[156] F. Frank, C. Arrell, T. Witting, W. A. Okell, J. McKenna, J. S. Robinson, C. A. Haworth, D. Austin, H. Teng, I. A. Walmsley, J. P. Marangos, and J. W.G. Tisch. Invited review article: Technology for attosecond science. *Review of Scientific Instruments*, 83(7), 2012.

[157] N. Nakano, H. Kuroda, T. Kita, and T. Harada. Development of a flat-field grazing-incidence XUV spectrometer and its application in picosecond XUV spectroscopy. *Applied Optics*, 23(14):2386, 7 1984.

[158] T. Kita, T. Harada, N. Nakano, and H. Kuroda. Mechanically ruled aberration-corrected concave gratings for a flat-field grazing-incidence spectrograph. *Applied Optics*, 22(4):512, 2 1983.

[159] T. Harada and T. Kita. Mechanically ruled aberration-corrected concave gratings. *Applied Optics*, 19(23):3987, 12 1980.

[160] C. J. Gerritsma and J. H. Haanstra. Infrared transmission of air under laboratory conditions. *Infrared Physics*, 10(2):79–90, 6 1970.

[161] H. R. Telle, G. Steinmeyer, A. E. Dunlop, J. Stenger, D. H. Sutter, and U. Keller. Carrier-envelope offset phase control: A novel concept for absolute optical frequency measurement and ultrashort pulse generation. *Applied Physics B*, 69(4):327–332, 10 1999.

[162] A. Baltuška, T. Fuji, and T. Kobayashi. Controlling the Carrier-Envelope Phase of Ultrashort Light Pulses with Optical Parametric Amplifiers. *Physical Review Letters*, 88(13):4, 2002.

[163] A. Thorpe, N. Boroumand, A. M. Parks, E. Goulielmakis, and T. Brabec. High harmonic generation in solids: Real versus virtual transition channels. *Physical Review B*, 107(7), 2 2023.

[164] A. Schleife, F. Fuchs, J. Furthmüller, and F. Bechstedt. First-principles study of ground- and excited-state properties of MgO, ZnO, and CdO polymorphs. *Physical Review B - Condensed Matter and Materials Physics*, 73(24), 2006.

[165] Y. N. Xu and W. Y. Ching. Self-consistent band structures, charge distributions, and optical-absorption spectra in MgO, α-Al2O3, and MgAl2O4. *Physical Review B*, 43(5):4461, 1991.

[166] V. E. Nefedova, S. Fröhlich, F. Navarrete, N. Tancogne-Dejean, D. Franz, A. Hamdou, S. Kaassamani, D. Gauthier, R. Nicolas, G. Jargot, M. Hanna, P. Georges, M. F. Ciappina, U. Thumm, W. Boutu, and H. Merdji. Enhanced extreme ultraviolet high-harmonic generation from chromium-doped magnesium oxide. *Applied Physics Letters*, 118(20), 5 2021.

[167] A. Korobenko, T. J. Hammond, C. Zhang, A. Yu. Naumov, D. M. Villeneuve, and P. B. Corkum. High-harmonic generation in solids driven by counter-propagating pulses. *Optics Express*, 27(22):32630, 2019.

[168] G. Vampa, Y. S. You, H. Liu, S. Ghimire, and D. A. Reis. Observation of backward high-harmonic emission from solids. *Optics Express*, 26(9):12210, 4 2018.

[169] T. J. Shao, L. J. Lü, J. Q. Liu, and X. B. Bian. Quantum path interferences and selection in interband solid high-order harmonic generation in MgO crystals. *Physical Review A*, 101(5), 5 2020.

[170] S. Z. Xu, T. Q. Jia, H. Y. Sun, C. B. Li, X. X. Li, D. H. Feng, J. R. Qiu, and Z. Z. Xu. Mechanisms of femtosecond laser-induced breakdown and damage in MgO. *Optics Communications*, 259(1):274–280, 3 2006.

[171] D. M. Roessler and W. C. Walker. Electronic Spectrum and Ultraviolet Optical Properties of Crystalline MgO. *Physical Review*, 159(3):733–738, 7 1967.

[172] D. H. Ko, G. G. Brown, C. Zhang, and P. B. Corkum. Delay measurement of attosecond emission in solids. *Journal of Physics B: Atomic, Molecular and Optical Physics*, 53(12), 6 2020.

[173] P. Juergens, S. D. C. Roscam Abbing, M. Mero, C. L. Garcia, G. G. Brown, M. J. J. Vrakking, A. Mermillod-Blondin, P. M. Kraus, and A. Husakou. Linking High-Harmonic Generation and Strong-Field Ionization in Bulk Crystals. *ACS Photonics*, 11(1):247–256, 1 2024.

[174] A. J. Uzan-Narovlansky, Á. Jiménez-Galán, G. Orenstein, R. E. F. Silva, T. Arusi-Parpar, S. Shames, B. D. Bruner, B. Yan, O. Smirnova, M. Ivanov, and N. Dudovich. Observation of light-driven band structure via multiband high-harmonic spectroscopy. *Nature Photonics*, 16(6):428–432, 6 2022.

[175] A. J. Uzan-Narovlansky, G. Orenstein, S. Shames, M. Even Tzur, O. Kneller, B. D. Bruner, T. Arusi-Parpar, O. Cohen, and N. Dudovich. Revealing the Interplay between Strong Field Selection Rules and Crystal Symmetries. *Physical Review Letters*, 131(22), 12 2023.

[176] Y. S. You, E. Cunningham, D. A. Reis, and S. Ghimire. Probing periodic potential of crystals via strong-field re-scattering. *Journal of Physics B: Atomic, Molecular and Optical Physics*, 51(11), 5 2018.

[177] M. Hussain, S. Kaassamani, T. Auguste, W. Boutu, D. Gauthier, M. Kholodtsova, J. T. Gomes, L. Lavoute, D. Gaponov, N. Ducros, S. Fevrier, R. Nicolas, T. Imran, P. Zeitoun, G. O. Williams, M. Fajardo, and H. Merdji. Spectral control of high order harmonics through non-linear propagation effects. *Applied Physics Letters*, 119(7), 8 2021.

[178] Y. T. Zhao, S. C. Jiang, X. Zhao, J. G. Chen, and Y. J. Yang. Effect of interband polarization on a solid's high-order-harmonic generation just belowthe band gap. *Optics Letters*, 45(10):2874, 5 2020.

[179] H. Kim, S. Han, Y. W. Kim, S. Kim, and S. W. Kim. Generation of Coherent Extreme-Ultraviolet Radiation from Bulk Sapphire Crystal. *ACS Photonics*, 4(7):1627–1632, 2017.

[180] H. Allegre, J. J. Broughton, T. Klee, Y. Li, K. M. Kowalczyk, N. Thatte, D. Lim, J. P. Marangos, M. M. Matthews, and J. W. G. Tisch. Extension of high-harmonic generation cutoff in solids to 50eV using MgO. *Optics Letters*, 50(5):1492, 3 2025.

[181] L. Li, Y. Zhang, P. Lan, T. Huang, X. Zhu, C. Zhai, K. Yang, L. He, Q. Zhang, W. Cao, and P. Lu. Dynamic Core Polarization in High Harmonic Generation from Solids: The Example of MgO Crystals. *Physical Review Letters*, 126(18), 5 2021.

[182] B.L. Henke, E.M. Gullikson, and J.C. Davis. X-Ray Interactions: Photoabsorption, Scattering, Transmission, and Reflection at E = 50-30,000 eV, Z = 1-92. *Atomic Data and Nuclear Data Tables*, 54(2):181–342, 7 1993.

[183] S. Gholam-Mirzaei, J. Beetar, and M. Chini. High harmonic generation in ZnO with a high-power mid-IR OPA. *Applied Physics Letters*, 110(6), 2 2017.

[184] B. J. Sussman. Five ways to the nonresonant dynamic Stark effect. *American Journal of Physics*, 79(5):477–484, 5 2011.

[185] A. Tóth, S. Borbély, Y. Zhou, and A. Csehi. Role of dynamic Stark shifts in strong-field excitation and subsequent ionization. *Physical Review A*, 107(5), 5 2023.

[186] D. Freeman, A. Kheifets, S. Yamada, A. Yamada, and K. Yabana. High-order harmonic generation in semiconductors driven at near- and mid-infrared wavelengths. *Physical Review B*, 106(7), 8 2022.

[187] Y. Qiao, J. Chen, Z. Li, Y. Liu, S. Jiang, W. Liu, Y. Yang, and J. Chen. Analysis on the minimum structure of harmonic spectra from MgO crystals. *Optics Letters*, 49(14):3986, 7 2024.

[188] Y. Zhao, X. Xu, S. Jiang, X. Zhao, J. Chen, and Y. Yang. Cooper minimum of high-order harmonic spectra from an MgO crystal in an ultrashort laser pulse. *Physical Review A*, 101(3):033413, 3 2020.

[189] S. Jiang, C. Yu, J. Chen, Y. Huang, R. Lu, and C. D. Lin. Smooth periodic gauge satisfying crystal symmetry and periodicity to study high-harmonic generation in solids. *Physical Review B*, 102(15):155201, 10 2020.

[190] Y. Qiao, J. Chen, Y. Huo, H. Liang, R. Yu, J. Chen, W. Liu, S. Jiang, and Y. Yang. Effect of the interference between interband currents on the crystal harmonic spectra. *Physical Review A*, 107(2):023523, 2 2023.

[191] S. T. Pantelides, D. J. Mickish, and A. B. Kunz. Electronic structure and properties of magnesium oxide. *Physical Review B*, 10(12):5203–5212, 12 1974.

[192] V. Skvortsova, N. Mironova-Ulmane, L. Trinkler, and L. Grigorjeva. Optical properties of hydrogen-containing MgO crystal. In *Sixth International Conference on Advanced Optical Materials and Devices (AOMD-6)*, volume 7142, pages 71420E–71420E–7. SPIE, 9 2008.

[193] B. E. Schmidt, P. Bjot, M. Gigùre, A. D. Shiner, C. Trallero-Herrero, É. Bisson, J. Kasparian, J. P. Wolf, D. M. Villeneuve, J. C. Kieffer, P. B. Corkum, and F. Légaré. Compression of 1.8 μm laser pulses to sub two optical cycles with bulk material. *Applied Physics Letters*, 96(12), 2010.

[194] E. Feldbach, I. Kuufmann, and G. Zimmerer. Excitons and edge luminescence in MgO. *Journal of Luminescence*, 24-25:433–436, 11 1981.

[195] T. Onuma, W. Kosaka, K. Kudo, Y. Ota, T. Yamaguchi, K. Kaneko, S. Fujita, and T. Honda. Identification of free and bound exciton emission of MgO single crystal in vacuum ultraviolet spectral range. *Applied Physics Letters*, 119(13), 9 2021.

[196] R. C. Whited and W. C. Walker. Exciton Spectra of CaO and MgO. *Physical Review Letters*, 22(26):1428–1430, 6 1969.

[197] M. Fox. *Optical Properties of Solids*. Oxford University Press, 2010.

[198] R. Géneaux, C. J. Kaplan, L. Yue, A. D. Ross, J. E. Bækhøj, P. M. Kraus, H. T. Chang, A. Guggenmos, M. Y. Huang, M. Zürch, K. J. Schafer, D. M. Neumark, M. B. Gaarde, and S. R. Leone. Attosecond Time-Domain Measurement of Core-Level-Exciton Decay in Magnesium Oxide. *Physical Review Letters*, 124(20):207401, 5 2020.

[199] C. Spindler, T. Galvani, L. Wirtz, G. Rey, and S. Siebentritt. Excitation-intensity dependence of shallow and deep-level photoluminescence transitions in semiconductors. *Journal of Applied Physics*, 126(17), 11 2019.

[200] S. V. B. Jensen, L. B. Madsen, A. Rubio, and N. Tancogne-Dejean. High-harmonic spectroscopy of strongly bound excitons in solids. *Physical Review A*, 109(6), 6 2024.

[201] D. Garrido-Diez and I. Baraia. Review of wide bandgap materials and their impact in new power devices. In *2017 IEEE International Workshop of Electronics, Control, Measurement, Signals and their Application to Mechatronics (ECMSM)*, pages 1–6. IEEE, 5 2017.

[202] C. Stelling, C. R. Singh, M. Karg, T. A.F. König, M. Thelakkat, and M. Retsch. Plasmonic nanomeshes: Their ambivalent role as transparent electrodes in organic solar cells. *Scientific Reports*, 7, 2 2017.

[203] M. A. Rahman. A Review on Semiconductors Including Applications and Temperature Effects in Semiconductors. *American Scientific Research Journal for Engineering,Technology,and Sciences*, 7:50–70, 2014.

[204] H. Morkoç and Ü. Özgür. *Zinc oxide : fundamentals, materials and device technology*. John Wiley & Sons, Ltd, 2009.

[205] M. A. Borysiewicz. ZnO as a Functional Material, a Review. *Crystals*, 9(10):505, 9 2019.

[206] S. Jiang, S. Gholam-Mirzaei, E. Crites, J. E. Beetar, M. Singh, R. Lu, M. Chini, and C. D. Lin. Crystal symmetry and polarization of high-order harmonics in ZnO. *Journal of Physics B: Atomic, Molecular and Optical Physics*, 52(22), 10 2019.

[207] S. Ghimire, A. D. Dichiara, E. Sistrunk, U. B. Szafruga, P. Agostini, L. F. DiMauro, and D. A. Reis. Redshift in the optical absorption of ZnO single crystals in the presence of an intense midinfrared laser field. *Physical Review Letters*, 107(16), 10 2011.

[208] S. Xu, H. Zhang, J. Yu, Y. Han, Z. Wang, and J. Hu. Ultrafast modulation of a high harmonic generation in a bulk ZnO single crystal. *Optics Express*, 30(23):41350, 11 2022.

[209] G. Vampa, T. J. Hammond, N. Thiré, B. E. Schmidt, F. Légaré, C. R. McDonald, T. Brabec, and P. B. Corkum. Linking high harmonics from gases and solids. *Nature*, 522(7557):462–464, 6 2015.

[210] R. Hollinger, P. Herrmann, V. Korolev, M. Zapf, V. Shumakova, R. Röder, I. Uschmann, A. Pugžlys, A. Baltuška, M. Zürch, C. Ronning, C. Spielmann, and D. Kartashov. Polarization dependent excitation and high harmonic generation from intense mid-IR laser pulses in ZnO. *Nanomaterials*, 11(1):1–10, 1 2021.

[211] K. Imasaka, T. Kaji, T. Shimura, and S. Ashihara. Antenna-enhanced high harmonic generation in a wide-bandgap semiconductor ZnO. *Optics Express*, 26(16):21364, 8 2018.

[212] Z. Hu, X. Xie, Z. Yang, Y. Wang, and S. Jiang. Orientation-Dependent High-Order Harmonic Generation from Monolayer ZnO. *Symmetry*, 15(7):1427, 7 2023.

[213] S. Gholam-Mirzaei, J. E. Beetar, A. Chacón, and M. Chini. High-harmonic generation in ZnO driven by self-compressed mid-infrared pulses. *Journal of the Optical Society of America B*, 35(4):A27, 4 2018.

[214] S. D. C. Roscam Abbing, N. Kuzkova, R. van der Linden, F. Campi, B. de Keijzer, C. Morice, Z. Y. Zhang, M. L. S. van der Geest, and P. M. Kraus. Enhancing the efficiency of high-order harmonics with two-color non-collinear wave mixing in silica. *Nature Communications*, 15(1):8335, 9 2024.

[215] R. Hollinger, D. Hoff, P. Wustelt, S. Skruszewicz, Y. Zhang, H. Kang, D. Würzler, T. Jungnickel, M. Dumergue, A. Nayak, R. Flender, L. Haizer, M. Kurucz, B. Kiss, S. Kühn, E. Cormier, C. Spielmann, G. G. Paulus, P. Tzallas, and M. Kübel. Carrier-envelope-phase measurement of few-cycle mid-infrared laser pulses using high harmonic generation in ZnO. *Optics Express*, 28(5):7314, 3 2020.

[216] V. N. Jafarova and G. S. Orudzhev. Structural and electronic properties of ZnO: A first-principles density-functional theory study within LDA(GGA) and LDA(GGA)+U methods. *Solid State Communications*, 325, 2 2021.

[217] Y. Wang, T. J. Shao, X. Li, Y. Liu, P. Jiang, W. Zheng, L. Zhang, X. B. Bian, Y. Liu, Q. Gong, and C. Wu. Trajectory-controlled high-order harmonic generation in ZnO crystals. *Optics Express*, 31(2):3379, 1 2023.

[218] A. Zaïr, M. Holler, A. Guandalini, F. Schapper, J. Biegert, L. Gallmann, U. Keller, A. S. Wyatt, A. Monmayrant, I. A. Walmsley, E. Cormier, T. Auguste, J. P. Caumes, and P. Salières. Quantum path interferences in high-order harmonic generation. *Physical Review Letters*, 100(14), 4 2008.

[219] Y. W. Kim, B. Kim, S. Choi, H. K. Nam, H. Kim, Y. J. Kim, and S. W. Kim. Compensation of laser propagation effects within solids for high harmonic generation of extreme ultraviolet radiation. *Optics and Laser Technology*, 145(June 2021):107507, 2022.

[220] N. Bloembergen and P. S. Pershan. Light Waves at the Boundary of Nonlinear Media. *Physical Review*, 128(2):606–622, 10 1962.

[221] L. Cheng, S. Zhu, W. Zheng, and F. Huang. Ultra-wide spectral range (0.4–8 μm) transparent conductive ZnO bulk single crystals: a leading runner for mid-infrared optoelectronics. *Materials Today Physics*, 14, 8 2020.

[222] A. Savitzky and M. J. E. Golay. Smoothing and Differentiation of Data by Simplified Least Squares Procedures. *Analytical Chemistry*, 36(8):1627–1639, 7 1964.

[223] A. Baltuška, Th. Udem, M. Uiberacker, M. Hentschel, E. Goulielmakis, Ch. Gohle, R. Holzwarth, V. S. Yakovlev, A. Scrinzi, T. W. Hänsch, and F. Krausz. Attosecond control of electronic processes by intense light fields. *Nature*, 421(6923):611–615, 2 2003.

[224] G. Sansone, C. Vozzi, S. Stagira, M. Pascolini, L. Poletto, P. Villoresi, G. Tondello, S. De Silvestri, and M. Nisoli. Observation of Carrier-Envelope Phase Phenomena in the Multi-Optical-Cycle Regime. *Physical Review Letters*, 92(11), 3 2004.

[225] G. Sansone, C. Vozzi, S. Stagira, and M. Nisoli. Nonadiabatic quantum path analysis of high-order harmonic generation: Role of the carrier-envelope phase on short and long paths. *Physical Review A*, 70(1):013411, 7 2004.

[226] J. Bamberg, G. Cairns, and D. Kilminster. The Crystallographic Restriction, Permutations, and Goldbach's Conjecture. *The American Mathematical Monthly*, 110(3):202, 3 2003.

[227] M. Wang, Y. Zhou, Y. Zhang, E. Jung Kim, S. Hong Hahn, and S. Gie Seong. Near-infrared photoluminescence from ZnO. *Applied Physics Letters*, 100(10), 3 2012.

[228] A. R. Holkundkar, R. Rajpoot, and J. N. Bandyopadhyay. High-order harmonic generation by sub-cycle laser pulses and associated scaling laws. *Physics Letters A*, 461:128645, 2 2023.

[229] T. Gaumnitz, A. Jain, Y. Pertot, M. Huppert, I. Jordan, F. Ardana-Lamas, and H. J. Wörner. Streaking of 43-attosecond soft-X-ray pulses generated by a passively CEP-stable mid-infrared driver. *Optics Express*, 25(22):27506, 10 2017.

[230] R. Geneaux, H. J. B. Marroux, A. Guggenmos, D. M. Neumark, and S. R. Leone. Transient absorption spectroscopy using high harmonic generation: a review of ultrafast X-ray dynamics in molecules and solids. *Philosophical Transactions of the Royal Society A: Mathematical, Physical and Engineering Sciences*, 377(2145):20170463, 5 2019.

[231] G. Sansone, E. Benedetti, F. Calegari, C. Vozzi, L. Avaldi, R. Flammini, L. Poletto, P. Villoresi, C. Altucci, R. Velotta, S. Stagira, S. De Silvestri, and M. Nisoli. Isolated Single-Cycle Attosecond Pulses. *Science*, 314(5798):443–446, 10 2006.

[232] M. Guan, S. Hu, H. Zhao, C. Lian, and S. Meng. Toward attosecond control of electron dynamics in two-dimensional materials. *Applied Physics Letters*, 116(4), 1 2020.

[233] M. R. Bionta, E. Haddad, A. Leblanc, V. Gruson, P. Lassonde, H. Ibrahim, J. Chaillou, N. Émond, M. R. Otto, Á. Jiménez-Galán, R. E.F. Silva, M. Ivanov, B. J. Siwick, M. Chaker, and F. Légaré. Tracking ultrafast solid-state dynamics using high harmonic spectroscopy. *Physical Review Research*, 3(2), 6 2021.

[234] G. Vampa, B. G. Ghamsari, S. Siadat Mousavi, T. J. Hammond, A. Olivieri, E. Lisicka-Skrek, A. Yu Naumov, D. M. Villeneuve, A. Staudte, P. Berini, and P. B. Corkum. Plasmon-enhanced high-harmonic generation from silicon. *Nature Physics*, 13(7):659–662, 7 2017.

[235] S. Kaassamani, T. Auguste, N. Tancogne-Dejean, X. Liu, W. Boutu, H. Merdji, and D. Gauthier. Polarization spectroscopy of high-order harmonic generation in gallium arsenide. *Optics Express*, 30(22):40531, 10 2022.

[236] Z. Lou, Y. Zheng, C. Liu, L. Zhang, X. Ge, Y. Li, J. Wang, Z. Zeng, R. Li, and Z. Xu. Ellipticity dependence of nonperturbative harmonic generation in few-layer MoS2. *Optics Communications*, 469, 8 2020.

[237] C. Heide, Y. Kobayashi, A. C. Johnson, F. Liu, T. F. Heinz, D. A. Reis, and S. Ghimire. Probing electron-hole coherence in strongly driven 2D materials using high-harmonic generation. *Optica*, 9(5):512, 5 2022.

[238] A. García-Cabrera, R. Boyero-García, Ó. Zurrón-Cifuentes, J. Serrano, J. S. Román, L. Plaja, and C. Hernández-García. Topological high-harmonic spectroscopy. *Communications Physics*, 7(1), 12 2024.

[239] Y. Yang, J. Lu, A. Manjavacas, T. S. Luk, H. Liu, K. Kelley, J. P. Maria, E. L. Runnerstrom, M. B. Sinclair, S. Ghimire, and I. Brener. High-harmonic generation from an epsilon-near-zero material. *Nature Physics*, 15(10):1022–1026, 10 2019.

[240] T. V. Perevalov, A. V. Shaposhnikov, V. A. Gritsenko, H. Wong, J. H. Han, and C. W. Kim. Electronic structure of α-Al2O3: Ab initio simulations and comparison with experiment. *JETP Letters*, 85(3):165–168, 4 2007.

[241] Jiaqi Chen, Zhaofu Zhang, Yuzheng Guo, and John Robertson. Electronic properties of CaF2 bulk and interfaces. *Journal of Applied Physics*, 131(21), 6 2022.

[242] J. Guo, D. E. Ellis, and D. J. Lam. Electronic structure and energetics of sapphire (0001) and (11^{-}02) surfaces. *Physical Review B*, 45(23):13647–13656, 6 1992.

[243] R. Adair, L. L. Chase, and S. A. Payne. Nonlinear refractive index of optical crystals. *Physical Review B*, 39(5):3337–3350, 2 1989.

[244] A. Major, F. Yoshino, I. Nikolakakos, J. S. Aitchison, and P. W. E. Smith. Dispersion of the nonlinear refractive index in sapphire. *Optics Letters*, 29(6):602, 3 2004.

[245] T. R. Ensley and N. K. Bambha. Ultrafast nonlinear refraction measurements of infrared transmitting materials in the mid-wave infrared. *Optics Express*, 27(26):37940, 12 2019.

[246] C. R. McDonald, G. Vampa, G. Orlando, P. B. Corkum, and T. Brabec. Theory of high-harmonic generation in solids. *Journal of Physics: Conference Series*, 594(1):012021, 3 2015.

[247] J. Seres, E. Seres, C. Serrat, and T. Schumm. Non-perturbative generation of DUV/VUV harmonics from crystal surfaces at 108 MHz repetition rate. *Optics Express*, 26(17):21900, 8 2018.

[248] Y. C. Sharma, P. Ansari, R. Sharma, D. Mathur, and R. A. Dar. Bandgap tuning of optical and electrical properties of zinc selenide. *Chalcogenide Letters*, 18(4):183–189, 2021.

[249] M. E. Levinshtein, S. L. Rumyantsev, and M. S. Shur. *Properties of Advanced Semiconductor Materials: GaN, AIN, InN, BN, SiC, SiGe*. John Wiley & Sons, 2001.

[250] B. Monemar. Fundamental energy gap of GaN from photoluminescence excitation spectra. *Physical Review B*, 10(2):676–681, 7 1974.

[251] K. Van Benthem, C. Elsässer, and R. H. French. Bulk electronic structure of SrTiO3: Experiment and theory. *Journal of Applied Physics*, 90(12):6156–6164, 12 2001.

[252] F. Kohrell, B. R. Nebgen, J. A. Spies, R. Hollinger, A. Zong, C. Uzundal, C. Spielmann, and M. Zuerch. A solid-state high harmonic generation spectrometer with cryogenic cooling. *Review of Scientific Instruments*, 95(2), 2 2024.

[253] J. Gutowski, K. Sebald, and T. Voss. ZnSe: exciton energies, binding energy. In *New Data and Updates for II-VI Compounds*, pages 304–305. Springer Berlin Heidelberg, Berlin, Heidelberg, 8 2008.

[254] A. Itoh, T. Kimoto, and H. Matsunami. Exciton-Related Photoluminescence in 4H-SiC Grown by Step-Controlled Epitaxy. *Japanese Journal of Applied Physics*, 35(8R):4373, 8 1996.

[255] D. P. Norton, Y. W. Heo, M. P. Ivill, K. Ip, S. J. Pearton, M. F. Chisholm, and T. Steiner. ZnO: growth, doping & processing. *Materials Today*, 7(6):34–40, 6 2004.

[256] K. S. Syed Ali, R. Saravanan, S. Israel, and R. K. Rajaram. Electron density distribution and bonding in ZnSe and PbSe using maximum entropy method (MEM). *Bulletin of Materials Science*, 29(2):107–114, 4 2006.

[257] H. Schulz and K. H. Thiemann. Crystal structure refinement of AlN and GaN. *Solid State Communications*, 23(11):815–819, 9 1977.

[258] J. Łażewski, P. T. Jochym, P. Piekarz, M. Sternik, K. Parlinski, J. Cholewiński, P. Dłużewski, and S. Krukowski. DFT modelling of the edge dislocation in 4H-SiC. *Journal of Materials Science*, 54(15):10737–10745, 8 2019.

[259] D. T. F. Marple. Electron effective mass in ZnSe. *Journal of Applied Physics*, 35(6):1879–1882, 1964.

[260] N. Armakavicius, S. Knight, P. Kühne, V. Stanishev, D. Q. Tran, S. Richter, A. Papamichail, M. Stokey, P. Sorensen, U. Kilic, M. Schubert, P. P. Paskov, and V. Darakchieva. Electron effective mass in GaN revisited: New insights from terahertz and mid-infrared optical Hall effect. *APL Materials*, 12(2), 2 2024.

[261] H. P. R. Frederikse, W. R. Thurber, and W. R. Hosler. Electronic Transport in Strontium Titanate. *Physical Review*, 134(2A):A442–A445, 4 1964.

[262] K. Nagai, K. Uchida, S. Kusaba, T. Endo, Y. Miyata, and K. Tanaka. Effect of incoherent electron-hole pairs on high harmonic generation in an atomically thin semiconductor. *Physical Review Research*, 5(4):043130, 11 2023.

[263] Á. Jiménez-Galán, C. Bossaer, G. Ernotte, A. M. Parks, R. E. F. Silva, D. M. Villeneuve, A. Staudte, T. Brabec, A. Luican-Mayer, and G. Vampa. Orbital perspective on high-harmonic generation from solids. *Nature Communications*, 14(1):8421, 12 2023.

[264] I. Pelant and J. Valenta. *Luminescence Spectroscopy of Semiconductors*. Oxford University PressOxford, 2 2012.

[265] J. Ji, A. M. Colosimo, W. Anwand, L. A. Boatner, A. Wagner, P. S. Stepanov, T. T. Trinh, M. O. Liedke, R. Krause-Rehberg, T. E. Cowan, and F. A. Selim. ZnO Luminescence and scintillation studied via photoexcitation, X-ray excitation, and gamma-induced positron spectroscopy. *Scientific Reports*, 6, 8 2016.

[266] E. Korican-Barlay, B. R. Nebgen, J. A. Spies, and M. W. Zuerch. Solid-State High Harmonic Generation in Common Large Bandgap Substrate Materials. *Journal of Physical Chemistry A*, 2024.

[267] M. A. Reshchikov. Measurement and analysis of photoluminescence in GaN. *Journal of Applied Physics*, 129(12), 3 2021.

[268] L. Huan-Yong, J. Wan-Qi, Z. Shi-An, S. Zhen-Rong, and X. Ke-Wei. The photoluminescence of ZnSe bulk single crystals excited by femtosecond pulse. *Chinese Physics*, 15(10):2407–2414, 10 2006.

[269] P. Balling and J. Schou. Femtosecond-laser ablation dynamics of dielectrics: basics and applications for thin films. *Reports on Progress in Physics*, 76(3):036502, 3 2013.

[270] S. Han, L. Ortmann, H. Kim, Y. W. Kim, T. Oka, A. Chacon, B. Doran, M. Ciappina, M. Lewenstein, S. W. Kim, S. Kim, and A. S. Landsman. Extraction of higher-order nonlinear electronic response in solids using high harmonic generation. *Nature Communications*, 10(1), 12 2019.

[271] X. Xie, W. Yu, Y. Xiao, S. Wang, and Z. Song. Energetic Materials Photolysis Footprint in High-Order Harmonic Generation. *Journal of Physical Chemistry A*, 2025.

[272] S. Dadgostar, J. L. Pura Ruiz, J. Serrano Gutierrez, B. Lepine, P. Schieffer, and J. Jimenez. Luminescence in undoped and Nb-doped SrTiO3 crystals: Bulk and surface emission. *Materials Science and Engineering: B*, 283, 9 2022.

[273] W. Lu, A. T. Tarekegne, Y. Ou, S. Kamiyama, and H. Ou. Temperature-dependent photoluminescence properties of porous fluorescent SiC. *Scientific Reports*, 9(1), 12 2019.

[274] A. O. Konstantinov, A. Henry, C. I. Harris, and E. Janzén. Photoluminescence studies of porous silicon carbide. *Applied Physics Letters*, page 2250, 1995.

[275] P. D. Cunningham, A. T. Hanbicki, K. M. McCreary, and B. T. Jonker. Photoinduced Bandgap Renormalization and Exciton Binding Energy Reduction in WS2. *ACS Nano*, 11(12):12601–12608, 2017.

[276] B. Zhu, X. Chen, and X. Cui. Exciton Binding Energy of Monolayer WS2. *Scientific Reports*, 5(1):9218, 3 2015.

[277] J. Gu and M. Kolesik. Full-Brillouin-zone calculation of high-order harmonic generation from solid-state media. *Physical Review A*, 106(6), 12 2022.

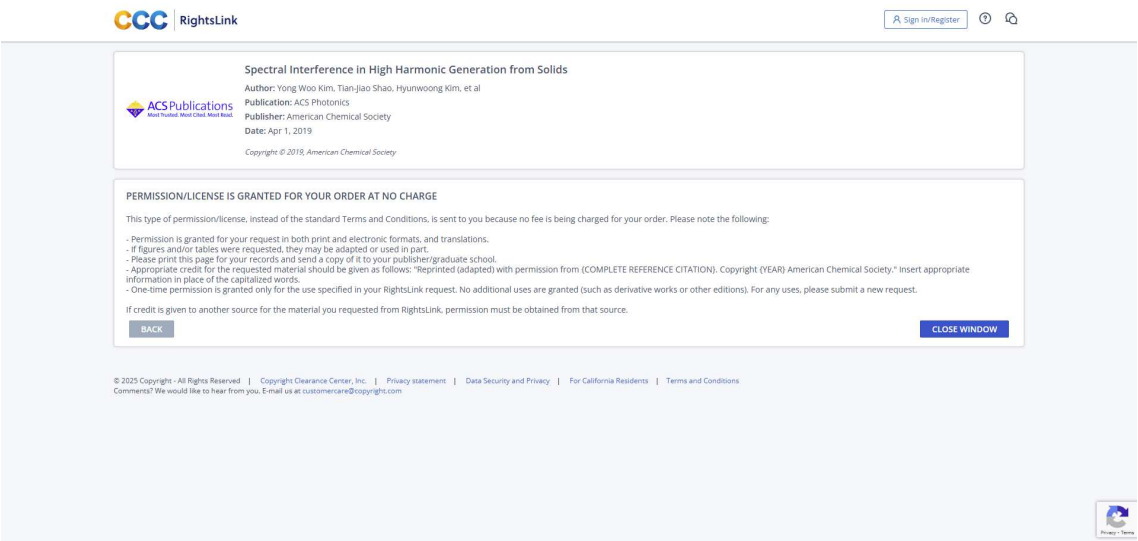
[278] D. Greening, B. Weaver, A. J. Pettipher, D. J. Walke, E. W. Larsen, J. P. Marangos, and J. W. G. Tisch. Generation and measurement of isolated attosecond pulses with enhanced flux using a two colour synthesized laser field. *Optics Express*, 28(16):23329, 8 2020.

[279] T. Y. Du and C. Ma. Temperature-induced dephasing in high-order harmonic generation from solids. *Physical Review A*, 105(5), 5 2022.

Appendix A

Copyright Permissions

I attach the permission to reproduce the figure from [87].



Appendix B

Micro-Channel Plate (MCP) Images of the Harmonics from MgO as a Function of Pulse Duration

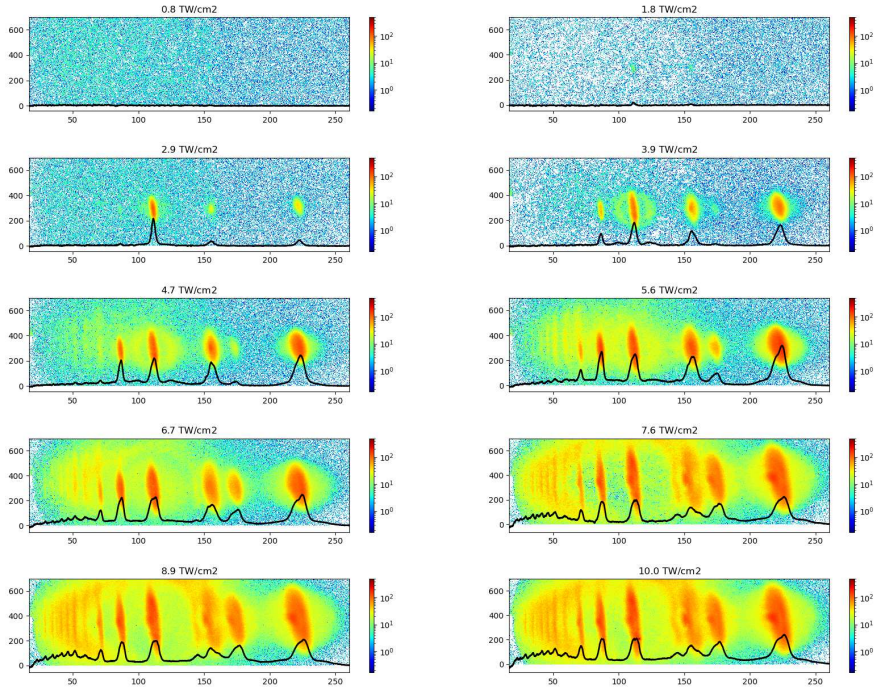


Figure B.1: MCP harmonic image for the 29 fs pulse.

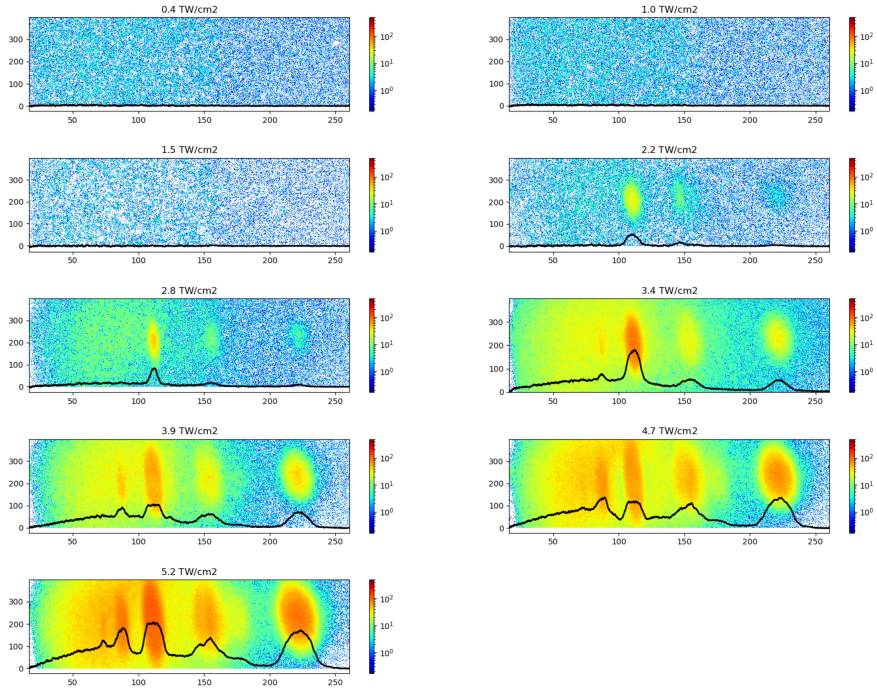


Figure B.2: MCP harmonic image for the 27 fs pulse.

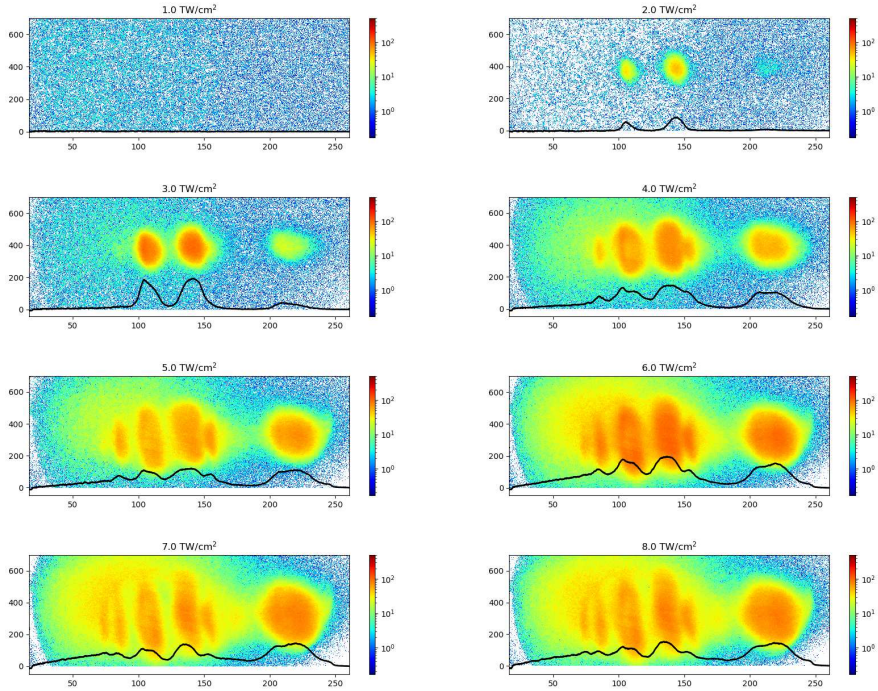


Figure B.3: MCP harmonic image for the 17 fs pulse.

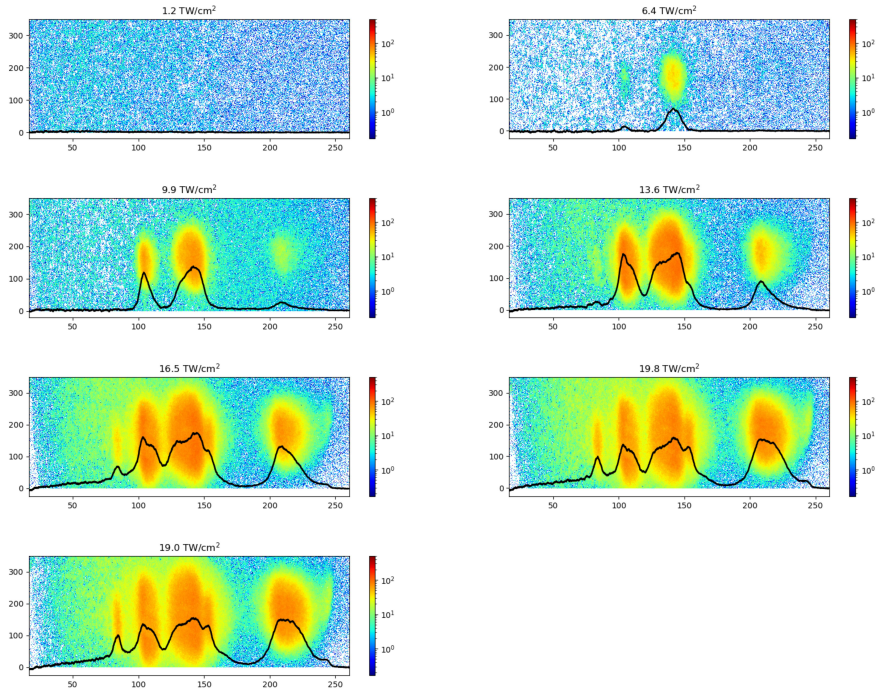


Figure B.4: MCP harmonic image for the 8 fs pulse.

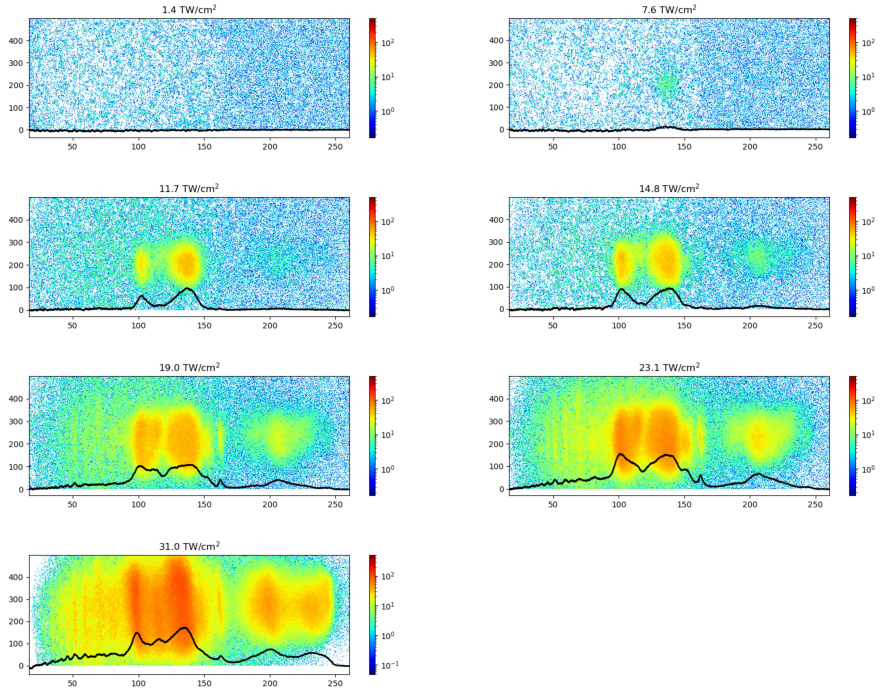


Figure B.5: MCP harmonic image for the 7 fs pulse.

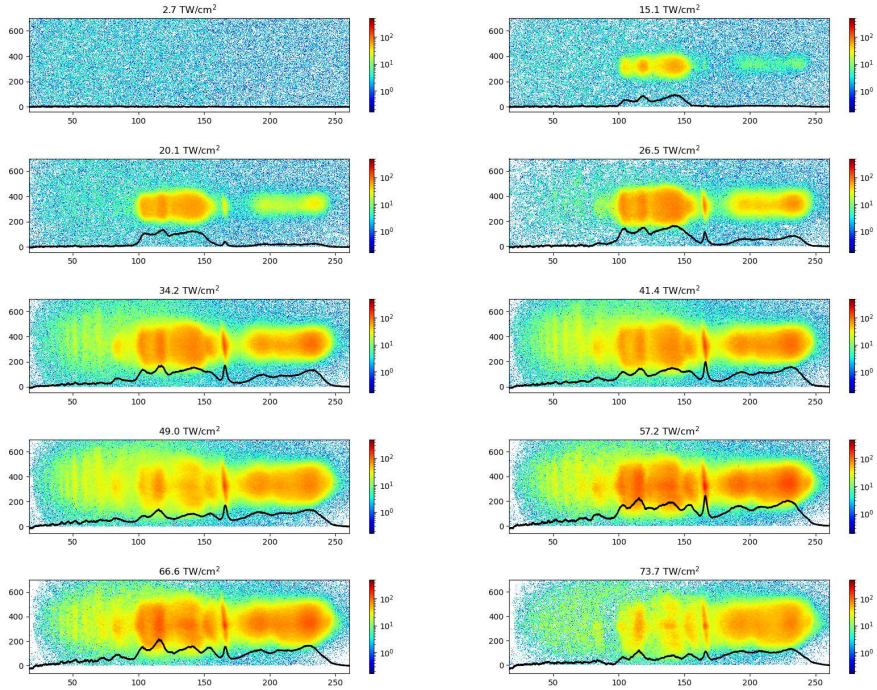


Figure B.6: MCP harmonic image for the 5 fs pulse.